NUMERICAL STUDY OF SOLITARY WAVE PROPAGATING THROUGH VEGETATION

CHEN HAOLIANG
(*B.Sci., Ocean University of China*)

A THESIS SUBMITTED
FOR THE DEGREE OF DOCTOR OF PHILOSOPHY
DEPARTMENT OF CIVIL ENGINEERING
NATIONAL UNIVERSITY OF SINGAPORE
2010

To My Parents

Acknowledgements

First of all, I would like to express my sincere gratitude to my supervisors, Professor Chan Eng Soon, and Professor Lin Pengzhi. Their patience and continuous encouragements support me to go through my initial struggling time in this long journey. Even though I progressed slowly especially in the early time, their persistent supervision, and their critical and rigorous attitudes help me gradually understand what is research and how to do research. I'm extremely grateful to them for all the efforts and concerns they provided. Their scholarship and quality will accompany me for the rest of my life. In particular, during the last stage of my study, Prof. Chan made an extreme effort on improving this thesis, and Prof. Lin created many valuable research opportunities to develop my ability. I appreciate them from my deep heart. Without them, this thesis would never have been possible.

I also like to thank my current principle investigator, Professor Paola Malanotte-Rizzoli in Massachusetts Institute of Technology, and collaborator, Dr. Pavel Tkalich in Tropical Marine Science Institute, for their support and valuable discussions in the last stage of my PhD study, and the worthwhile opportunities of visiting M.I.T. they provided.

I'm indebted to prof.dr.ir. G.S. Stelling in TU Delft, who taught me to appreciate the wonderful world of wave and hydraulic modeling through numerous inspiring talks with him.

I am also grateful to my thesis committee members, Professor Cheong Hin Fatt and A/Prof Vladan Babovic, for their insightful advice and comments on my thesis study.

The thesis has benefited from many other people's works and efforts. The numerical model developed in this study was based on the work of Dr. Wu Yongsheng and Dr. Liu Dongming, who provided a very robust platform for my further R&D of the numerical model. Their works and generosity are appreciated.

I would like to thank the technicians at Hydraulic Laboratory, especially Mr. Krishna Sanmugam and Ms. Norela Bte Buang for solving the computer problems and facilitating the experimental process during my study.

Additional thanks go to my classmates and friends, Dr. Ma Peifeng, Dr. Lin Quanhong, Mr. Sun Yabin, Mr. Xu Haihua, Dr. Su Xiaohui, Dr. Gu Hanbin, Dr. Teng Mingqing, Ms. Liu Xuemei, Mr. Zhang Dan, Mr. Zhang Wenyu, Dr. Shen Linwei, Mr. Shen Wei, Dr. Fernando and Dr. Anuja, for their friendship and valuable discussion during the study. Special thanks go to Dr. Cheng Yonggang for helping me solve many computer and software problems. I also would like to thank my other friends, Mr. Zhou Jinxin and Dr. Xie Yi. I really spent a great time with you and cherish the brotherhood among us.

Last but not least, I like to express my gratitude from the bottom of my heart to my parents. They have been protecting me from the hardship of life they have suffered. They have also been teaching and encouraging me to overcome the challenges of life with the determination and persistence they showed in front of difficulties. Thank them very much for their continuous and invaluable support in my life. I also like to thank my wife for her love, patience and care. The marriage with her is one of my best achievements during this study. I could not finish the whole study without the supports from all of them.

Table of Contents

Summary

Many lives were lost when the devastating tsunami hit the Indian Ocean in December 2004. The devastating impact has urged the coastal engineering community to understand the extend of the flooding area caused by tsunami waves and to explore the mitigation measures to reduce the wave run-up or slow down the speed of the flooding. In this study, the effects of vegetation on the tsunami wave propagation are investigated through the study of solitary wave propagating past vegetation. The overall objective is to understand the physics of wave height reduction and wave energy dissipation in the presence of non-submerged rigid vegetation with different vegetation conditions. A combined theoretical, experimental and numerical approach is adopted.

Theoretically, a temporal-volume double averaging method is employed to average the original three dimensional Navier-Stokes equations to introduce the vegetation effect into the fluid governing equations. This approach avoids the problem of a simple addition of the drag-related body force in the momentum equation which does not represent the energy budget correctly. After the double averaging, a system of modified momentum equations and energy budget equation is obtained by parameterizing the vegetation-related terms. The new system of equations has been successfully applied to the general three-dimensional fluid-vegetation problems, along with vegetation-related parameters that have been systematically derived, calibrated and validated.

In the above modified equations, drag force coefficient and inertial force coefficient are among the most significant parameters to be quantified. A series of experiments of wave

propagating within the vegetation are conducted to investigate the variation of drag force coefficient and inertial force coefficient with wave conditions. Based on the experimental data, an empirical formula to calculate the vegetation drag force coefficient has been derived as a function of not only the Renolds number Re and porosity, which are largely used in vegetation-open channel flow problem, but also KC number that can feature the wave characteristic. The formula can be used in the numerical modeling of vegetation effect on wave propagation.

Incorporating the above work, a new three-dimensional wave/flow model has been developed based on NEWTANK (Liu, D M, 2007) to study the fluid-vegetation interaction problem. The numerical model solves the newly derived system of equations for the two phase flow. The rigid vegetation is represented by the distribution of porosity which provides the convenient treatment of non-homogeneous distributed vegetation. A two-step projection method has been employed in the numerical solution, accompanied by a Bi-CGSTAB technique to solve the Pressure Poisson Equation (PPE) for the averaged pressure field. Volume-of-Fluid (VOF) method that is of second-order accuracy in interface reconstruction is used to track the free surface evolution. The drag and inertial force coefficients from current experiments are imbedded in the model.

The numerical model has been successfully validated against available analytical wave solutions and experiments without vegetation in terms of accuracies of free surface and velocity field. The model has also been used to study several cases of solitary wave propagating through vegetation. The results show that porosity and the coverage length of the vegetative region are two of the dominant factors on reducing wave height and current velocities. The effect of increasing the coverage length of vegetation can be

equally achieved by reducing the porosity. In practice, an optimal arrangement of vegetation length and spacing should consider the vegetation characteristics. The force coefficients seem to be insignificant in the wave height dissipation at least in the condition of large porosity. The gap in vegetation region can amplify the current velocities and form a water jet which can cause more severe damages on the assets or human beings on its way. For the general porosity of mangrove (85%-95%), the coverage length of 10-20m can reduce half of the incident wave height. However, special attention should be paid to the region having a vegetation gap. Coastal structures such as breakwaters are required to protect the assets along the gap. The spacing of the vegetation gap is suggested to be as small as possible with the fulfillment of usage. In general, the numerical model has been approved to be a robust model for the study of wave-vegetation problem and can be used in the future coastal engineering studies.

List of Tables

List of Figures

List of Symbols

A	The frontal area of vegetation normal to the flow/wave direction
$A_{\beta\sigma}$	interface between the fluid phase and vegetation phase
Cd	Drag force coefficient of vegetation
Cm	Inertial force coefficient of vegetation
$C_{\varepsilon 1}, C_{\varepsilon 2}$	Coefficient in turbulent ε-equation
C_D	empirical coefficient related with ν_t
c	Wave phase celerity
D	Diameter of vegetation rod
F	volume of fluid (VOF) function
Fi	The total force of vegetation on fluid in i-direction
F_{Di}	The drag force of vegetation on fluid in i-direction
Fi	The inertial force of vegetation on fluid in i-direction

g_i	mass force per unit mass in i direction
H	Wave height
h	Still water depth
k	Wave number
k	turbulence kinetic energy (TKE)
KC	Keulegan-Carpenter number
m_1, m_2, m_3	X,y,z-components of the unit normal vector
M	Average mass flux
n_i	the unit normal direction pointing from fluid into solid phase
P_W	the wake production
p	pressure of fluid
Re	Reynolds number
S	Spacing of vegetation rod
T	Wave period
U	Uniform current flow velocity
u_i	the fluid velocity in i direction
u_o	maximum horizontal water particle velocity
u_*	friction velocity
V	Control volume
V_β	Volume occupied by fluid
$\alpha_0, \alpha_1, \alpha_2$	Empirical coefficient in the formula of drag coefficient
κ	von Karman constant
ρ	density of fluid
ρ_a	Density of air
ρ_w	Density of water

ψ	A physical variable
$\bar{\psi}$	Time averaged variable
ψ''	Deviation of a variable from its volume averaged value
ψ'	Fluctuation of a variable from its time average
ν	kinematic viscosity of the fluid
ν_t	Eddy viscosity
η	Free surface elevation
η_ε	efficiency of production of $\langle\varepsilon\rangle^\beta$
η_k	the efficiency of TKE
σ_k	Coefficient in turbulent k-equation
σ_ε	Coefficient in turbulent ε-equation
ε	Turbulent dissipation rate
θ	porosity
ΔR	Residual between calculated and measured vegetation force
δ_{ij}	Kronecker delta
$\forall$	The volume of vegetation submerged in the fluid
$\langle\ \rangle^s$	Superficial average
$\langle\ \rangle^\beta$	Intrinsic average

Chapter 1

Introduction

1.1 Background

Many lives were lost when the devastating tsunami hit Indian Ocean in December 2004. Vast damages along the coastal areas of Indian Ocean, especially at the northwest side of the island of Sumatra, have been reported. These occurrences and the devastating impact have reminded the coastal engineering community that, while the damages are expected, much of the physics of tsunami waves is still not understood. In particular, the extends of flooding areas caused by tsunami waves and the mitigation measures to reduce the wave run-up or slow down the speed of the flooding are not well understood. In recent years, the ability of vegetation in damping or dissipating fluid flows has attracted the attention of more and more researchers. Most of the publications, however, were limited to open channel flow studies. Few of them were developed for coastal hydraulics (Turker, U., et al. 2006), especially the interaction between waves and vegetation during a wave run-up process. Typically speaking, the problem has been studied under two broad categories. One is the wave problem of a wave run-up process on a slope of bottom

and the other is the influence of vegetation on the wave transformation. A significant improvement on the understanding of this problem is needed for the development of more efficient and economic techniques to protect coast and human lives. In this dissertation, the physics of a tsunami wave runup through vegetation is studied.

1.2 Literature review

1.2.1 Studies of wave run-up

The earlier work on long wave runup relied largely on analytical approaches. In one well-known paper, Carrier and Greenspan (1958) (referred to herein as CG) proposed a nonlinear transformation to convert the nonlinear shallow water equations to a single linear equation so that analytical solutions can be obtained for a few specific initial-value problems. Synolakis (1987) used Carrier and Greenspan's solution and presented an analytical solution for nonbreaking solitary waves propagating over constant depth and then climbing on a sloping beach. Using the linear shallow water equations, Kanoglu and Synolakis (1998) presented analytical results for a beach with composite linear slopes. Recently, Carrier, et al.(2003) reconsidered and modified CG's original approach and provided a general solution technique accounting for arbitrary initial-value conditions.

With the fast advancement of computer speed and the continuous improvement of the computational techniques, more and more numerical models have been developed to investigate wave run-up and the subsequent breaking processes. Based on the shallow water equations, under the assumption of hydrostatic pressure, Kobayashi et al. (1987) developed a numerical model using the Lax-Wendroff method to study long wave run-up on slope. Liu et al. (1994) employed the staggered leap-frog method to solve the shallow

water equations and studied the large scale tsunami propagation in ocean and inundation in coastal area. Using the same model, Liu et al. (1995) also simulated the solitary wave runup on a circular island. However, the shallow water equations couldn't provide complete information of the wave and the accompanied turbulence evolution in three-dimensions.

Considering the flow problems where vertical variations of the velocity are significant, Kim et al. (1983) first used the boundary integral equation method (BIEM) to study the two-dimensional solitary wave runup. Grilli and Svendsen (1990) refined the BIEM model to investigate the runup of other types of nonlinear waves. This method was further successfully adopted by Skyner (1996) to simulate the plunging breakers in deep water. Grilli et al. (1997) simulated solitary wave shoaling on slopes. Yasuda et al. (1997) and Grilli et al. (1994) studied the solitary wave breaking on submerged breakwaters. Evidently, the BIEM model is an excellent tool for the study of nonbreaking wave runup and rundown in laboratory experiments. However, the model is limited by the physical hypotheses of irrotational motion of an inviscid fluid and the neglect of air effects. If the wave surface jet touches the front water-air interface, a rotational, viscous, and two-phase flow model must be developed to simulate the generation and transport of vorticity and turbulence.

To overcome the above limitations, a more robust hydrodynamic model which solves the basic incompressible Navier-Stokes equations (NSE) must be developed. In principle, the direct numerical simulation (DNS) for the NSE can be used for any turbulence flow and breaking wave study. However, because of the high demand of computational time required by the DNS, most applications are only conducted at low or

intermediate Reynolds number (Kim et al., 1987; Hendrickson and Yue, 1997). For water waves problems at high Reynolds number, with the additional complication of strong free surface deformation, an alternative method is to solve the Reynolds Averaged Navier Stokes(RANS) equations. In RANS equations, only ensemble averaged flow motion is described. The effects of turbulence on the mean flow are represented by Reynolds stresses which are in turn resolved with a turbulence closure model. Such an approach has been used to simulate breaking waves (e.g. Lemos (1992) and Lin and Liu (1998a, 1998b)). Another increasingly popular method is the large eddy simulation (LES) approach. Turbulence is taken into consideration in the spatially averaged Navier Stokes equations by using a sub-grid scale (SGS) model (Deardorff, 1970) to simulate the small scale turbulence effect. Zhao and Tanimoto (1998) first applied the LES method to breaking waves and are able to produce accurate results when compared with experimental data. Recently, Christensen (2006) used the LES method to study wave breaking process, undertow and the turbulence in breaking waves. Good results are obtained.

1.2.2 Studies on the interaction between fluid flows and vegetation

Early works on flow in watercourse with vegetation are summarized by Chow (1954) and Henderson (1966). Initially, many studies attempted to expand the conventional flow resistance formulae to account for the effect of vegetation with empirically determined resistance coefficients, such as Manning's roughness coefficient (n), Chezy's resistance factor (C), and the Darcy-Weisbach friction factor (f). Based on this concept, Ree and Palmer (1949) presented a set of graphical-format design n-VR (V is average velocity and

R is the hydraulic radius) curves for different resistance classes for flow with submerged vegetation. In their curve, *n* was a function of *VR*, the product of the average velocity and the hydraulic radius. Later, Kouwen and Unny (1973) for the first time defined a biomechanical parameter *MEI* (the product of stem density *M*, stem modulus of elasticity *E*, inertia of the second moment of the stem area *I*), which could then be related to the hydraulic resistance. Li and Shen (1973) used cylinders in a flume to represent trees on floodplains to study the flow resistance by investigating the wakes caused by various cylinder set-ups. They demonstrated that staggering the cylinders were much more effective in reducing flow rates than if the cylinders were directly aligned. Their work was extended resulting in a method to calculate the drag coefficient for a single plant in a group and further the friction factor for the vegetation in non-submerged conditions (Pasche and Rouvé, 1985).

Following the above-mentioned pioneers, many researchers have made significant advances on the understanding of resistance effect of vegetation in channel flow. Experimentally, Kouwen and Fathi-Maghadam (Kouwen, 1992; Fathi-Maghadam and Kouwen, 1997; Kouwen and Fathi-Maghadam, 2000) conducted flume experiments using coniferous tress saplings and branches, and derived relations between the Darcy-Weisbach friction factor and several dominant non-dimensional parameters with regard to conifers from those experiment results. They showed that the friction factor varied greatly with the mean flow velocity due to bending of the vegetation and with flow depth as a result of an increase in the submerged momentum absorbing area (Järvelä, 2002). By carrying out flume experiment with horsehair simulating the vegetation, Wu et al. (1999) revealed that the roughness coefficient decreased with increasing depth under the

unsubmerged condition. Further, when fully submerged, the roughness coefficient increased at low inundation but then decreased to an asymptotic constant with rising water level. To simplify and generalize the characteristics of different kinds of vegetation, some researchers assumed the vegetation as rigid cylinders and used rigid rods to conduct experiments. By this way, flow resistance under the conditions of both emergent and submerged vegetation have been examined (James et al. 2004; Musleh and Cruise, 2006). The influence of the Reynolds number on the drag coefficient was widely analyzed by Nepf who also used non-submerged rigid cylinders to simulate the plants (Nepf, 1999). One of the important conclusions was that the upstream plants affected the wakes dynamics of downstream plants due to the sheltering effect. However, considering the large variety of properties of different vegetation, natural plants are irreplaceable in the experiments. Järvelä (2002) investigated the variation of friction factor with the corresponding *Re*, flow velocity, and water depth in the conditions of different combinations of natural stiff and flexible vegetation. Later, Järvelä (2005) carried out the flume studies to investigate flow structure above flexible vegetation and reported a new data set of mean velocity profiles and turbulence characteristics from experiments with wheat. Through experiments conducted with the macrophyte, Stephan and Gutknecht (2002) defined a characteristic hydraulic roughness parameter to quantify the resistance of aquatic vegetation. Sand-Jensen(2003) noted that increasing bending and streamlining of the plant by increasing the external velocities would reduce the effective size of the macrophyte, and hence drag. A comprehensive review on the understanding of how aquatic macrophytes influence flow resistance was presented by Green (2005). It has been generally agreed that vegetation not only increases the flow resistance, but also

controls the mean and turbulent flow structure in channels and coastal regions (Yen, 2002; Nepf and Vivoni, 2000).

Considerable advances in the understanding of vegetation effects on the turbulence structure and energy budgets have been achieved by meteorologists who have thoroughly investigated the plant canopy air flow through theoretical, experimental and numerical manners since 1970s. One of these important work could be attributed to Wilson and Shaw (1977), who developed a higher order closure model for canopy flow. They are the first to recognize the necessity of spatial, as well as temporal, averaging of the governing equations for the proper 1D representation of the problem (López and Garcia, 2001). Based on the Wilson and Show's work, Raupach and Shaw (1982) clearly stated the rules governing the communication of spatial averaging operators and spatial differentiation, then obtained the momentum and energy equations for multi-connected flows. Their work identified different momentum and energy dispersive terms, associated with the 3D nature of the flow structure and the non-commutation of the operators. The historical developments to date in the area of canopy flow have been rigorously surveyed by Raupach and Thom (1981) and Finnigan (2000).

In spite of late awareness on this topic by the hydraulic community, significant progress has been made in the past decade. Through experiments, Tsujimoto and Kitamura (1992) pointed out that transverse mixing is caused by rather organized and low-frequency fluctuation of transverse velocity, and is associated with the fluctuation of free surface. Many researchers (Tamai et al.,1986; Chu et al., 1991; and Ikeda et al. 1994) reported the existence of horizontal large scale eddies at the places of sharp velocity gradient both in the field and laboratory. Nepf and Vivoni (2000) conducted experiments

on a simulated plant canopy. They examined the transition from emergent to submerged flow conditions, and investigated the turbulence structure. They found that in the submerged conditions, the Reynolds stress profile reaches a peak at the interface and decays within and above the canopy, which is demonstrated by other's experiments (Righetti and Armanini, 2002; Wilson, et al., 2003). More recently, Nepf and her collaborators have also focused on the dispersion phenomenon in the vegetated flow (Murphy, E. et al. 2007; Tanino, Y. and Nepf, H., 2008).

Numerically, by relating vegetation effect to roughness or resistance equation and grouping it with bed roughness as a factor, researchers have obtained the stage-discharge relation for vegetated channels or rivers. Darby and Thorne (1996) developed a method to predict stage-discharge curves for straight gravel-bed channels with flexible vegetation on the floodplains and steady uniform flow, using an eddy viscosity model and Kouwen's (1988) roughness estimation methods of flexible vegetation. Later, Darby (1999) included sand bed and rigid floodplain vegetation in the model. Subsequently, Helmiö (2002) proposed a 1D unsteady flow model with Darcy-Weisbach friction factor computed by Nuding's method. Results from this model are applied to the Rhine River which showed strong correlation between predicted and measured flow resistance characteristics (Helmiö, 2005). Similar work can also been found in other literatures (Yoshida, H. and Dittrich A., 2002; Anderson B.G., et al., 2006).

Several researchers have also studied the flow resistance of rigid surface-piercing vegetation. In their studies, the vegetation was simulated by a group of cylinders with the same height and diameter at a regular or random spacing (Meijer and Van Velzen, 1999; Nepf, 1999; Su and Li, 2002). An interesting approach is from Baptist and his

colleagues (2007), who for the first time applied genetic programming to vegetation-related hydraulic analysis.

More and more researchers are conducting numerical experiments to understand the turbulent characteristics in vegetated flow. Early literatures have suggested that the simple local-diffusion models of turbulence transport are seriously deficient (Raupach and Tom, 1981). Subsequently, in a study of the flow field above a plant canopy, Shimizu et al. (1992) used a $k-\varepsilon$ turbulent model with additional drag-related source terms to account for the presence of vegetation. Weighting factors in these source terms were fit to reproduce observed distributions of mean velocity and Reynolds stresses. Relatively good agreement with the experimental data was obtained. Similarly, based on Raupach and Show's (1982) analysis, Lopez and Garcia (1997,2001) employed two-equation $k-\varepsilon$ and $k-\omega$ turbulence closure models to solve the double-averaged governing equations but using different treatment of drag coefficient and the weighting coefficients from Shimizu's work. Shimizu's (1992) and Lopez and Garcia's (1997,2001) work have been compared, re-computed and commented by several researchers (Neary, 2003; Defina, A., Bixio, A. C., 2005). There were also other turbulence closure models including vegetation effect. Naot et al. (1996) developed a steady three-dimensional flow model with an algebraic stress model (ASM) of turbulence to study the turbulent flow in compound open channel with vegetation. In this model, the importance of the distribution pattern of vegetation on the shading factors is highlighted. However, as a steady model, it is unable to simulate the dynamic evolution of horizontal large scale eddies, and the influence of flow geometry on the development of shear layer with large eddies may not be reproduced. Based on the time and spatial-averaged velocity and Reynolds stress

profiles, Righetti and Armanini (2002) proposed an analytical two-layer model in order to describe the characteristics of open channel flow with sparsely distributed bushed on the bed. However, the turbulent structure through and above the vegetation has not been fully understood yet.

In the last decade, large eddy simulation (LES) attracted more and more interests of researchers. This method has been used to study flow dynamics in and above different kinds of vegetation in the atmospheric boundary layer (Shaw and Schumann, 1992; Patton et al., 1998; Fitzmaurice L., et al. 2003; Poggi D. et al. 2004; Watanabe, T. 2004). For the open channel flow with vegetated domain, there have been few detailed studies using LES. Using a two-dimensional depth-integrated model, Nadaoka and Yagi (1998) computed shallow water turbulence for flow in channel with vegetation bank and found that the model could account for the effects of flow geometry on the large-scale eddy development, and the model performance was better than the depth-integrated $K-\varepsilon$ model. However, this two-dimensional depth-integrated LES model is only applicable to shallow water environment with non-submerged vegetation. Besides Nadaoka and Yagi's work, large eddy simulation of flow through vegetation has been reported by Su and Li (2002), and Cui and Neary (2002), who used the dynamic subgrid scale turbulence model. To take the flexibility of vegetation into consideration, Ikeda et al. (2001) proposed a 2D-LES model in which a concept of "plant grid" is used to treat the movement of plant in addition to the ordinary LES grid. The model identified the effect of the movement of the plant on the turbulent flow via the resistance to flow, the turbulence production and the dissipation.

Compared with experimental and numerical work, an analytical solution of velocity distribution for the flow passing vegetation is much more difficult, especially given the complex configurations and biomechanical properties of various vegetation. By treating vegetation as a homogenous field of identical cylindrical stems and considering the scaling effect, Huthoff and his colleagues (2007) derived an analytical model for the depth-averaged flow velocity in the presence of submerged vegetation. In another study, Hsieh and Shiu (2006) has also used an analytical approach to investigate the vertical velocity profile of flow passing over a vegetal area. In the study, the soil and vegetation layers were modeled as homogeneous and isotropic porous media.

1.2.3 The studies of the interaction between waves and vegetation

Compared to flows in vegetated channels, the problem of waves propagating through vegetated domain is much less understood. Detailed field measurements and laboratory experiments with specific vegetation have, however, shown that the effects of vegetation varied widely. Elwany and his colleagues (Elwany, et al., 1995; Elwany and Flick, 1996) investigated the effect of giant kelp (*Macrocystic pyrifera*) on shoreward propagating surface gravity waves in Southern California and concluded that there was no significant effect on waves as well as no direct influence on adjacent-beach width. On the contrary, by using the digital photographic method, field measurements and numerical modeling, Möller and his team (Möller et al., 1999; Möller, 2006) showed that saltmarsh environment in a variety of physical settings, which is common in the north-eastern of UK and north-west European open coast environment, can significantly

increase attenuation of incident waves compared to unvegetated sand/mudflats. The reduction can be even up to 50% over the first 10-20m of vegetated saltmarsh surface for northwest European marshes. Other reports include the work from Dubi (1995), Mork (1996), Andersen et al.(1996), Massel et al.(1999), Lovas and Torum (2001) et al.

Numerical and analytical models to study wave-vegetation interaction have been developed. But most approaches are based on the investigations of flow in porous media (Liu and Dalrymple, 1984; Gu and Wang, 1991; Breugem et al., 2005; Karunarathna and Lin, 2006). Differently, Kobayashi et al. (1993), and Sawaragi and Deguchi (1992) made some of the pioneering works. Dalrymple, et al. (1984) studied the wave diffraction caused by energy dissipation to calculate the damping due to a cluster of cylinders which represent the effect of a dense stand of giant kelp. Kobayashi et al. (1993) developed an analytical model to describe the vertically two-dimensional problem of small amplitude waves propagating over submerged or sub-aerial vegetation. The vegetation resistance is described by quadratic friction law with an empirical drag coefficient. Later, Asano et al. (1993) extends Kobayashi et al.'s model by including the interaction between the wave and vegetation swaying motion which is modeled as a forced vibration with one degree of freedom. Recently, starting from Dalrymple et al.'s (1984) theory, Mendez and Losada (2004) carried out several extensions to take into account the bottom variations, the randomness of waves and to include both vegetation and breaking dissipation in the surf zone. Their model depends on a single parameter similar to the drag coefficient, which can be parameterized from experiments for each type of plant. The model is able to reproduce the root-mean-square wave height transformation obtained from laboratory data. To have a comprehensive understanding of the numerical modeling on this subject,

Teeter et al.(2001) have listed detailed aspects to be considered in numerical modeling of the effect of vegetation on wind waves and sediment transport in shallow water system. As for the latest status and results from modelers on this topic, it is presented by Li and Yan (2007) on investigation of wave-current-vegetation interaction.

Compared to the literature on wave-vegetation interaction, the availability of literature on the specific effect of forest or vegetation on tsunami is worse. Many Japanese researchers have conducted extensive studies on this topic. Harada and Imamura (2005) discussed the effects of coastal forest on tsunami hazard and presented results of numerical simulation for various forest width, density, tsunami heights and period, to quantitatively examine the effect of coastal forests. Imai and Matsutomi (2005) conducted their flume experiments to evaluate the fluid forces of tsunami acting on coastal vegetation and showed the temporal variation of drag force, inertia force and wave-making resistance forces, as well as estimation of drag and inertial coefficients.

Most of the above studies, while providing insights to the details of the flow through vegetations, are mostly analyzed to understand the flow regime in open channels and especially in flood plains, and only a few are developed for coastal hydrodynamics. Very little is done to understand the physics of waves approaching the sloping beach with vegetation, including wave deformation and energy dissipation at the coastal regions.

1.3 Objective and scope of present study

Although there were numerous studies on flows past vegetation, very little is done to understand the problem of waves propagating through vegetation. In particular, the

process and the amount of energy dissipation, the dependence on key vegetation parameters, and how the significant parameters affect the wave propagation are still poorly understood. The overall objective of the present study is to better understand the physics of tsunami wave propagation, deformation and dissipation with the presence of vegetation by the combination of rigorous theoretical derivation, experiments and numerical modeling, which explore different aspects of this problem. Different factors of vegetation, such as vegetation drag and inertial coefficients, vegetation coverage length, vegetation porosity, are studied to quantify their effects and relative importance on the wave dissipation and deformation. More specifically, the objectives are:

1. To derive a set of governing equations for the study of general fluid-vegetation problem by analytically introducing the vegetation drag force and inertial force into the momentum equations and energy budget equation.
2. To develop a full 3-D model capable of simulating the process of wave propagation through the vegetation domain based on the derived general governing equations.
3. To conduct experiments to estimate Cd and Cm and propose an empirical formula for the calculation of vegetation forces in the modeling.
4. To simulate the wave propagation within vegetation domain using the developed model and proposed empirical formula of Cd and Cm.
5. To better understand the physics of wave propagation and deformation through vegetation with designed numerical cases.

The theoretical derivation is first introduced in Chapter 2, in which the vegetation effects are introduced into the equations of the momentum balance and energy budget based on

the spatial-temporal double averaging process. As a result, the unsteady three-dimensional governing equations with vegetation effects are obtained, which are the general governing equations for all kinds of the studies of rigid vegetated flow problems, especially for the wave evolution on vegetated slopes with the aid of Volume of Fluid (VOF) method.

To close the governing equations, several vegetation-related parameters are introduced which can only be quantified by experiments. Among those parameters, the drag and inertial force coefficients, which present in both the momentum equations and energy budget equation, are of significant importance. In Chapter 3, designed experiments and their results are presented to quantify the drag and inertial force coefficients, and try to provide a generalized expression, which can be used in the numerical modeling.

In Chapter 4, the details of the numerical implementations of the derived governing equations are given. Once the model is established, the numerical model is first validated by the non-vegetated channel flow and wave propagation problems, which are presented in Chapter 5. In the same chapter, the channel flow and wave problem with the existence of vegetation are studied and compared with available experimental data. Generally speaking, good agreements are achieved, showing the robustness of the new developed model. The effects of different characteristics of vegetation domain are also studied with several numerical cases. The importance of the vegetation coverage length and porosity on wave reduction is quantified. The potential damage of a gap within vegetation region is studied as well.

In the last chapter (Chapter 6), the summaries of the study are given. The contributions and main discoveries of current studies are highlighted.

Chapter 2

Governing Equations for Turbulent Flow Motion under the Effect of Vegetation

2.1 Introduction

The effects of vegetation on fluid flows are inherently three dimensional. These effects normally take place in three ways: 1) drag force and inertial force which extract momentum from the flow, 2) generation of wake turbulence behind the obstructions which converts kinetic energy of the mean flow into turbulent kinetic energy, 3) breaking-down of large scale turbulent motions into smaller motions in the wake region, which increases the energy dissipation.

As mentioned in the previous chapter, meteorologists have made significant contributions on the study of plant canopy effect on atmospheric flows in both theoretical and

experimental analysis since 1980s as well as numerical investigations in recent years. Theoretically, based on Wilson and Shaw's (1977) work, Raupach and Shaw (1982) (referred as RS) proposed two horizontal averaging schemes to incorporate the canopy effect into the air-flow equations. One is pure horizontal averaging of the flow variables at a single instant (Scheme I), and the other is time averaging followed by horizontal averaging (Scheme II). Appling these two schemes to free surface open channel flows, Lopez and Garcia (1997) (referred as LG) obtained the averaged continuity equation and momentum equations as well as energy budget equation for each scheme. Traditionally, in hydraulic and coastal engineering, the vegetation effect is considered in the modeling by directly introducing a drag force term into the momentum governing equations (Fischer-Antze, Stoesser, et al., 2001). Raupach and Shaw (1982) and Lopez and Garcia (2001) argued that the simple addition of drag-related body forces in the momentum equation is incorrect, because a retarding body force would have the effect of suppressing turbulence and extracting momentum from the flow. However, both of RS and LG's work were conducted in one-dimension framework, and only considered the vertical derivative of flow and turbulent quantities. It would be oversimplified for coastal wave issues. In this chapter, more general averaged-governing equations will be derived by considering the problem in fully three-dimensional framework.

Given the complexity of leaves, branches and other components of plants and trees in the natural environment, coastal vegetation is typically simulated as regular or random arrays of vertical, rigid cylinders in non-submerged or submerged conditions. In studies of flow in porous media, Whitaker (1986, 1996) has been improving on the volume averaging method. Recently, Belcher et al. (2003) adopted Whitaker's approach to investigate

porous flow and canopy flow. Essentially, volume averaging and horizontal thin-plane averaging are both specific realizations of spatial averaging. Each averaging is suitable for its corresponding characteristic of the problem. Due to the three-dimensionality of wave-vegetation interaction, the method of Whitaker's volume-averaging is adopted in this thesis. Further improvements including more rigorous assumptions and derivation to achieve the three-dimensional governing equations for general wave-vegetation interaction problem are pursued.

2.2 Assumptions and definitions

The system considered in this thesis is as shown in Fig 2.1. In this system, the vegetation is idealized as straight, rigid, and smooth cylinders. Since the key concern in the present study is the macro-scale effect of vegetation on wave propagation, the volume averaging method is employed in conjunction with the incompressible Reynolds Averaged Navier-Stokes (RANS) equations. The top view of the control volume, including both fluid domain and solid plant parts, is as shown in Fig 2.2.

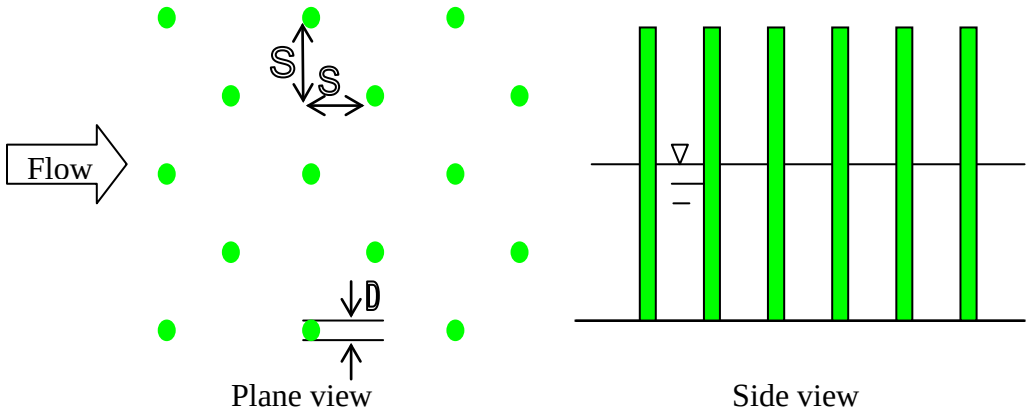

Figure 2. 1 The sketch of vegetation model. D represents the diameter of a stem of vegetation, and S is the characteristic spacing between stems.

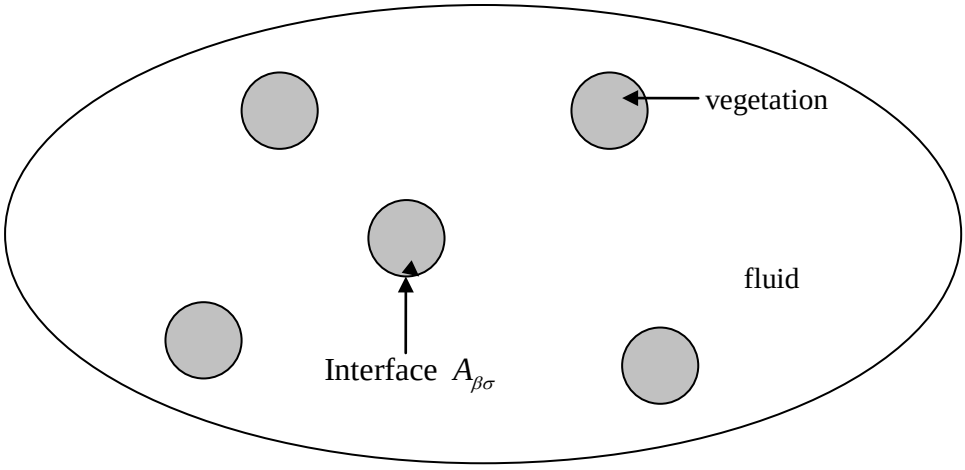

Figure 2. 2 Top view of a control volume.

With reference to Fig 2.2, the whole control volume including both fluid and vegetation is denoted by V, and the volume occupied by the fluid is denoted by V_β. It is assumed that the horizontal scale of this control volume is large compared to the horizontal length scales of the vegetation and the influence of the vegetations is incorporated through the bulk parameter rather than plant-to-plant variations. Vertically, the scale is thin enough to preserve the characteristic variation of properties in the vertical. It is shown in Fig. 2.2 that the control volume is multi-connected since it is intersected by vegetation stems.

Following the definitions and concepts of Whitaker (1986, 1996), for a scalar quantity defined in the fluid, there are two ways of volume averaging, namely, superficial average and intrinsic average, respectively. The superficial average for a quantity ψ is given by:

$$\langle \psi \rangle^s = \frac{1}{V} \int_{V_\beta} \psi dV \tag{2.1}$$

while the intrinsic average is given by:

$$\langle \psi \rangle^{\beta} = \frac{1}{V_{\beta}} \int_{V_{\beta}} \psi dV \tag{2.2}$$

The above-defined two averaging operators satisfy all of the commutation properties with one exception that the spatial differentiation and volume averaging do not commute for variables that are not constant along the fluid-vegetation interface (Raupach and Shaw, 1982). It is shown (Howes and Whitaker, 1985; Finnigan, 2000) that:

$$\left\langle \frac{\partial \varphi_j}{\partial x_i} \right\rangle^{s} = \frac{\partial \langle \varphi_j \rangle^{s}}{\partial x_i} + \frac{1}{V} \iint_{A_{\beta\sigma}} \varphi_j n_i dS \tag{2.3}$$

where n_i is the unit normal direction pointing from fluid into solid phase and $A_{\beta\sigma}$ is the interface between the fluid phase and vegetation phase.

By defining the porosity parameter as:

$$\theta = \frac{V_{\beta}}{V}, \tag{2.4}$$

The superficial and intrinsic averages defined above are related by:

$$\langle \psi \rangle^{s} = \theta \langle \psi \rangle^{\beta} \tag{2.5}$$

Further, it could be shown (Whitaker, 1986) that

$$\frac{1}{V} \iint_{A_{\beta\sigma}} n_i dS = -\nabla \theta \tag{2.6}$$

Based on the above definitions, the following equalities are easily obtained:

(a) If $\psi = 1$, $\quad \langle \psi \rangle^{s} = \langle 1 \rangle^{s} = \frac{V_{\beta}}{V} = \theta$

(b) $\left\langle \langle \psi \rangle^{s} \right\rangle^{s} = \theta \langle \psi \rangle^{s}$

(c) $\left\langle \left\langle \psi \right\rangle^{\beta} \right\rangle^{\beta} = \left\langle \psi \right\rangle^{\beta}$

(d) $\left\langle \psi_1 \cdot \left\langle \psi_2 \right\rangle^{\beta} \right\rangle^{\beta} = \left\langle \psi_1 \right\rangle^{\beta} \cdot \left\langle \psi_2 \right\rangle^{\beta}$

2.3 Derivation of the momentum governing equations

Using an over-bar and a prime to denote the time average of the variable and its corresponding fluctuation, respectively, the variable ψ could be expressed as

$$\psi = \overline{\psi} + \psi' \tag{2.7}$$

With the above definition, the RANS equations are given as:

$$\frac{\partial \overline{u}_i}{\partial x_i} = 0 \tag{2.8}$$

$$\frac{\partial \overline{u}_i}{\partial t} + \overline{u}_j \frac{\partial \overline{u}_i}{\partial x_j} = -\frac{1}{\rho}\frac{\partial \overline{p}}{\partial x_i} + \nu \frac{\partial^2 \overline{u}_i}{\partial x_j \partial x_j} - \frac{\partial}{\partial x_j}\overline{u_i' u_j'} + g_i \tag{2.9}$$

In Eq.(2.8) and (2.9), the subscripts i, j=1, 2, 3, for the three-dimensional problem. u_i is the fluid velocity in i direction, ρ is the density of fluid, p is the pressure of fluid, g_i is mass force per unit mass in i direction, and ν is the kinematic viscosity of the fluid. On the right hand side (RHS) of Eq. (2.9), $\overline{u_i' u_j'}$ is the Reynold's stress resulting from time averaging.

Exercising the volume averaging on each term of Eq. (2.8) and Eq. (2.9) in the form of intrinsic average, the averaged continuity equation could be expressed as:

$$\left\langle \frac{\partial \overline{u}_i}{\partial x_i} \right\rangle^s = \frac{\partial \left\langle \overline{u}_i \right\rangle^s}{\partial x_i} + \frac{1}{V}\iint_{A_{\beta\sigma}} \overline{u}_i n_i dS = 0 \tag{2.10}$$

On the surface of a solid body, such as rigid vegetation, the no-slip conditions apply, that is, $\overline{u}_i = 0$. The continuity equation reduces to

$$\frac{\partial \langle \overline{u}_i \rangle^s}{\partial x_i} = 0 \tag{2.11}$$

Substituting Eq. (2.5) into Eq. (2.11) yields

$$\frac{\partial}{\partial x_i} \theta \langle \overline{u}_i \rangle^\beta = 0 \tag{2.12}$$

With the assumption that the vegetation boundaries are rigid, the volume of the fluid contained within the control volume as well as the porosity is independent of time, the momentum equations therefore reduce to

$$\left\langle \frac{\partial \overline{u}_i}{\partial t} \right\rangle^s = \frac{\partial \langle \overline{u}_i \rangle^s}{\partial t} = \frac{\partial}{\partial t} \theta \langle \overline{u}_i \rangle^\beta = \theta \frac{\partial}{\partial t} \langle \overline{u}_i \rangle^\beta \tag{2.13}$$

Similarly, the convection term in Eq. (2.9) can be expressed as:

$$\left\langle \overline{u}_j \frac{\partial \overline{u}_i}{\partial x_j} \right\rangle^s = \frac{\partial}{\partial x_j} \langle \overline{u}_i \overline{u}_j \rangle^s + \frac{1}{V} \iint_{A_{\beta\sigma}} (\overline{u}_i \overline{u}_j) n_i dS = \frac{\partial}{\partial x_j} \langle \overline{u}_i \overline{u}_j \rangle^s \tag{2.14}$$

Hereinafter, if double-prime is used to denote a departure of a time-averaged quantity from its intrinsic volume average, $\overline{\psi}$ could be decomposed as:

$$\overline{\psi} = \langle \overline{\psi} \rangle^\beta + \overline{\psi}'' \tag{2.15}$$

And it could be readily shown that

$$\langle \overline{\psi}'' \rangle^s = 0 \tag{2.16}$$

Substituting the above decomposition, Eq. (2.15), into the last term of Eq. (2.14), considering Eq. (2.5) and Eq. (2.16) yields:

$$\begin{aligned}\left\langle \overline{u}_i \overline{u}_j \right\rangle^s &= \left\langle (\left\langle \overline{u}_i \right\rangle^\beta + \overline{u}_i")(\left\langle \overline{u}_j \right\rangle^\beta + \overline{u}_j") \right\rangle^s \\ &= \theta \left\langle \overline{u}_i \right\rangle^\beta \left\langle \overline{u}_j \right\rangle^\beta + \left\langle \overline{u}_i" \overline{u}_j" \right\rangle^s\end{aligned} \tag{2.17}$$

Therefore,

$$\begin{aligned}\left\langle \overline{u}_j \frac{\partial \overline{u}_i}{\partial x_j} \right\rangle^s &= \frac{\partial}{\partial x_j} \theta \left\langle \overline{u}_i \right\rangle^\beta \left\langle \overline{u}_j \right\rangle^\beta + \frac{\partial}{\partial x_j} \left\langle \overline{u}_i" \overline{u}_j" \right\rangle^s \\ &= \theta \left\langle \overline{u}_j \right\rangle^\beta \frac{\partial}{\partial x_j} \left\langle \overline{u}_i \right\rangle^\beta + \frac{\partial}{\partial x_j} \left\langle \overline{u}_i" \overline{u}_j" \right\rangle^s\end{aligned} \tag{2.18}$$

Similarly, the terms on the RHS of the momentum equations can be expressed as

$$\begin{aligned}\left\langle -\frac{1}{\rho} \frac{\partial \overline{p}}{\partial x_i} \right\rangle^s &= -\frac{1}{\rho} \frac{\partial}{\partial x_i} \left\langle \overline{p} \right\rangle^s - \frac{1}{\rho} \frac{1}{V} \iint_{A_{\beta\sigma}} \overline{p} n_i dS \\ &= -\frac{1}{\rho} \theta \frac{\partial}{\partial x_i} \left\langle \overline{p} \right\rangle^\beta - \frac{1}{\rho} \frac{1}{V} \iint_{A_{\beta\sigma}} \overline{p}" n_i dS\end{aligned} \tag{2.19}$$

$$\begin{aligned}\left\langle \nu \frac{\partial^2 \overline{u}_i}{\partial x_j \partial x_j} \right\rangle^s &= \nu \frac{\partial^2}{\partial x_j \partial x_j} \left\langle \overline{u}_i \right\rangle^s + \nu \frac{1}{V} \iint_{A_{\beta\sigma}} n_j \frac{\partial \overline{u}_i}{\partial x_j} dS \\ &= \nu \frac{\partial^2}{\partial x_j \partial x_j} \theta \left\langle \overline{u}_i \right\rangle^\beta - \nu \frac{\partial \theta}{\partial x_j} \frac{\partial \left\langle \overline{u}_i \right\rangle^\beta}{\partial x_j} + \nu \frac{1}{V} \iint_{A_{\beta\sigma}} n_j \frac{\partial \overline{u}_i"}{\partial x_j} dS \\ &= \nu\theta \frac{\partial^2}{\partial x_j \partial x_j} \left\langle \overline{u}_i \right\rangle^\beta + \nu \frac{\partial \theta}{\partial x_j} \frac{\partial \left\langle \overline{u}_i \right\rangle^\beta}{\partial x_j} + \nu \left\langle \overline{u}_i \right\rangle^\beta \frac{\partial^2}{\partial x_j \partial x_j} \theta + \nu \frac{1}{V} \iint_{A_{\beta\sigma}} n_j \frac{\partial \overline{u}_i"}{\partial x_j} dS\end{aligned} \tag{2.20}$$

$$\left\langle -\frac{\partial}{\partial x_j} \overline{u_i' u_j'} \right\rangle^s = -\frac{\partial}{\partial x_j} \left\langle \overline{u_i' u_j'} \right\rangle^s - \frac{1}{V} \iint_{A_{\beta\sigma}} n_j \cdot \overline{u_i' u_j'} dS \tag{2.21}$$

Applying the no-slip boundary condition on the surface of the vegetation, i.e. $u_i = 0$ and $\overline{u}_i = 0$, gives $u_i' = 0$. Eq. (2.21) reduces to

$$\left\langle -\frac{\partial}{\partial x_j} \overline{u_i' u_j'} \right\rangle^s = -\frac{\partial}{\partial x_j} \left\langle \overline{u_i' u_j'} \right\rangle^s \tag{2.22}$$

Incorporating the above expressions into the governing equations and dividing by θ yields

$$\frac{\partial}{\partial t}\langle \overline{u}_i \rangle^{\beta} + \langle \overline{u}_j \rangle^{\beta} \frac{\partial}{\partial x_j}\langle \overline{u}_i \rangle^{\beta} + \underbrace{\frac{1}{\theta}\frac{\partial}{\partial x_j}\langle \overline{u}_i^{"}\overline{u}_j^{"} \rangle^{\beta} \cdot \theta}_{\text{I}}$$

$$= -\frac{1}{\rho}\frac{\partial}{\partial x_i}\langle \overline{p} \rangle^{\beta} + \nu \frac{\partial^2}{\partial x_j \partial x_j}\langle \overline{u}_i \rangle^{\beta} + \nu \frac{1}{\theta}\frac{\partial \theta}{\partial x_j}\frac{\partial \langle \overline{u}_i \rangle^{\beta}}{\partial x_j} + \nu \frac{1}{\theta}\langle \overline{u}_i \rangle^{\beta} \frac{\partial^2}{\partial x_j \partial x_j}\theta + g_i \qquad (2.23)$$

$$\underbrace{-\frac{1}{\rho}\frac{1}{\theta}\frac{1}{V}\iint_{A_{\beta\sigma}} \overline{p}^{"} n_i dS}_{\text{II}} + \underbrace{\nu \frac{1}{V}\frac{1}{\theta}\iint_{A_{\beta\sigma}} n_j \frac{\partial \overline{u}_i^{"}}{\partial x_j} dS}_{\text{III}} \underbrace{-\frac{1}{\theta}\frac{\partial}{\partial x_j}\theta \left\langle \overline{u_i^{'} u_j^{'}} \right\rangle^{\beta}}_{\text{IV}}$$

Eq. (2.12) and Eq. (2.23) are the general temporal-spatial-averaged governing equations within the vegetated domain with variable porosity. Note that these two equations are fully three dimensional and nonlinear. They can be used to study both the vegetative flow and wave problems without any constraint on the order of waves. Furthermore, in real word, the volume of vegetation changes in all directions due to the variations of its branches and spacing. In current derivation, the porosity is treated as a variable, which is more realistic than the constant porosity assumption that is commonly adopted in earlier studies (Lopez and Garcia, 2001, Shimizu and Tsujimoto, 1994). For simplicity, in the following derivations, most equations are expressed in the form of constant porosity. However, the developed numerical model is based on the general equation and applicable for the conditions of the variable porosity.

In Eq. (2.23), the identified term I is the “dispersive flux” or “dispersive covariance”, a covariance arising from the spatial correlation of quantities averaged in time but varying with position (Raupach and Shaw, 1982). This term is argued to be normally negligible compared with the drag force and Reynolds shear stress in the air-plant interaction

(Raupach and Shaw, 1982). However, for water flow or wave environments, the relative magnitude of this term requires more deep investigation. In the current study, Lopez and Garcia's (2001) assumption that this term is small enough to be neglected will be adopted. Term II represents the form drag. In a wave environment, it should include both the form-drag and the inertial force. The inertial force was ignored in most the earlier studies relating to the wave-vegetation interaction. However, this force is important when the vegetation stems are relatively large. Term III represents the friction drag force. And term IV denotes the Reynolds shear stress.

If the vegetation is uniformly distributed in space, implying that the porosity coefficient is a constant, Eq. (2.23) can be simplified to

$$\begin{aligned}
&\frac{\partial}{\partial t}\langle \overline{u}_i \rangle^{\beta} + \langle \overline{u}_j \rangle^{\beta} \frac{\partial}{\partial x_j}\langle \overline{u}_i \rangle^{\beta} + \frac{\partial}{\partial x_j}\langle \overline{u}_i "\overline{u}_j " \rangle^{\beta} \\
&\quad = -\frac{1}{\rho}\frac{\partial}{\partial x_i}\langle \overline{p} \rangle^{\beta} + \nu \frac{\partial^2}{\partial x_j \partial x_j}\langle \overline{u}_i \rangle^{\beta} + g_i \\
&\quad\quad -\frac{1}{\rho}\frac{1}{\theta}\frac{1}{V}\iint_{A_{\beta\sigma}} \overline{p}"n_i dS + \nu \frac{1}{V}\frac{1}{\theta}\iint_{A_{\beta\sigma}} n_j \frac{\partial \overline{u}_i^{"}}{\partial x_j} dS - \frac{\partial}{\partial x_j}\left\langle \overline{u_i^{'} u_j^{'}} \right\rangle^{\beta}
\end{aligned} \tag{2.24}$$

Noting that Raupach and Shaw's (1982) scheme II is essentially an intrinsic averaging in a specific horizontal control volume, and recalling that $V_\beta = \theta \cdot V$, it can be shown that Eq. (2.24) and Raupach and Shaw's result under scheme II are similar. Both represent a special form of the governing equation, Eq. (2.23), under the condition of constant porosity.

2.4 Parameterization of wave forces on vegetation

For the problem of vegetated flow, if the bottom resistance is ignored, the total external force is the sum of pressure force or form drag, which is term II in Eq. (2.23), and the skin friction, which corresponds to term III in the same equation. In wave environments, term II represents two kinds of forces with two different generating mechanisms. One is the drag force arising from the pressure differences around the surface of a structure, while the other is the inertial force associated with the acceleration and deceleration of water particles around the structure. Skin friction (term III) contributes to the total drag force and the latter is normally accounted for through the drag force coefficient. Hence, in analogy with the Morison equation which is a general formula for estimating the total wave forces exerting on a relatively small structure, the vegetation effect can be parameterized as an external force Fi given by:

$$
\begin{aligned}
f_i &= -\frac{1}{\rho}\frac{1}{\theta}\frac{1}{V}\iint_{A_{\beta\sigma}} \overline{p}''\, n_i dS + \nu\frac{1}{V}\frac{1}{\theta}\iint_{A_{\beta\sigma}} n_j \frac{\partial \overline{u}_i''}{\partial x_j} dS \\
&= f_{Di} + f_{Ii} \\
&= -\frac{1}{\rho}\frac{1}{\theta}\frac{1}{V}\left\{(-\frac{1}{2}\rho A C_d \theta^2 \sqrt{(\langle\overline{u}\rangle^{\beta})^2 + (\langle\overline{v}\rangle^{\beta})^2 + (\langle\overline{w}\rangle^{\beta})^2}\,\langle\overline{u}_i\rangle^{\beta}) + (-\rho\forall C_m \theta \frac{\partial\langle\overline{u}_i\rangle^{\beta}}{\partial t})\right\} \\
&= -\frac{1}{2} a C_d \theta \sqrt{(\langle\overline{u}\rangle^{\beta})^2 + (\langle\overline{v}\rangle^{\beta})^2 + (\langle\overline{w}\rangle^{\beta})^2}\,\langle\overline{u}_i\rangle^{\beta} - (1-\theta) C_m \frac{\partial\langle\overline{u}_i\rangle^{\beta}}{\partial t}
\end{aligned}
\tag{2.25}
$$

In which Cd is the drag force coefficient and Cm is the inertial force coefficient. $a = A/V$ is a ratio between the total frontal area A in the control volume projected on a plane perpendicular to the wave direction and the total control volume and has a dimension of L^{-1}. $\forall$ is the volume occupied by the vegetation in the control volume.

When dealing with channel flow problem, the above external force only has the part of drag force.

2.5 Turbulent kinetic energy equation

Under the averaging concept introduced in section 2.3, the total kinetic energy, defined as $\frac{1}{2}\left\langle \overline{u_i u_i} \right\rangle^{\beta}$, could be decomposed in the following form,

$$\frac{1}{2}\left\langle \overline{u_i u_i} \right\rangle^{\beta} = \frac{1}{2}\left\langle \overline{u}_i \overline{u}_i \right\rangle^{\beta} + \frac{1}{2}\left\langle \overline{u_i' u_i'} \right\rangle^{\beta} = \frac{1}{2}\left\langle \overline{u}_i \right\rangle^{\beta} \left\langle \overline{u}_i \right\rangle^{\beta} + \frac{1}{2}\left\langle \overline{u}_i'' \overline{u}_i'' \right\rangle^{\beta} + \frac{1}{2}\left\langle \overline{u_i' u_i'} \right\rangle^{\beta} \tag{2.26}$$

As mentioned above, the second term on the RHS of Eq. (2.26) results from the spatial difference of the time averaged quantities. The last term of Eq. (2.26) is the Reynold's stress which comes from instantaneous fluctuations from its time-averaged value. Because the first term on the RHS of Eq. (2.26) represents the mean kinetic energy (MKE) computed by the temporal-spatial averaged velocity, and because the turbulent kinetic energy (TKE) could be obtained from the difference of total kinetic energy and MKE, TKE could be defined as

$$TKE = \frac{1}{2}\left\langle \overline{u}_i'' \overline{u}_i'' \right\rangle^{\beta} + \frac{1}{2}\left\langle \overline{u_i' u_i'} \right\rangle^{\beta} \tag{2.27}$$

To get the governing equation of TKE, the expressions for both terms on the RHS of Eq. (2.27) should be obtained first. For simplicity, only the second term on the RHS of Eq. (2.27) is taken as an example to illustrate the derivation process. Firstly, from Eq. (2.9) and the original momentum equation of NS equations, temporal fluctuation of velocity u_i' could be expressed as

$$\frac{\partial}{\partial t}u_i^{'}+\frac{\partial}{\partial x_j}\overline{u_i}u_j^{'}+\frac{\partial}{\partial x_j}u_i^{'}\overline{u_j}+\frac{\partial}{\partial x_j}u_i^{'}u_j^{'}-\frac{\partial}{\partial x_j}\overline{u_i^{'}u_j^{'}}=-\frac{1}{\rho}\frac{\partial p^{'}}{\partial x_i}+\nu\nabla^2 u_i^{'} \tag{2.28}$$

Multiplying Eq. (2.28) by $u_i^{'}$, and taking the time averaging,

$$\begin{aligned}\frac{\partial}{\partial t}\frac{1}{2}\overline{u_i^{'}u_i^{'}}+\overline{u}_j\frac{\partial}{\partial x_j}\frac{1}{2}\overline{u_i^{'}u_i^{'}}=&-\overline{u_i^{'}u_j^{'}}\frac{\partial}{\partial x_j}\overline{u}_i-\frac{\partial}{\partial x_j}\frac{1}{2}\overline{u_i^{'}u_i^{'}u_j^{'}}-\overline{u_i^{'}}\frac{\partial}{\partial x_j}\overline{u_i^{'}u_j^{'}}\\&-\frac{1}{\rho}\frac{\partial}{\partial x_i}\overline{p^{'}u_i^{'}}+\nu\overline{u_i^{'}\nabla^2 u_i^{'}}\end{aligned} \tag{2.29}$$

Taking the volume averaging on Eq. (2.29) and conducting similar process as in last section, the general equation for the second term on RHS of Eq. (2.27), $\frac{1}{2}\left\langle\overline{u_i^{'}u_i^{'}}\right\rangle^{\beta}$, with varying porosity yields as

$$\begin{aligned}&\frac{\partial}{\partial t}\theta\frac{1}{2}\left\langle\overline{u_i^{'}u_i^{'}}\right\rangle^{\beta}+\left\langle\overline{u}_j\right\rangle^{\beta}\frac{\partial}{\partial x_j}\theta\frac{1}{2}\left\langle\overline{u_i^{'}u_i^{'}}\right\rangle^{\beta}+\theta\left\langle\overline{u}_j^{"}\frac{\partial}{\partial x_j}\frac{1}{2}\overline{u_i^{'}u_i^{'}}^{"}\right\rangle^{\beta}\\&=-\left\langle\overline{u_i^{'}u_j^{'}}\right\rangle^{\beta}\frac{\partial}{\partial x_j}\theta\left\langle\overline{u}_i\right\rangle^{\beta}-\theta\left\langle\overline{u_i^{'}u_j^{'}}^{"}\frac{\partial}{\partial x_j}\overline{u}_i\right\rangle^{\beta}-\frac{\partial}{\partial x_j}\frac{1}{2}\theta\left\langle\overline{u_i^{'}u_i^{'}u_j^{'}}\right\rangle^{\beta}\\&-\frac{1}{\rho}\frac{\partial}{\partial x_i}\theta\left\langle\overline{p^{'}u_i^{'}}\right\rangle^{\beta}+\nu\theta\left\langle\overline{u_i^{'}\nabla^2 u_i^{'}}\right\rangle^{\beta}\end{aligned} \tag{2.30}$$

Considering the transformation:

$$\begin{aligned}\theta\left\langle\overline{u}_j^{"}\frac{\partial}{\partial x_j}\frac{1}{2}\overline{u_i^{'}u_i^{'}}^{"}\right\rangle^{\beta}&=\left\langle\overline{u}_j^{"}\frac{\partial}{\partial x_j}\frac{1}{2}\overline{u_i^{'}u_i^{'}}^{"}\right\rangle^{s}\\&=\left\langle\frac{\partial}{\partial x_j}\frac{1}{2}\overline{u_i^{'}u_i^{'}}^{"}\overline{u}_j^{"}-\frac{1}{2}\overline{u_i^{'}u_i^{'}}^{"}\frac{\partial}{\partial x_j}\overline{u}_j^{"}\right\rangle^{s}\\&=\left\langle\frac{\partial}{\partial x_j}\frac{1}{2}\overline{u_i^{'}u_i^{'}}^{"}\overline{u}_j^{"}\right\rangle^{s}\\&=\frac{\partial}{\partial x_j}\frac{1}{2}\theta\left\langle\overline{u_i^{'}u_i^{'}}^{"}\overline{u}_j^{"}\right\rangle^{\beta}\end{aligned} \tag{2.31}$$

which employs the property of $\partial \overline{u}_j^{"} / \partial x_j = 0$ and $\overline{u}_j^{"}$ is zero along the surface of vegetation stems.

Assuming a constant porosity, Eq. (2.30) could be reduced to be:

$$\frac{\partial}{\partial t}\frac{1}{2}\left\langle \overline{u_i' u_i'} \right\rangle^{\beta} + \left\langle \overline{u}_j \right\rangle^{\beta} \frac{\partial}{\partial x_j}\frac{1}{2}\left\langle \overline{u_i' u_i'} \right\rangle^{\beta}$$

$$= -\left\langle \overline{u_i' u_j'} \right\rangle^{\beta} \frac{\partial}{\partial x_j}\left\langle \overline{u}_i \right\rangle^{\beta} - \left\langle \overline{u_i' u_j'}^{"} \frac{\partial}{\partial x_j}\overline{u}_i \right\rangle^{\beta} - \frac{\partial}{\partial x_j}\frac{1}{2}\left\langle \overline{u_i' u_i' u_j'} \right\rangle^{\beta} \tag{2.32}$$

$$-\frac{\partial}{\partial x_j}\frac{1}{2}\left\langle \overline{u_i' u_i'}^{"} \overline{u}_j^{"} \right\rangle^{\beta} - \frac{1}{\rho}\frac{\partial}{\partial x_i}\left\langle \overline{p' u_i'} \right\rangle^{\beta} + \nu \left\langle \overline{u_i' \nabla^2 u_i'} \right\rangle^{\beta}$$

Similarly, with constant porosity, the first term on the RHS of Eq. (2.27), $\frac{1}{2}\left\langle \overline{u}_i^{"} \overline{u}_i^{"} \right\rangle^{\beta}$ could be expressed as:

$$\frac{\partial}{\partial t}\frac{1}{2}\left\langle \overline{u}_i^{"} \overline{u}_i^{"} \right\rangle^{\beta} + \left\langle \overline{u}_j \right\rangle^{\beta} \frac{\partial}{\partial x_j}\frac{1}{2}\left\langle \overline{u}_i^{"} \overline{u}_i^{"} \right\rangle^{\beta} = -\left\langle \overline{u}_i^{"} \overline{u}_j^{"} \right\rangle^{\beta} \frac{\partial}{\partial x_j}\left\langle \overline{u}_i \right\rangle^{\beta} + \left\langle \overline{u_i' u_j'}^{"} \frac{\partial}{\partial x_j}\overline{u}_i^{"} \right\rangle^{\beta}$$

$$-\frac{\partial}{\partial x_j}\left(\left\langle \overline{u_i' u_j'}^{"} \overline{u}_i^{"} \right\rangle^{\beta} + \frac{1}{2}\left\langle \overline{u}_i^{"} \overline{u}_i^{"} \overline{u}_j^{"} \right\rangle^{\beta} + \frac{1}{\rho}\left\langle \overline{p}^{"} \overline{u}_j^{"} \right\rangle^{\beta}\right) \tag{2.33}$$

$$+\frac{1}{\rho}\left\langle \overline{u}_i \right\rangle^{\beta} \left\langle \frac{\partial \overline{p}^{"}}{\partial x_i} \right\rangle^{\beta} + \nu \left\langle \overline{u}_i^{"} \nabla^2 \overline{u}_i^{"} \right\rangle^{\beta}$$

Therefore, by summing Eq. (2.32) and Eq. (2.33) together, the conserved equation of TKE with constant porosity is given by:

$$
\begin{aligned}
(\frac{\partial}{\partial t}+\langle \overline{u}_j \rangle^\beta \frac{\partial}{\partial x_j})(\frac{1}{2}\langle \overline{u_i^{'}u_i^{'}} \rangle^\beta + \frac{1}{2}\langle \overline{u}_i^{"}\overline{u}_i^{"} \rangle^\beta) &= -(\langle \overline{u_i^{'}u_j^{'}} \rangle^\beta + \langle \overline{u}_i^{"}\overline{u}_j^{"} \rangle^\beta)\frac{\partial}{\partial x_j}\langle \overline{u}_i \rangle^\beta \\
&-\frac{\partial}{\partial x_j}(\frac{1}{2}\langle \overline{u_i^{'}u_i^{'}u_j^{'}} \rangle^\beta + \frac{1}{2}\langle \overline{u_i^{'}u_i^{'}}^{"}\overline{u}_j^{"} \rangle^\beta + \langle \overline{u_i^{'}u_j^{'}}^{"}\overline{u}_i^{"} \rangle^\beta \\
&+\frac{1}{2}\langle \overline{u}_i^{"}\overline{u}_i^{"}\overline{u}_j^{"} \rangle^\beta + \frac{1}{\rho}\langle \overline{p^{'}u_j^{'}} \rangle^\beta + \frac{1}{\rho}\langle \overline{p}^{"}\overline{u}_j^{"} \rangle^\beta) \\
&\underbrace{+\frac{1}{\rho}\langle \overline{u}_i \rangle^\beta \langle \frac{\partial \overline{p}^{"}}{\partial x_i} \rangle^\beta}_{I} + \nu \langle \overline{u_i^{'}\nabla^2 u_i^{'}} \rangle^\beta + \nu \langle \overline{u}_i^{"}\nabla^2 \overline{u}_i^{"} \rangle^\beta
\end{aligned}
\tag{2.34}
$$

In the above equation, the identified term '*I*' is physically significant. This term represents the rate of work done by the mean flow against form drag, being a scalar product of the mean velocity and form drag force. It is called the "wake production" term, since it converts MKE to TKE in the turbulent wakes of vegetation elements.

2.6 Turbulent dissipation rate equation

Traditionally, the turbulent dissipation rate is defined as a time-averaged quantity, which is expressed as:

$$
\varepsilon = \nu \overline{\frac{\partial u_i^{'}}{\partial x_l}\frac{\partial u_i^{'}}{\partial x_l}} \tag{2.35}
$$

Following the preceding definition, a new spatial-temporal-averaged quantity could be defined as:

$$
\langle \varepsilon \rangle^\beta = \left\langle \nu \overline{\frac{\partial u_i^{'}}{\partial x_l}\frac{\partial u_i^{'}}{\partial x_l}} \right\rangle^\beta \tag{2.36}
$$

This will be referred to as the spatial-averaged turbulent dissipation rate. Correspondingly, the spatial fluctuation of ε will be the difference between ε and $\langle \varepsilon \rangle^\beta$, which is written as:

$\varepsilon^{"} = \varepsilon - \langle \varepsilon \rangle^{\beta}$.

The typical time-averaged equation of ε (Chen, C-J and Jaw, S-Y, 1998) is given by:

$$\frac{\partial \varepsilon}{\partial t} + \overline{u_k}\frac{\partial \varepsilon}{\partial x_k} = \frac{\partial}{\partial x_k}(-\overline{\varepsilon' u_k'} - \frac{2\nu}{\rho}\overline{\frac{\partial u_k'}{\partial x_j}\frac{\partial p'}{\partial x_j}} + \nu\frac{\partial \varepsilon}{\partial x_k})$$
$$- 2\nu\overline{u_k'\frac{\partial u_i'}{\partial x_j}}\frac{\partial^2 \overline{u_i}}{\partial x_k \partial x_j} - 2\nu\frac{\partial \overline{u_i}}{\partial x_j}(\overline{\frac{\partial u_k'}{\partial x_i}\frac{\partial u_k'}{\partial x_j}} + \overline{\frac{\partial u_i'}{\partial x_k}\frac{\partial u_j'}{\partial x_k}}) \tag{2.37}$$
$$- 2\nu\overline{\frac{\partial u_i'}{\partial x_j}\frac{\partial u_i'}{\partial x_k}\frac{\partial u_j'}{\partial x_k}} - 2(\overline{\nu\frac{\partial^2 u_i'}{\partial x_k \partial x_j}})^2$$

where $\varepsilon' = \nu\frac{\partial u_i'}{\partial x_l}\frac{\partial u_i'}{\partial x_l}$

Taking the superficial average defined by Eq. (2.1) on each term of the above Eq. (3.37) yields the equation of turbulent dissipation rate in intrinsic average defined in Eq. (2.2):

$$\left\langle \frac{\partial \varepsilon}{\partial t} \right\rangle^s = \frac{\partial}{\partial t}\langle \varepsilon \rangle^s = \theta\frac{\partial}{\partial t}\langle \varepsilon \rangle^{\beta} \tag{2.38}$$

$$\left\langle \overline{u_k}\frac{\partial \varepsilon}{\partial x_k} \right\rangle^s = \left\langle \frac{\partial \overline{u_k}\varepsilon}{\partial x_k} \right\rangle^s$$
$$= \frac{\partial}{\partial x_k}\langle \overline{u_k}\varepsilon \rangle^s + \frac{1}{V}\int_{A_{\beta\sigma}} \overline{u_k}\varepsilon n_k dA$$
$$= \frac{\partial}{\partial x_k}\left\langle (\langle \overline{u_k} \rangle^{\beta} + \overline{u_k}^{"})(\langle \varepsilon \rangle^{\beta} + \varepsilon^{"}) \right\rangle^s \tag{2.39}$$
$$= \frac{\partial}{\partial x_k}\langle \overline{u_k} \rangle^{\beta} \langle \varepsilon \rangle^{\beta} \theta + \frac{\partial}{\partial x_k}\left\langle \overline{u_k}^{"} \varepsilon^{"} \right\rangle^s$$
$$= \theta\langle \overline{u_k} \rangle^{\beta}\frac{\partial}{\partial x_k}\langle \varepsilon \rangle^{\beta} + \frac{\partial}{\partial x_k}\theta\left\langle \overline{u_k}^{"} \varepsilon^{"} \right\rangle^{\beta}$$

$$\left\langle \frac{\partial}{\partial x_k}\overline{\varepsilon' u_k'} \right\rangle^s = \frac{\partial}{\partial x_k}\langle \overline{\varepsilon' u_k'} \rangle^s + \frac{1}{V}\int_{A_{\beta\sigma}} \overline{\varepsilon' u_k'} \cdot n_k dA \tag{2.40}$$

$$\left\langle \frac{\partial}{\partial x_k}\frac{2\nu}{\rho}\overline{\frac{\partial u_k^{'}}{\partial x_j}\frac{\partial p^{'}}{\partial x_j}}\right\rangle^s = \frac{\partial}{\partial x_k}\frac{2\nu}{\rho}\left\langle\overline{\frac{\partial u_k^{'}}{\partial x_j}\frac{\partial p^{'}}{\partial x_j}}\right\rangle^s + \frac{2\nu}{\rho}\frac{1}{V}\int_{A_{\beta\sigma}}\overline{\frac{\partial u_k^{'}}{\partial x_j}\frac{\partial p^{'}}{\partial x_j}}\cdot n_k dA \tag{2.41}$$

$$\begin{aligned}\left\langle \frac{\partial}{\partial x_k}\nu\frac{\partial \varepsilon}{\partial x_k}\right\rangle^s &= \frac{\partial}{\partial x_k}\nu\left\langle\frac{\partial \varepsilon}{\partial x_k}\right\rangle^s + \frac{\nu}{V}\int_{A_{\beta\sigma}}\frac{\partial \varepsilon}{\partial x_k}\cdot n_k dA \\ &= \frac{\partial}{\partial x_k}\nu\frac{\partial}{\partial x_k}\langle\varepsilon\rangle^s + \frac{\partial}{\partial x_k}(\frac{\nu}{V}\int_{A_{\beta\sigma}}\varepsilon\cdot n_k dA) + \frac{\nu}{V}\int_{A_{\beta\sigma}}\frac{\partial \varepsilon}{\partial x_k}\cdot n_k dA\end{aligned} \tag{2.42}$$

$$\begin{aligned}&\left\langle 2\nu\overline{u_k^{'}\frac{\partial u_i^{'}}{\partial x_j}}\frac{\partial^2\overline{u_i}}{\partial x_k\partial x_j}\right\rangle^s \\ &= \left\langle 2\nu\overline{u_k^{'}\frac{\partial u_i^{'}}{\partial x_j}}\frac{\partial^2}{\partial x_k\partial x_j}(\langle\overline{u_i}\rangle^\beta + \overline{u_i}^{"})\right\rangle^s \\ &= 2\nu\left\langle\overline{u_k^{'}\frac{\partial u_i^{'}}{\partial x_j}}\right\rangle^s\frac{\partial^2}{\partial x_k\partial x_j}\langle\overline{u_i}\rangle^\beta + \left\langle 2\nu(\left\langle\overline{u_k^{'}\frac{\partial u_i^{'}}{\partial x_j}}\right\rangle^\beta + \overline{u_k^{'}\frac{\partial u_i^{'}}{\partial x_j}}^{"})\frac{\partial^2\overline{u_i}^{"}}{\partial x_k\partial x_j}\right\rangle^s \\ &= 2\nu\left\langle\overline{u_k^{'}\frac{\partial u_i^{'}}{\partial x_j}}\right\rangle^s\frac{\partial^2}{\partial x_k\partial x_j}\langle\overline{u_i}\rangle^\beta + 2\nu\left\langle\overline{u_k^{'}\frac{\partial u_i^{'}}{\partial x_j}}\right\rangle^\beta\left\langle\frac{\partial^2}{\partial x_k\partial x_j}\overline{u_i}^{"}\right\rangle^s + 2\nu\left\langle\overline{u_k^{'}\frac{\partial u_i^{'}}{\partial x_j}}^{"}\frac{\partial^2\overline{u_i}^{"}}{\partial x_k\partial x_j}\right\rangle^s \\ &= 2\nu\left\langle\overline{u_k^{'}\frac{\partial u_i^{'}}{\partial x_j}}\right\rangle^s\frac{\partial^2}{\partial x_k\partial x_j}\langle\overline{u_i}\rangle^\beta + 2\nu\left\langle\overline{u_k^{'}\frac{\partial u_i^{'}}{\partial x_j}}\right\rangle^\beta\cdot\frac{1}{V}\cdot\int_{A_{\beta\sigma}}\frac{\partial\overline{u_i}^{"}}{\partial x_j}\cdot n_k dA + 2\nu\left\langle\overline{u_k^{'}\frac{\partial u_i^{'}}{\partial x_j}}^{"}\frac{\partial^2\overline{u_i}^{"}}{\partial x_k\partial x_j}\right\rangle^s\end{aligned} \tag{2.43}$$

In the above derivations, the velocity of the fluid-vegetation interface is taken to be zero.

The other three terms in Eq. (2.37) could be averaged in a similar manner.

Assembling the above terms together, the equation for the turbulent dissipation in intrinsic form for variable porosity is given by:

$$(\frac{\partial}{\partial t}+\langle\overline{u_k}\rangle^{\beta}\frac{\partial}{\partial x_k})\langle\varepsilon\rangle^{\beta}=-\frac{1}{\theta}\frac{\partial}{\partial x_k}\theta\left\langle\overline{u_k}^{"}\varepsilon^{"}\right\rangle^{\beta}-\frac{1}{\theta}\frac{\partial}{\partial x_k}\theta\left\langle\overline{\varepsilon^{'}u_k^{'}}\right\rangle^{\beta}-\frac{1}{\theta}\frac{1}{V}\int_{A_{\beta\sigma}}\overline{\varepsilon^{'}u_k^{'}}\cdot n_k dA$$

$$-\frac{1}{\theta}\frac{\partial}{\partial x_k}(\theta\frac{2\nu}{\rho}\left\langle\overline{\frac{\partial u_k^{'}}{\partial x_j}\frac{\partial p^{'}}{\partial x_j}}\right\rangle^{\beta})-\frac{2\nu}{\rho}\frac{1}{\theta}\frac{1}{V}\int_{A_{\beta\sigma}}\overline{\frac{\partial u_k^{'}}{\partial x_j}\frac{\partial p^{'}}{\partial x_j}}\cdot n_k dA$$

$$+\frac{1}{\theta}\frac{\partial}{\partial x_k}(\nu\frac{\partial}{\partial x_k}\theta\langle\varepsilon\rangle^{\beta})+\frac{1}{\theta}\frac{\nu}{V}\frac{\partial}{\partial x_k}(\int_{A_{\beta\sigma}}\varepsilon\cdot n_k dA)+\frac{1}{\theta}\frac{\nu}{V}\int_{A_{\beta\sigma}}\frac{\partial\varepsilon}{\partial x_k}\cdot n_k dA$$

$$-2\nu\left\langle\overline{u_k^{'}\frac{\partial u_i^{'}}{\partial x_j}}\right\rangle^{\beta}\frac{\partial^2}{\partial x_k\partial x_j}\langle\overline{u_i}\rangle^{\beta}-\frac{2\nu}{\theta}\left\langle\overline{u_k^{'}\frac{\partial u_i^{'}}{\partial x_j}}\right\rangle^{\beta}\cdot\frac{1}{V}\cdot\int_{A_{\beta\sigma}}\frac{\partial\overline{u_i}^{"}}{\partial x_j}\cdot n_k dA \qquad (2.44)$$

$$-2\nu\left\langle\overline{u_k^{'}\frac{\partial u_i^{'}}{\partial x_j}}^{"}\frac{\partial^2\overline{u_i}^{"}}{\partial x_k\partial x_j}\right\rangle^{\beta}-2\nu\frac{\partial}{\partial x_j}\langle\overline{u_i}\rangle^{\beta}(\left\langle\overline{\frac{\partial u_k^{'}}{\partial x_i}\frac{\partial u_k^{'}}{\partial x_j}}\right\rangle^{\beta}+\left\langle\overline{\frac{\partial u_i^{'}}{\partial x_k}\frac{\partial u_j^{'}}{\partial x_k}}\right\rangle^{\beta})$$

$$-2\nu\left\langle\frac{\partial\overline{u_i}^{"}}{\partial x_j}(\overline{\frac{\partial u_k^{'}}{\partial x_i}\frac{\partial u_k^{'}}{\partial x_j}}^{"}+\overline{\frac{\partial u_i^{'}}{\partial x_k}\frac{\partial u_j^{'}}{\partial x_k}}^{"})\right\rangle^{\beta}-2\nu\left\langle\overline{\frac{\partial u_i^{'}}{\partial x_j}\frac{\partial u_i^{'}}{\partial x_k}\frac{\partial u_j^{'}}{\partial x_k}}\right\rangle^{\beta}-2\left\langle\overline{(\nu\frac{\partial^2 u_i^{'}}{\partial x_k\partial x_j})^2}\right\rangle^{\beta}$$

2.7 Parameterization of TKE equations, turbulent dissipation rate and turbulence closure

Traditionally, the turbulence kinetic energy is expressed by k， defined as

$$k=\frac{1}{2}\overline{u_i^{'}u_i^{'}} \qquad (2.45)$$

Similarly, for the TKE in intrinsic form, we introduce the definition:

$$\langle k\rangle^{\beta}=\frac{1}{2}\left\langle\overline{u_i^{'}u_i^{'}}\right\rangle^{\beta}+\frac{1}{2}\left\langle\overline{u_i}^{"}\overline{u_i}^{"}\right\rangle^{\beta} \qquad (2.46)$$

Incorporating Eq. (2.46) into Eq. (2.34), and re-arranging the terms would yield the intrinsic form of the TKE which, for constant porosity, could be written as:

$$
\begin{aligned}
(\frac{\partial}{\partial t}+\langle\overline{u}_j\rangle^\beta\frac{\partial}{\partial x_j})(\frac{1}{2}\langle\overline{u_i'u_i'}\rangle^\beta+\frac{1}{2}\langle\overline{u_i}''\overline{u_i}''\rangle^\beta) &= \underbrace{-(\langle\overline{u_i'u_j'}\rangle^\beta+\langle\overline{u_i}''\overline{u_j}''\rangle^\beta)\frac{\partial}{\partial x_j}\langle\overline{u}_i\rangle^\beta}_{I} \\
&\underbrace{-\frac{\partial}{\partial x_j}(\frac{1}{2}\langle\overline{u_i'u_i'u_j'}\rangle^\beta+\frac{1}{2}\langle\overline{u_i'u_i'}''\overline{u}_j''\rangle^\beta+\langle\overline{u_i'u_j'}''\overline{u}_i''\rangle^\beta+\frac{1}{2}\langle\overline{u}_i''\overline{u}_i''\overline{u}_j''\rangle^\beta)}_{II} \\
&\underbrace{+\frac{\partial}{\partial x_j}(\frac{1}{\rho}\langle\overline{p'u_j'}\rangle^\beta+\frac{1}{\rho}\langle\overline{p}''\overline{u_j}''\rangle^\beta)}_{III}+\underbrace{\frac{1}{\rho}\langle\overline{u}_i\rangle^\beta\left\langle\frac{\partial\overline{p}''}{\partial x_i}\right\rangle^\beta}_{IV} \\
&\underbrace{+\nu\langle\overline{u_i'\nabla^2u_i'}\rangle^\beta+\nu\langle\overline{u}_i''\nabla^2\overline{u}_i''\rangle^\beta}_{V}
\end{aligned}
\tag{2.47}
$$

On the right hand side of Eq. (2.47), the terms grouped into I, II, III essentially have the same physical interpretations as in the standard k-equation. They represent the TKE production due to mean shear flow, turbulent diffusion by velocity fluctuation, and turbulent diffusion by pressure fluctuation, respectively. Grouped term V is the combination of molecular diffusion of TKE and viscous dissipation. Therefore, groups I, II, III, V could be parameterized as the standard k-equation. Specifically, the shear production term could be parameterized as

$$
\mathrm{I} = -\nu_t(\frac{\partial\langle\overline{u}_i\rangle^\beta}{\partial x_j}+\frac{\partial\langle\overline{u}_j\rangle^\beta}{\partial x_i})\frac{\partial\langle\overline{u}_i\rangle^\beta}{\partial x_j}
$$

Grouped term II, III, and the implicit diffusion part in term V could be grouped and parameterized as

$$
\text{diffusion} = \frac{\partial}{\partial x_j}(\frac{\nu_t}{\sigma_k}\frac{\partial\langle k\rangle^\beta}{\partial x_j})
$$

The non-parameterized part in term V is the turbulent dissipation rate, which could be denoted as $\langle\varepsilon\rangle^\beta$.

In term IV, $\left\langle \frac{\partial \overline{p}^{"}}{\partial x_i} \right\rangle^{\beta}$ is associated with the form drag and the inertial force acting on the vegetation in the wave environment. Physically, term IV represents the rate of work done by the mean flow against the form drag and inertial forces. It converts MKE to TKE in the turbulent wakes of vegetation and may be referred to as "wake production" term.

Denoting sum of the form drag and inertial force as f_i, the wake production could be approximated as

$$\frac{1}{\rho}\langle \overline{u}_i \rangle^{\beta} \left\langle \frac{\partial \overline{p}^{"}}{\partial x_i} \right\rangle^{\beta} = \eta_k \langle \overline{u}_i \rangle^{\beta} f_i$$

where η_k is the efficiency of TKE (Naot, 1996), and i = 1,2,3 in three dimensional condition.

As a result, the governing equation of TKE could be parameterized as

$$\begin{aligned} \frac{D\langle k \rangle^{\beta}}{Dt} = & \frac{\partial}{\partial x_j}\left(\frac{\nu_t}{\sigma_k}\frac{\partial \langle k \rangle^{\beta}}{\partial x_j}\right) + \nu_t\left(\frac{\partial \langle \overline{u}_i \rangle^{\beta}}{\partial x_j} + \frac{\partial \langle \overline{u}_j \rangle^{\beta}}{\partial x_i}\right)\frac{\partial \langle \overline{u}_i \rangle^{\beta}}{\partial x_j} \\ & + \frac{\partial}{\partial x_j}\left(\nu \frac{\partial \langle k \rangle^{\beta}}{\partial x_j}\right) - \langle \varepsilon \rangle^{\beta} + \eta_k \langle \overline{u}_i \rangle^{\beta} f_i \end{aligned} \tag{2.48}$$

Regarding the turbulent dissipation rate, for convenience, only the equation under the condition of constant porosity in described here. Hence, Eq. (2.44) could be written as:

$$
\begin{aligned}
&(\frac{\partial}{\partial t}+\langle\overline{u_k}\rangle^{\beta}\frac{\partial}{\partial x_k})\langle\varepsilon\rangle^{\beta}=\underbrace{-\frac{\partial}{\partial x_k}\langle\overline{u_k}^{"}\varepsilon^{"}\rangle^{\beta}-\frac{\partial}{\partial x_k}\langle\overline{\varepsilon^{'}u_k^{'}}\rangle^{\beta}-\frac{1}{\theta}\frac{1}{V}\int_{A_{\beta\sigma}}\overline{\varepsilon^{'}u_k^{'}}\cdot n_k dA}_{A}\\
&\underbrace{-\frac{\partial}{\partial x_k}(\frac{2\nu}{\rho}\langle\overline{\frac{\partial u_k^{'}}{\partial x_j}\frac{\partial p^{'}}{\partial x_j}}\rangle^{\beta})-\frac{2\nu}{\rho}\frac{1}{\theta}\frac{1}{V}\int_{A_{\beta\sigma}}\overline{\frac{\partial u_k^{'}}{\partial x_j}\frac{\partial p^{'}}{\partial x_j}}\cdot n_k dA}_{B}\\
&\underbrace{+\frac{\partial}{\partial x_k}(\nu\frac{\partial}{\partial x_k}\langle\varepsilon\rangle^{\beta})+\frac{1}{\theta}\frac{\nu}{V}\frac{\partial}{\partial x_k}(\int_{A_{\beta\sigma}}\varepsilon\cdot n_k dA)+\frac{1}{\theta}\frac{\nu}{V}\int_{A_{\beta\sigma}}\frac{\partial\varepsilon}{\partial x_k}\cdot n_k dA}_{C}\\
&\underbrace{-2\nu\langle\overline{u_k^{'}\frac{\partial u_i^{'}}{\partial x_j}}\rangle^{\beta}\frac{\partial^2}{\partial x_k\partial x_j}\langle\overline{u_i}\rangle^{\beta}-\frac{2\nu}{\theta}\langle\overline{u_k^{'}\frac{\partial u_i^{'}}{\partial x_j}}\rangle^{\beta}\cdot\frac{1}{V}\cdot\int_{A_{\beta\sigma}}\frac{\partial\overline{u_i}^{"}}{\partial x_j}\cdot n_k dA}_{D}\qquad(2.49)\\
&\underbrace{-2\nu\langle\overline{u_k^{'}\frac{\partial u_i^{'}}{\partial x_j}}^{"}\frac{\partial^2\overline{u_i}^{"}}{\partial x_k\partial x_j}\rangle^{\beta}}_{E}\underbrace{-2\nu\frac{\partial}{\partial x_j}\langle\overline{u_i}\rangle^{\beta}(\langle\overline{\frac{\partial u_k^{'}}{\partial x_i}\frac{\partial u_k^{'}}{\partial x_j}}\rangle^{\beta}+\langle\overline{\frac{\partial u_i^{'}}{\partial x_k}\frac{\partial u_j^{'}}{\partial x_k}}\rangle^{\beta})}_{F}\\
&\underbrace{-2\nu\langle\frac{\partial\overline{u_i}^{"}}{\partial x_j}(\overline{\frac{\partial u_k^{'}}{\partial x_i}\frac{\partial u_k^{'}}{\partial x_j}}^{"}+\overline{\frac{\partial u_i^{'}}{\partial x_k}\frac{\partial u_j^{'}}{\partial x_k}}^{"})\rangle^{\beta}}_{G}\underbrace{-2\nu\langle\overline{\frac{\partial u_i^{'}}{\partial x_j}\frac{\partial u_i^{'}}{\partial x_k}\frac{\partial u_j^{'}}{\partial x_k}}\rangle^{\beta}}_{H}\underbrace{-2\langle\overline{(\nu\frac{\partial^2 u_i^{'}}{\partial x_k\partial x_j})^2}\rangle^{\beta}}_{I}
\end{aligned}
$$

In the above equation, the physical meaning of each grouped term is

A: turbulent diffusion

B: diffusion by pressure fluctuation

C: molecular diffusion

D: production due to the mean shear flow

E: production due to the dispersive components of turbulence

F: production due to the mean shear flow

G: production due to the dispersive component of turbulence (wake production)

H: production due to vortex stretching

I: viscous dissipation

By comparing Eq. (2.49) with the standard governing equation of turbulent dissipation rate (Chen, C-J and Jaw, S-Y, 1998), the grouped terms in Eq. (2.49) could be expressed as:

$A+B \approx \frac{\partial}{\partial x_k}(\frac{\nu_t}{\sigma_\varepsilon}\frac{\partial \langle\varepsilon\rangle^\beta}{\partial x_k})$ which represents the diffusion term

$D+F \approx \frac{\langle\varepsilon\rangle^\beta}{\langle k\rangle^\beta} C_{\varepsilon 1} \langle \overline{u_i' u_j'} \rangle^\beta \frac{\partial \langle \overline{u_i} \rangle^\beta}{\partial x_j}$ which represents the production due to the shear stress

$H+I \approx -C_{\varepsilon 2}\frac{(\langle\varepsilon\rangle^\beta)^2}{\langle k\rangle^\beta}$ which represents the destruction of $\langle\varepsilon\rangle^\beta$ as suggested by Chen, C-J and Jaw, S-Y (1998).

The molecular diffusion is normally neglected due to its insignificance in turbulence. Terms E and G are also production terms similar to D and F but associated with different mechanisms, and may be expressed as,

$E+G \approx \frac{\langle\varepsilon\rangle^\beta}{\langle k\rangle^\beta} C_{\varepsilon 1} P_w$, in which P_W is the wake production, given by:

$P_w = \eta_\varepsilon \langle \overline{u}_i \rangle^\beta f_i$ where η_ε is the efficiency of production of $\langle\varepsilon\rangle^\beta$.

Finally, the governing equation of $\langle\varepsilon\rangle^\beta$ could be formularized as

$$\frac{D\langle\varepsilon\rangle^\beta}{Dt} = \frac{\partial}{\partial x_j}(\frac{\nu_t}{\sigma_\varepsilon}\frac{\partial\langle\varepsilon\rangle^\beta}{\partial x_j}) + \frac{\langle\varepsilon\rangle^\beta}{\langle k\rangle^\beta}[C_{\varepsilon 1}(\langle \overline{u_i' u_j'} \rangle^\beta \frac{\partial \langle \overline{u_i} \rangle^\beta}{\partial x_j} + \eta_\varepsilon \langle \overline{u}_i \rangle^\beta f_i) - C_{\varepsilon 2}\langle\varepsilon\rangle^\beta] \qquad (2.50)$$

As discussed earlier, the term IV in Eq. (2.23) needs to be closed by a turbulence model. By using the modified parameterized equations of TKE and turbulent dissipation rate, which are applicable for the existence of vegetation, the classical two

equation $k-\varepsilon$ turbulence model is adopted here (Rodi, 1984). Thus, the stress term could be approximated by

$$\left\langle \overline{u_i' u_j'} \right\rangle^{\beta} = -\nu_t \left(\frac{\partial \left\langle \overline{u}_i \right\rangle^{\beta}}{\partial x_j} + \frac{\partial \left\langle \overline{u}_j \right\rangle^{\beta}}{\partial x_i} \right) + \frac{2}{3} \left\langle k \right\rangle^{\beta} \delta_{ij} \tag{2.51}$$

where δ_{ij} is the Kronecker delta and ν_t is the eddy viscosity. ν_t depends on the local state of turbulence and can be modeled by

$$\nu_t = C_D \frac{\left(\left\langle k \right\rangle^{\beta} \right)^2}{\left\langle \varepsilon \right\rangle^{\beta}} \tag{2.52}$$

in which, C_D is another empirical coefficient.

In Eqs. (2.48) and (2.50) as well as the Reynolds stress term, typical values of the coefficients are follows:

$C_{\varepsilon 1} = 1.44, \quad C_{\varepsilon 2} = 1.92, \quad \sigma_k = 1.0, \quad \sigma_\varepsilon = 1.3, \quad C_D = 0.09$

As for the other two parameters associated with the presence of vegetation η_k and η_ε, Shimizu and Tsujimoto (1994) has suggested that η_k =0.07 for wide and long vegetated open channel flow. Lopez and Garcia (2001) further showed that $\eta_\varepsilon = C_{\varepsilon 2} / C_{\varepsilon 1} \cdot \eta_k$ with the assumption of a steady, horizontal flow through vertical, infinitely long cylinders.

2.8 Quantification of Cd and Cm

In the derived governing equations of momentum, TKE and turbulent dissipation rate in the previous sections, all the vegetation-related terms requires the quantification of the vegetation drag force coefficient Cd and inertial force coefficient Cm in the wave

environments. In literature, there are many experimental reports on the values of Cd and Cm in different wave conditions for a simple structure, such as a circular cylinder, a sphere, or a cylinder with square cross-section (Chakrabarti, S. K., 1987). There are also a few researchers who investigate the variation of drag force coefficient for groups of cylinders. However, the studies on the drag force coefficient of array of cylinders are few and are scarcely reported. As for inertial force coefficient of grouped cylinders, the reports are much more limited. These two coefficients are of significant importance for the modeling or computation of wave characteristics in vegetative region, and in turn, are important for the evaluation of relative engineering projects.

Under these circumstances, substantial wave experiments with vegetation are demanding to understand and quantify the variations of Cd and Cm in different wave and vegetation conditions. For a single cylinder, its Cd and Cm can be investigated by placing the cylinder horizontally in an oscillating water tunnel, in which each segment along the cylinder experiences the same drag force and inertial force. In this way, the Cd and Cm of a cylinder can be estimated with measured force and velocities through Morison equation. However, this is not the case for an array of non-submerged vegetation in the waves.

In this study, to estimate Cd and Cm, only the horizontal wave forces on the incident direction are concerned. These horizontal forces may be attributed to the horizontal velocities and their rates of variation. Following Eq. (2.25), the total force may be expressed and simplified as:

$$F_x = F_D + F_I$$

$$= \left(\frac{1}{2}\rho A C_d \frac{\sqrt{\left(\left\langle \bar{u} \right\rangle^{\beta}\right)^2 + \left(\left\langle \bar{v} \right\rangle^{\beta}\right)^2 + \left(\left\langle \bar{w} \right\rangle^{\beta}\right)^2}\left\langle \bar{u} \right\rangle^{\beta}}{\theta^2}\right) + \left(\rho \forall C_m \frac{1}{\theta}\frac{\partial \left\langle \bar{u} \right\rangle^{\beta}}{\partial t}\right) \tag{2.53}$$

In the wave environments, the horizontal velocities change with water depth, resulting in the different forces exerted on different segments of on vegetation rod. Therefore, the above formula is only valid for a small vertical segment of the vegetation rod. Given that in wave flume experiments, the problem is essentially two dimensional, the transversal and vertical velocity components, v and w, have no effects on the total horizontal force in the x-direction. The total element force acting on a small segment could be given as

$$dF_x = \frac{1}{2} C_d \rho \cdot dA \cdot \frac{1}{\theta^2} \left\langle \bar{u} \right\rangle^{\beta} \left| \left\langle \bar{u} \right\rangle^{\beta} \right| + C_m \rho \cdot dV \cdot \frac{1}{\theta} \frac{D \left\langle \bar{u} \right\rangle^{\beta}}{Dt} \tag{2.54}$$

where dA is the projected area of the segment of one vegetation rod on the plane perpendicular to the wave propagation and dV is the volume of the segment.

Nevertheless, it is difficult to separately measure the force on each segment in experiments. By deploying the force gauge on the top or bottom of one cylinder or a group of cylinders, the total wave force exerting on the vegetation can be measured. This total force measured by force gauge can be obtained by integrating the segmented force dF_x through the whole submerged depth, which yields

$$\begin{aligned} F_x &= \int_d \frac{1}{2} C_d \rho \cdot dA \cdot \frac{1}{\theta^2} u|u| + \int_d C_m \rho \cdot dV \cdot \frac{1}{\theta} \frac{Du}{Dt} \\ &= \frac{1}{\theta^2} \int_d \frac{1}{2} C_d \rho \cdot D \cdot dz \cdot u(z)|u(z)| + \frac{1}{\theta} \int_d C_m \rho \cdot (\frac{\pi}{4} D^2) \cdot dz \cdot \frac{Du(z)}{Dt} \\ &= \frac{1}{\theta^2} \sum_m \frac{1}{2} C_d \rho \cdot D \cdot \Delta z_m \cdot u_m |u_m| + \frac{1}{\theta} \sum_m C_m \rho \cdot (\frac{\pi}{4} D^2) \cdot \Delta z_m \cdot \frac{Du_m}{Dt} \end{aligned} \tag{2.55}$$

In the above formula, the geometric properties of round cylinder are used to compute the projection area and the submerged volume, where D is the diameter of one rod, and dz represents the infinitesimal length of the segment of the rod in the integration. In experiments, it is unrealistic to measure the vertical distribution of horizontal velocities at

infinite layers. Only finite number of layers can be used to conduct the measurements. Therefore, the integration in the above equation is converted to the summation of forces at finite layers, where Δz_m is the length of the m_{th} layer and u_m is the measured velocity at that layer. In the above equation, for simplicity, the bracket and over-bar associated with horizontal velocities are omitted.

Based on Eq. (2.55), a series of wave experiments can be designed and conducted to quantify the vegetation Cd and Cm under wave conditions. The experiments carried out in this study will be presented in next chapter.

2.9 Summary of governing equations

In the preceding sections, the fully three-dimensional governing equations for waves propagating through the vegetation have been developed as well as the vegetation-modified energy budget equations. It is highlighted that this is the first time to present the 3D general equations for both momentum conservation and energy budget of vegetative flows under the condition of variable porosity. As a conclusion, the governing equations for uniform distributed vegetation are simplified and summarized as follows:

For mass and momentum conservation,

$$\frac{\partial}{\partial x_i}\langle \overline{u}_i \rangle^{\beta} = 0 \tag{2.56}$$

$$\frac{\partial}{\partial t}\langle \overline{u}_i \rangle^{\beta} + \langle \overline{u}_j \rangle^{\beta} \frac{\partial}{\partial x_j}\langle \overline{u}_i \rangle^{\beta} \qquad (i, j = 1,2,3)$$

$$= -\frac{1}{\rho}\frac{\partial}{\partial x_i}\langle \overline{p} \rangle^{\beta} + \nu \frac{\partial^2}{\partial x_j \partial x_j}\langle \overline{u}_i \rangle^{\beta} + g_i + \frac{\partial}{\partial x_j}\nu_t \left(\frac{\partial \langle \overline{u}_i \rangle^{\beta}}{\partial x_j} + \frac{\partial \langle \overline{u}_j \rangle^{\beta}}{\partial x_i}\right)$$

$$+ \left(-\frac{1}{2}\rho A C_{di} \frac{\sqrt{(\langle \overline{u} \rangle^{\beta})^2 + (\langle \overline{v} \rangle^{\beta})^2 + (\langle \overline{w} \rangle^{\beta})^2}\, \langle \overline{u}_i \rangle^{\beta}}{\theta^2}\right) \tag{2.57}$$

$$+ \left(-\rho \forall C_{mi} \frac{1}{\theta}\frac{\partial \langle \overline{u}_i \rangle^{\beta}}{\partial t}\right)$$

For turbulence model,

$$\frac{D\langle k \rangle^{\beta}}{Dt} = \frac{\partial}{\partial x_j}\left(\frac{\nu_t}{\sigma_k}\frac{\partial \langle k \rangle^{\beta}}{\partial x_j}\right) + \nu_t \left(\frac{\partial \langle \overline{u}_i \rangle^{\beta}}{\partial x_j} + \frac{\partial \langle \overline{u}_j \rangle^{\beta}}{\partial x_i}\right)\frac{\partial \langle \overline{u}_i \rangle^{\beta}}{\partial x_j}$$

$$+ \frac{\partial}{\partial x_j}\left(\nu \frac{\partial \langle k \rangle^{\beta}}{\partial x_j}\right) - \langle \varepsilon \rangle^{\beta} + \eta_k \langle \overline{u}_i \rangle^{\beta} F_i \tag{2.58}$$

$$\frac{D\langle \varepsilon \rangle^{\beta}}{Dt} = \frac{\partial}{\partial x_j}\left(\frac{\nu_t}{\sigma_\varepsilon}\frac{\partial \langle \varepsilon \rangle^{\beta}}{\partial x_j}\right) + \frac{\langle \varepsilon \rangle^{\beta}}{\langle k \rangle^{\beta}}\left[C_{\varepsilon 1}\left(\langle \overline{u_i' u_j'} \rangle^{\beta} \frac{\partial \langle \overline{u}_i \rangle^{\beta}}{\partial x_j} + \eta_\varepsilon \langle \overline{u}_i \rangle^{\beta} F_i\right) - C_{\varepsilon 2} \langle \varepsilon \rangle^{\beta}\right] \tag{2.59}$$

Chapter 3

Experimental Study of Drag Force and Inertial Force on Vegetation

3.1 Introduction

In the three dimensional equations of momentum conservation and energy budget for the various porosity of vegetation derived in previous chapter, two important parameters to be quantified for the computation of vegetation force are the vegetation drag force coefficient and inertial force coefficient. In section 2.8, the theoretical consideration in the estimates of Cd and Cm was articulated. According to the argument, experiments were conducted in a laboratory to measure the desired velocities and wave forces on the vegetation in order to compute the coefficients and propose an empirical formula for the application in numerical modeling and engineering estimation of wave-vegetation

problems. In this chapter, the experimental setup and procedures as well as the analysis of experimental results will be presented.

3.2 Experimental facilities and set-up

3.2.1 Wave flume

The experimental study was carried out in a two-dimensional wave flume at the Hydraulic Engineering Laboratory, National University of Singapore. The wave flume measures 38.5m in length, 0.92m in width and 1.0m in depth with a maximum working water depth of 0.9m. A piston-type wave paddle is installed at one end of the flume, while a gravel beach is provided at the other end with an average slope of 1:6. A schematic sketch of the wave flume is shown in Fig. 3.1

3.2.2 Wave generating system

The wave generating system is servo controlled piston type wave maker fixed at one end of the flume. This provides a facility to generate both monochromatic and random waves depending on the input signal. The wave paddle motion is controlled by a personal computer via the servo controller. Regular wave digital signals are generated and converted to analog signals by a National Instruments (NI) Labview software and a NI9263 module respectively. The National Instruments NI 9263, shown in Fig. 3.2, is a 4-Channel, 100KS/s, 16-bit, +/-10V, D/A converter. The generated analog signals are sent to the wave maker through the servo controller.

During the generation of regular waves, if pure sine-form signals are sent to the wave maker directly, a sudden initiation of the paddle creates a large irregular leading wave which can substantially disturb the subsequent regular waves. On the other hand, if the waves are continuously generated for a long time, the unavoidable reflected waves from the gravel beach can affect the measurements as well. To minimize adverse effects of the above two factors, 25-30 cycles of sine wave signals were first tapered by a cosine-window function and then were sent to the wave maker during the experiments. A tapered series of 29-cycle sine waves is compared with the un-tapered waves in Fig. 3.3. As shown in the figure, after the cosine window tapering, the strokes of the wave paddle can gradually increase to the desired amplitude at the beginning and decrease to zero at the end before the reflective waves approach the study region.

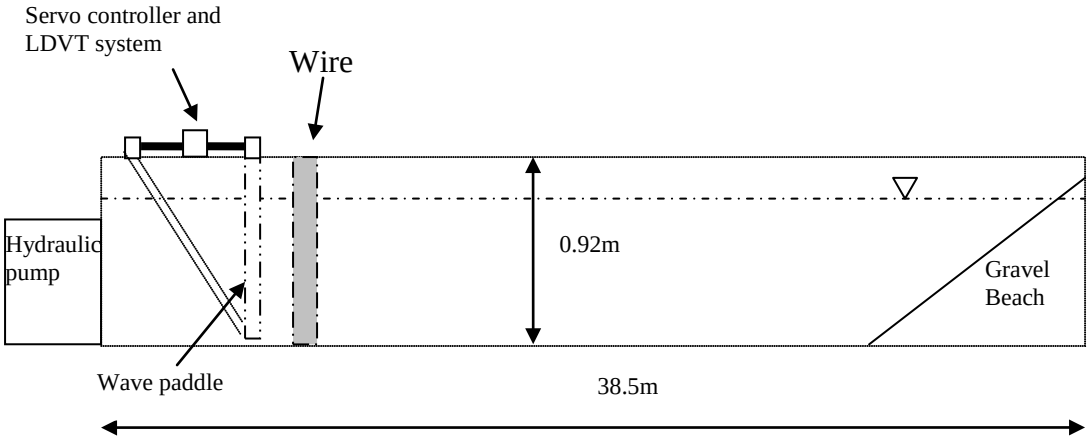

Figure 3. 1 Sketch of the wave flume

Figure 3. 2 Photo of NI9263 module used for the signal output

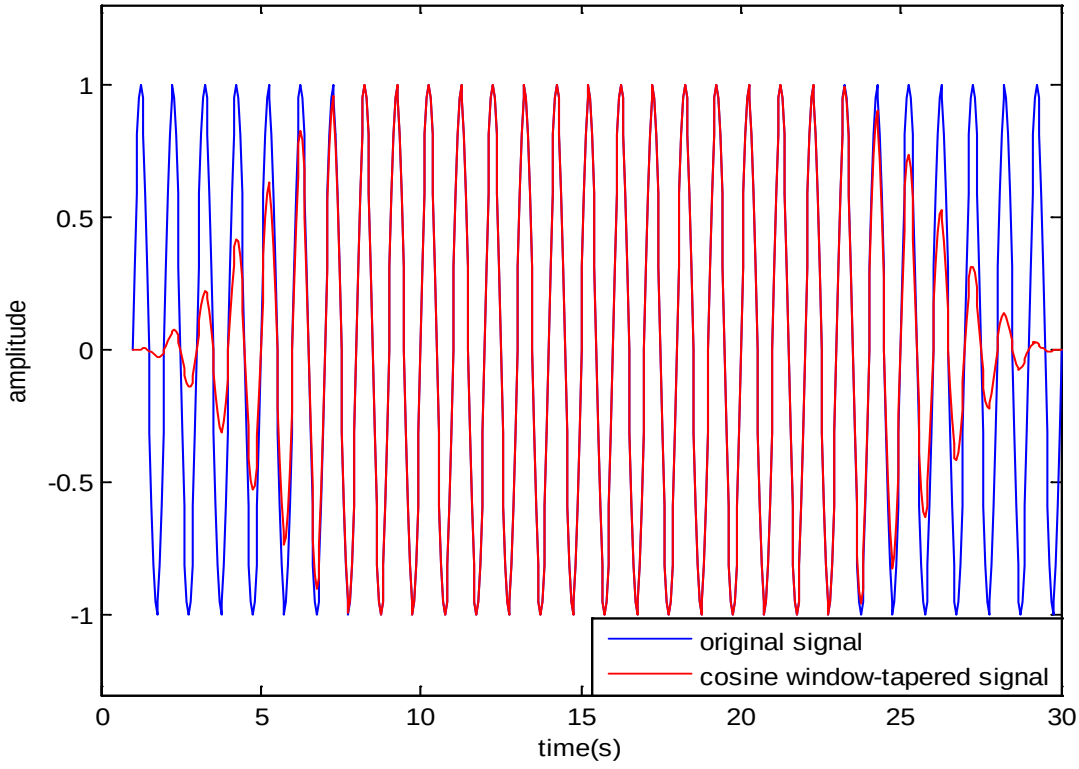

Figure 3. 3 Comparison of the taperred waves and the original sine waves

3.2.3 Experiment set-up

The set-up of the experiment is as shown in Fig. 3.4. 666 of 8mm aluminum rods were used to represent the rigid vegetation. Each aluminum rod measured 55cm long. One end of the rod was chamfered for the ease of being inserted into the holes of the bottom plywood. The other end of the rod was threaded, so that the rod could be fixed onto a constraining plywood at the top. To facilitate the installation, two pieces of plywood were drilled with 8.4mm diameter holes. The diameter of each hole was a little larger than the diameter of each rod. This was to allow for the expansion of the plywood after the drilling in the hydraulic laboratory environment which has a relatively high humidity. The arrangement of the holes is shown in Fig. 3.5. Each piece of plywood was 2m long and 0.9m wide. The spacing between the centers of two neighboring holes was 50mm in both in-line and transverse directions. After the drilling, a piece of the drilled plywood was placed on the bottom in the middle range of the wave flume. Due to the finite thickness of the plywood (1.5cm), one piece of plywood without holes was placed in front of the drilled plywood while another one behind the drilled plywood to avoid sudden depth changes on both ends of the vegetation. Silicone was used to generate a smoother transition at the ends of the bottom plywood. After the preparation of the bottom, all 666 rods were inserted with the chamfered end attached snugly in the holes of the bottom drilled plywood. The threaded ends were inserted into the holes of the top plywood and securely fastened by two nuts, one on each side of the plywood. However, the weight of the top plywood was taken up by a motor-controlled carriage.

As shown in Fig 3.4, the free surface elevations were recorded using resistance-type wave gauges while the fluid particle velocities were recorded by 50-Hz Acoustic Doppler

Velocimeter (Micro-ADV). The wave forces on the vegetation were measured with a DHI 3-component Force Transducer (Type 206/3C). Within the vegetation region, three positions were chosen to record the surface elevations, wave forces and water particle velocities. The relative positions denoted as position1, 2 and 3are shown in Fig. 3.6. The details of the instruments are described in the following sections.

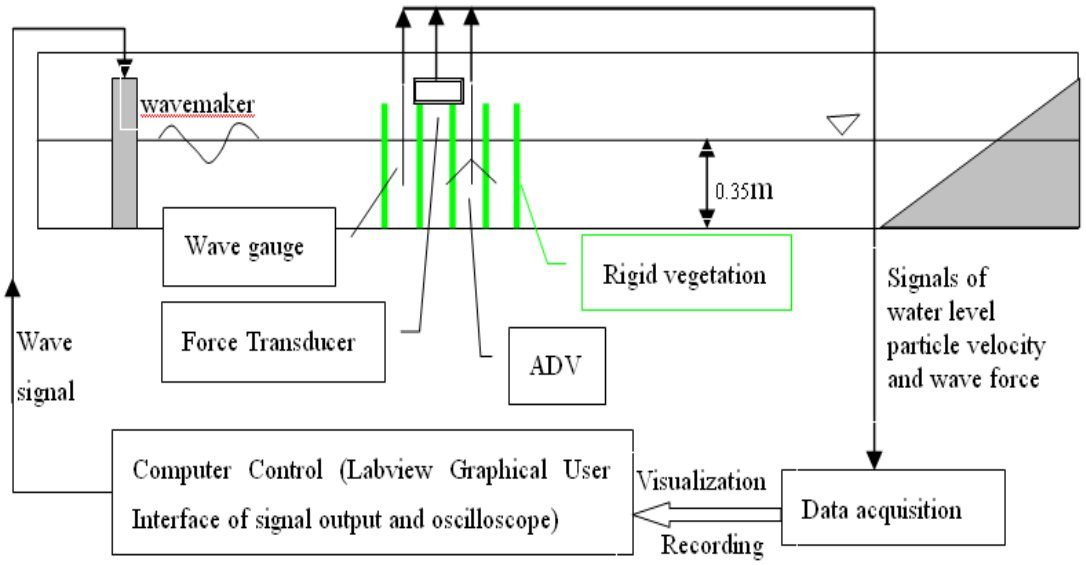

Figure 3. 4 Set-up of the experiments.

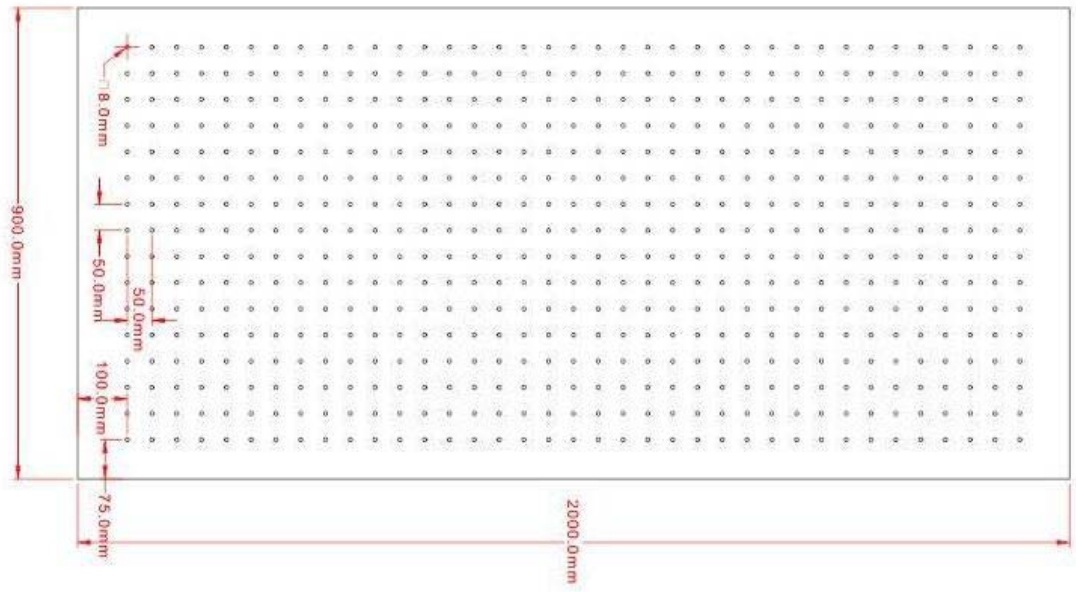

Figure 3. 5 Configurations of the holes arrangement drilled onto the top and bottom plywood pieces.

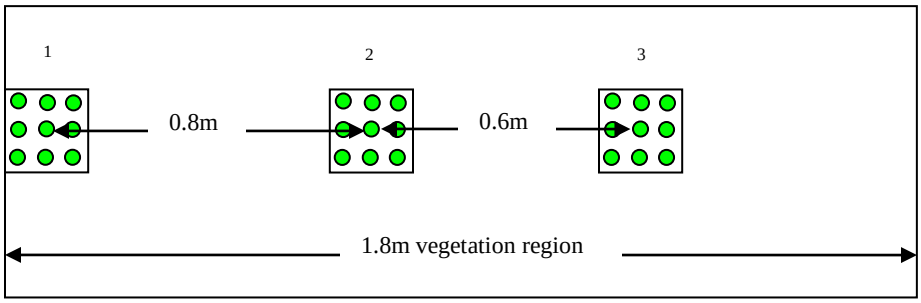

Figure 3. 6 Three measurement positions in the vegetation region, marked as position1, 2 and 3. The small square which covers 3x3 green circles represents the area of one plate of the force transducer.

3.2.4 Wave gauges

The time histories of surface elevations were measured using three wave gauges. One of the wave gauges was located at a position 2.9m in front of vegetation region. The second wave gauge was used to measure the surface elevation within the vegetation region. The third wave gauge was placed 3.5m downstream of the vegetation region. Within the vegetation region, the measurements were carried out at three positions which are shown in Fig 3.6. The wave probe (KENEK, CHT-30) is of the resistance type and has a length of 0.6m. It can measure wave heights of up to 30cm within the linear range. The wave probe consists of two vertical stainless steel wires. The changes in resistance depend on the depth of submergence. These changes are translated into changes in voltages proportional to the changes in the surface elevation.

Prior to each run of the experiments, the wave gauges were carefully calibrated to establish the voltage/wave height relationship.The calibration of the wave probes were carried out in flume to minimize the calibration errors. During the calibration, an adjustable stand was used to vary the submergence of the probe. The wave probe was attached to an adjustable stand and was initially half submerged. The output voltage was zeroed at this level of submergence to provide the datum. The stand could vary the submergence of the probe. The submergence varied up to +/-6cm in steps of 1cm and the output voltage was noted at each level. The calibration factor between the water surface elevation and the output voltage from the wave probe meter was then fine tuned so that every 0.1V difference in voltages represents 1 cm displacement of the water free surface. This was done for all the probes.

3.2.5 Velocity measurement

The particle velocity fields within the vegetated region were monitored using a SonTek 16-MHz Acoustic Doppler Velocimeter (MicroADV) with 50Hz sampling frequency. The ADV is a remote-sensing, three-dimensional velocity sensor. It measures the flow velocity using a Doppler effect.

The Sontek ADV probe is as shown in Fig. 3.7. During the experiments, it was mounted on a bracket which was fixed onto the sidewalls of the wave flume. The acoustic sensor consists of three receivers and one acoustic transmitter. When the probe is down-looking submerged in the water, the receivers, slanted at 30^0 from the vertical axis of the transmitter, focus on a common sampling volume which is 0.09 cubic centimeters and 5cm away from the tip of transmitter. The transmitter generates pulses of sound at a known frequency, which propagates through the water along the axis of its beam. As the pulses pass through the sampling volume, they are reflected by small particles suspended in the water such as sediments, powders or contaminants. Parts of these reflected pulses are received by the receivers. These received acoustic signals are sampled and the specific Doppler shifts of the frequencies between signals at the transmitter and each receiver are measured. Subsequently, the ADV combines velocity measurements from each receiver to calculate the 3D water velocities in the sampling volume. After the velocities are measured and calculated by ADV, they are collected, displayed and preliminarily processed by SonTek HorizonADV software(v1.04).

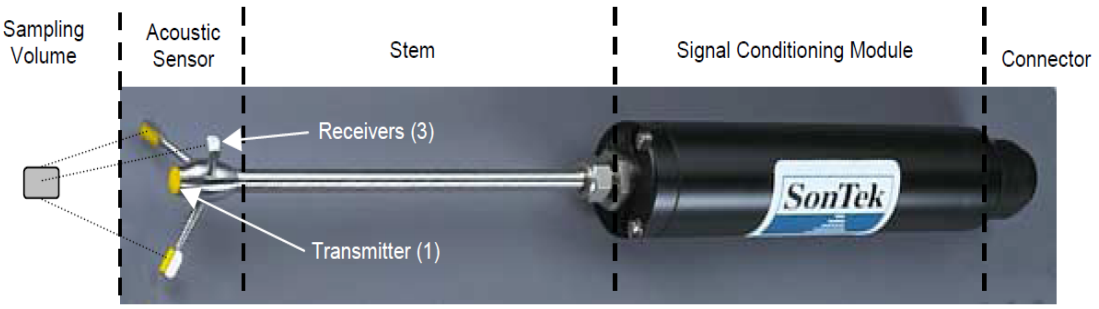

Figure 3. 7 Elements of Micro-ADV probe hardware.

3.2.6 Force transducer

To measure the vegetation-induced in-line forces on the waves, a DHI 3-component force transducer (Type 206/3C, s/n 108) was employed. The transducer was designed for measurements of two forces (Fx, Fy) and one moment (Mz). Since the goal of the experiments was to quantify the drag force and inertial force coefficients of vegetation, only the in-line force (Fx) was concerned. The top view and side view of the configurations of the force transducer is shown in Fig 3.8. As shown in the figure, two square plates are connected by four beams on which the strain gauges are mounted. The force transducer works on the principle of measurements of deflection of four beams. It has four strain gauges for each force/moment component, two on each side of one beam, connected as a full bridge.

When the DHI 106E strain gauge amplifier is connected to the force transducer, a bridge voltage is applied to the bridge. The resistance change will produce a voltage difference at the bridge, and this voltage difference is amplified with the strain gauge amplifier. Based on the specified sensitivity and the calibration factors, the forces are calculated.

Before the measurements, two plates of the force transducer were mounted to the vegetation rods and a fixed base, respectively, using eight bolts of size M6. The depth of the M6 thread is 15mm.

In the experiments, the forces on 9 aluminum rods were monitored as shown in Fig. 3.6. Because the diameter and spacing of the mounting holes on the transducer are different from the diameter and spacing of the aluminum rods. A 2cm thick stainless steel plate was fabricated to facilitate the coupling as shown in Fig. 3.9. The top of the force transducer was connected onto a cast iron C-channel that in turn was tightly mounted onto the sidewalls of the wave flume. This arrangement is shown in Fig. 3.10.

3.2.7 Data acquisition system

The output signals from wave gauges and force transducer were amplified and sampled at 100Hz. These output signals were converted to the physical values using the corresponding calibration factors. For ease of post-processing, the signals are recorded simultaneously using a 4-channel, 24-bit data acquisition module NI9237 as shown in Fig. 3.11. The high sampling rate and bandwidth of the NI9237 offer a high-quality and high-speed data acquisition with zero inter-channel phase delay. The data acquisition system consisted of a microcomputer, the A/D converter (NI9237) and the Labview software. The signal cables from the wave probes and pressure transducers were connected to the microcomputer through their amplifiers and the NI9237 module. The wave height and force time histories were recorded using Labview software. The velocity measurements were recorded by its own software WinADV.

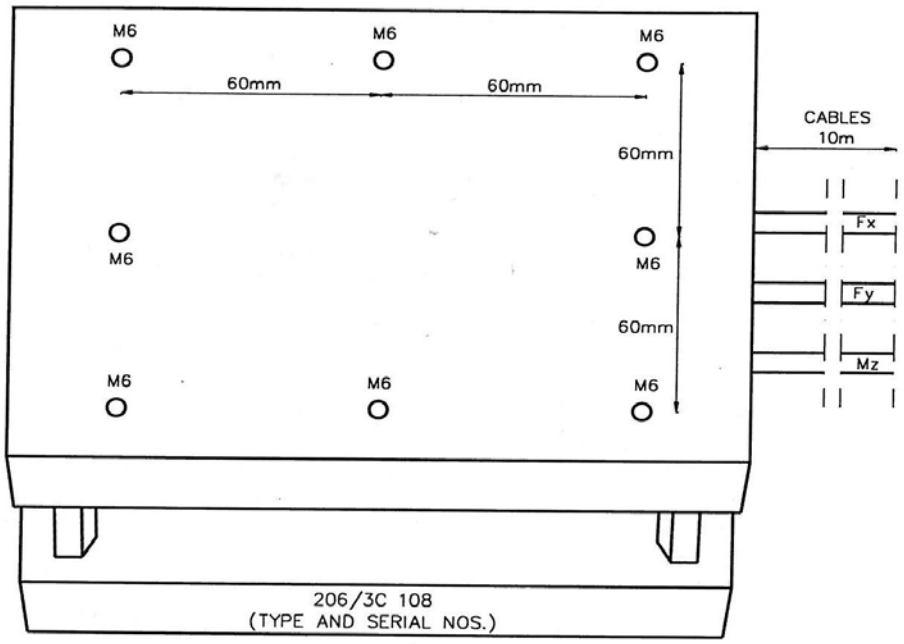

(a) top-view of one square plate of the force transducer (not to scale)

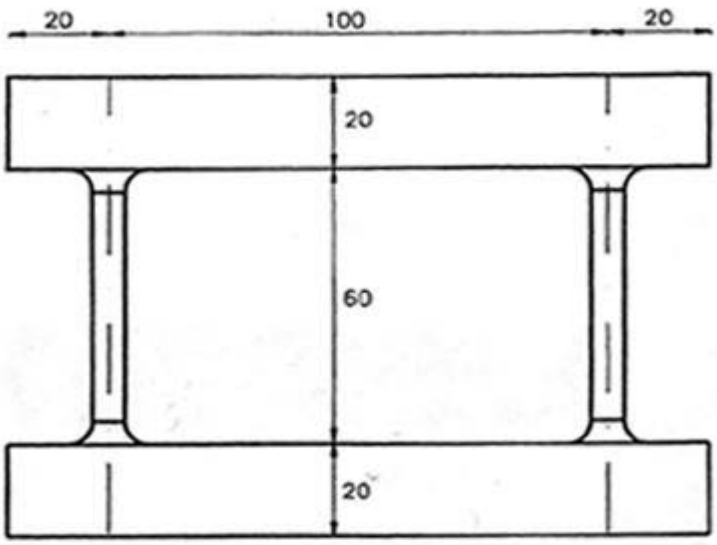

(b) Side-view of the force transducer

Figure 3. 8 Sketch of the force transducer.

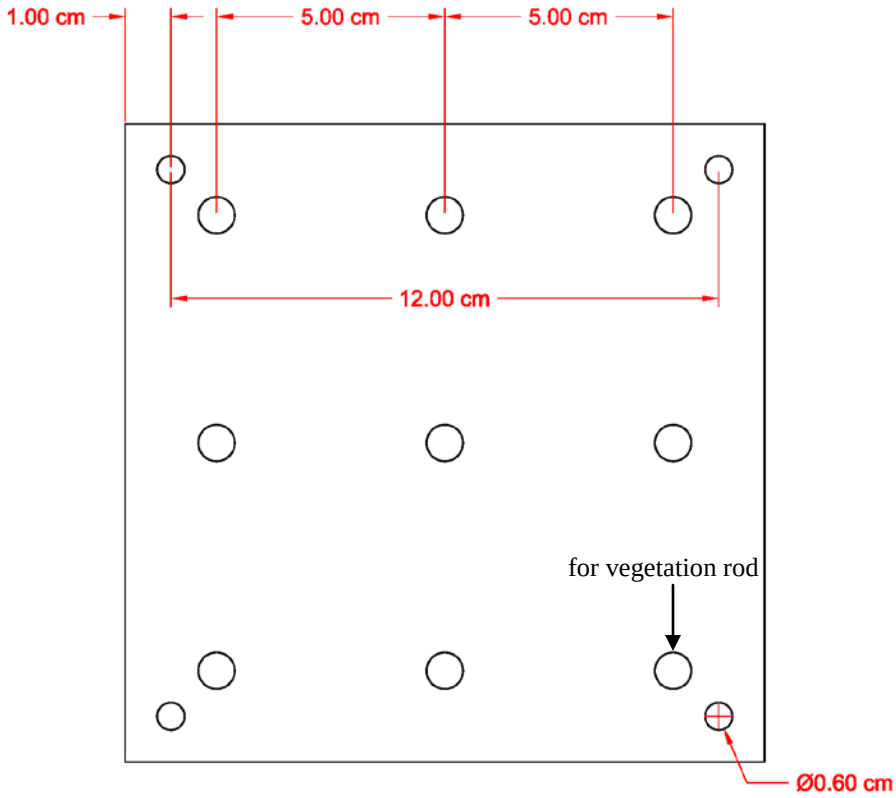

Figure 3. 9 Specifications of the connecting plate between the rods and the bottom plate of the force transducer (top view).

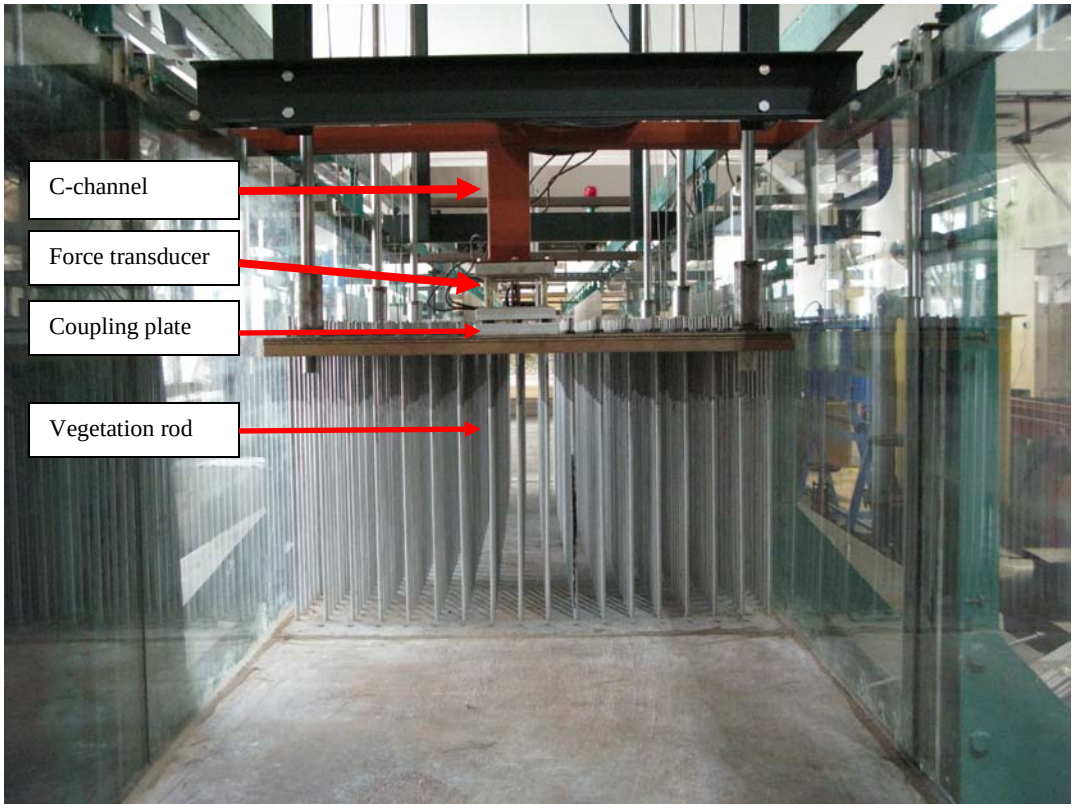

Figure 3. 10 Front view of the experimental setting-up before the water is filled in.

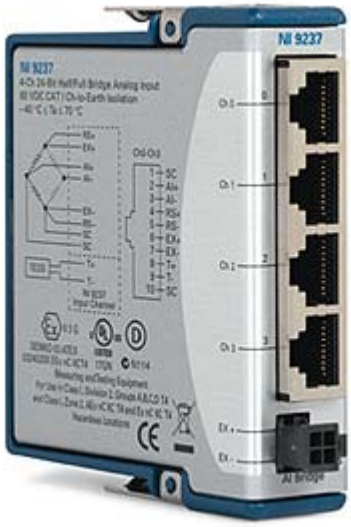

Figure 3. 11 Photo of NI9237 module for the signal recording.

3.3 Experimental procedure and results

3.3.1 Experimental procedure

Before the whole vegetation model was placed into the wave flume, the repeatability of the wave generation system was systematically tested through a series of wave simulation trials. Sinusoidal analog signals with frequencies of 1.0Hz and amplitude of 0.5 Volts were sent to the wave paddle. After five repeated runs with the desired wave frequency and amplitude, the locations of three wave gauges were switched. Fig. 3.12 shows a typical comparison of 3 recordings of different wave probes at the same position. Except for the first leading small wave which was affected by the initiation of the wave paddle movement, the time histories were repeatable suggesting that the wave generation was well controlled and repeatable and the readings of the three wave gauges were consistent. After having successfully tested the wave simulation, the vegetation model was put into the wave flume and installed as designed in section 3.2.3.

Waves with frequencies of 0.8Hz, 1.0Hz, and 1.2Hz were simulated. For each simulated wave case, velocities were recorded at five to eight vertical levels at prescribed locations as shown in Fig. 3.6. To capture the spatial fluctuations of the velocities within the vegetation, velocities at three points around one rod were monitored at each of the chosen elevation. Considering the symmetric distribution of the rods, these three points were fixed at the center of neighboring rods as shown by red crosses in Fig. 3.13.

To minimize the influences of residual flows of each run on the subsequent test, enough time was allocated between two consecutive runs allowing the water to calm down. Typically, this was about 20 to 30 minutes. The experiments were focused on small

amplitude waves, which meant that a train of small amplitude sinusoidal waves was generated to go through the vegetation region, and that the measured physical quantities could be compared with or analyzed using linear wave theory.

In a typical run, one wave gauge, the Micro-ADV, and the force transducer were deployed at the three measurement positions, respectively. After the required quantities were recorded, the positions of these instruments were switched and the wave simulations were repeated until the wave forces, surface elevations and water particle velocities were all collected at the three positions. The other two wave gauges were fixed upstream and downstream of the vegetation region.

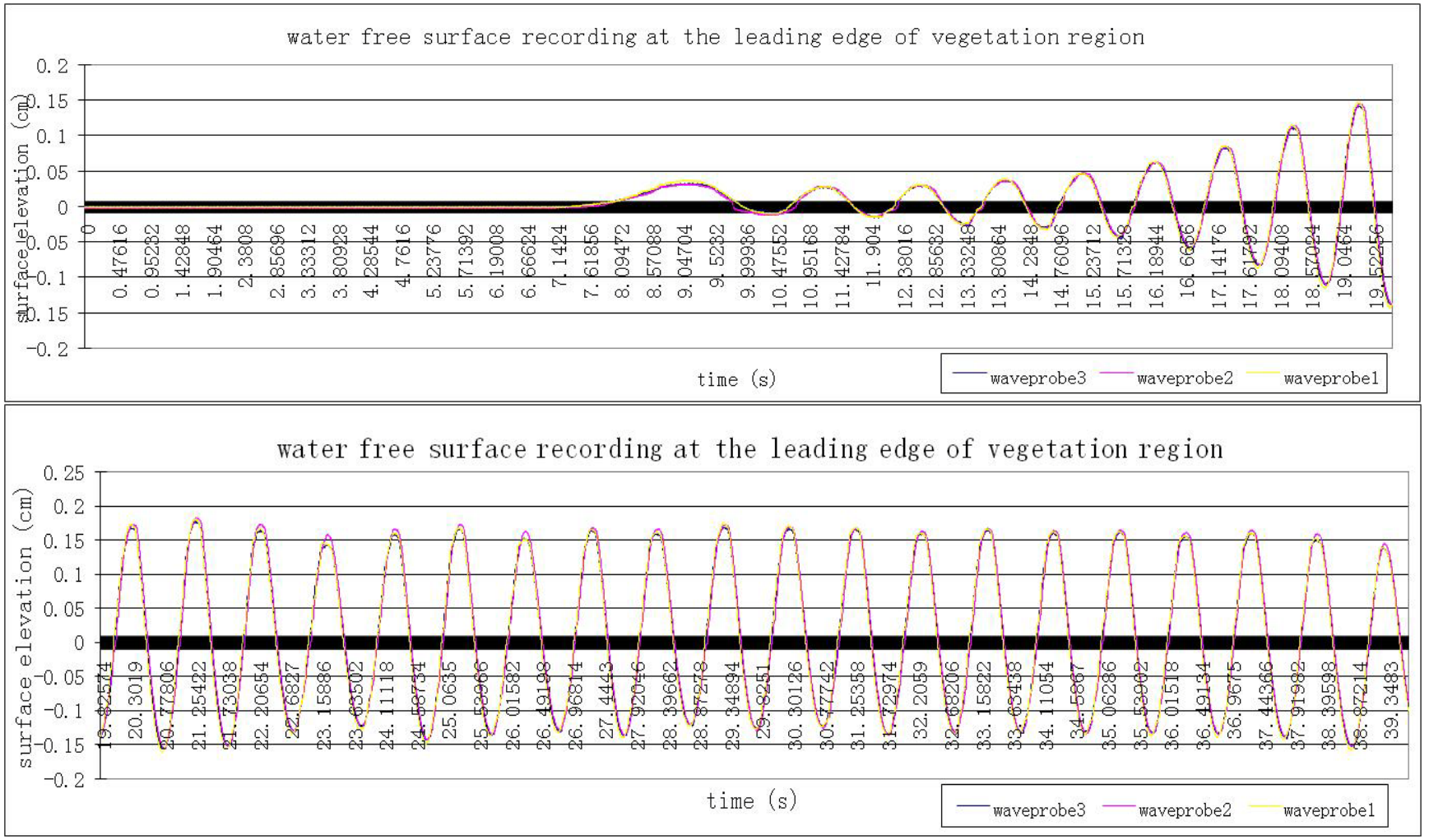

Figure 3. 12 The comparison of the recordings of three wave gauges at the same position for different runs of the same wave signals.

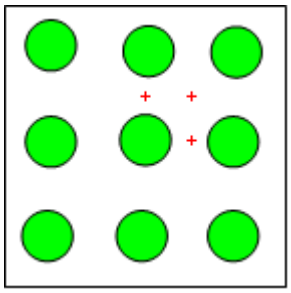

Figure 3. 13 Locations of three measurement points (red crosses) for the velocity at each layer of one position.

3.3.2 Analysis of experimental results

During each run of the experiments, water surface elevation, particle velocities and the bulk horizontal forces on nine rigid rods were recorded. To process these data and analyze the drag/inertial coefficients, the velocity data and horizontal force data were first filtered by a 25Hz-low pass filter. The purpose of this treatment was to eliminate the ground noise and other sampling noise. The main energy of the dominant frequency of the waves was conserved.

To synchronize the data collected from different wave runs, the time history of the reference wave gauge upstream of the vegetation was used for the alignment. This was possible due to the repeatability of the wave simulations. In particular, a specific zero-up-crossing point of the upstream surface elevation time history was chosen and used to align the time reference of signals obtained in repeated runs. Once the time histories of the upstream reference wave gauges from two runs were aligned, the measurements of the surface elevations and wave forces at the same position are aligned. In terms of water particle velocity, due to the small amplitude wave used in the experiments, the horizontal particle velocities and the surface elevations at the same position were in phase. As long as the zero-up-crossing points of the velocity time history and the surface elevation history at the same position were aligned, the velocity signals are aligned with the force signals which had been aligned with the surface elevations. As a result, the calculations of force coefficients were feasible through the relationship between force and velocity.

After alignment, the “synchronized” time series of various measurements were cropped to cover 20 cycles of the wave period (for 1.2Hz cases, 18 cycles were used to have an

integer number of seconds in the time range). The latter shortened signals were then used for further analysis.

In Fig.3.14 to Fig.3.22, the free surface elevations of different runs at each position are compared. It is clear that the overall agreement between the time series is good. The small discrepancies at the crests and troughs of different runs are reasonable considering the limits of the wave generation system and the signal noise.

At each position, the velocities were measured at three points around one rod as shown in Fig. 3.13. At each point, multiple runs were carried out.The aligned velocity measurements at the same elevation were averaged, resulting in the spatial-temporal averaging velocities.They were corresponding to the velocities in Eq. (2.55) for the calculation of wave forces.

Fig. 3.23 through Fig. 3.31 show the averaged velocities at different elevation above the bottom and their comparison with the computed velocities derived using linear wave theory. The mean amplitude of the measured surface elevation was used in the computation of the velocities. The figures show that at location 1 upstream of the vegetation zone, the measured velocities have a good agreement with linear theory. However, at the locations 2 and 3, the farther it was from the leading edge of the vegetation zone, the more the deviations from the linear theory. The reason is that due to existence of the rigid vegetation, the waves would be subjected to reflection, dissipation and other transformative processes. Because the vegetation was distributed in line with large void, the deformations were not large. However, it can be seen that from lower elevation to the higher elevation, the deviations of the mean velocities from the sine wave

are more and more large, which means that the surface velocities experienced more influences of vegetation.

In Fig. 3.32 to Fig. 3.41, the ensemble averaged force recordings are shown. In general, along the vegetation region, the forces gradually decrease due to the decreasing of particle velocities. Because the void rate (98%) in vegetation region is large, the reduction of particle velocities from position 1 to position 3 is relatively small, and so is the reduction of the corresponding forces.

The goal of current experiments is to quantify the drag force and inertial force coefficients through the instantaneous velocities directly surrounding the measured cylinders. The recording starts when the waves pass through the vegetation and stops before the reflected waves from both of the beach absorber and wave paddle reach the vegetated region. In this way, the recording data exclude the influence of reflected waves.

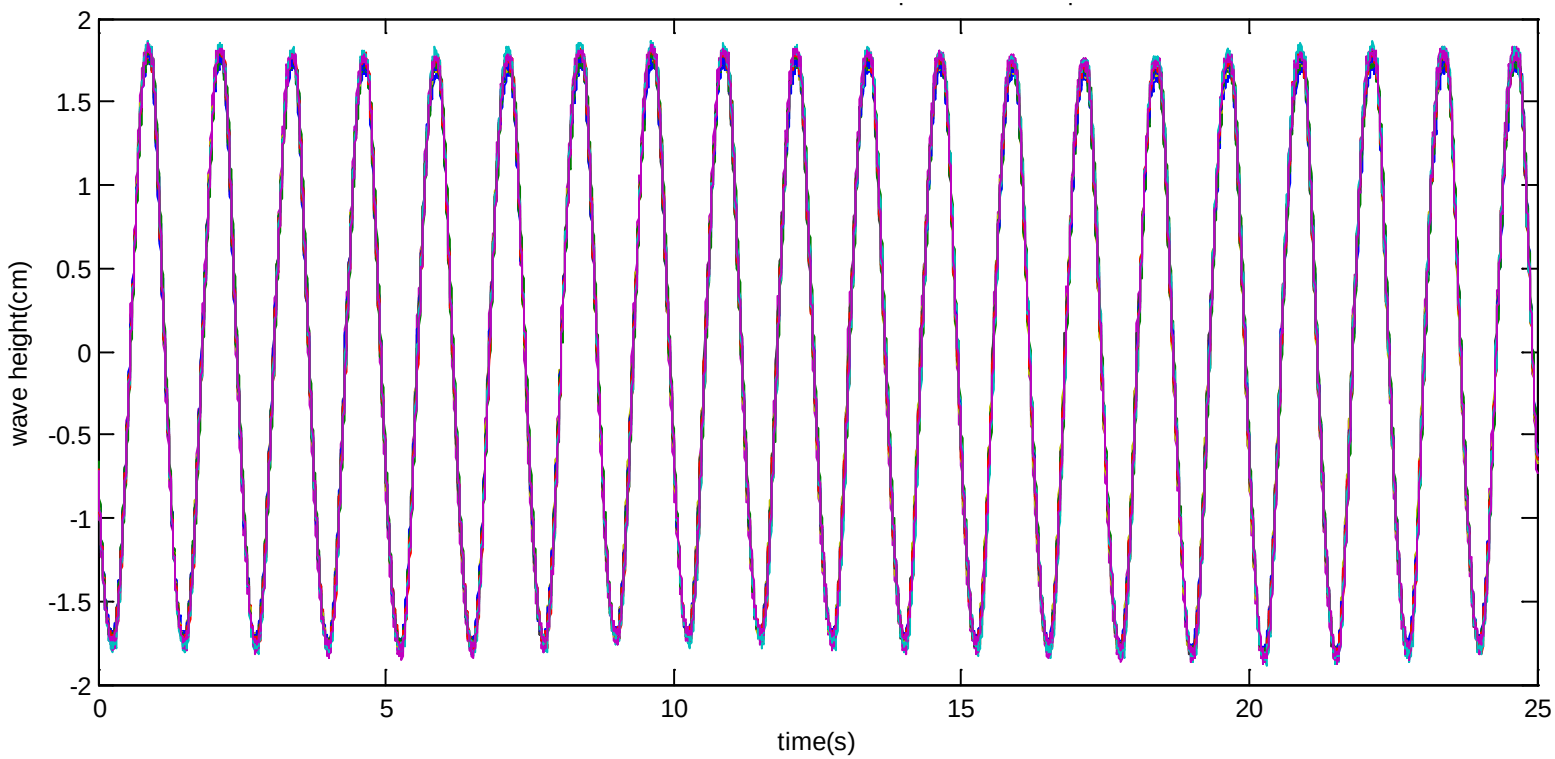

Figure 3. 14 Time histories of free surface elevation measured at the position 1 with1.25s waves (different colors represent different experimental sequences).

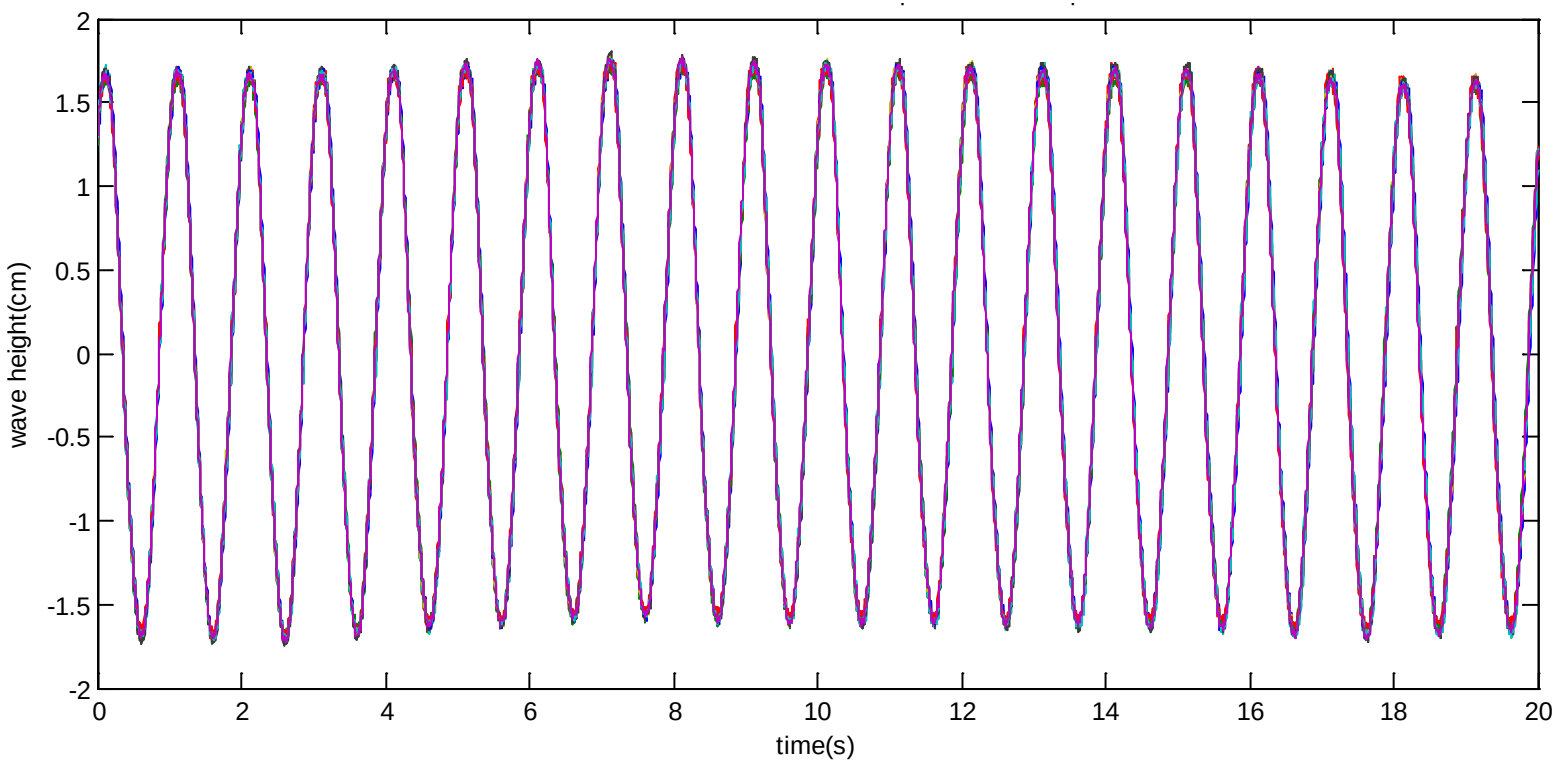

Figure 3. 15 Time histories of free surface elevation measured at the position 1 with1.0s waves.

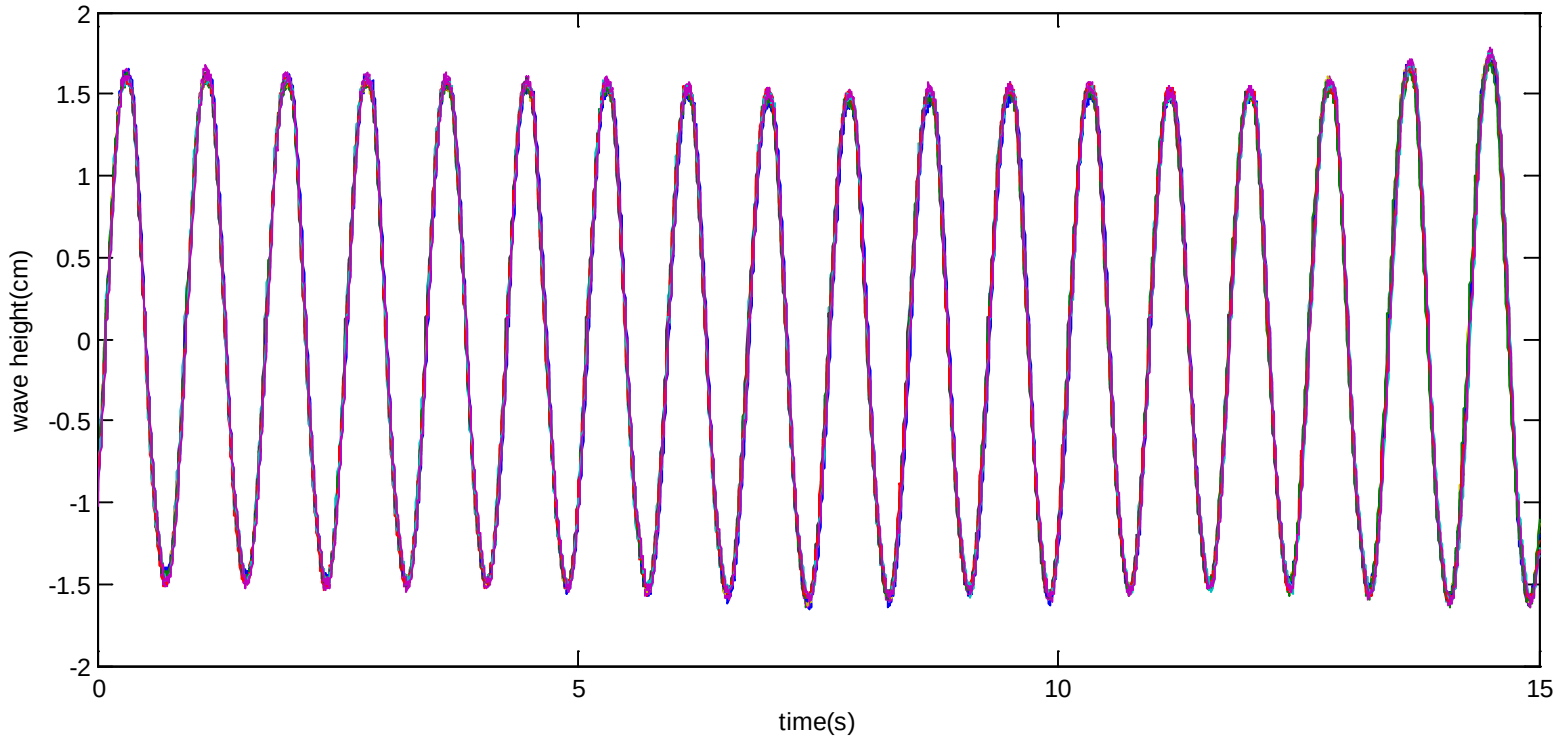

Figure 3. 16 Time histories of free surface elevation measured at the position 1 with0.83s waves.

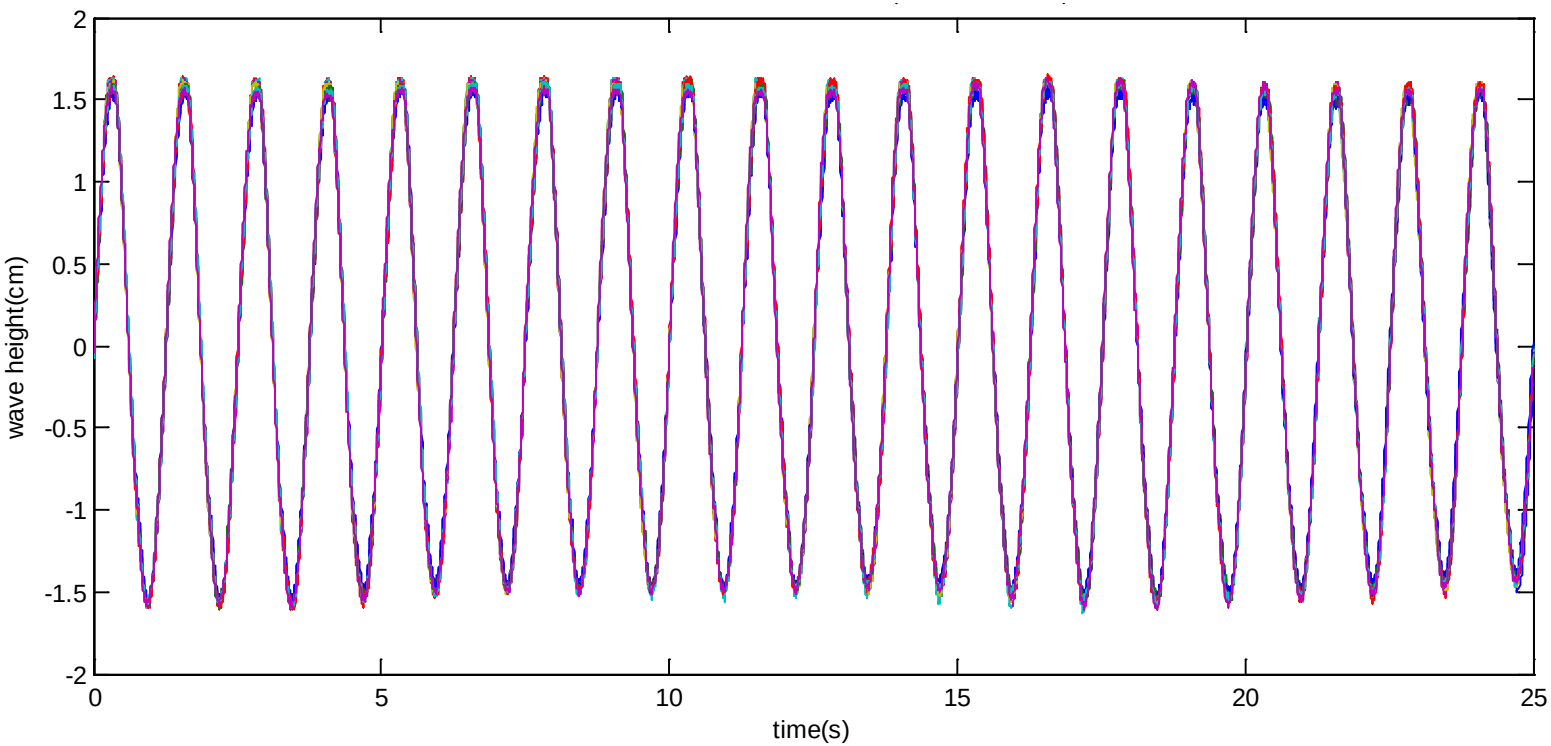

Figure 3. 17 Time histories of free surface elevation measured at the position 2 with1.25s waves.

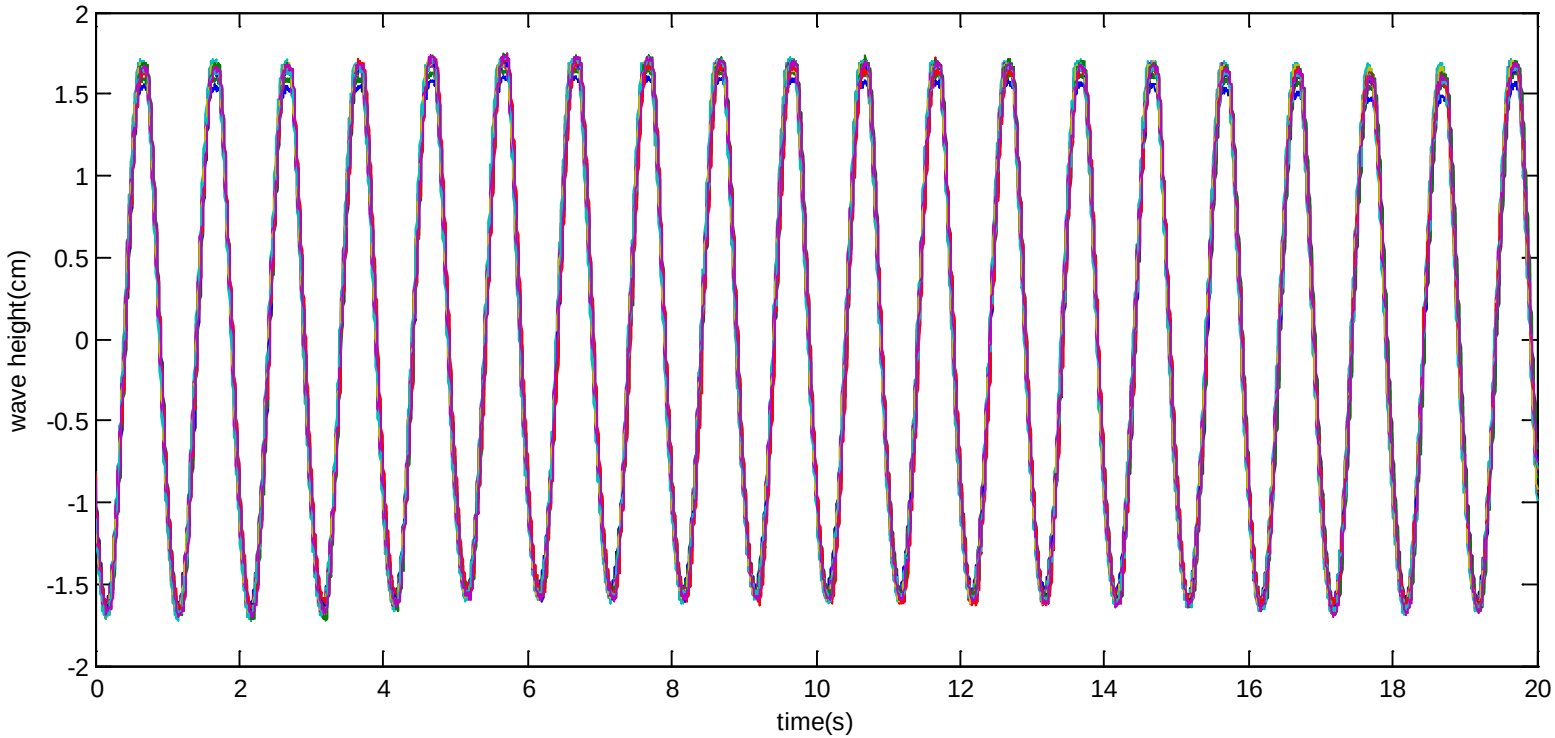

Figure 3. 18 Time histories of free surface elevation measured at the position 2 with1.0s waves.

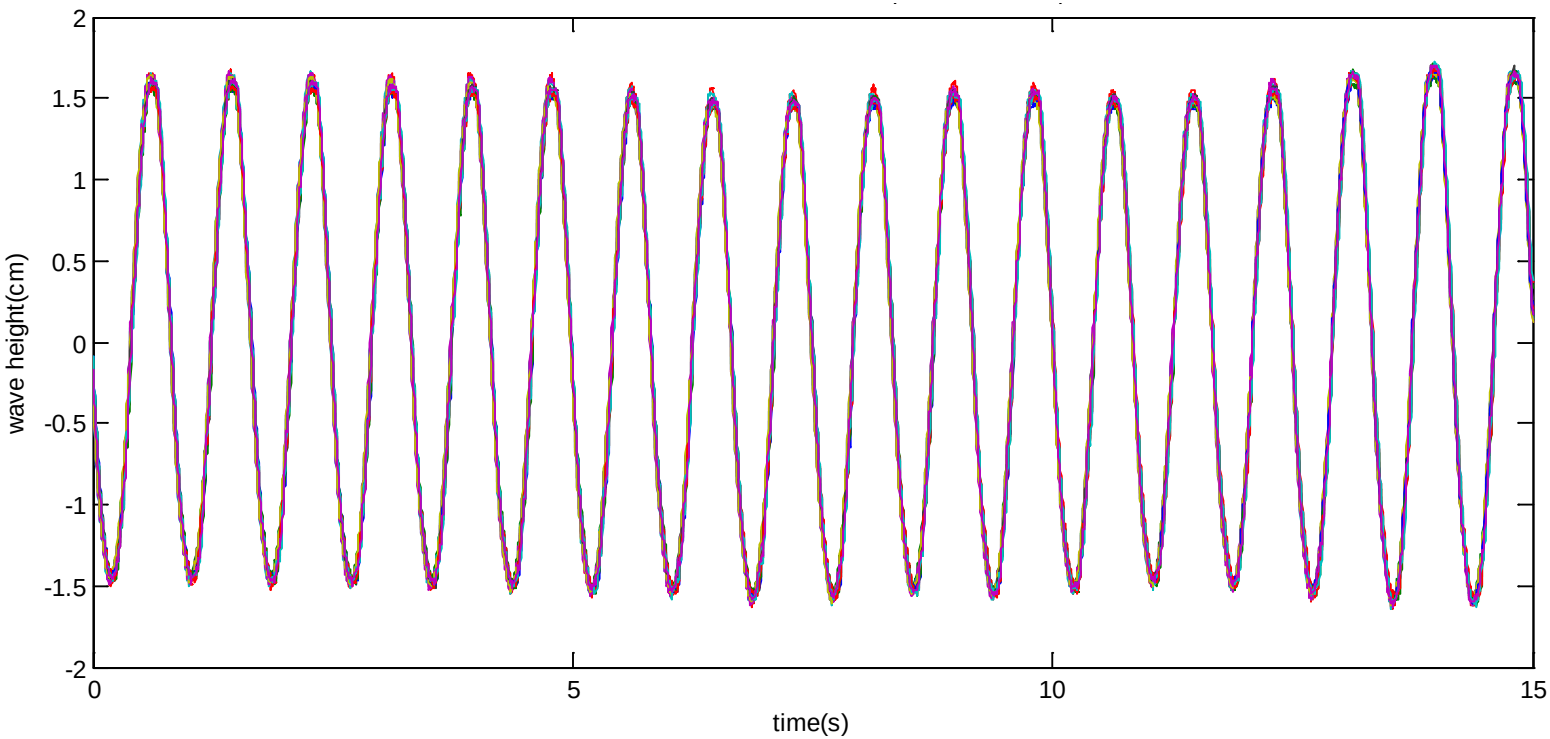

Figure 3. 19 Time histories of free surface elevation measured at the position 2 with0.83s waves.

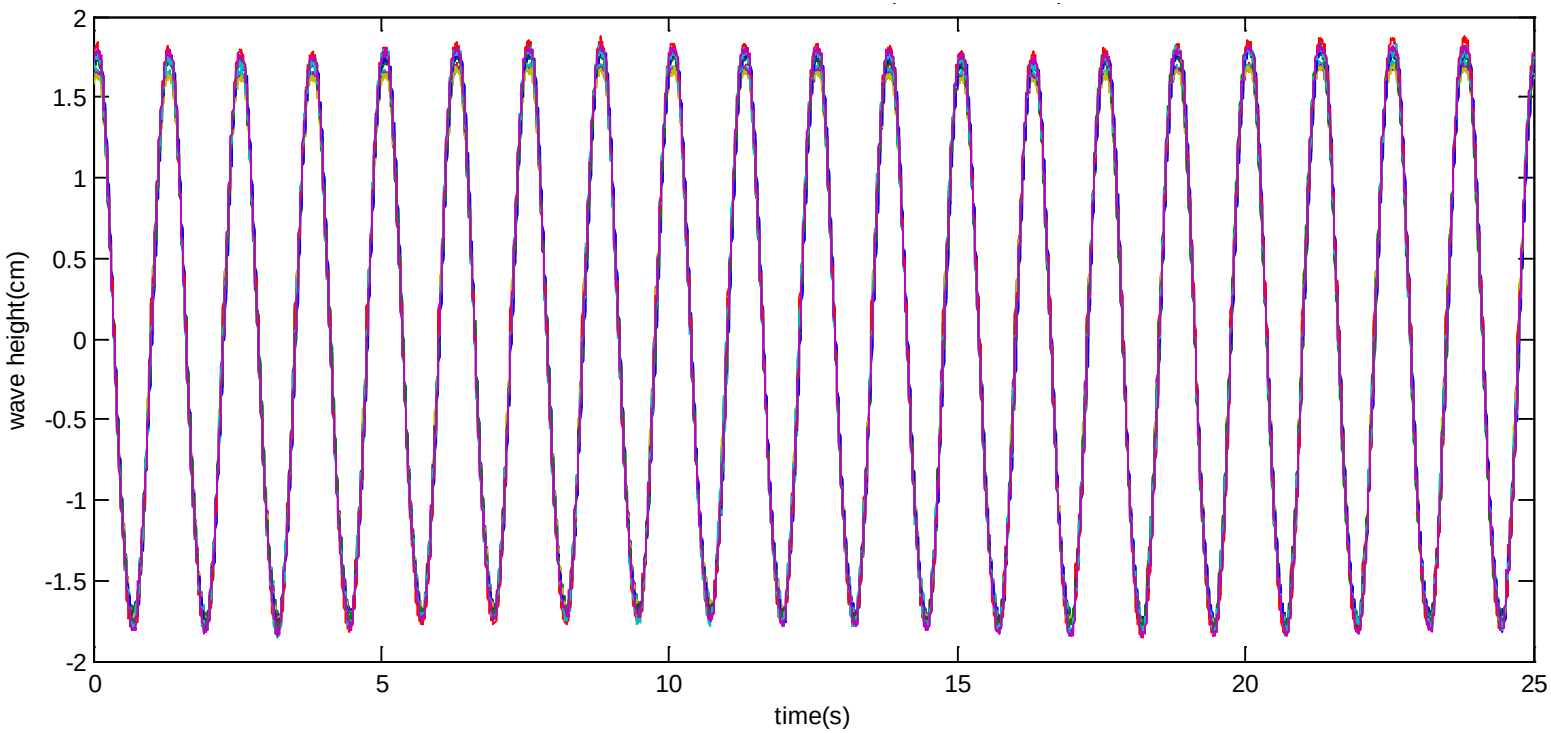

Figure 3. 20 Time histories of free surface elevation measured at the position 3 with period1.25s waves.

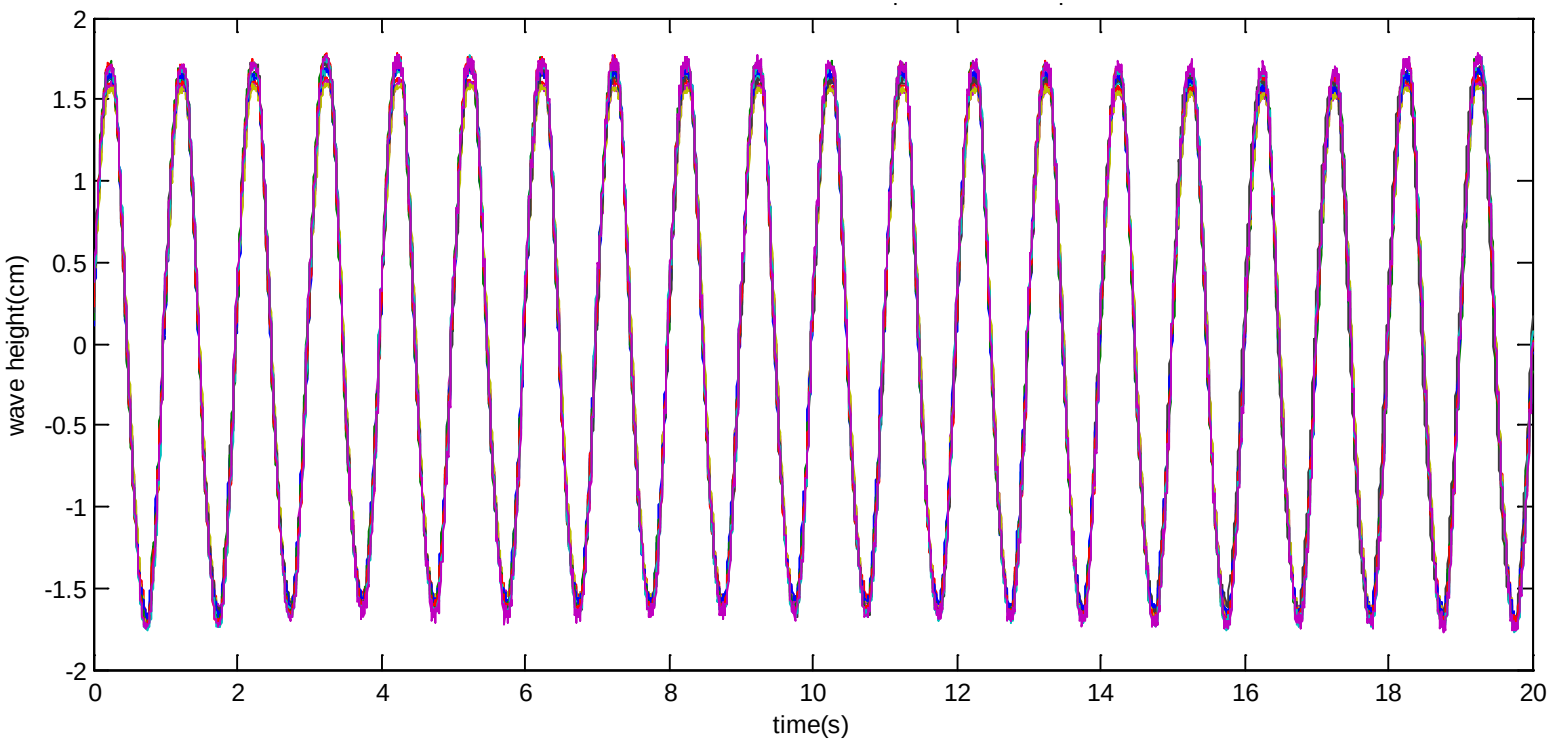

Figure 3. 21 Time histories of free surface elevation measured at the position 3 with1.0s waves.

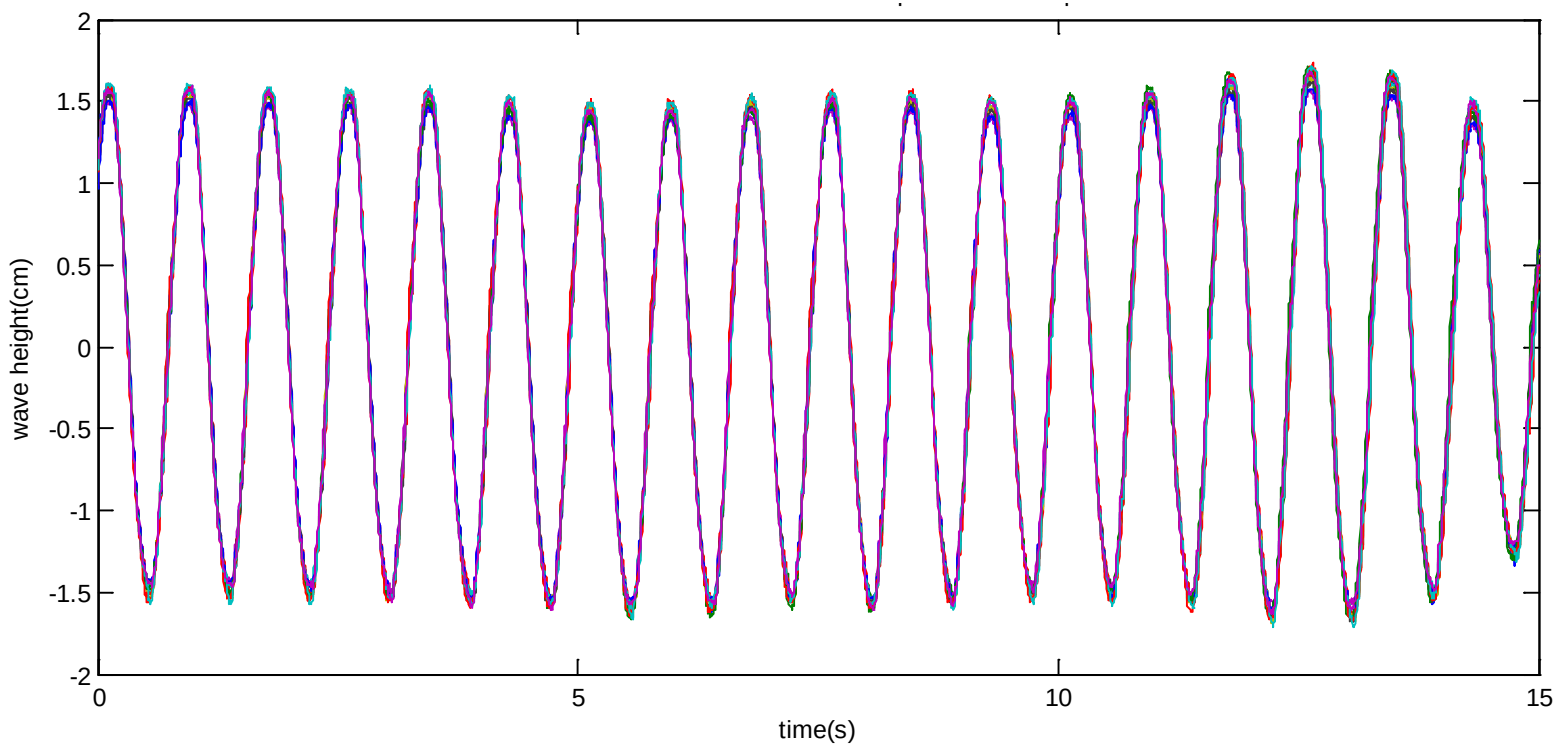

Figure 3. 22 Time histories of free surface elevation measured at the position 3 with0.83s waves.

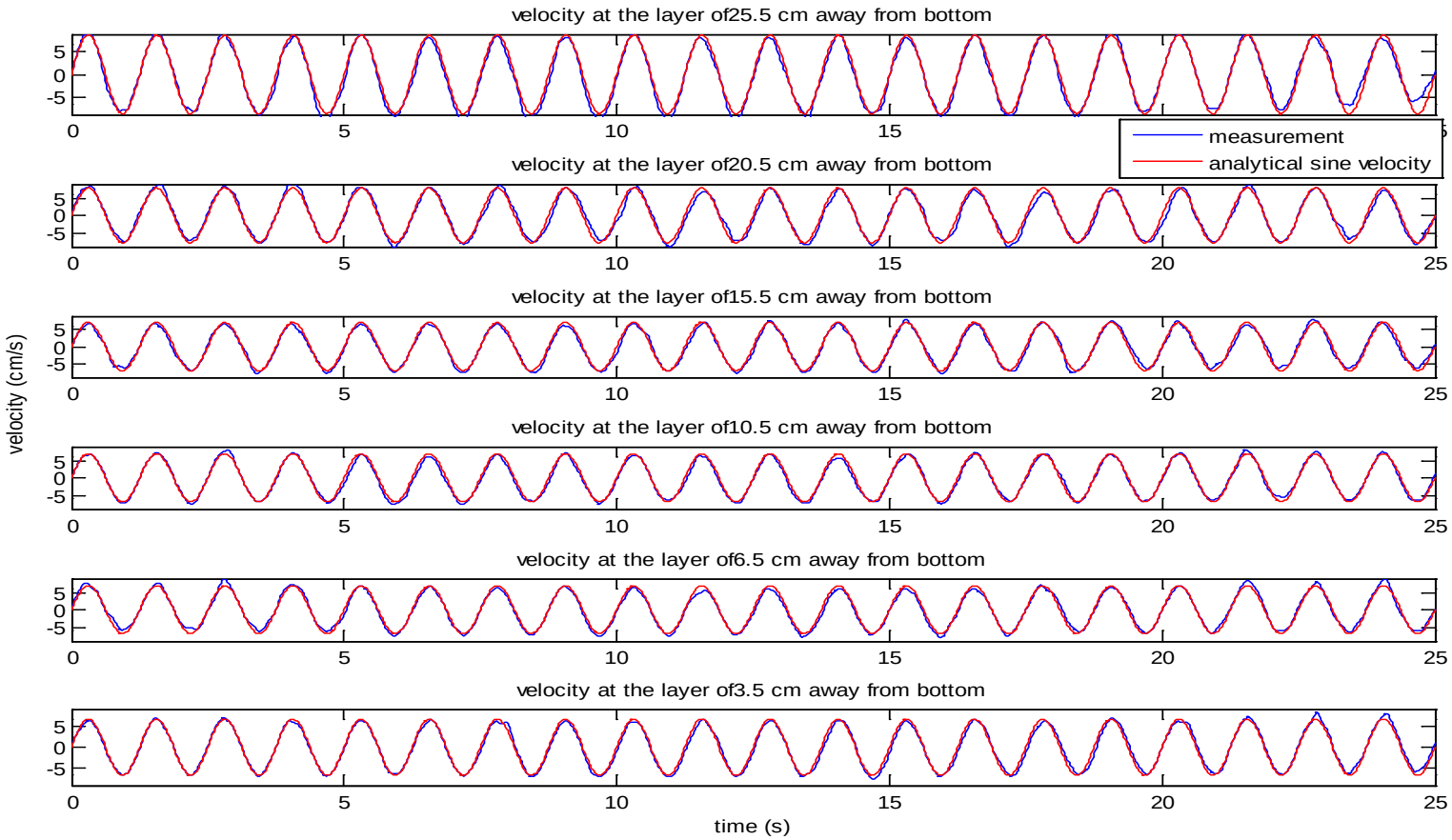

Figure 3. 23 Time histories of measured velocity and pure sine wave velocity with amplitude of measured velocity at different elevations above the bottom at position 1 for 1.25s waves.

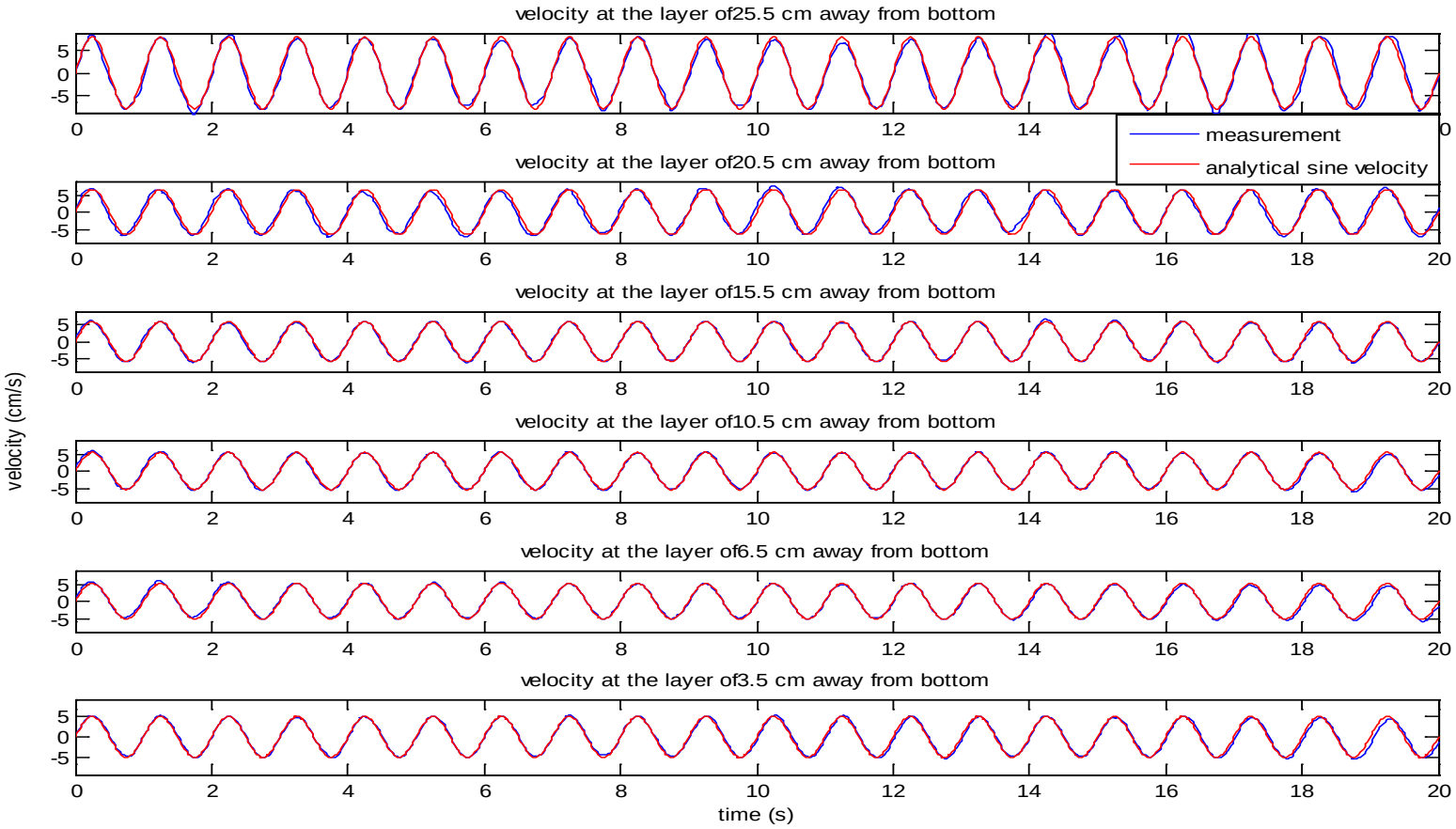

Figure 3. 24 Time histories of measured velocity and pure sine wave velocity with amplitude of measured velocity at different water elevations at position 1 for 1.0s waves.

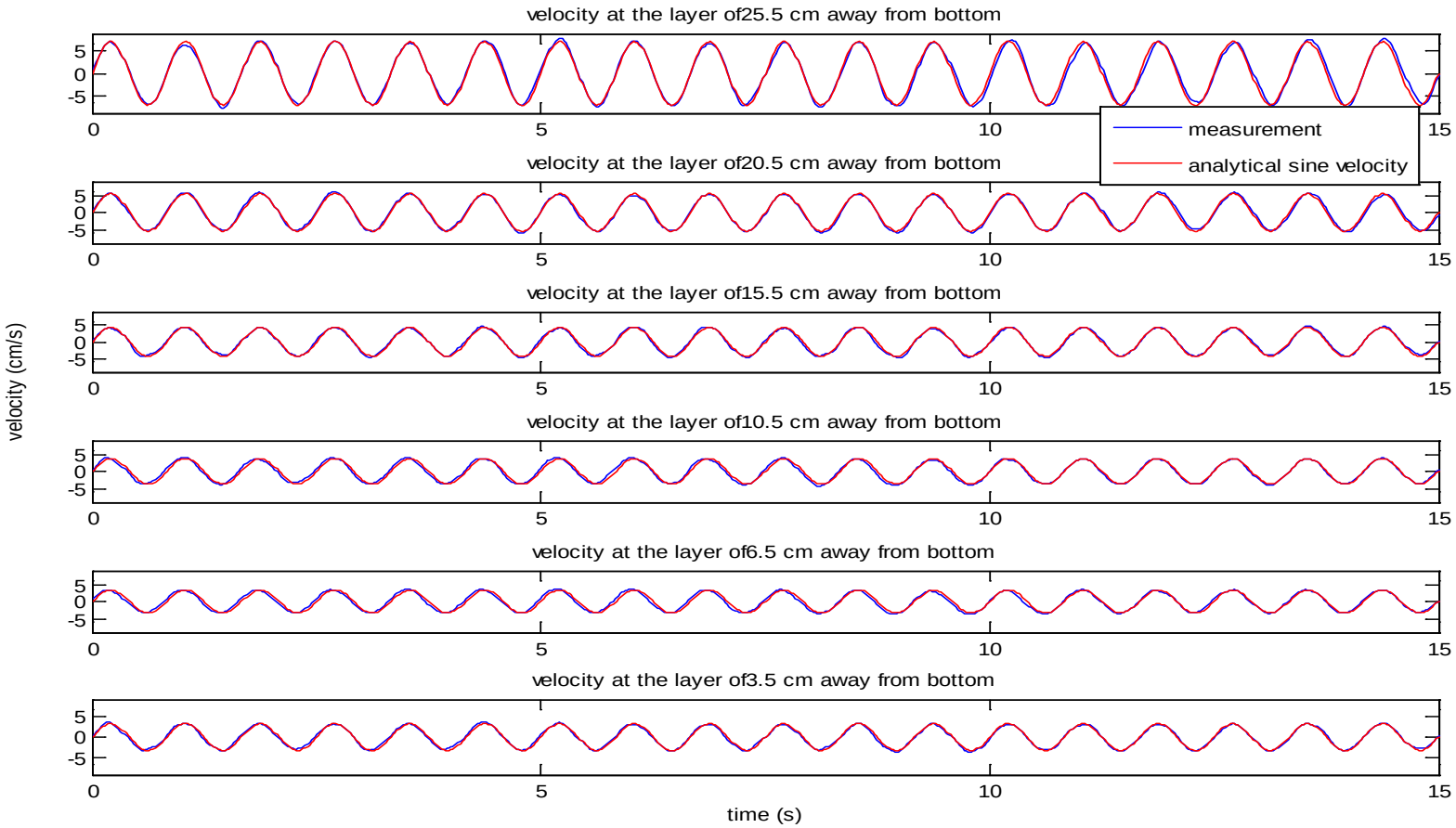

Figure 3. 25 Time histories of measured velocity and pure sine wave velocity with amplitude of measured velocity at different water elevations at position 1 for 0.83s waves.

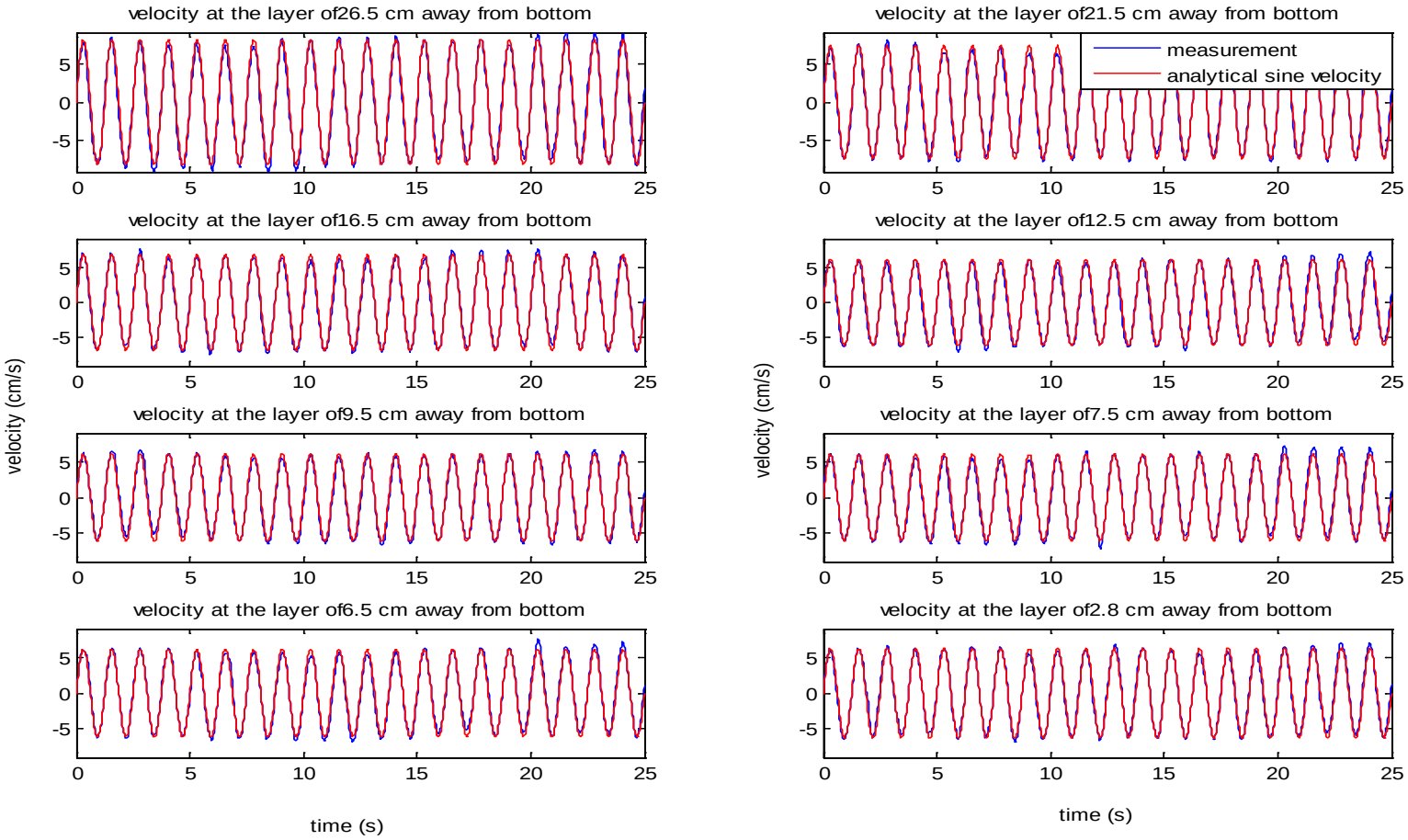

Figure 3. 26 Time histories of measured velocity and pure sine wave velocity with amplitude of measured velocity at different water elevations at position 2 for 1.25s waves.

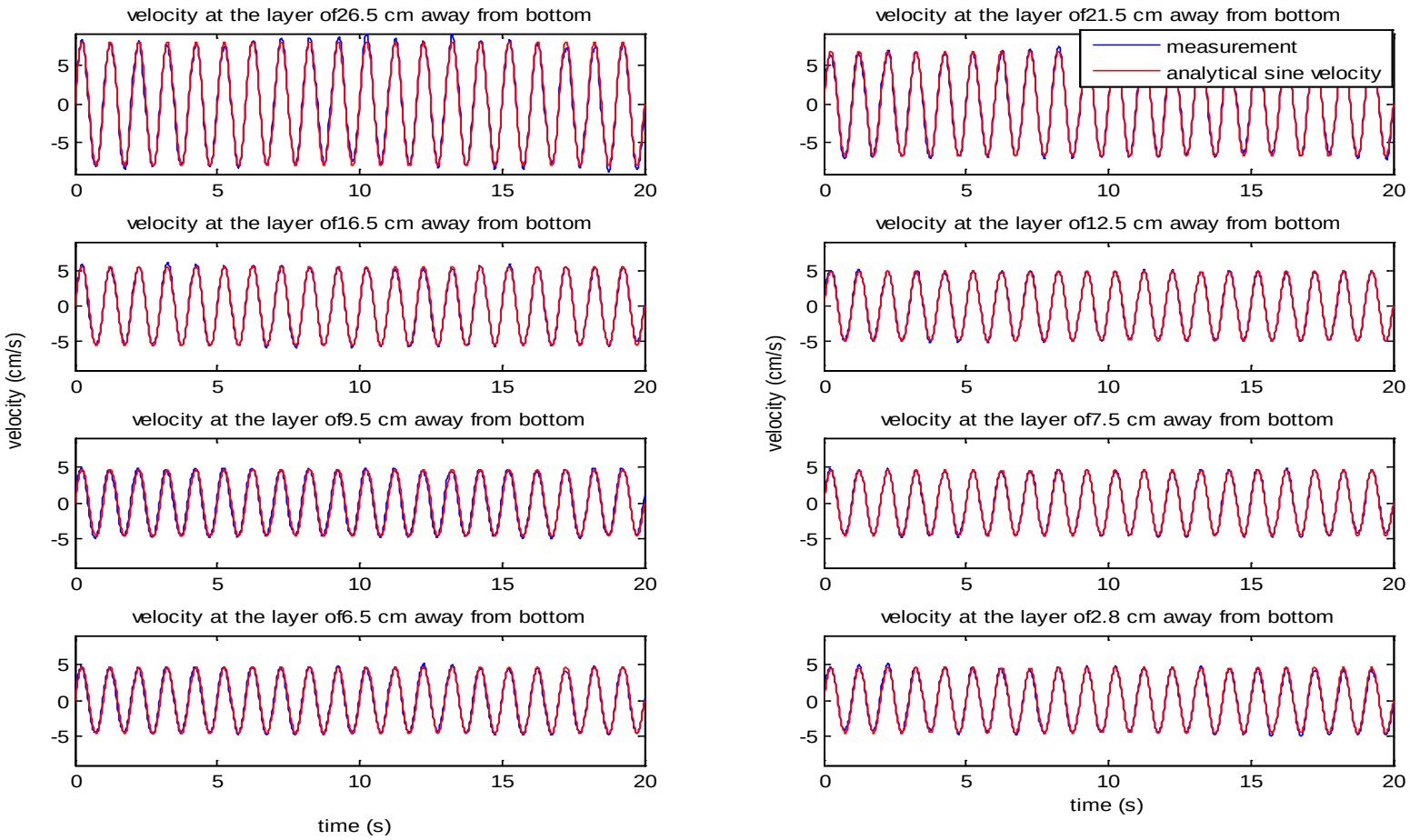

Figure 3. 27 Time histories of measured velocity and pure sine wave velocity with amplitude of measured velocity at different water elevations at position 2 for 1.0s waves.

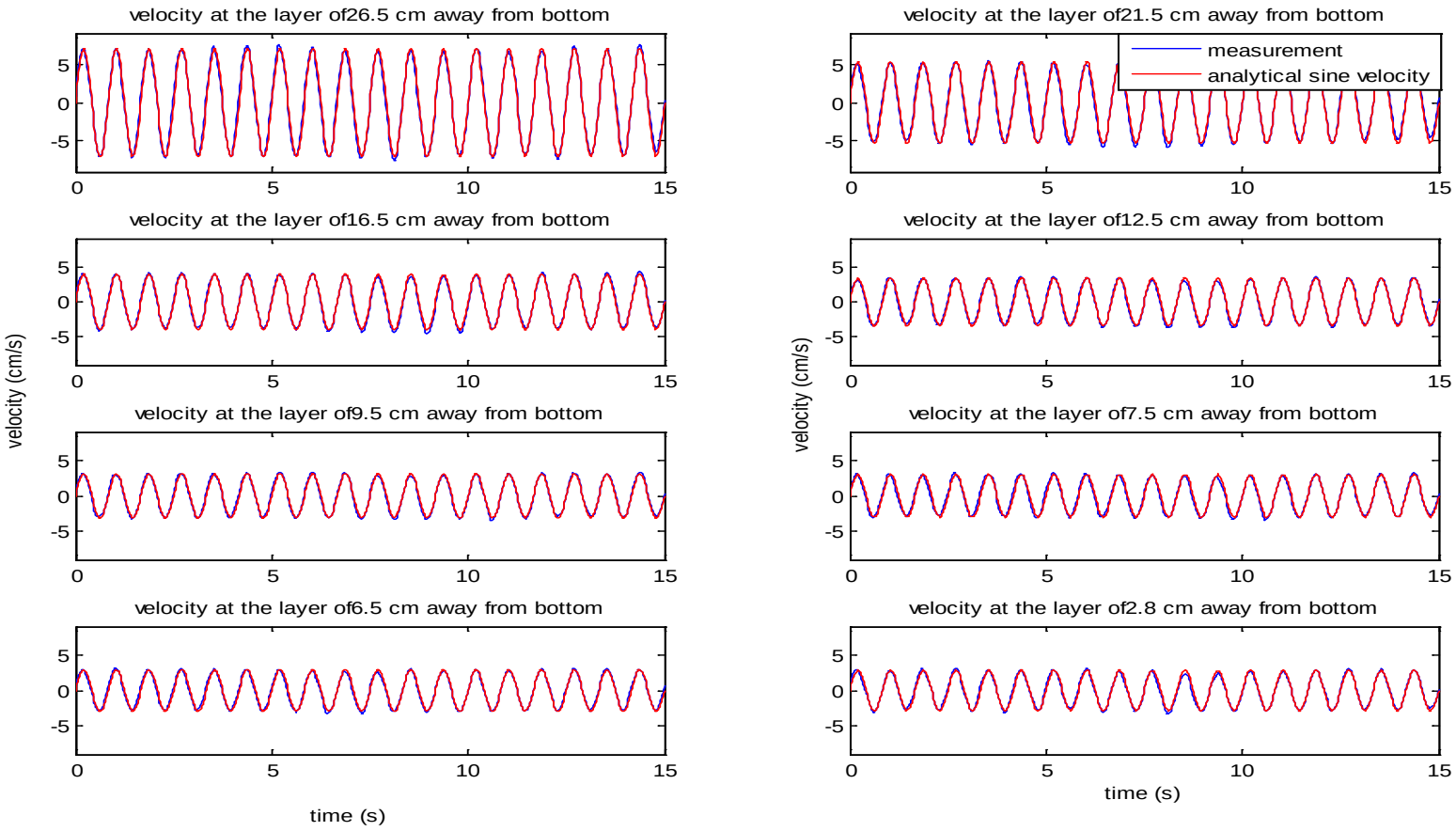

Figure 3. 28 Time histories of measured velocity and pure sine wave velocity with amplitude of measured velocity at different water elevations at position 2 for 0.83s waves.

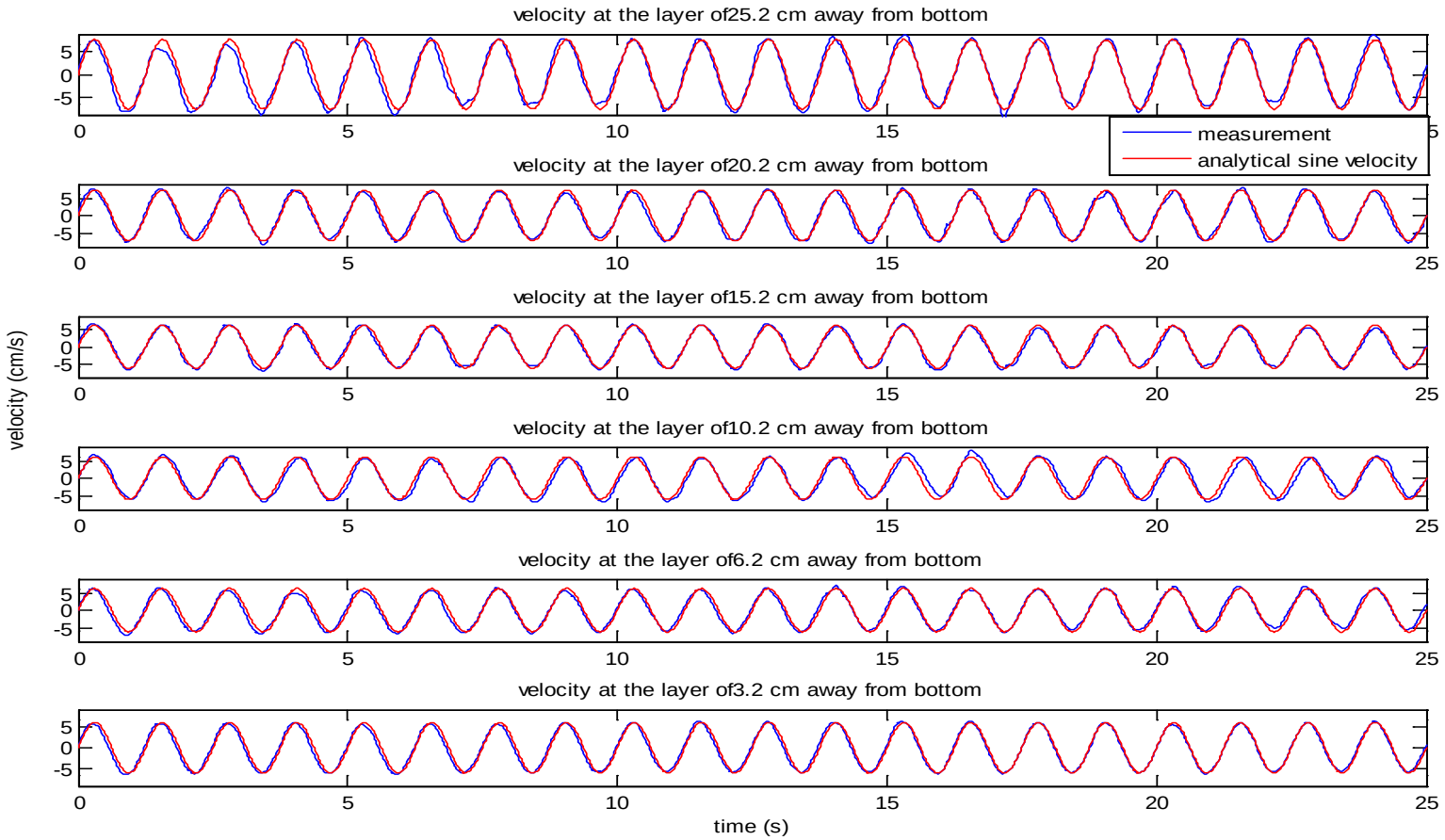

Figure 3. 29 Time histories of measured velocity and pure sine wave velocity with amplitude of measured velocity at different water elevations at position 3 for 1.25s waves.

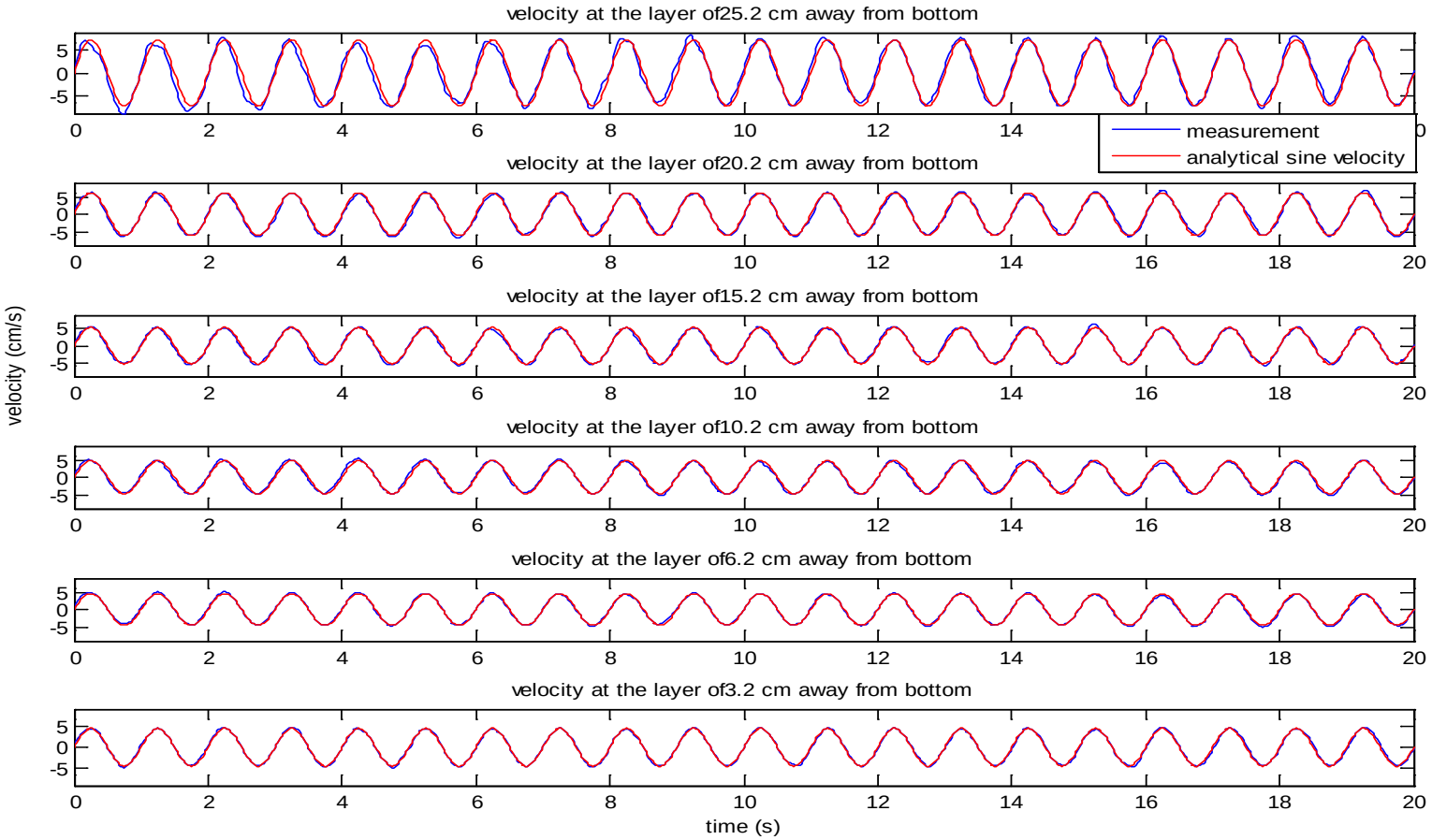

Figure 3. 30 Time histories of measured velocity and pure sine wave velocity with amplitude of measured velocity at different water elevations at position 3 for 1.0s waves of period of 1.0Hz.

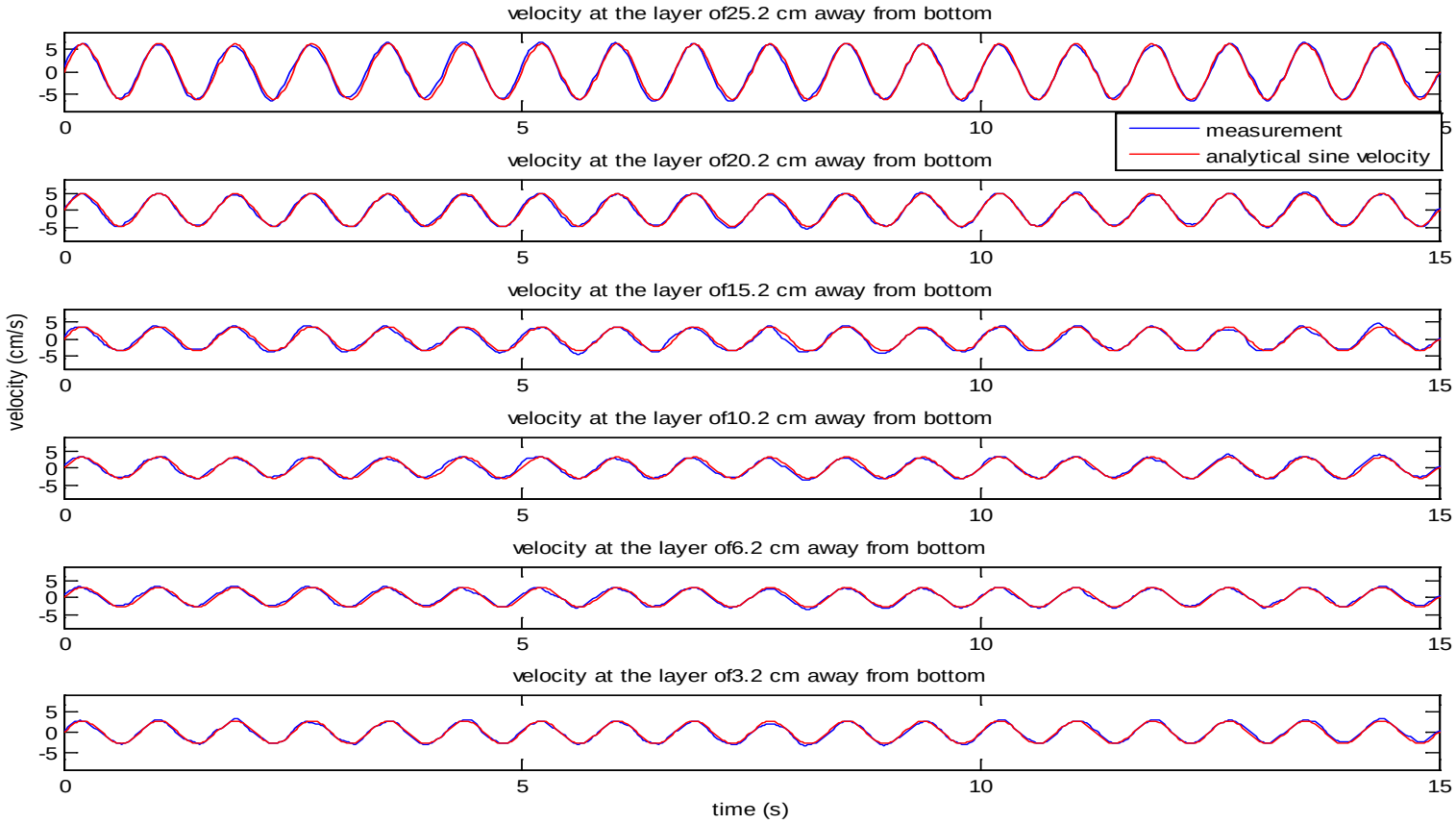

Figure 3. 31 Time histories of measured velocity and pure sine wave velocity with amplitude of measured velocity at different water elevations at position 3 for 0.83s waves.

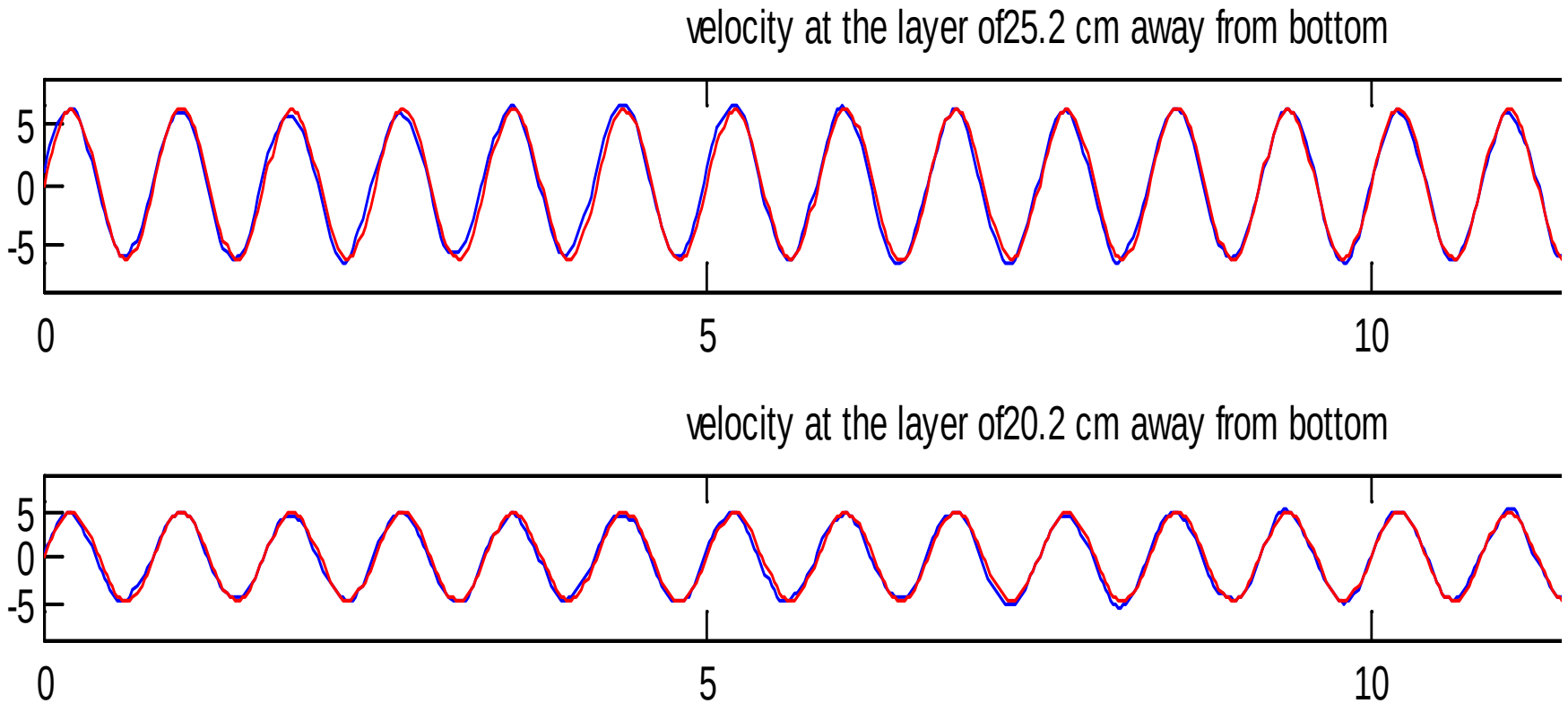

Figure 3. 32 Zooming-in of the comparison of measured velocity and pure sine wave velocity with amplitude of measured velocity at different water elevations at position 3 for 0.83s waves (blue line is measured data).

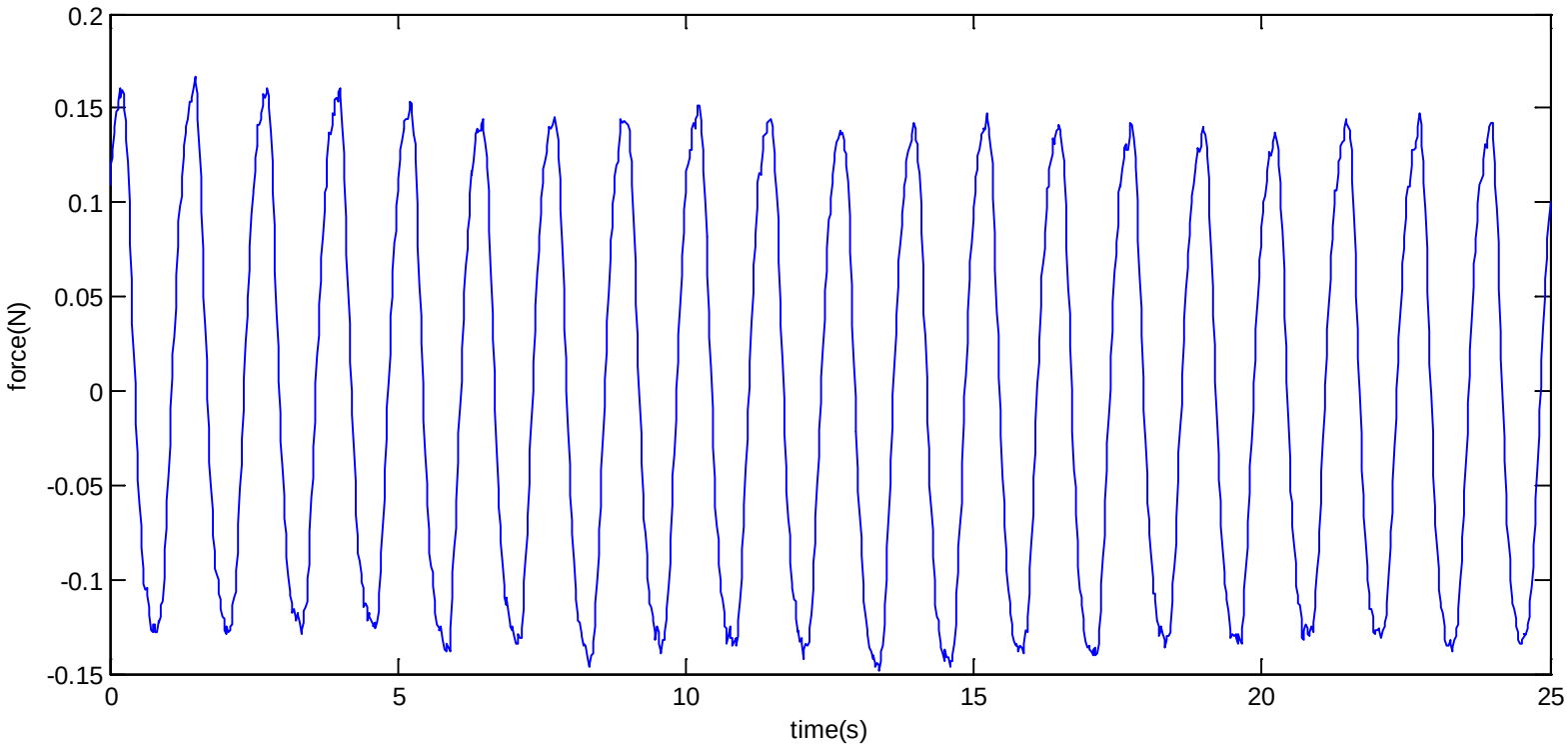

Figure 3. 33 Mean force averaging all of the series of force recording at position 1 for 1.25s waves.

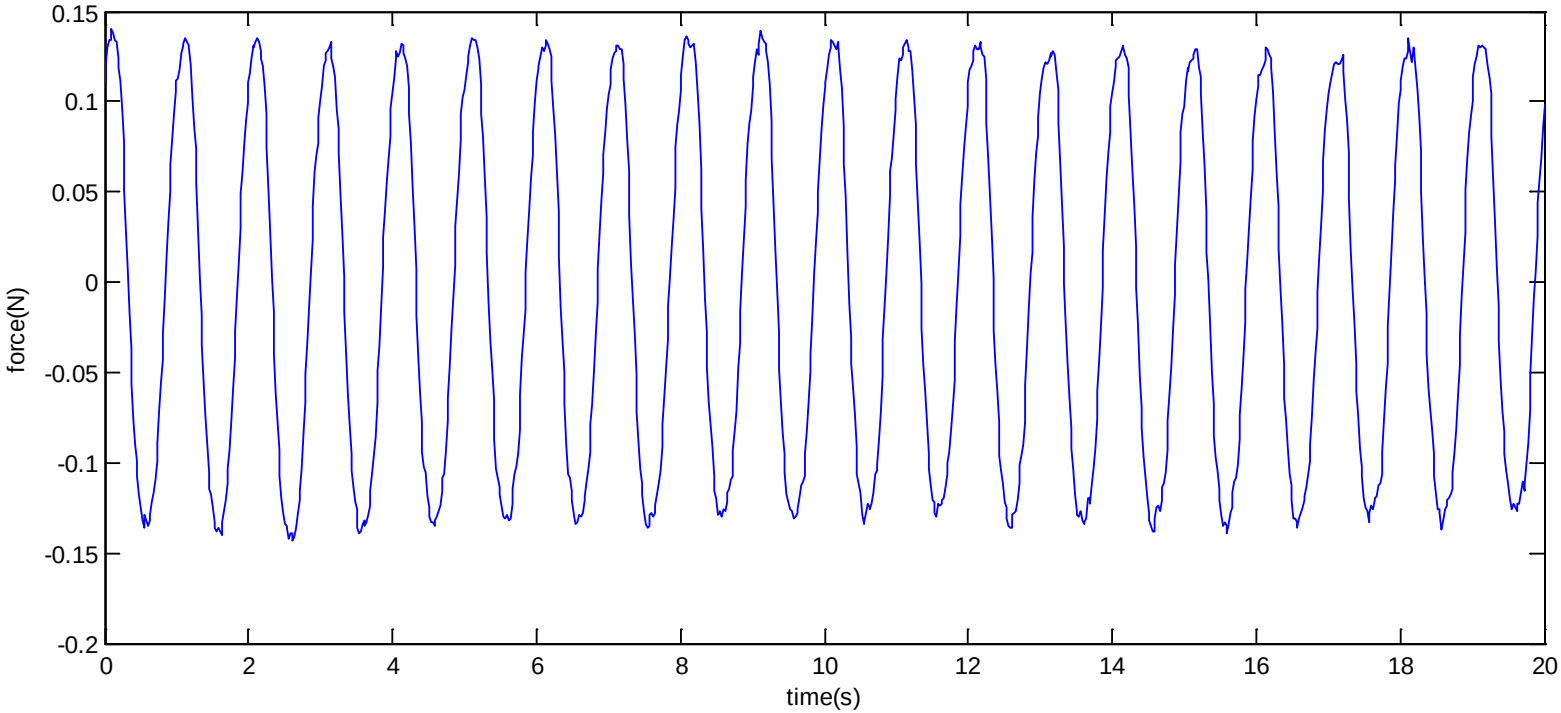

Figure 3. 34 Mean force averaging all of the series of force recording at position 1 for 1.0s waves.

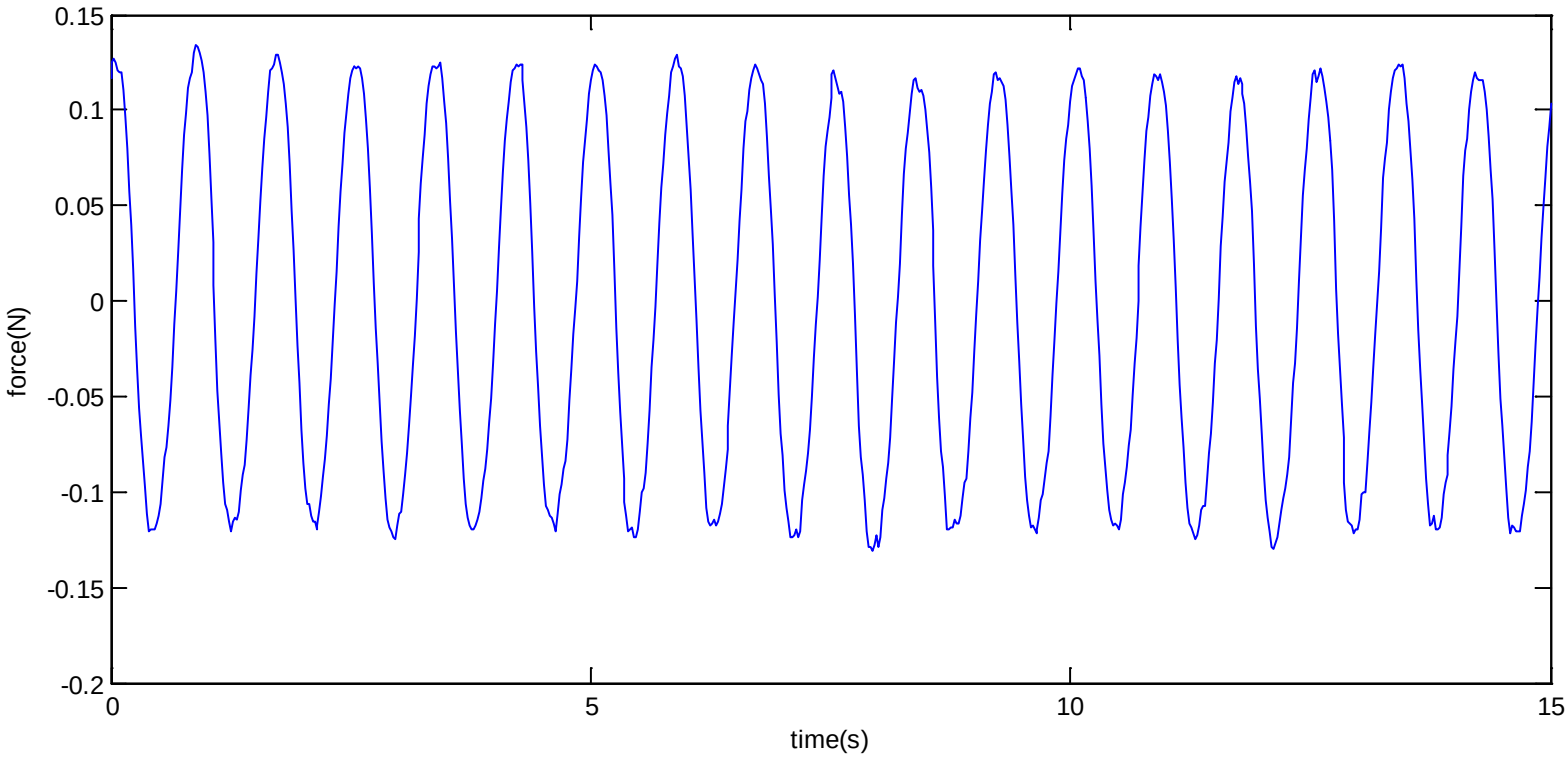

Figure 3. 35 Mean force averaging all of the series of force recording at position 1 for 0.83s waves.

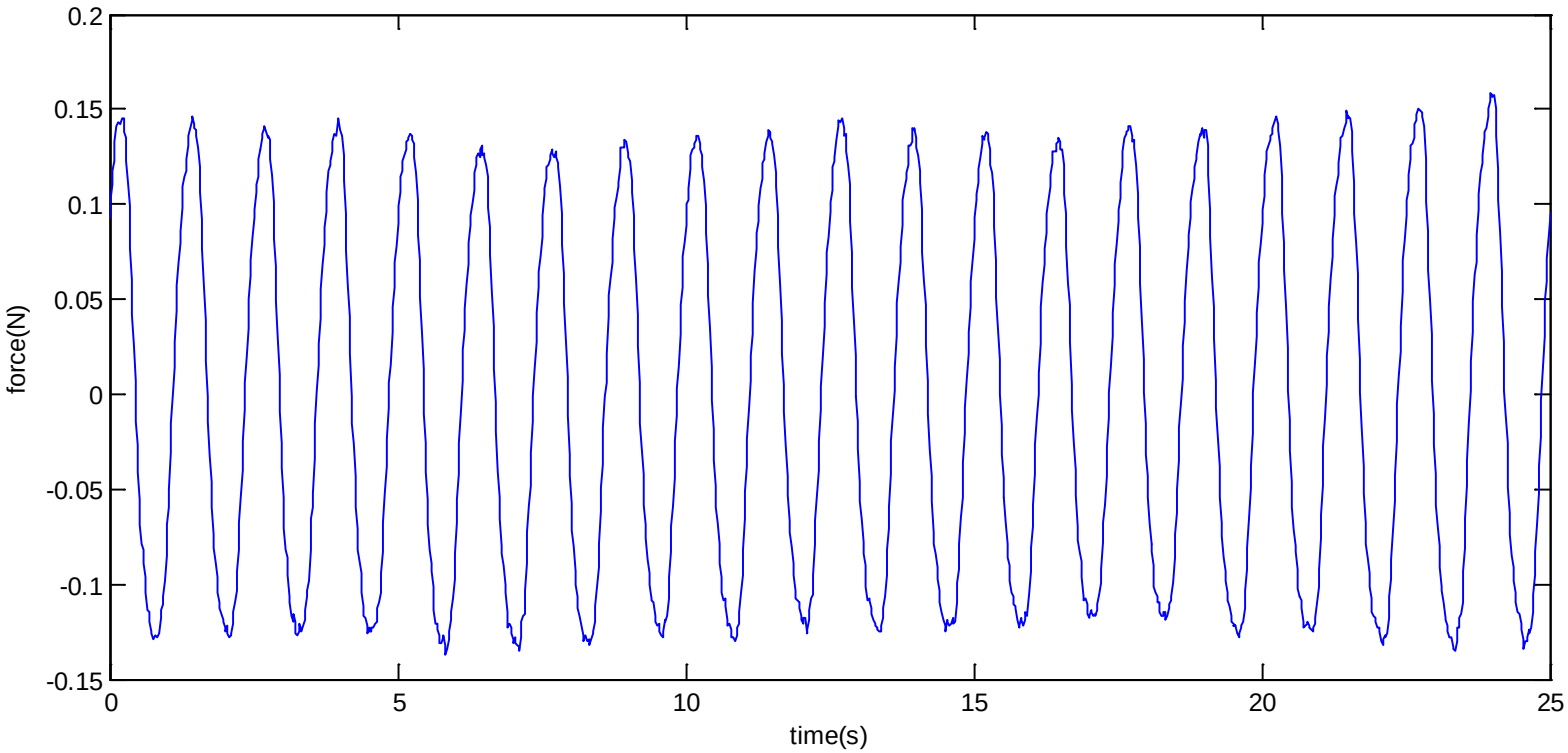

Figure 3. 36 Mean force averaging all of the series of force recording at position 2 for 1.25s waves.

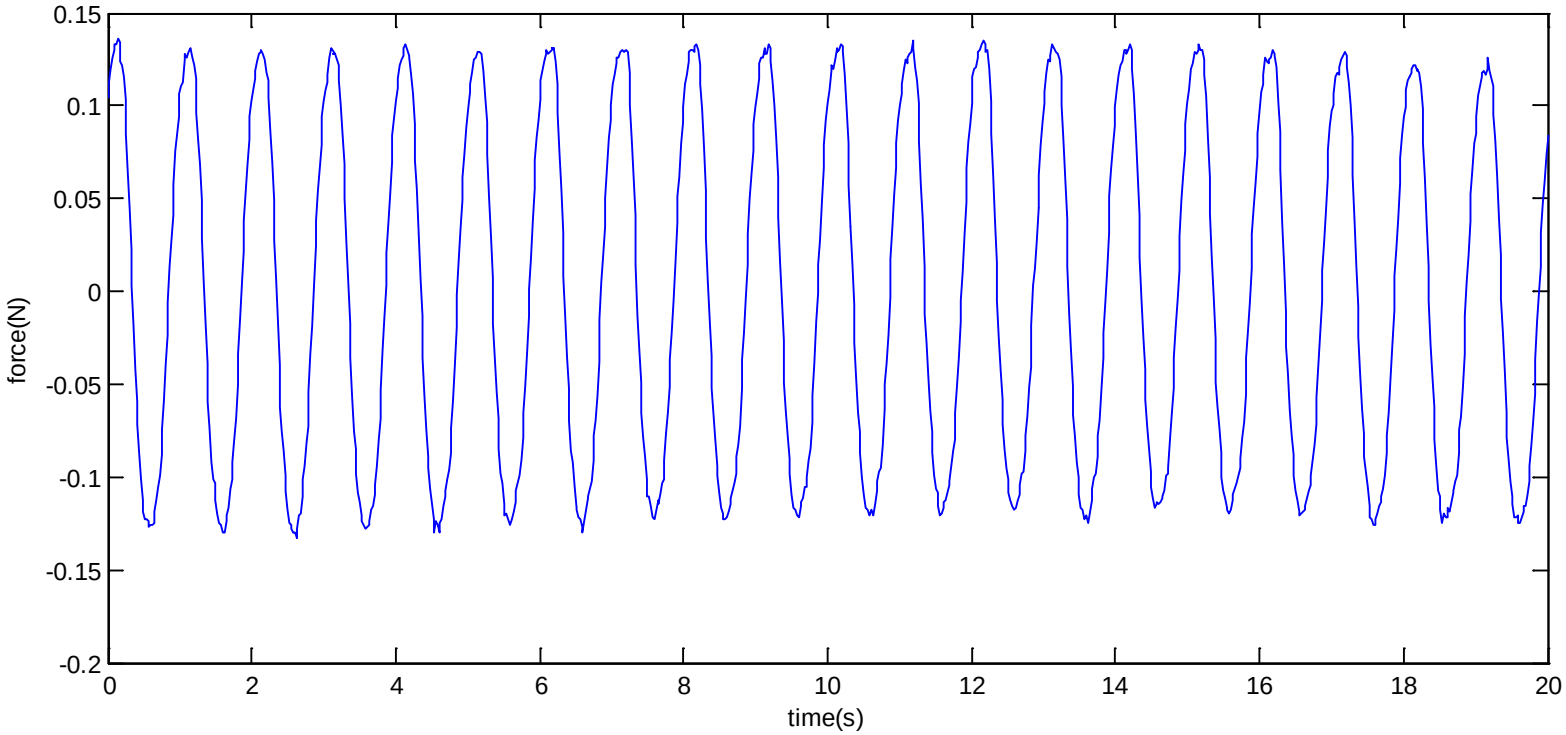

Figure 3. 37 Mean force averaging all of the series of force recording at position 2 for 1.0s waves.

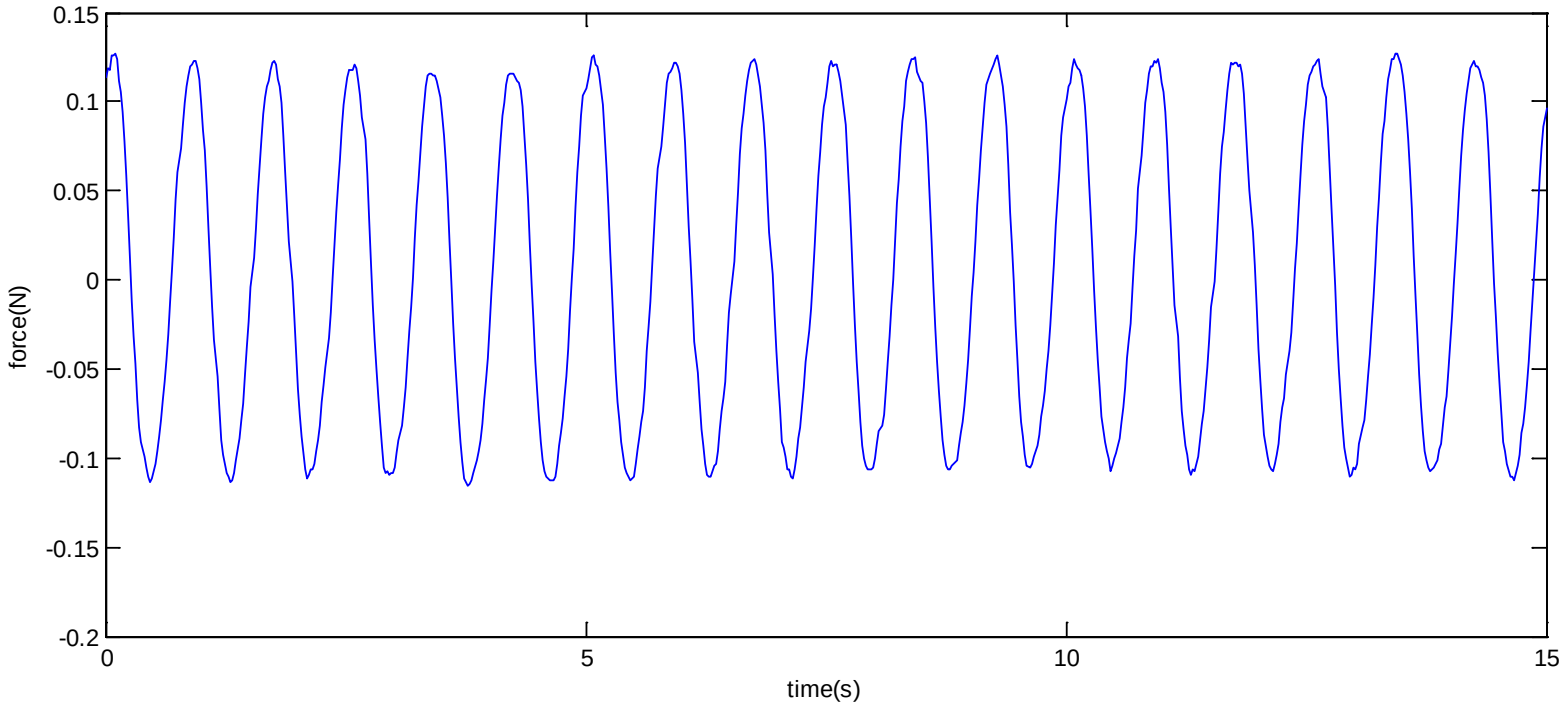

Figure 3. 38 Mean force averaging all of the series of force recording at position 2 for 0.83s waves.

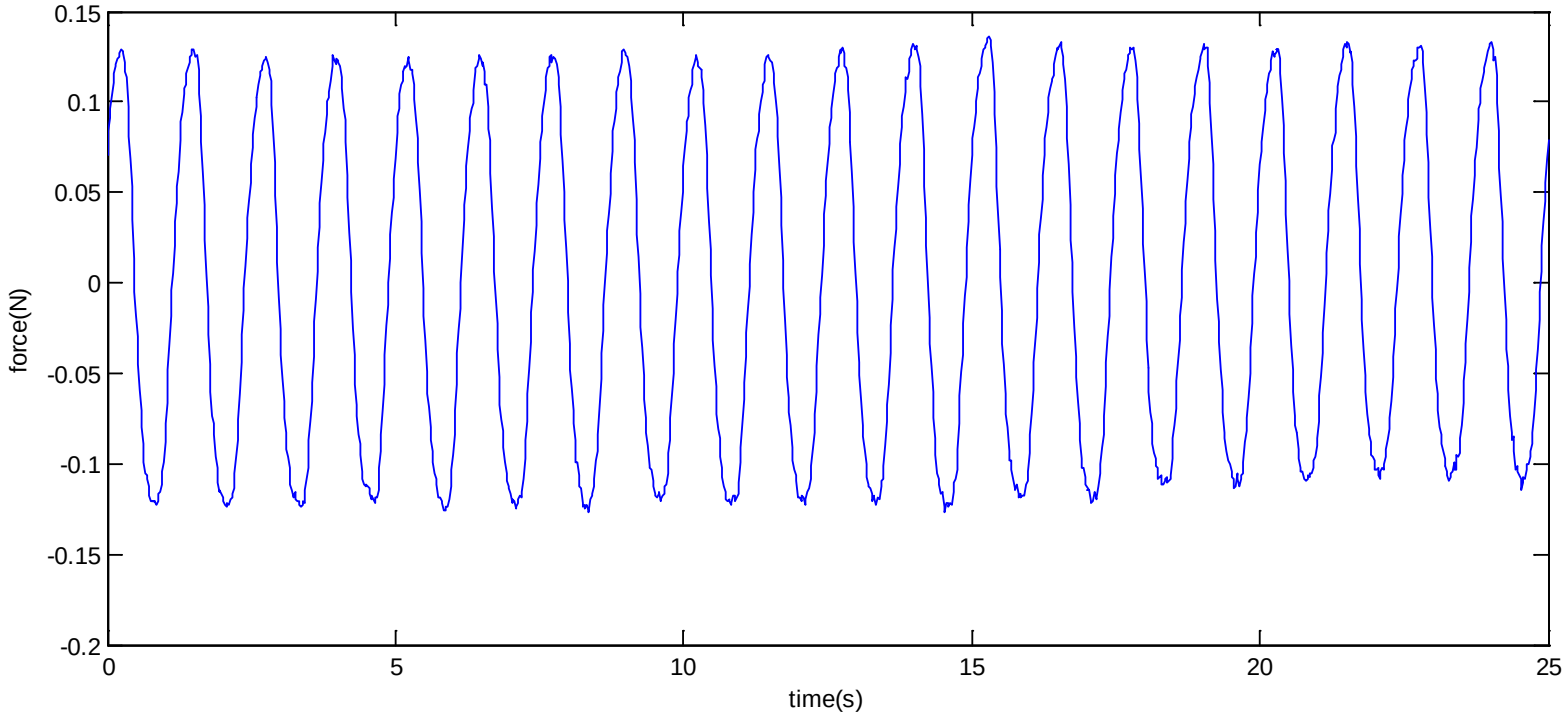

Figure 3. 39 Mean force averaging all of the series of force recording at position 3 for 1.25s waves.

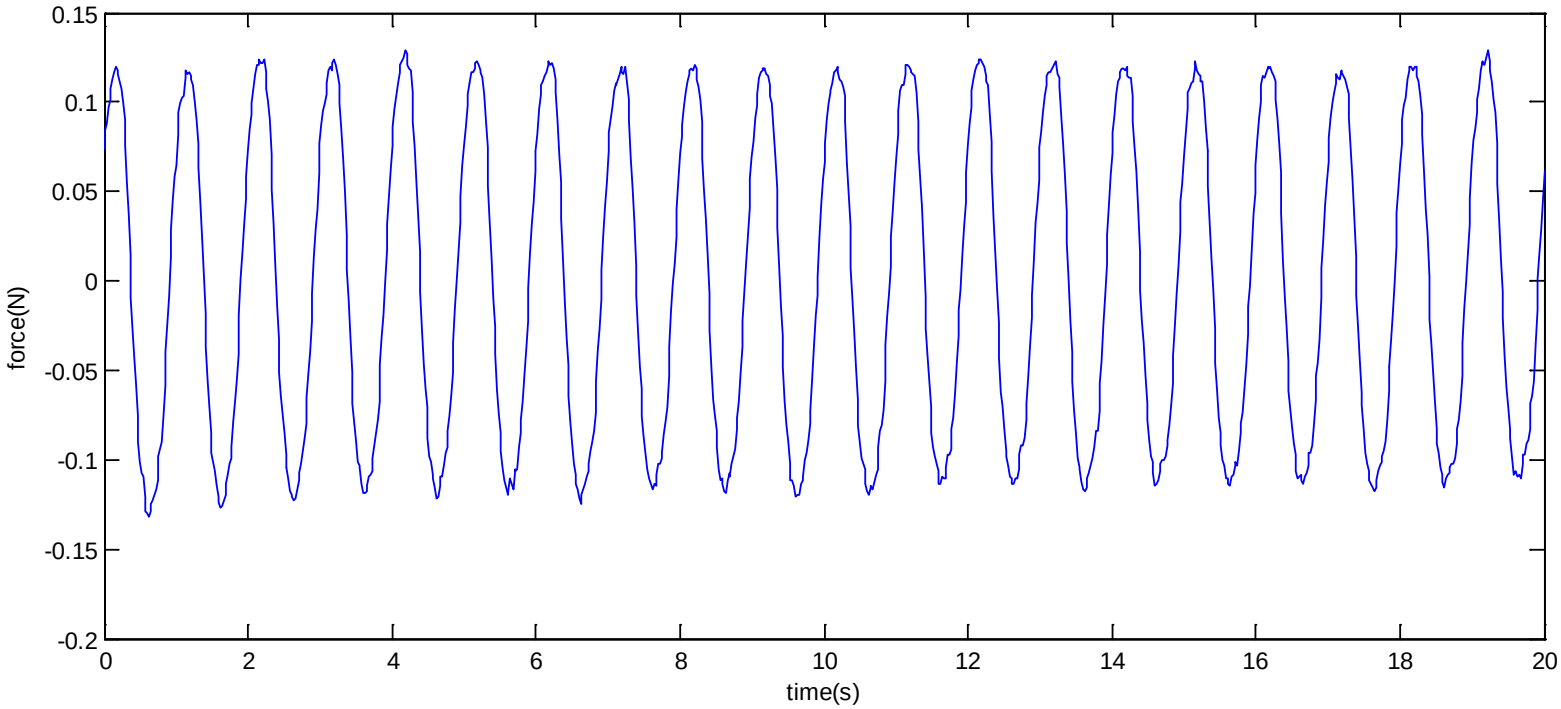

Figure 3. 40 Mean force averaging all of the series of force recording at position 3 for 1.0s waves.

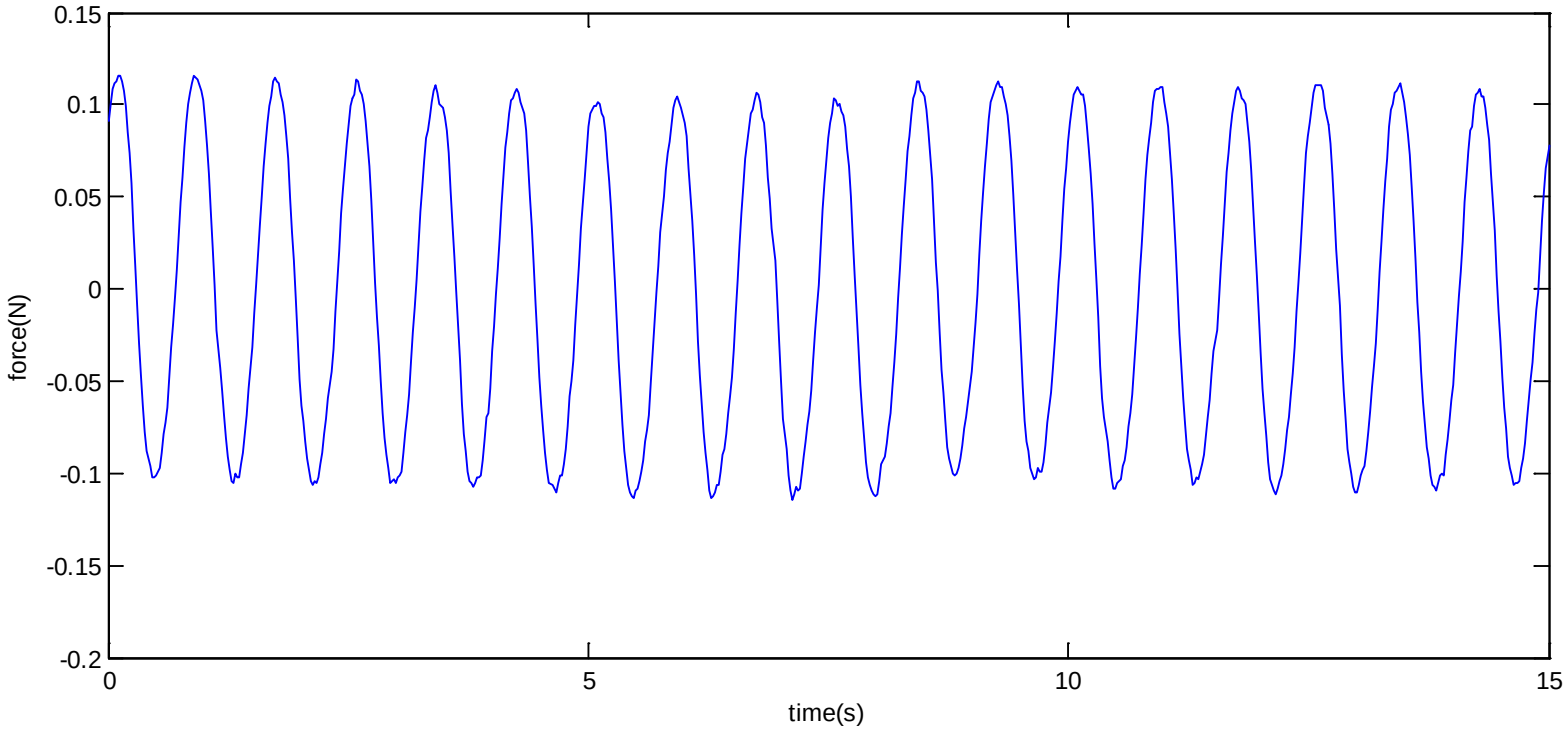

Figure 3. 41 Mean force averaging all of the series of force recording at position 3 for 0.83s waves.

3.3.3 Wheeler stretching approximation of the velocities above the free surface

By examining Eq. 2.55, it's clear that accurate approximations of both the wave elevation and the wave kinematics are crucial to the success of this formula. Since the magnitudes of velocity and acceleration increase at elevations close to the free surface, near-surface kinematics play a significant role. Unfortunately, the ADV can work only when its sampling tip is submerged in the water. In the experiments, the highest elevation for velocity measurement was just below the wave troughs. To accurately estimate the drag and inertial force coefficients, it was necessary to extrapolate the measured velocities up to the free surface elevation. Many methods exist for approximating the kinematics from a known wave elevation series. One widely adopted method is "Wheeler stretching" which was designed to correct the linear Airy theory results by introducing a local scaling which maps the free surface to the still water level (Wheeler, 1970; Zhang et al. 1991). In linear theory, the horizontal velocity can be expressed as

$$u = \frac{\pi H}{T} \frac{\cosh k(h+z)}{\sinh kh} \cos(kx - \sigma t) \tag{3.1}$$

By using Wheeler stretching, the above expression is modified as

$$u = \frac{\pi H}{T} \frac{\cosh kh(\frac{h+z}{h+\eta})}{\sinh kh} \cos(kx - \sigma t) \tag{3.2}$$

where η is the free surface elevation. Mathematically, this stretching method is applied by making the coordinate transformation $(z+h)$ to $h(z+h)/(\eta+h)$ in each linear expression. Since the free surface elevations at each position were recorded, the analytically vertical distribution of horizontal velocities at any time could be estimated by using the

corresponding surface elevation. Therefore, the maximum and minimum velocities at each layer from measurements are compared with the computed vertical distributions of velocities under crests and troughs. Fig. 3.42 to Fig. 3.44 shows their comparison. It is shown that Wheeler stretching could provide a good estimate for the velocity distribution, especially for the upper water depth. In the runs with 1.0s wave, there are a little larger discrepancies near the bottom than in the upper water body, which indicates that there was a small back flow during the wave propagation in the wave tank. However, these unavoidable back flows in the available experimental system will not affect the accuracy of calculation of Cd and Cm. The reason is following. For a cylinder under both wave and uniform current conditions, Morison equation provides a modified form to calculate the force exerting on the structure (S. K. Chakrabarti, 1987), which is

$$\begin{aligned} dF_x &= dF_D + dF_I \\ &= 0.5C_D\rho A(U-\dot{x})\,|U-\dot{x}\,| + C_M\rho V\ddot{x} \end{aligned} \tag{3.3}$$

In the above formula, U is the uniform current while $\dot{x}$ and $\ddot{x}$ represent the particle periodically oscillatory velocity and its acceleration, respectively. In experiments, the measured velocities are the resultant velocities under both effects of wave and back flow near the bottom, which is just $(U-\dot{x})$. Therefore, if u is used to represent $(U-\dot{x})$, which results in $\dot{u}=\ddot{x}$, the horizontal force could still be computed by Eq (2.55).

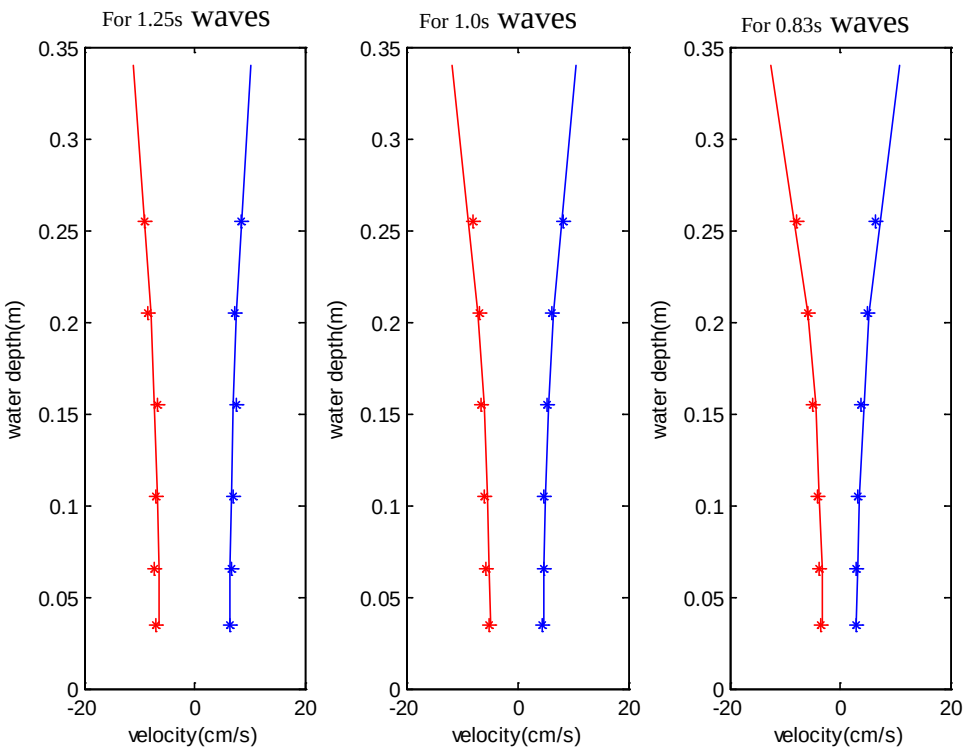

Figure 3. 42 the comparisons of the maximum and minimum velocities from measurement and Wheeler stretching based on the measured wave heights at position 1. (The solid lines are from the Wheeler stretching, and the star points are the experimental data.)

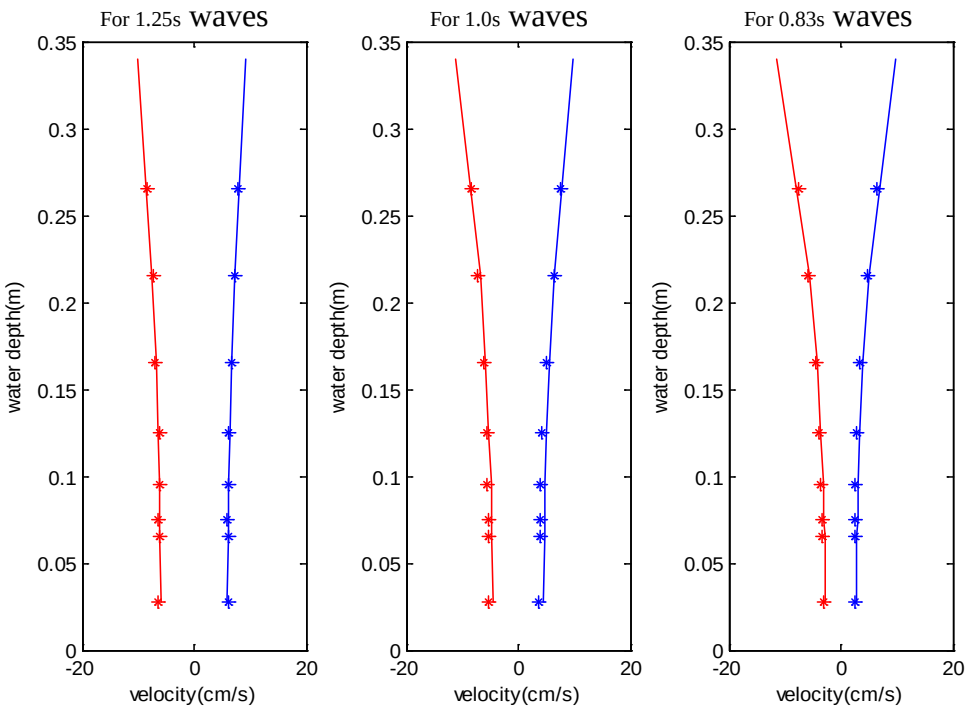

Figure 3. 43 the comparisons of the maximum and minimum velocities from measurement and Wheeler stretching based on the measured wave heights at position 2.

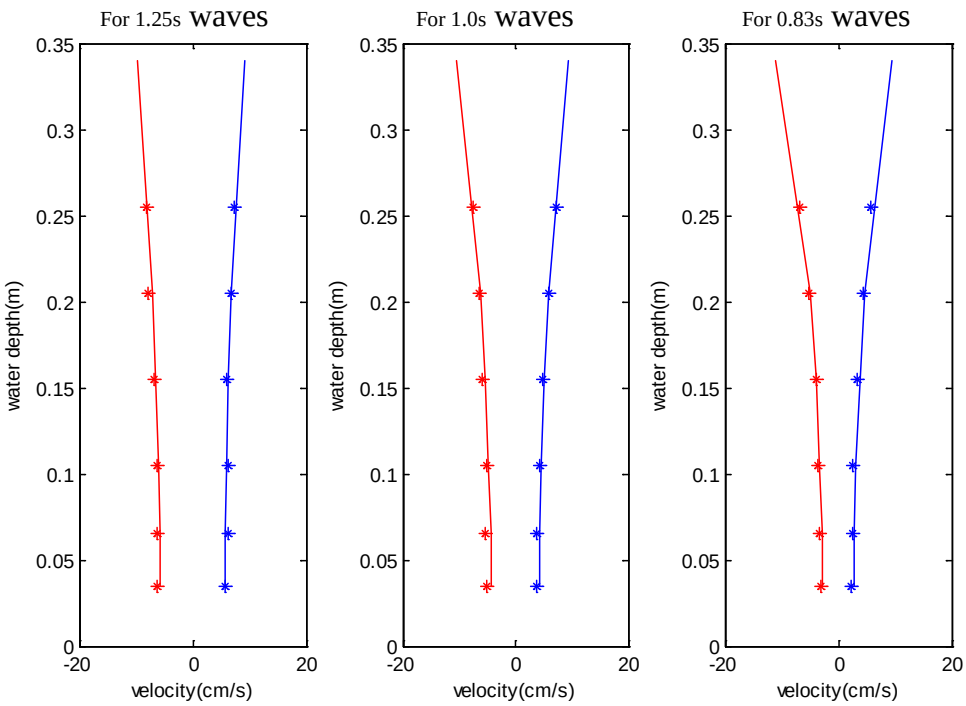

Figure 3. 44 the comparisons of the maximum and minimum velocities from measurement and Wheeler stretching based on the measured wave heights at position 3.

3.3.4 Estimation of drag/inertial force coefficients from experimental data

With reference to Eq. (2.55), it is clear that if the total forces and velocities have been measured, the only two unknowns left are Cd and Cm. Several methods could be employed to estimate the values of Cd and Cm. These methods usually assume that Cd and Cm are invariant over a wave cycle. In particular, for the vertical non-submerged cylinders, the averaged values of Cd and Cm over the whole water depth are used in the calculation.

One method for estimating Cd and Cm is the so-called zero-crossing method. For a linear wave train, when u reaches its maximum value under the wave crest, Du/Dt=0. Thus, based on the measured force at this moment, it is possible to estimate Cd. On the other hand, when Du/Dt reaches its maximum, u=0, the value of Cm could be derived. This method is useful when the data are quite regular with nearly no scattering. In the current study, the data are smooth enough(refer to figures of the averaged forces, Fig.3.32 to Fig.3.41) so that this method can be used.

Another method of estimating Cd and Cm is to use the least square method that minimizes the total errors between the calculated results and measured data (Chakrabarti, S.K., 1987). It can also be applied in cases where the water particle kinematics are not necessarily sinusoidal (e.g., irregular waves, or nonlinear waves). For simplicity, rewriting Eq. (2.55) as

$$F_x = C_d A_D + C_m A_I \tag{3.4}$$

Where $A_D = \frac{1}{\theta^2}\sum_m \frac{1}{2}\rho \cdot D \cdot \Delta z_m \cdot u_m |u_m|$ and $A_I \frac{1}{\theta}\sum_m \rho \cdot (\frac{\pi}{4}D^2) \cdot \Delta z_m \cdot \frac{Du_m}{Dt}$

If a recording series includes N sampling points with a sampling interval of 0.02s according to the ADV sampling frequecy, in which case the total recording time of each series is N*0.02s, a total residual between the measure forces and the estimated forces from Eq. (3.4) is

$$(\Delta R)^2 = \sum_{n=1}^{N} (F_{xn} - C_d A_D - C_m A_I)^2 \tag{3.5}$$

where ΔR is the residual and F_{xn} is the measured move force at a sampling point.

In a least square sense, the best estimates of Cd and Cm are obtained by minimizing the residual ΔR. Mathematically, it means that the residual's derivatives with Cd or Cm are zero. This will produce two independent equations which can be solved for Cd and Cm. The final formulae for the calculation of Cd and Cm are expressed as

$$C_m = \frac{\sum_{n=1}^{N}(F_{xn}A_I)\sum_{n=1}^{N}A_D{}^2 - \sum_{n=1}^{N}(F_{xn}A_D)\sum_{n=1}^{N}(A_D A_I)}{\sum_{n=1}^{N}A_I{}^2\sum_{n=1}^{N}A_D{}^2 - (\sum_{n=1}^{N}(A_D A_I))^2} \tag{3.6}$$

$$C_d = \frac{\sum_{n=1}^{N}(F_{xn}A_D)\sum_{n=1}^{N}A_D{}^2 - \sum_{n=1}^{N}(F_{xn}A_I)\sum_{n=1}^{N}(A_D A_I)}{\sum_{n=1}^{N}A_I{}^2\sum_{n=1}^{N}A_D{}^2 - (\sum_{n=1}^{N}(A_D A_I))^2} \tag{3.7}$$

To obtain the desired velocities in Eq. (3.6) and (3.7),for the water body above the highest measurement layer, the velocities are calculated by Wheeler stretching. Within the monitored layer, the average of measured velocities at each layer were used.For the desired wave force, the measured and aligned vegetation forces at each position for the same wave condition were averaged first and divided by nine because the force transducer plate covered nine rods in the experiments.

Based on the above-introduced idea, the zero-crossing method and the least squared method are employed to calculate Cd and Cm at each measurement position. The estimated drag and inertial force coefficients under different wave conditions at different positions are listed in Table 3.1. The fitted forces computed from the measured velocities and the estimated coefficients are compared with the measured forces in Fig.3.45 to Fig.3.53. These comparisons show that, by substituting two sets of coefficients into force equation, we are able to recover the total force field quite accurately with both methods.

Table 3. 1 The estimated drag and inertial force coefficients by two methods for different wave conditions at three measurement positions.

Zero crossing method

	1.25s			1.0s			0.83s		
position	1	2	3	1	2	3	1	2	3
Cd	1.5	1.8	1.9	1.6	1.8	2.1	1.4	1.9	2.1
Cm	1.7	1.7	1.4	1.8	1.7	1.3	1.8	1.7	1.6

Least square method

	1.25s			1.0s			0.83s		
position	1	2	3	1	2	3	1	2	3
Cd	1.6	1.9	2.1	1.7	1.9	2.4	1.5	2	2.3
Cm	1.8	1.7	1.3	1.8	1.7	1.3	1.9	1.8	1.6

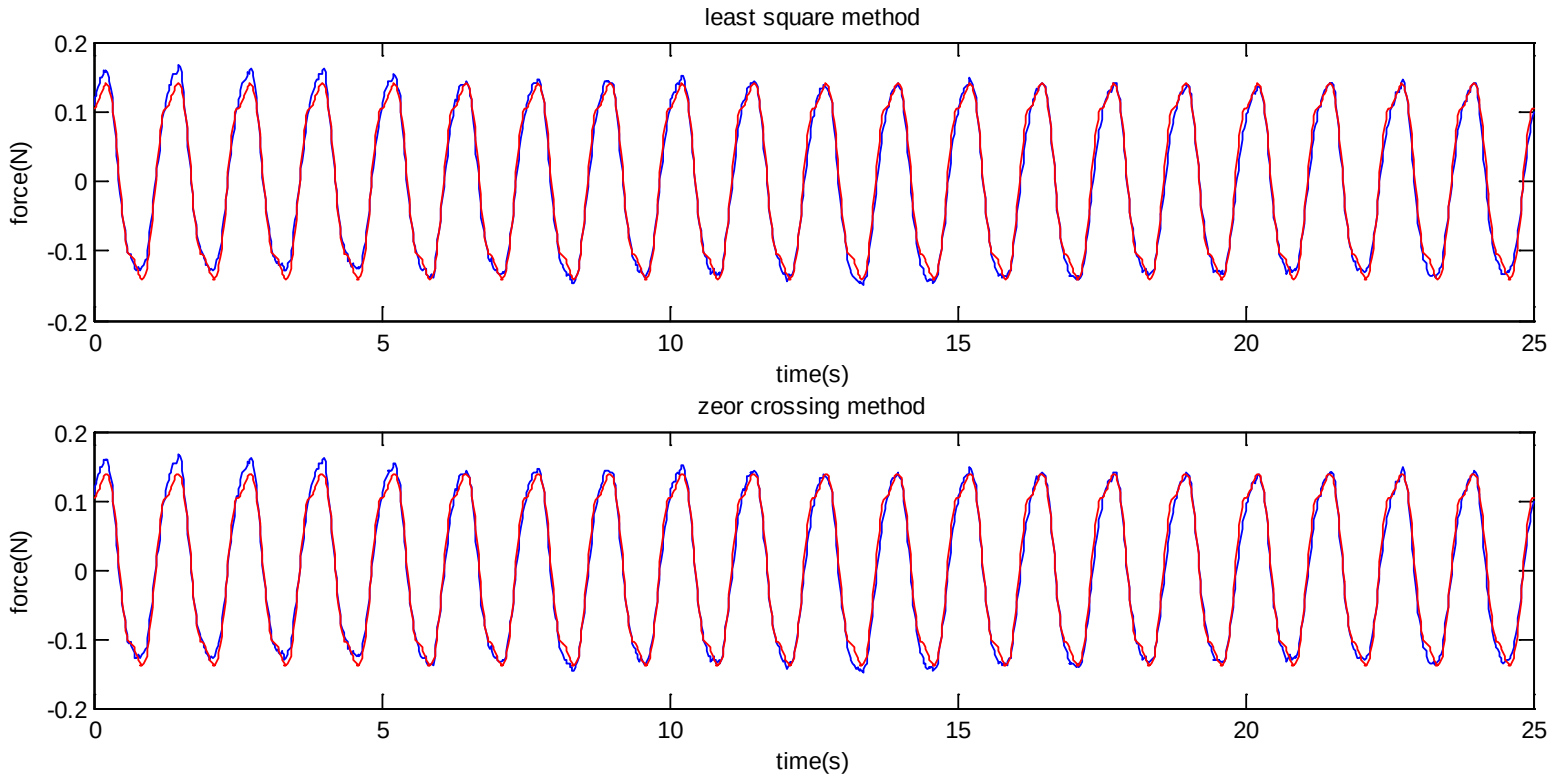

Figure 3. 45 Comparison of fitted forces and the measured forces at position 1 for 1.25s waves with estimated Cd and Cm in Table 3.1. (The blue line is the averaged measurements of force. The red line is the fitted line with calculated Cd and Cm with each method)

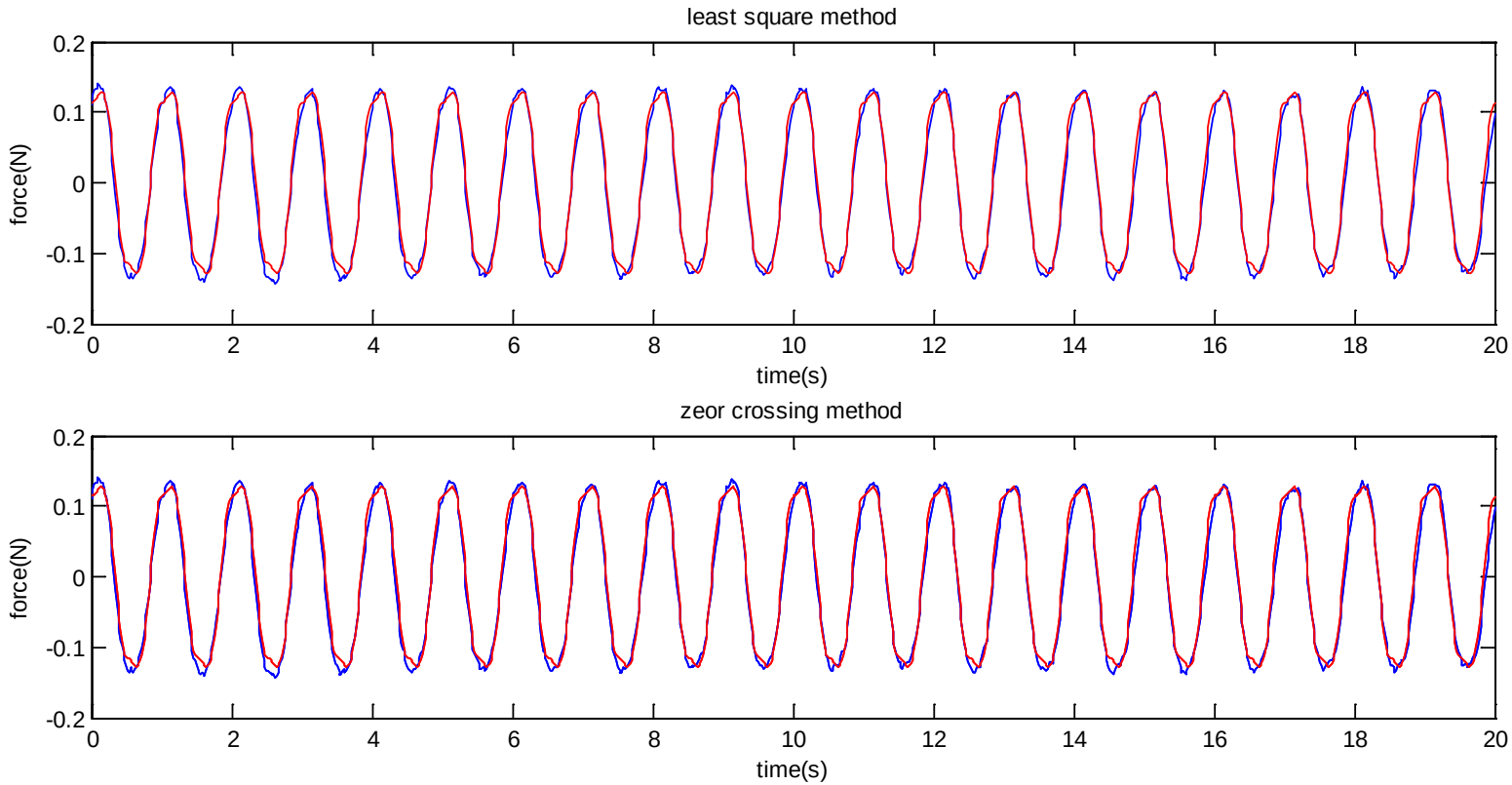

Figure 3. 46 Comparison of fitted forces and the measured forces at position 1 for 1.0s waves with estimated Cd and Cm in Table 3.1.

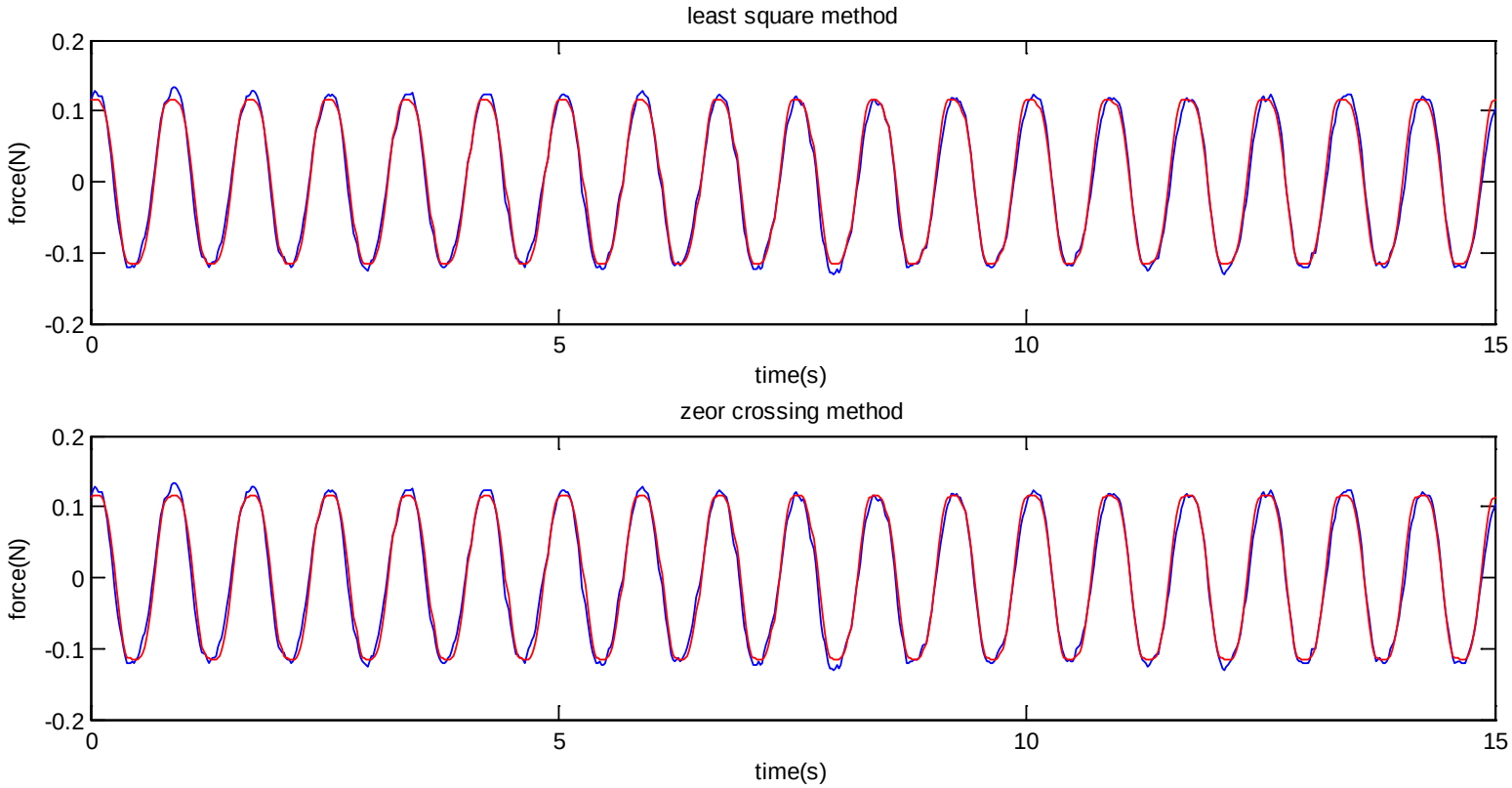

Figure 3. 47 Comparison of fitted forces and the measured forces at position 1 for 0.83s waves with estimated Cd and Cm in Table 3.1.

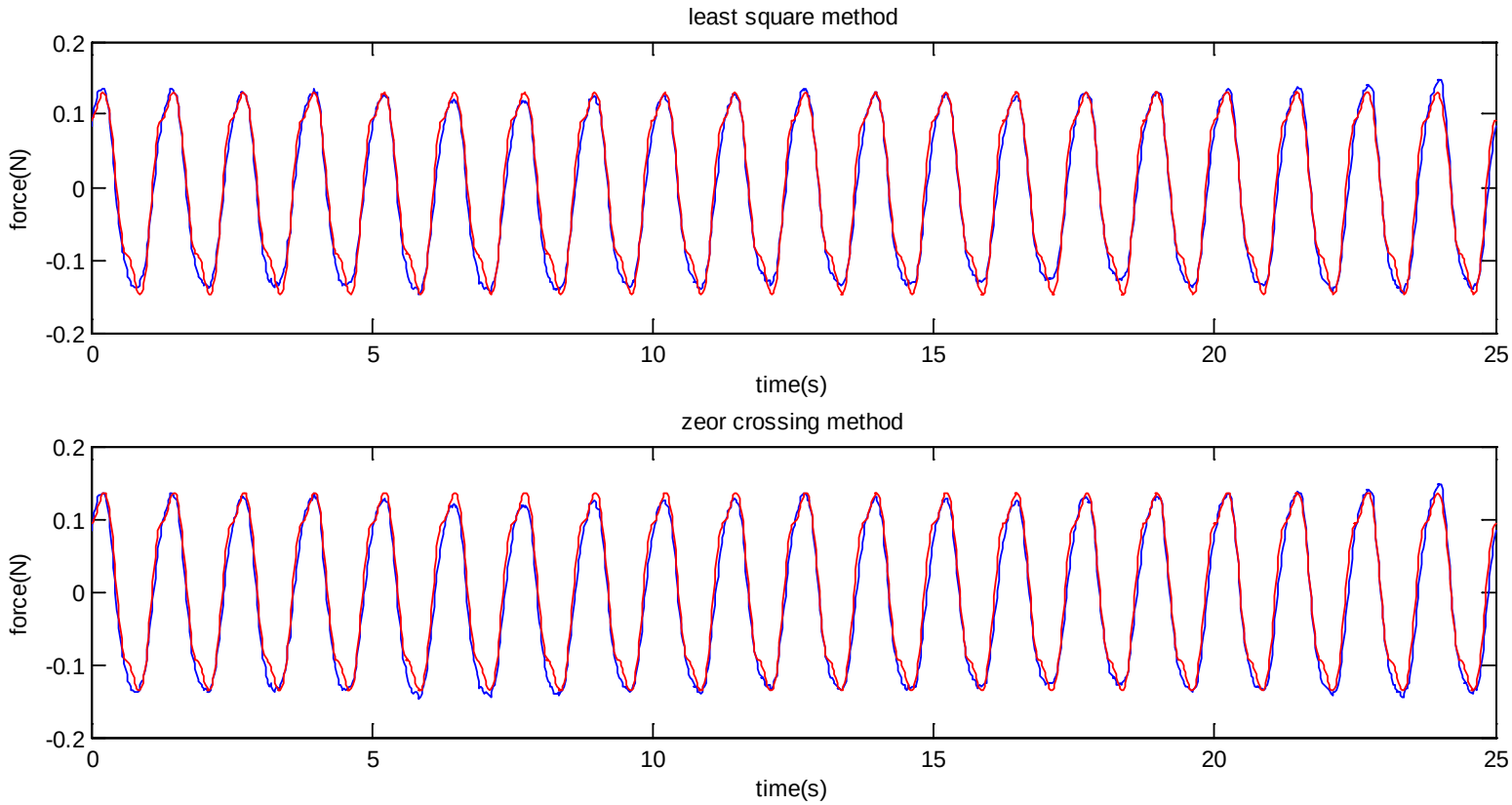

Figure 3. 48 Comparison of fitted forces and the measured forces at position 2 for 1.25s waves with estimated Cd and Cm in Table 3.1.

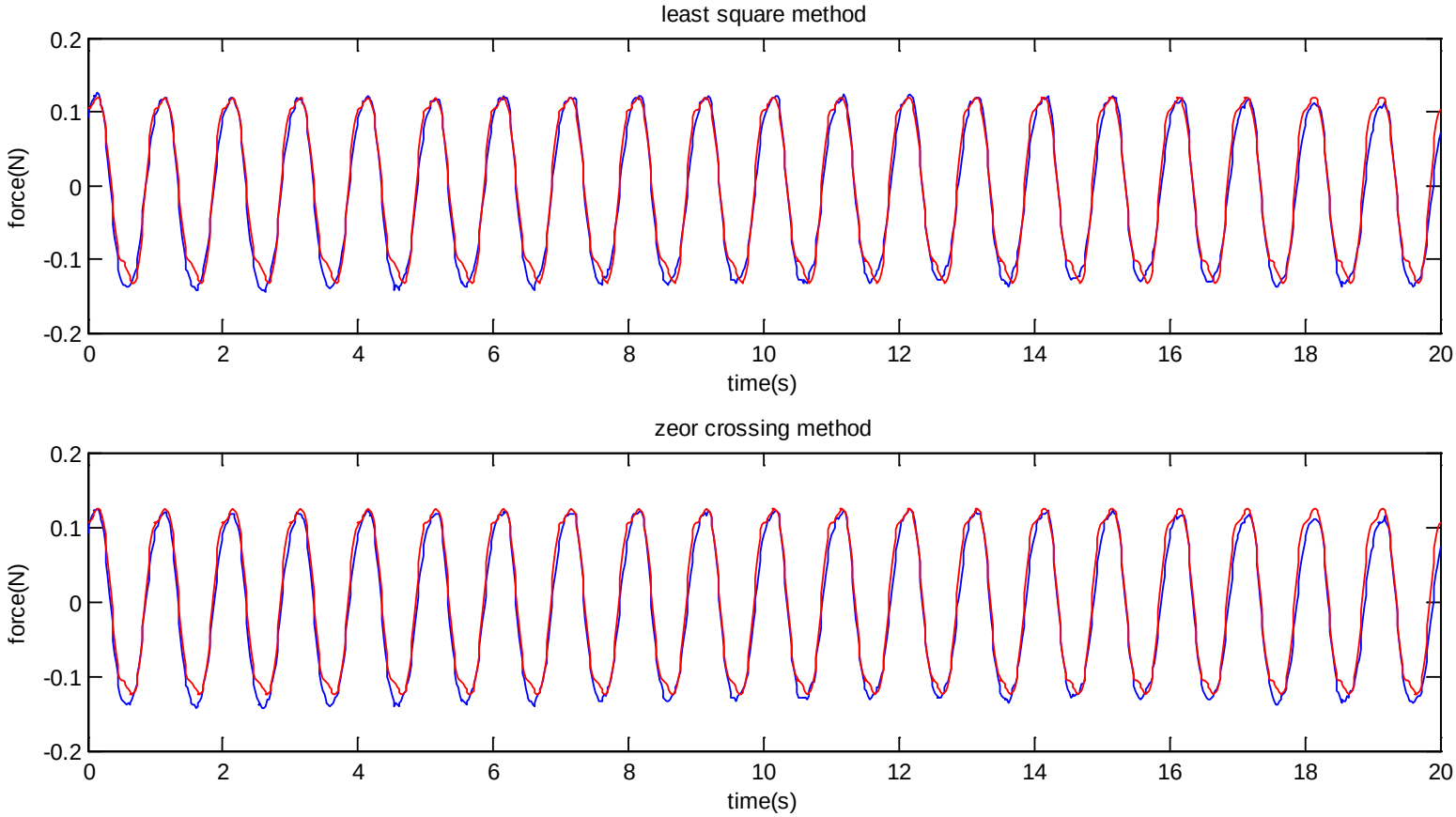

Figure 3. 49 Comparison of fitted forces and the measured forces at position 2 for 1.0s waves with estimated Cd and Cm in Table 3.1.

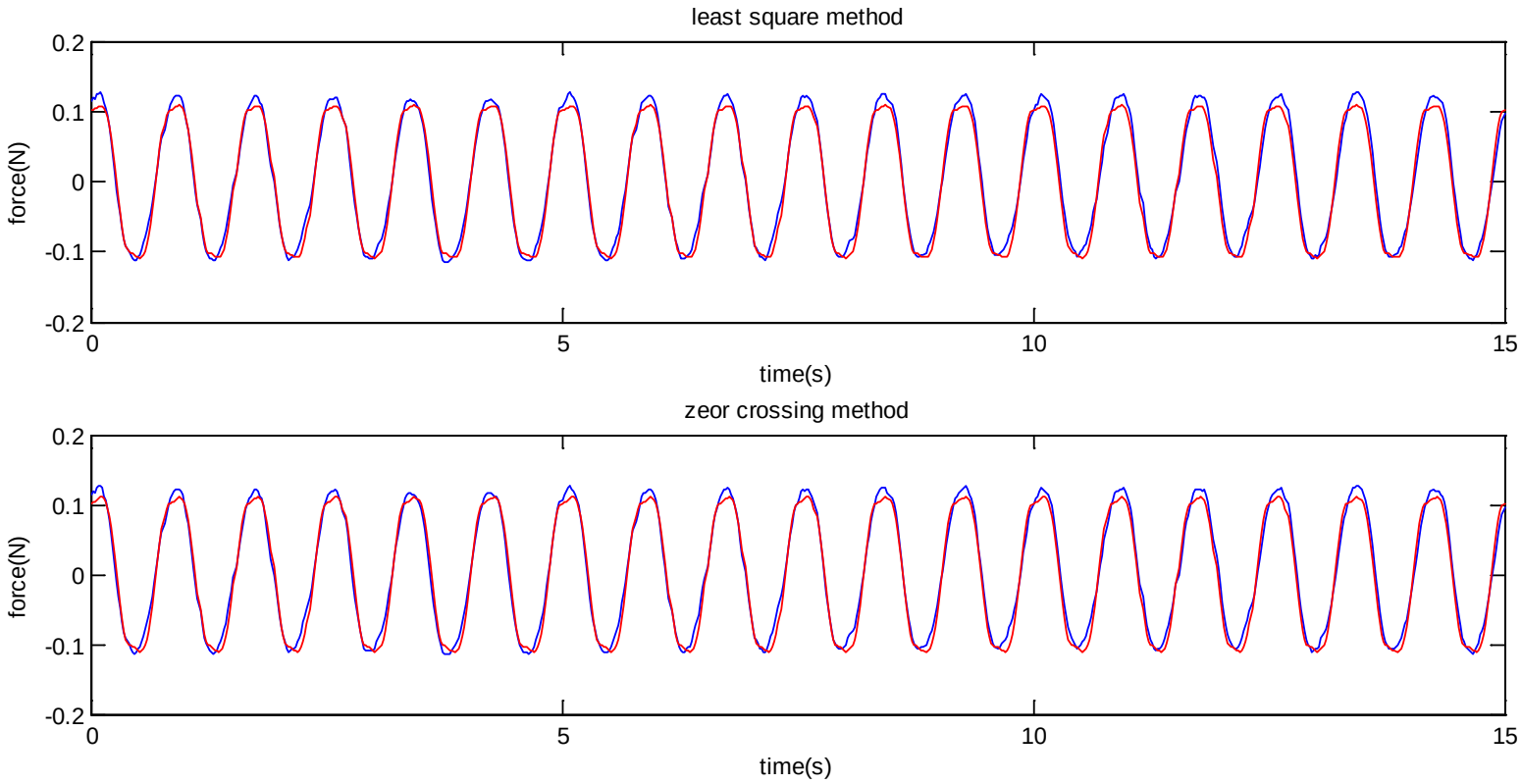

Figure 3. 50 Comparison of fitted forces and the measured forces at position 2 for 0.83s waves with estimated Cd and Cm in Table 3.1.

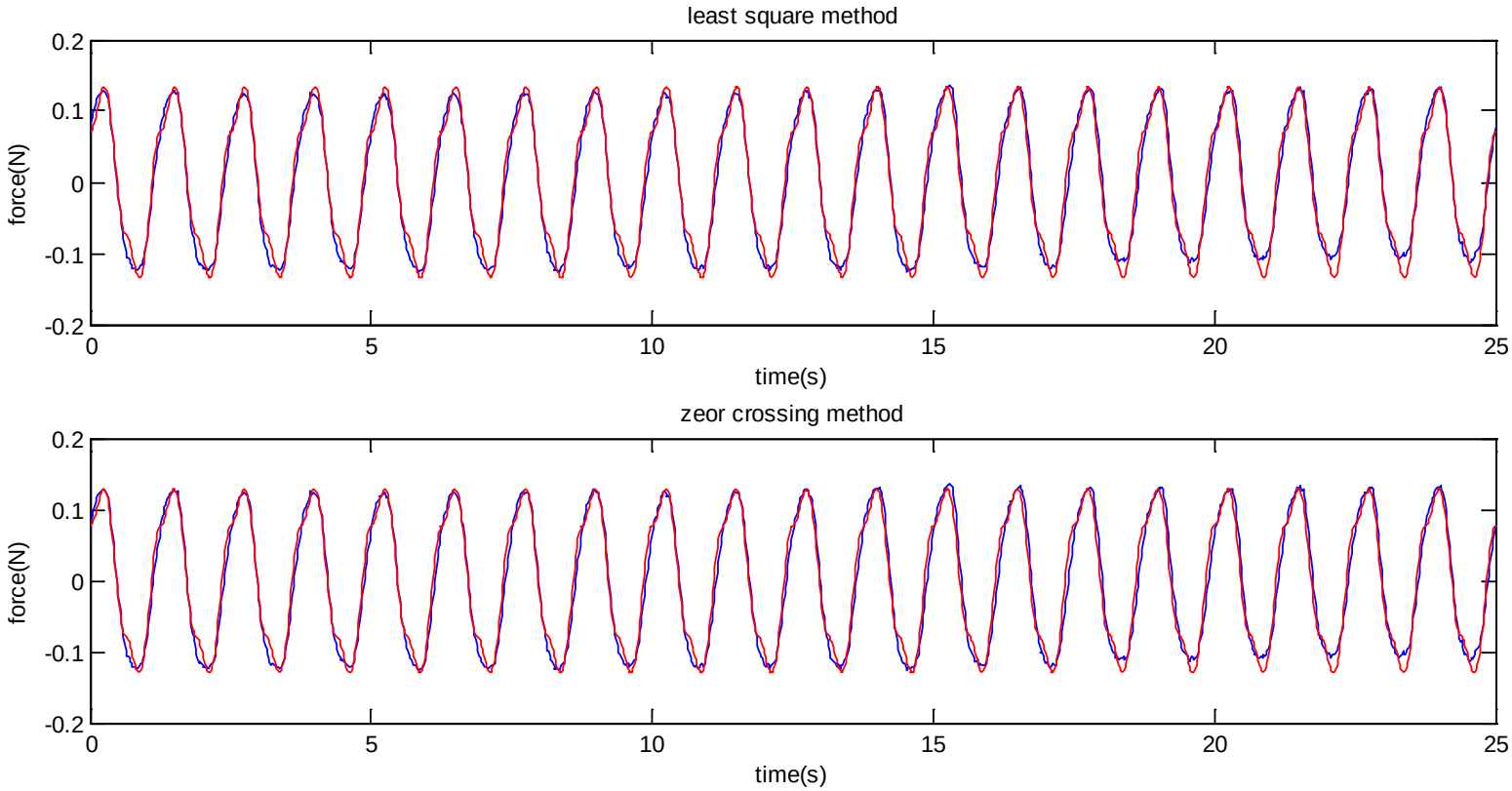

Figure 3. 51 Comparison of fitted forces and the measured forces at position 3 for 1.25s waves with estimated Cd and Cm in Table 3.1.

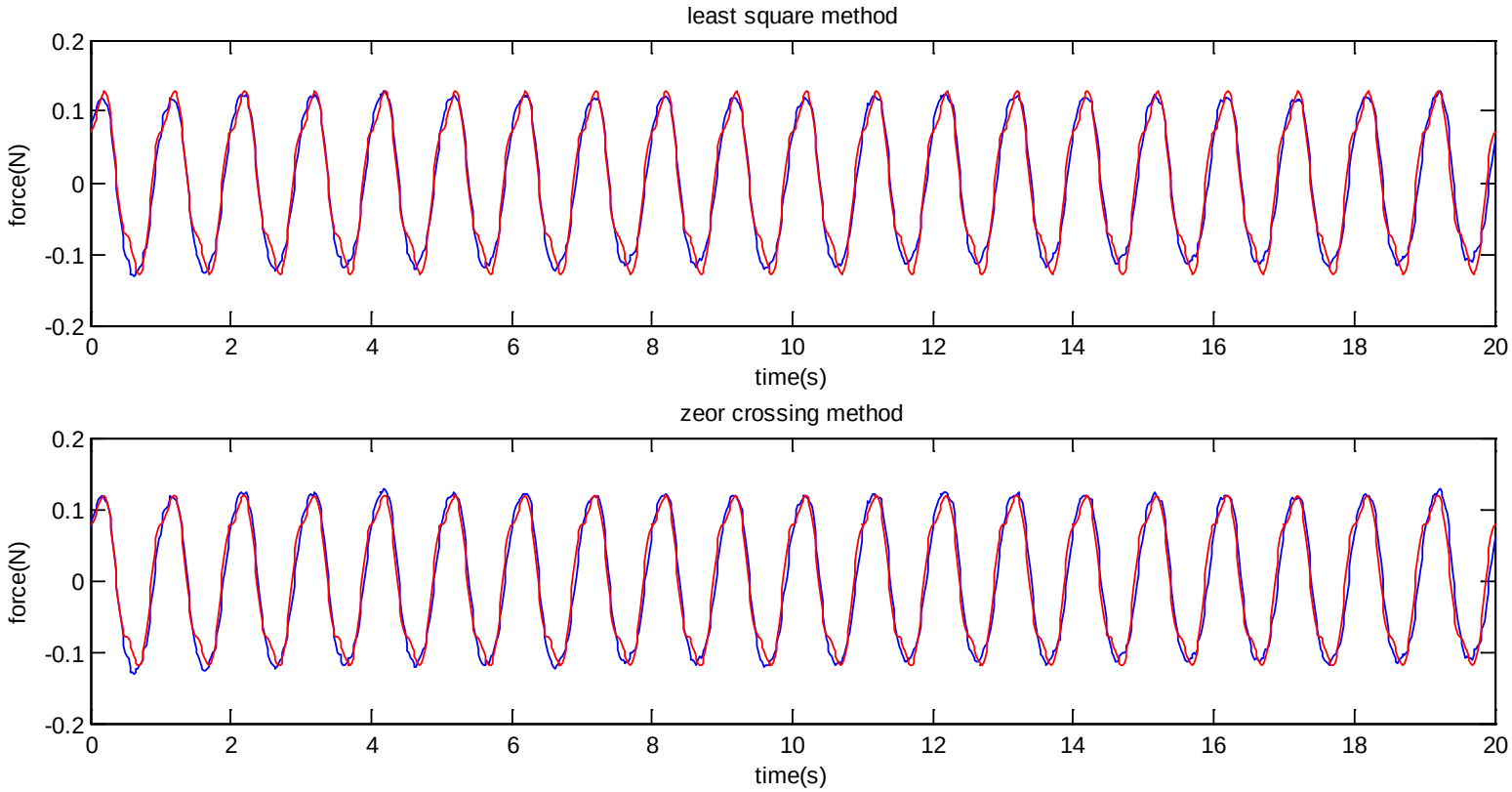

Figure 3. 52 Comparison of fitted forces and the measured forces at position 3 for 1.0s waves with estimated Cd and Cm in Table 3.1.

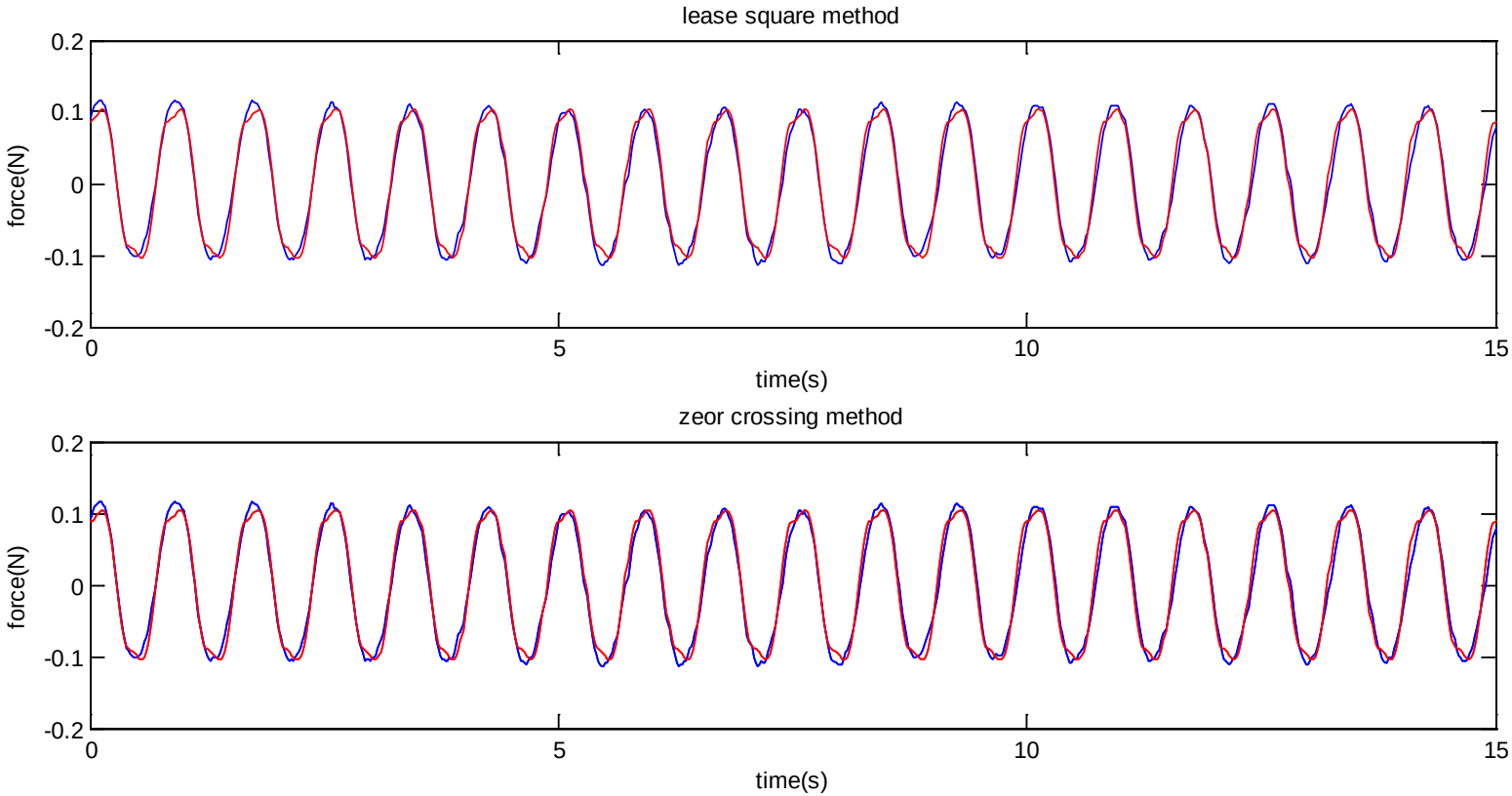

Figure 3. 53 Comparison of fitted forces and the measured forces at position 3 for 0.83s waves with estimated Cd and Cm in Table 3.1.

3.3.5 Discussion of the estimated drag/inertial force coefficients

The drag and inertial force coefficients associated with waves on vertical cylinders have been studied extensively through experiments (Chakrabarti, S. K., 1987). Results have been presented to elucidate the dependence of Cd and Cm on the Keulegan-Carpenter number (KC number; calculated by $u_0 T / D$, where u_o is the maximum horizontal water particle velocity, T is the wave period and D is the diameter of the vertical cylinder) and the Reynolds number (Re number; calculated as $u_0 D / v$, where v is the kinematic viscosity of the water, also called the cylinder Reynolds number by Tanino and Nepf (2008)). . Two figures to show how Cd and Cm vary with KC based on Chakrabati (1987) are presented in Fig. 3.54 and Fig. 3.55. In these two figures, both Cd and Cm are investigated over a large range of KC number. The estimated Cd and Cm of vegetation obtained in the current experiments are compared with the corresponding values of a single cylinder in Fig. 3.56. It can be seen that, generally, the coefficients of vegetation are higher than the coefficients for a single cylinder at the same KC number. This is reasonable because the group of vegetation would surely increase the resistance to flows compared to a single cylinder of the same diameter at the same flow conditions. To the author's knowledge, so far, there has been no report on the experimental investigation of the variance of Cd and Cm of vegetation with KC number. In the numerical modeling of wave-vegetation interaction, Li and Yan (2007) had stated that a typical value of Cm is around 2.0. Through flume experiments of tsunami waves passing through coastal forests, Harada and Imamura (2005) estimated the Cm value to be around 1.7, while Imai and

Matsutomi (2005) found that Cm varies between 1.5 ~2.5. Comparing with the above values, our current experimental results are consistent with them.

It's generally agreed that the Cd varies with not only the KC number but also the Re number. There have been a few reports of the vegetation drag coefficient as a function of Reynolds number in the open channel condition, each of which focused on different parameters besides Re (James, C. S., et al. 2004, Wu, F-C, Shen, H. W. and Chou, Y-J, 1999, Tamino Y. and Nepf, H., 2008). James et al.(2004) monitored the drag force in a horizontal flume with different stems, including 5-mm round rod and real reed stems.. In the tests, the stems were tested with, firstly, all the leaves (Test D6), then with just six leaves (Test D7), then with three leaves (Test D8), and finally with only a bare stem (Test D9). Fig 3.57 shows the values of Cd changing with Re for different stem conditions. The estimated Cd from the present experiments is also plotted in the figure. In the figure, the "standard" value is the Cd value for a single circular rod from the generally accepted value (Schlichting H. and Gersten K., 2000). The figure shows that the drag force coefficient increases with the density of leaves of each stem. The results obtained in the present study are consistent with those in James' experiments. In his tests, Test D9 was carried out with bare stem, while metal rods were used to represent the vegetation stems without leaves in the present experiment. Based on tsunami-wave experiments, Imai and Matsutomi (2005) found the drag coefficient Cd to be 0.9-1.5. Our experimental results seem a little higher compared to the values from Imai and Matsutomi. However, in Imai and Matsutomi's experiments, the real trees with leaves, and waves with periods of 7.5~9.1 minutes were used. Their waves were also much longer than the present study and may all contribute to the difference.

The magnitude of vegetation drag force coefficient is influenced by not only the flow conditions but also the properties of vegetation including the distribution pattern, stem concentration, stem roughness and stiffness. Tanino and Nepf (2008) investigated the drag force on randomly distributed, rigid emergent circular cylinders with different solid volume fraction which is physically equivalent to the stem concentration. In Tanino and Nepf's experiments, the solid volume fraction is designed as $\phi = m\pi D^2 / 4$, in which m is the number of cylinders per unit horizontal area. Following Ergun(1952), Tanino and Nepf expressed the Cd as a function of Re, which is

$$C_d = 2(\frac{\alpha_0}{\mathrm{Re}} + \alpha_1) \tag{3.8}$$

In the above formula, α_0 and α_1 are functions of Re. The first term in Eq. (3.8) is to represent the viscous contribution that arises from the viscous shear stress on the cylinder surface, which corresponds to the second term in Eq. (2.25). The second term in Eq. (3.8) is to represent the inertial contribution arising from the pressure loss in the cylinder wake, which corresponds to the first term in Eq. (2.25). Tanino and Nepf's experiments yielded the results

$$\alpha_1 = (0.46 \pm 0.11) + (3.8 \pm 0.5)\phi \tag{3.9}$$

However, in Tanino and Nepf's results, α_0 didn't show the similar dependence on ϕ as α_1. In Tanino and Nepf's studies, α_0 increases from 25 ± 12 at $\phi = 0.091$ to 84 ± 14 at $\phi = 0.15$, but remains constant at 83.8 for $\phi = 0.15 - 0.35$.

Tanino and Nepf used Eq. (3.8) to calculate the Cd. It is reasonable to consider Cd only as a function of Re in channel flow situations. However, under the wave environments, the KC number, which reflects the effect of wave period and the relative length between

the wave length and structure scale, is another significant factor to be considered. Hence, a modified formula of Cd is proposed in current study, which includes both effects of Re and KC. In the study of unsteady flow in porous structure, Karunarathna and Lin's (2006) suggested a modified Cd formula for porous materials including the wave effect. Considering the similarity of methods modeling vegetation flow in the present flow and porous flow at large Re number, in the proposed modified formula, the term related to KC takes a similar form as Karunarathna and Lin's form while the Re-related term takes Tanino and Nepf's form. The modified formula is expressed as

$$C_d = 2(\frac{\alpha_0}{\mathrm{Re}} + \alpha_1)(1 + \frac{\alpha_2}{KC}) \tag{3.10}$$

In the above expression, α_0 , α_1 and α_2 are all functions of porosity (or rigid volume fraction), and other properties of vegetation, such as different vegetation configurations, stiffness of the vegetation stems. To make the empirical formula more applicable in a broad range conditions, extensive experiments should be conducted in the future. Since the period of a steady flow can be viewed as infinite, which will result in an infinite KC number, Eq. (3.10) is compatible with Eq. (3.8) in a channel flow problem. In this study, the values of α_0 and α_1 adopt Tanino and Nepf's experimental values. Specifically, for current fraction of 0.02, the values for $\phi = 0.091$ from Tanino and Nepf's results are used. That is, $\alpha_0 = 25 \pm 12$ and $\alpha_1 = (0.46 \pm 0.11) + (3.8 \pm 0.5)\phi$. Then, by nonlinear regression, α_2 is found to be within a 95% confidence interval (CI) of 7.86 ± 2.06 .

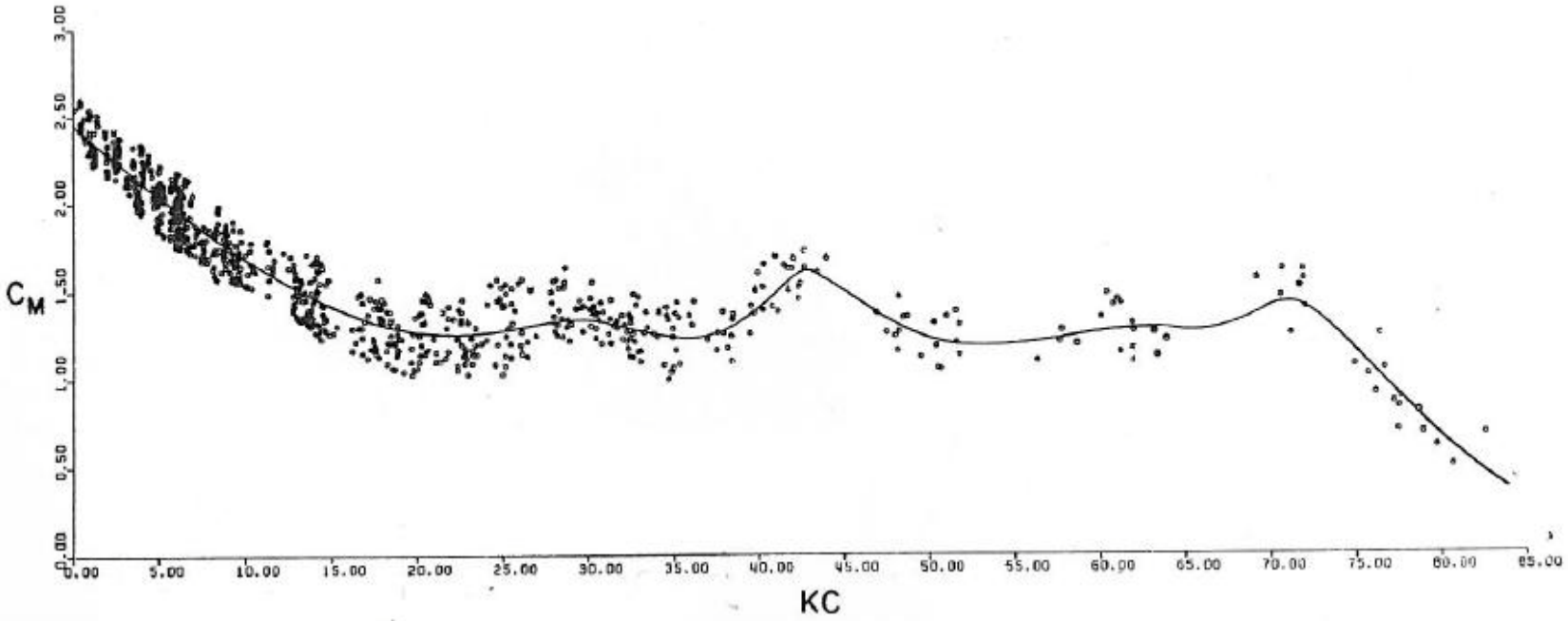

Figure 3. 54 Inertial coefficient .vs. KC for a smooth circular cylinder in waves. The dots are the test data, and the solid line is the mean fitted line. (from Fig. 6.18 of S. K. Chakrabarti (1987))

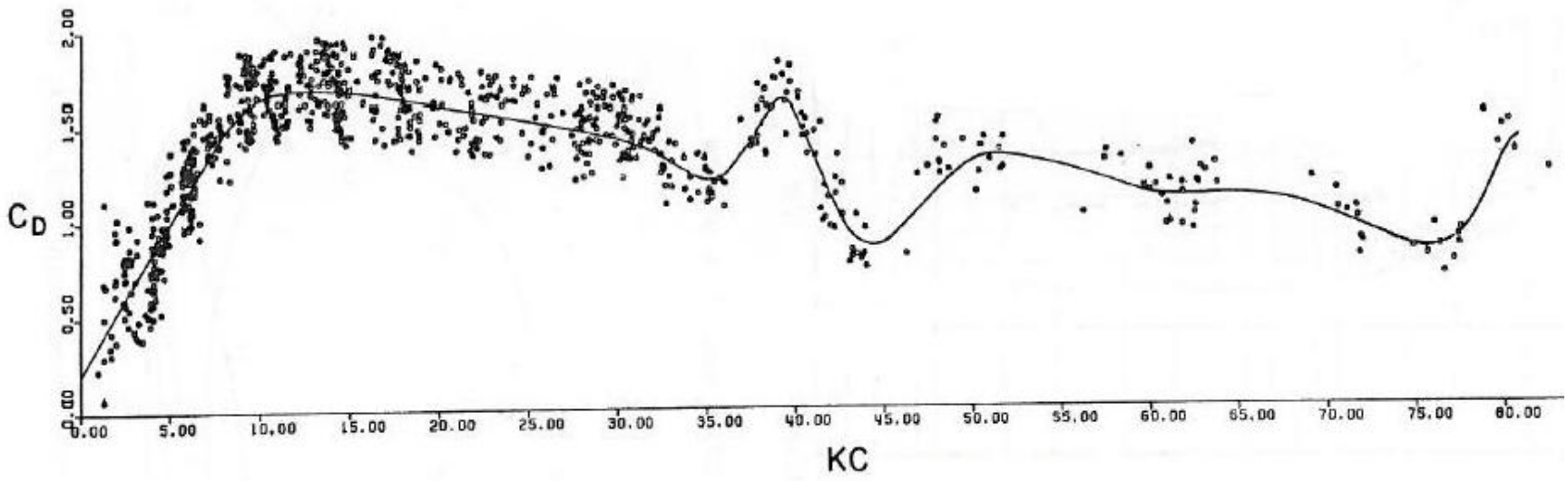

Figure 3. 55 Drag coefficient .vs. KC for a smooth circular cylinder in waves. The dots are the test data, and the solid line is the mean fitted line. (from Fig. 6.19of S. K. Chakrabarti (1987))

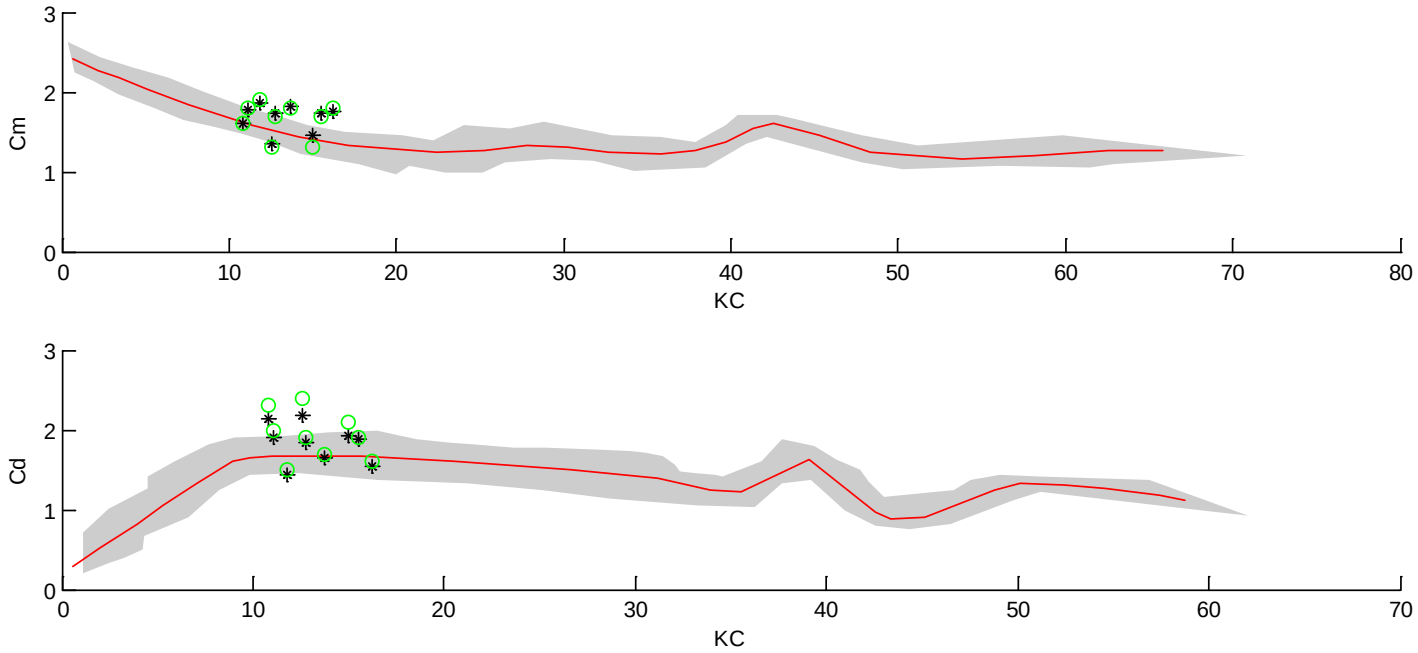

Figure 3. 56 Comparison of Cm and Cd of vegetation .vs. Cm and Cd of a single cylinder varying with KC. In the figure, the red line is the mean fitted line for a single cylinder. The grey parts represent the distribution region covering the test data in Fig. 3.14 and Fig. 3.15. The black asteroids represent the calculated Cm and Cd of vegetation by zero-crossing method, and the green circles are by least square method.

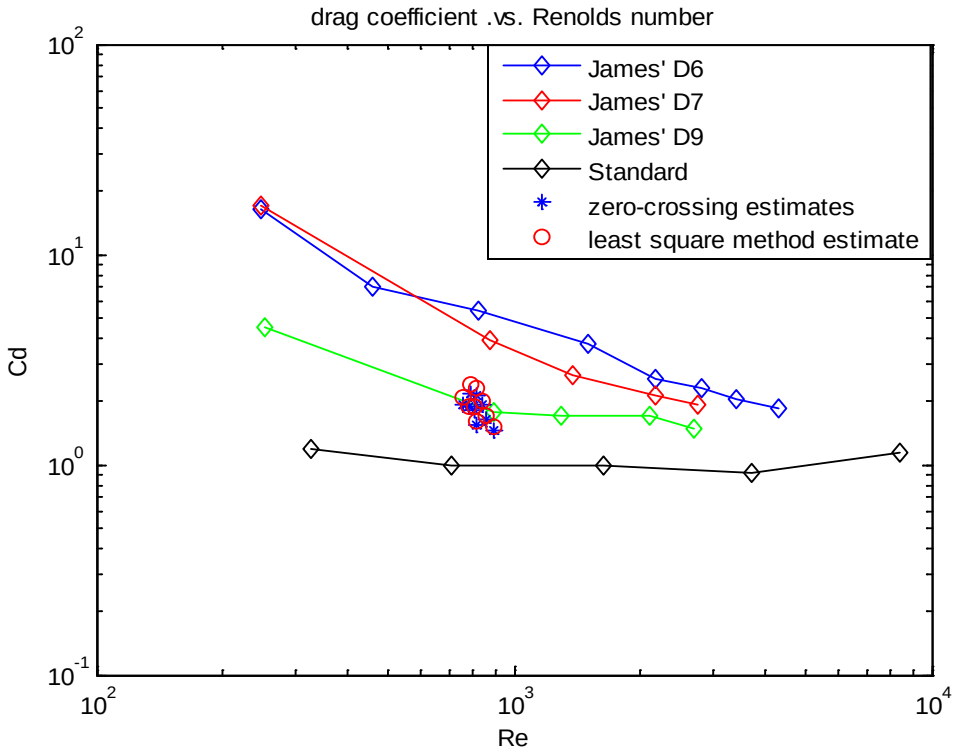

Figure 3. 57 Vegetation drag coefficients from James' and current experiments.

Chapter 4

Numerical Model Setting-up and Implementation

4.1 Sketch of computational domain

The finite difference solutions to the governing equations derived in Chapter 2 are presented in this section. First of all, the whole computational domain is discretized by the $M \times N \times L$ rectangular prism cells as sketched in Figure 4.1. A staggered grids system is used in this model as shown in Figure 4.2 (only *x*-*z* plane is plotted for easier visibility). All the scalar quantities, i.e., the pressure p and the turbulent k and ε, are defined in the center of the cell, while all the vectors, i.e., the *x*-, *y*- and *z*-component of the velocities, u, v and w, are defined in the cell faces.

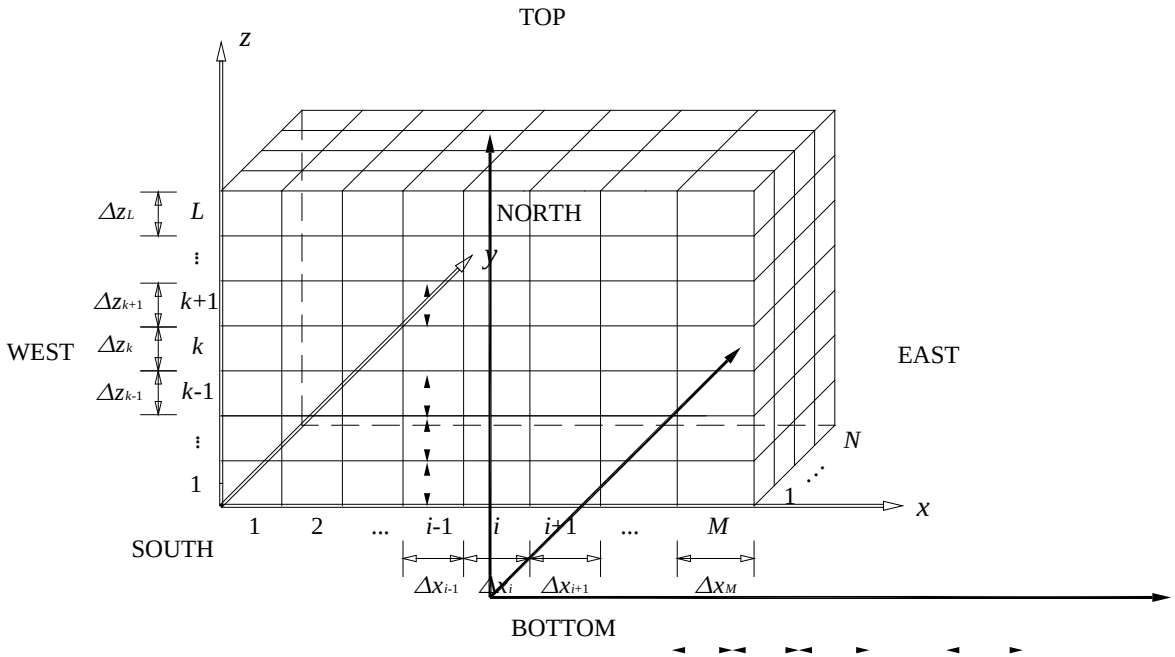

Figure 4. 1 Schematic plot of mesh definition with six boundaries.

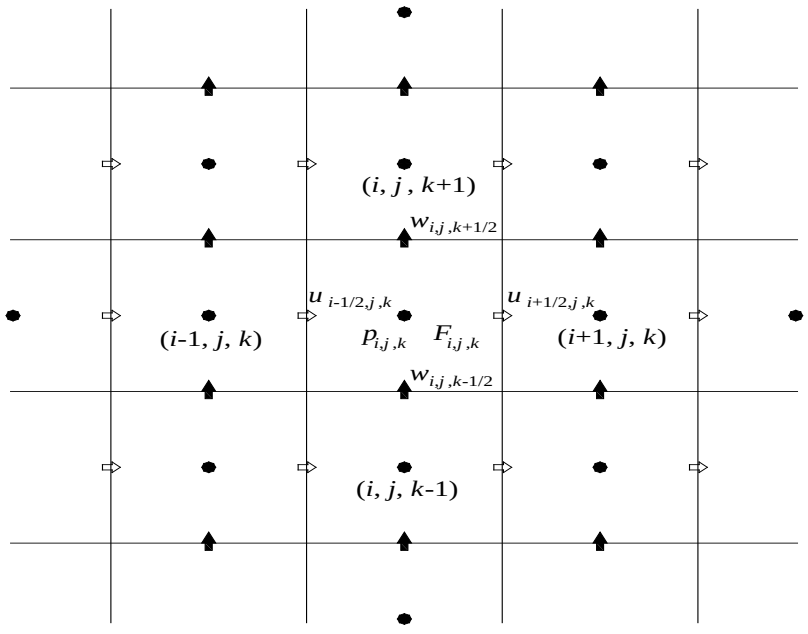

Figure 4. 2 The staggered grid system.

4.2 Two-step projection method

The continuity equation and the x-component momentum equation under the condition of constant porosity are rewritten here as examples to show the numerical implementation. The y and z components of the momentum equation can be processed similarly. When the porosity is inhomogeneous, it can be discretized similarly with the other scalars, such as density, which will be introduced below. For simplicity, the symbols of double-averaging are dropped hereinafter.

Continuity equation

$$\frac{\partial u}{\partial x}+\frac{\partial v}{\partial y}+\frac{\partial w}{\partial z}=0 \tag{4.1a}$$

X-component momentum equation

$$\begin{aligned}\frac{\partial u}{\partial t}+u\frac{\partial u}{\partial x}+v\frac{\partial u}{\partial y}+w\frac{\partial u}{\partial z}&=-\frac{1}{\rho}\frac{\partial p}{\partial x}+g_x\\&+\frac{\partial \tau_{xx}}{\partial x}+\frac{\partial \tau_{xy}}{\partial y}+\frac{\partial \tau_{xz}}{\partial z}+\frac{\partial R_{xx}}{\partial x}+\frac{\partial R_{xy}}{\partial y}+\frac{\partial R_{xz}}{\partial z}\\&+(-\frac{1}{2}\rho A C_d\frac{\sqrt{u^2+v^2+w^2}u}{\theta^2})+(-\rho\forall C_m\frac{1}{\theta}\frac{\partial u}{\partial t})\end{aligned} \tag{4.1b}$$

Before the numerical scheme is introduced, the Eq. (4.1b) should be transformed by combining the like terms, which yields:

$$\begin{aligned}(1)+\rho\forall C_m\frac{1}{\theta}\ \frac{\partial u}{\partial t}+u\frac{\partial u}{\partial x}+v\frac{\partial u}{\partial y}+w\frac{\partial u}{\partial z}&=-\frac{1}{\rho}\frac{\partial p}{\partial x}+g_x\\&+\frac{\partial \tau_{xx}}{\partial x}+\frac{\partial \tau_{xy}}{\partial y}+\frac{\partial \tau_{xz}}{\partial z}+\frac{\partial R_{xx}}{\partial x}+\frac{\partial R_{xy}}{\partial y}+\frac{\partial R_{xz}}{\partial z}\\&+(-\frac{1}{2}\rho A C_d\frac{\sqrt{u^2+v^2+w^2}u_i}{\theta^2})\end{aligned} \tag{4.2a}$$

Dividing two sides of the Eq. (4.2a) by the coefficient of the time derivative term, Eq. (4.2a) may be rewritten as

$$\frac{\partial u}{\partial t}+C(u\frac{\partial u}{\partial x}+v\frac{\partial u}{\partial y}+w\frac{\partial u}{\partial z})=-\frac{C}{\rho}\frac{\partial p}{\partial x}+Cg_x$$
$$+C(\frac{\partial \tau_{xx}}{\partial x}+\frac{\partial \tau_{xy}}{\partial y}+\frac{\partial \tau_{xz}}{\partial z})+C(\frac{\partial R_{xx}}{\partial x}+\frac{\partial R_{xy}}{\partial y}+\frac{\partial R_{xz}}{\partial z})-C_f u_c u \quad (4.2b)$$

where $C=\frac{1}{1+\rho\forall C_m\frac{1}{\theta}}$, and $C_f=\frac{\frac{1}{2}\rho A C_d\frac{1}{\theta^2}}{1+\rho\forall C_m\frac{1}{\theta}}$ and $u_c=\sqrt{u^2+v^2+w^2}$

A two-step projection method (Chorin, 1968, 1969), which was proved to be very robust by Liu and Lin (1997), has been employed to solve the Navier-Stokes equations widely. It will be used in our numerical model by considering the special arrangement of vegetation force term. In the first step, the time derivative is discretized by the forward difference method and an intermediate velocity which carries the correct vorticity is introduced, as

$$\frac{\tilde{u}^{n+1}-u^n}{\Delta t}=-C(u^n\frac{\partial u^n}{\partial x}+v^n\frac{\partial u^n}{\partial y}+w^n\frac{\partial u^n}{\partial z})$$
$$+C(\frac{\partial \tau_{xx}^n}{\partial x}+\frac{\partial \tau_{xy}^n}{\partial y}+\frac{\partial \tau_{xz}^n}{\partial z})+C(\frac{\partial R_{xx}^n}{\partial x}+\frac{\partial R_{xy}^n}{\partial y}+\frac{\partial R_{xz}^n}{\partial z}) \quad (4.3)$$

where the superscript indicates the time level and Δt is the time step size. In Eq. (4.3), the pressure gradient term and the gravitational acceleration term as well as the source term are not included. As a result, the intermediate velocities $\tilde{u},\tilde{v},\tilde{w}$ do not, in general, satisfy the continuity equation.

The second step is to project the intermediate velocity field onto a divergence-free plane to obtain the final velocity:

$$\frac{u^{n+1}-\tilde{u}^{n+1}}{\Delta t}=-\frac{C}{\rho^n}\frac{\partial p^{n+1}}{\partial x}+Cg_x-C_f\tilde{u}_c^{n+1}u^{n+1} \quad (4.4)$$

$$\frac{\partial u^{n+1}}{\partial x}+\frac{\partial v^{n+1}}{\partial y}+\frac{\partial w^{n+1}}{\partial z}=0 \quad (4.5)$$

The combination of Eq. (4.3) and (4.4) shows that the momentum equation of the Navier-Stokes equation can be approximately satisfied with the pressure gradient being evaluated at the (n+1)-th time level:

$$\frac{u^{n+1}-u^n}{\Delta t}+C(u^n\frac{\partial u^n}{\partial x}+v^n\frac{\partial u^n}{\partial y}+w^n\frac{\partial u^n}{\partial z})=-\frac{C}{\rho}\frac{\partial p^{n+1}}{\partial x}+Cg_x+ C(\frac{\partial \tau_{xx}^n}{\partial x}+\frac{\partial \tau_{xy}^n}{\partial y}+\frac{\partial \tau_{xz}^n}{\partial z})+C(\frac{\partial R_{xx}^n}{\partial x}+\frac{\partial R_{xy}^n}{\partial y}+\frac{\partial R_{xz}^n}{\partial z})-C_f\tilde{u}_c^{n+1}u^{n+1} \tag{4.6}$$

However, due to the presence of vegetation force term, the Poisson Pressure Equation (PPE) can not be achieved by simply taking the divergence of Eq. (4.4) and its corresponding y and z components and applying the continuity Eq. (4.5) to the resulting equation. Hence, special attention should be paid to the second step of the method where the nonlinear friction term is linearized by using the product of tentative total velocity $\tilde{u}_c$ and the new level velocity u_i^{n+1}. This treatment has two advantages: (1) with the linearization, it is possible to form the linear matrix for Possion Pressure Equation (PPE); (2) with the implicit treatment of the friction term, there is no additional time step restriction enforced by this source term, even when $C_f \to \infty$. The latter is very important when we want to use special porous media (e.g., $\theta \to 0$) to represent the impermeable solid body. When the conventional steps are employed on Eq. (4.4) attempting to obtain the PPE, the additional terms are resulted from the force term, even though it is already linearized. To solve this problem, a novel approach is proposed here by first re-expressing Eq. (4.4) as follows:

$$u^{n+1}=\frac{1}{\gamma}\tilde{u}-\frac{C\Delta t}{\rho\gamma}\frac{\partial p^{n+1}}{\partial x}+\frac{C\Delta t g_x}{\gamma} \tag{4.7}$$

where $\gamma = 1+\Delta t C_f \tilde{u}_c$

Now by taking the divergence of the equation and applying Eq. (4.5), we have

$$\frac{\partial}{\partial x}\left(\frac{C}{\rho\gamma}\frac{\partial p^{n+1}}{\partial x}\right)+\frac{\partial}{\partial y}\left(\frac{C}{\rho\gamma}\frac{\partial p^{n+1}}{\partial y}\right)+\frac{\partial}{\partial z}\left(\frac{C}{\rho\gamma}\frac{\partial p^{n+1}}{\partial z}\right)$$
$$=\frac{\partial}{\partial x}\left(\frac{\tilde{u}}{\Delta t\gamma}\right)+\frac{\partial}{\partial y}\left(\frac{\tilde{v}}{\Delta t\gamma}\right)+\frac{\partial}{\partial z}\left(\frac{\tilde{w}}{\Delta t\gamma}\right)+\frac{\partial}{\partial x}\left(\frac{Cg_x}{\gamma}\right)+\frac{\partial}{\partial y}\left(\frac{Cg_y}{\gamma}\right)+\frac{\partial}{\partial z}\left(\frac{Cg_z}{\gamma}\right) \quad (4.8)$$

Comparing this with the conventional PPE, the differences arise in that both the matrix and the RHS are modified. In particular, the additional source term $\frac{\partial}{\partial x}\left(\frac{Cg_x}{\gamma}\right)+\frac{\partial}{\partial y}\left(\frac{Cg_y}{\gamma}\right)+\frac{\partial}{\partial z}\left(\frac{Cg_z}{\gamma}\right)$ is required even when the gravitational acceleration is a constant.

After solving Eq. (4.8) with appropriate boundary conditions, the resulting pressure information at the (n+1)-th time level will be applied to Eq. (4.4) to update the velocity field to (n+1)-th time level. These processes will make sure the divergence-free constraint to be true according to Eq. (4.5).

The numerical program was written to a serial code based on the above-introduced method and can be easily run on a single processor of workstations or personal desktop.

4.3 Spatial discretization in finite difference form

4.3.1 Interpolation

In the two-step projection method, the finite difference forms are employed to express the spatial discretization of the velocity components and the pressure field. As discussed and shown in Figure 4.2 earlier, the present scheme defines the velocity components u, v, and w on the cell faces. On the other hand, the scalar such as pressure p is defined at the center of the cell. However, some variables are needed at the place where they are not originally defined. In such circumstances, the linear interpolation will be used to solve this problem. The interpolated variables that will be used later are given as follows:

$$u_{i,j,k} = \frac{1}{2}\left(u_{i+1/2,j,k} + u_{i-1/2,j,k}\right) \tag{4.9}$$

$$u_{i,j+1/2,k} = \frac{u_{i,j+1,k}\Delta y_j + u_{i,j,k}\Delta y_{j+1}}{\Delta y_j + \Delta y_{j+1}} \tag{4.10}$$

$$u_{i,j,k+1/2} = \frac{u_{i,j,k+1}\Delta z_k + u_{i,j,k}\Delta z_{k+1}}{\Delta z_k + \Delta z_{k+1}} \tag{4.11}$$

$$\Delta x_{i+1/2} = \frac{1}{2}\left(\Delta x_i + \Delta x_{i+1}\right) \tag{4.12}$$

For the velocities and other related quantities in y and z direction, they are interpolated in the similar manner.

4.3.2 Advection terms

In Eq. (4.3), all the advection terms and diffusion terms are evaluated at the *n*-th time level. The advection terms in *x*-momentum equation and those in *y*- and *z*-momentum equations are calculated according to the following formulae:

$$\left(u\frac{\partial u}{\partial x} + v\frac{\partial u}{\partial y} + w\frac{\partial u}{\partial z}\right)_{i+1/2,j,k} = u_{i+1/2,j,k}\left(\frac{\partial u}{\partial x}\right)_{i+1/2,j,k} + v_{i+1/2,j,k}\left(\frac{\partial u}{\partial y}\right)_{i+1/2,j,k} + w_{i+1/2,j,k}\left(\frac{\partial u}{\partial z}\right)_{i+1/2,j,k} \tag{4.13}$$

$$\left(u\frac{\partial v}{\partial x} + v\frac{\partial v}{\partial y} + w\frac{\partial v}{\partial z}\right)_{i,j+1/2,k} = u_{i,j+1/2,k}\left(\frac{\partial v}{\partial x}\right)_{i,j+1/2,k} + v_{i,j+1/2,k}\left(\frac{\partial v}{\partial y}\right)_{i,j+1/2,k} + w_{i,j+1/2,k}\left(\frac{\partial v}{\partial z}\right)_{i,j+1/2,k} \tag{4.14}$$

$$\left(u\frac{\partial w}{\partial x}+v\frac{\partial w}{\partial y}+w\frac{\partial w}{\partial z}\right)_{i,j,k+1/2}=u_{i,j,k+1/2}\left(\frac{\partial w}{\partial x}\right)_{i,j,k+1/2}+v_{i,j+1/2,k}\left(\frac{\partial w}{\partial y}\right)_{i,j,k+1/2}+w_{i,j+1/2,k}\left(\frac{\partial w}{\partial z}\right)_{i,j,k+1/2} \tag{4.15}$$

To calculate the spatial derivatives in Eq. (4.13), a combination of upwind and central differencing is used with the more dissipative upwind scheme employed to stabilize the central difference which alone is numerically unstable. A weighted combination of the two differencing schemes normally yields a numerical solution with satisfactory accuracy. The upwind method is represented by

$$\left(\frac{\partial u}{\partial x}\right)_{i+1/2,j,k}=\begin{cases}\left(\dfrac{\partial u}{\partial x}\right)_{i,j,k}, \text{ if } u_{i+1/2,j,k}>0\\ \left(\dfrac{\partial u}{\partial x}\right)_{i+1,j,k}, \text{ if } u_{i+1/2,j,k}<0\end{cases} \tag{4.16}$$

while the center difference method is represented by

$$\left(\frac{\partial u}{\partial x}\right)_{i+1/2,j,k}=\frac{\Delta x_{i+1}\left(\dfrac{\partial u}{\partial x}\right)_{i,j,k}+\Delta x_i\left(\dfrac{\partial u}{\partial x}\right)_{i+1,j,k}}{\Delta x_i+\Delta x_{i+1}}. \tag{4.17}$$

In both Eq. (4.16) and (4.17),

$$\left(\frac{\partial u}{\partial x}\right)_{i,j,k}=\frac{u_{i+1/2,j,k}-u_{i-1/2,j,k}}{\Delta x_i}, \tag{4.18}$$

$$\left(\frac{\partial u}{\partial x}\right)_{i+1,j,k}=\frac{u_{i+3/2,j,k}-u_{i+1/2,j,k}}{\Delta x_{i+1}}, \tag{4.19}$$

are defined. Therefore, the final formula for the spatial derivative is as follows:

$$\left(\frac{\partial u}{\partial x}\right)_{i+1/2,j,k} = \left\{\left[1+\alpha\,\mathrm{sgn}\left(u_{i+1/2,j,k}\right)\right]\Delta x_{i+1}\left(\frac{\partial u}{\partial x}\right)_{i,j,k} + \left[1-\alpha\,\mathrm{sgn}\left(u_{i+1/2,j,k}\right)\right]\Delta x_i\left(\frac{\partial u}{\partial x}\right)_{i+1,j,k}\right\} / \Delta x_\alpha \tag{4.20}$$

where

$$\Delta x_\alpha = \Delta x_{i+1} + \Delta x_i + \alpha\,\mathrm{sgn}\left(u_{i+1/2,j,k}\right)\left(\Delta x_{i+1} - \Delta x_i\right). \tag{4.21}$$

Similarly, we can get

$$\left(\frac{\partial u}{\partial y}\right)_{i+1/2,j,k} = \left\{\left[1+\alpha\,\mathrm{sgn}\left(v_{i+1/2,j,k}\right)\right]\Delta y_{j+1/2}\left(\frac{\partial u}{\partial y}\right)_{i+1/2,j-1/2,k} + \left[1-\alpha\,\mathrm{sgn}\left(v_{i+1/2,j,k}\right)\right]\Delta y_{j-1/2}\left(\frac{\partial u}{\partial y}\right)_{i+1/2,j+1/2,k}\right\} / \Delta y_\alpha \tag{4.22}$$

where

$$\Delta y_\alpha = \Delta y_{j+1/2} + \Delta y_{j-1/2} + \alpha\,\mathrm{sgn}\left(v_{i+1/2,j,k}\right)\left(\Delta y_{j+1/2} - \Delta y_{j-1/2}\right), \tag{4.23}$$

and

$$\left(\frac{\partial u}{\partial y}\right)_{i+1/2,j+1/2,k} = \frac{u_{i+1/2,j+1,k} - u_{i+1/2,j,k}}{\Delta y_{j+1/2}}, \tag{4.24}$$

$$\left(\frac{\partial u}{\partial y}\right)_{i+1/2,j-1/2,k} = \frac{u_{i+1/2,j,k} - u_{i+1/2,j-1,k}}{\Delta y_{j-1/2}}. \tag{4.25}$$

We can also get

$$\left(\frac{\partial u}{\partial z}\right)_{i+1/2,j,k} = \left\{\left[1+\alpha\,\mathrm{sgn}\left(w_{i+1/2,j,k}\right)\right]\Delta z_{k+1/2}\left(\frac{\partial u}{\partial z}\right)_{i+1/2,j,k-1/2}\right.$$

$$\left.+\left[1-\alpha\,\mathrm{sgn}\left(w_{i+1/2,j,k}\right)\right]\Delta z_{k-1/2}\left(\frac{\partial u}{\partial z}\right)_{i+1/2,j,k+1/2}\right\}/\,\Delta z_{\alpha}\,, \tag{4.26}$$

where

$$\Delta z_{\alpha} = \Delta z_{k+1/2} + \Delta z_{k-1/2} + \alpha\,\mathrm{sgn}\left(w_{i+1/2,j,k}\right)\left(\Delta z_{k+1/2} - \Delta z_{k-1/2}\right), \tag{4.27}$$

and

$$\left(\frac{\partial u}{\partial z}\right)_{i+1/2,j,k+1/2} = \frac{u_{i+1/2,j,k+1} - u_{i+1/2,j,k}}{\Delta z_{k+1/2}}, \tag{4.28}$$

$$\left(\frac{\partial u}{\partial z}\right)_{i+1/2,j,k-1/2} = \frac{u_{i+1/2,j,k} - u_{i+1/2,j,k-1}}{\Delta z_{k-1/2}}. \tag{4.29}$$

The coefficient α is the weighting factor between the upwind method and the central difference method. When $\alpha = 0$, the finite difference form becomes the central difference; while $\alpha = 1$, the difference form becomes the upwind difference. In practice, α is selected in the range of 0.3 to 0.5 in order to produce the stable and accurate results. In addition, the finite difference form for the advection terms in the *y*- and *z*- momentum equations will be obtained in a similar way.

4.3.3 Stress terms

In x direction, the gradients of the viscous stresses in Eq. (4.3) can be written as,

$$\frac{\partial}{\partial x}\tau_{xx}+\frac{\partial}{\partial y}\tau_{xy}+\frac{\partial}{\partial z}\tau_{xz} \tag{4.30}$$

The first term of Eq. (4.30) can be written in the following finite difference form,

$$\left(\frac{\partial}{\partial x}\tau_{xx}\right)_{i+1/2,\,j,k}=\frac{(\tau_{xx})_{i+1,\,j,k}-(\tau_{xx})_{i,\,j,k}}{\Delta x_{i+1/2}}, \tag{4.31}$$

where

$$(\tau_{xx})_{i,\,j,k}=2\mu\left(\frac{\partial u}{\partial x}\right)_{i,\,j,k} \tag{4.32}$$

and can be discretized by Eq. (4.18).

The second term and the third term in Eq. (4.30) can be written as,

$$\left(\frac{\partial}{\partial y}\tau_{xy}\right)_{i+1/2,\,j,k}=\frac{(\tau_{xy})_{i+1/2,\,j+1/2,k}-(\tau_{xy})_{i+1/2,\,j-1/2,k}}{\Delta y_j}, \tag{4.33}$$

where

$$(\tau_{xy})_{i+1/2,\,j+1/2,k}=\mu\left(\frac{\partial u}{\partial y}+\frac{\partial v}{\partial x}\right)_{i+1/2,\,j+1/2,k} \tag{4.34}$$

and $\left(\frac{\partial u}{\partial y}\right)_{i+1/2,\,j+1/2,k}$ can be discretized by Eq. (4.24); and

$$\left(\frac{\partial}{\partial z}\tau_{xz}\right)_{i+1/2,\,j,k}=\frac{(\tau_{xz})_{i+1/2,\,j,k+1/2}-(\tau_{xz})_{i+1/2,\,j,k-1/2}}{\Delta z_k}, \tag{4.35}$$

where

$$(\tau_{xz})_{i+1/2,j,k+1/2} = \mu\left(\frac{\partial u}{\partial z} + \frac{\partial w}{\partial x}\right)_{i+1/2,j,k+1/2} \tag{4.36}$$

and $\left(\frac{\partial u}{\partial z}\right)_{i+1/2,j,k+1/2}$ can be discretized by Eq. (4.28). The similar finite difference formulae can be obtained for the stress gradient terms in the *y*-momentum equation and *z*-momentum equation.

Similarly, the Reynolds stress term $\partial R_{ij} / \partial x_j$ could be discretized with the above finite difference formulae.

4.3.4 Pressure terms

In the second step of the projection method, the Poisson Pressure Equation (4.8) is to be solved. In the three dimensional form, Eq. (4.8) can be rewritten as:

$$\begin{aligned} &\frac{\partial}{\partial x}\left(\frac{C}{\gamma\rho^n}\frac{\partial p^{n+1}}{\partial x}\right) + \frac{\partial}{\partial y}\left(\frac{C}{\gamma\rho^n}\frac{\partial p^{n+1}}{\partial y}\right) + \frac{\partial}{\partial z}\left(\frac{C}{\gamma\rho^n}\frac{\partial p^{n+1}}{\partial z}\right) \\ &= \frac{1}{\Delta t}\left(\frac{\partial}{\partial x}\frac{\tilde{u}}{\gamma} + \frac{\partial}{\partial y}\frac{\tilde{v}}{\gamma} + \frac{\partial}{\partial z}\frac{\tilde{w}}{\gamma}\right) + \frac{\partial}{\partial z}\left(\frac{Cg_z}{\gamma}\right) \end{aligned}. \tag{4.37}$$

The PPE will be evaluated at the center. Since the coefficients of γ and C in each term are scalars and can be discretized similarly as the density ρ, for simplicity, they will be dropped in the following difference formulae. Therefore, the left hand side of Eq. (4.37) can be calculated as:

$$\left\{\frac{\partial}{\partial x}\left(\frac{1}{\rho^n}\frac{\partial p^{n+1}}{\partial x}\right)\right\}_{i,j,k} = \frac{1}{\Delta x_i}\left\{\frac{1}{\rho^n_{i+1/2,j,k}}\left(\frac{\partial p}{\partial x}\right)^{n+1}_{i+1/2,j,k} - \frac{1}{\rho^n_{i-1/2,j,k}}\left(\frac{\partial p}{\partial x}\right)^{n+1}_{i-1/2,j,k}\right\}$$
$$= \frac{1}{\Delta x_i}\left\{\frac{1}{\rho^n_{i+1/2,j,k}}\left(\frac{p^{n+1}_{i+1,j,k} - p^{n+1}_{i,j,k}}{\Delta x_{i+1/2}}\right) - \frac{1}{\rho^n_{i-1/2,j,k}}\left(\frac{p^{n+1}_{i,j,k} - p^{n+1}_{i-1,j,k}}{\Delta x_{i-1/2}}\right)\right\}, \tag{4.38}$$

$$\left\{\frac{\partial}{\partial y}\left(\frac{1}{\rho^n}\frac{\partial p^{n+1}}{\partial y}\right)\right\}_{i,j,k} = \frac{1}{\Delta y_j}\left\{\frac{1}{\rho^n_{i,j+1/2,k}}\left(\frac{\partial p}{\partial y}\right)^{n+1}_{i,j+1/2,k} - \frac{1}{\rho^n_{i,j-1/2,k}}\left(\frac{\partial p}{\partial y}\right)^{n+1}_{i,j-1/2,k}\right\}$$
$$= \frac{1}{\Delta y_j}\left\{\frac{1}{\rho^n_{i,j+1/2,k}}\left(\frac{p^{n+1}_{i,j+1,k} - p^{n+1}_{i,j,k}}{\Delta y_{j+1/2}}\right) - \frac{1}{\rho^n_{i,j-1/2,k}}\left(\frac{p^{n+1}_{i,j,k} - p^{n+1}_{i,j-1,k}}{\Delta y_{j-1/2}}\right)\right\}, \tag{4.39}$$

$$\left\{\frac{\partial}{\partial z}\left(\frac{1}{\rho^n}\frac{\partial p^{n+1}}{\partial z}\right)\right\}_{i,j,k} = \frac{1}{\Delta z_k}\left\{\frac{1}{\rho^n_{i,j,k+1/2}}\left(\frac{\partial p}{\partial z}\right)^{n+1}_{i,j,k+1/2} - \frac{1}{\rho^n_{i,j,k-1/2}}\left(\frac{\partial p}{\partial z}\right)^{n+1}_{i,j,k-1/2}\right\}$$
$$= \frac{1}{\Delta z_k}\left\{\frac{1}{\rho^n_{i,j,k+1/2}}\left(\frac{p^{n+1}_{i,j,k+1} - p^{n+1}_{i,j,k}}{\Delta z_{k+1/2}}\right) - \frac{1}{\rho^n_{i,j,k-1/2}}\left(\frac{p^{n+1}_{i,j,k} - p^{n+1}_{i,j,k-1}}{\Delta z_{k-1/2}}\right)\right\}. \tag{4.40}$$

The right-hand side of Eq. (4.37) is expressed as,

$$\left(\frac{\partial \tilde{u}}{\partial x} + \frac{\partial \tilde{v}}{\partial y} + \frac{\partial \tilde{w}}{\partial z}\right)_{i,j,k} = \frac{\tilde{u}_{i+1/2,j,k} - \tilde{u}_{i-1/2,j,k}}{\Delta x_i} + \frac{\tilde{v}_{i,j+1/2,k} - \tilde{v}_{i,j-1/2,k}}{\Delta y_j} + \frac{\tilde{w}_{i,j,k+1/2} - \tilde{w}_{i,j,k-1/2}}{\Delta z_k} \tag{4.41a}$$

$$\left(\frac{\partial}{\partial z}\frac{Cg_z}{\gamma}\right)_{i,j,k} = \frac{\left(\frac{Cg_z}{\gamma}\right)^n_{i,j,k+1/2} - \left(\frac{Cg_z}{\gamma}\right)^n_{i,j,k-1/2}}{\Delta z_k} \tag{4.41b}$$

The density at the cell faces can be obtained by the linear interpolation, i.e.,

$$\rho^n_{i+1/2,j,k} = \frac{\rho^n_{i,j,k}\Delta x_{i+1} + \rho^n_{i+1,j,k}\Delta x_i}{\Delta x_i + \Delta x_{i+1}}, \tag{4.42}$$

$$\rho^n_{i,j+1/2,k} = \frac{\rho^n_{i,j,k}\Delta y_{j+1} + \rho^n_{i,j+1,k}\Delta y_j}{\Delta y_j + \Delta y_{j+1}}, \tag{4.43}$$

$$\rho^n_{i,j+1/2,k} = \frac{\rho^n_{i,j,k}\Delta y_{j+1} + \rho^n_{i,j+1,k}\Delta y_j}{\Delta y_j + \Delta y_{j+1}}. \tag{4.44}$$

Substituting Eq. (4.38) ~ (4.44) into Poisson Pressure Eq. (4.37) with the proper boundary conditions yields a set of linear algebraic equations for the pressure field which can be solved by standard matrix solvers. In current model, Bi-CGSTAB method with the preconditioner of incomplete LU is used to solve the resulting sparse system of equations. The matrix solver is coded with reference to the flow chart in the templates (Barrett, et al., 2006).

4.4 $k-\varepsilon$ equations

Both k and ε are scalars and are defined at the center of a cell. Similar with Lemos' method (1992), the $k-\varepsilon$ equation can be symbolically expressed in the finite-difference form as

$$\frac{k^{n+1}_{i,j,k} - k^n_{i,j,k}}{\Delta t} + FkX + FkY + FkZ = VISk + \frac{1}{2}(P^{n+1}_{i,j,k} + P^n_{i,j,k} - \varepsilon^{n+1}_{i,j,k} - \varepsilon^n_{i,j,k}) + \eta_k u^{n+1}_{i,j,k} F^{n+1}_{xi,j,k} + \eta_k v^{n+1}_{i,j,k} F^{n+1}_{yi,j,k} + \eta_k w^{n+1}_{i,j,k} F^{n+1}_{zi,j,k} \tag{4.45}$$

$$\frac{\varepsilon^{n+1}_{i,j,k} - \varepsilon^n_{i,j,k}}{\Delta t} + F\varepsilon X + F\varepsilon Y + F\varepsilon Z = VIS\varepsilon + \frac{\varepsilon^n_{i,j,k}}{k^n_{i,j,k}}(C_{\varepsilon 1} P^{n+1}_{i,j,k} + \eta_\varepsilon (u^{n+1}_{i,j,k} F^{n+1}_{xi,j,k} + v^{n+1}_{i,j,k} F^{n+1}_{yi,j,k} + w^{n+1}_{i,j,k} F^{n+1}_{zi,j,k}) - C_{\varepsilon 2}\varepsilon^{n+1}_{i,j,k}) \tag{4.46}$$

In the Eq. (4.45) and (4.46), the advection terms ($FkX, FkY, FkZ, F\varepsilon X, F\varepsilon Y, F\varepsilon Z$), diffusion terms ($VISk, VIS\varepsilon$), and the production terms $P_{i,j,k}$ need to be defined and calculated at the corresponding points. Taking the k equation as an example, the numerical implementation will be described below.

First, the x-component of the advection term in Eq. (4.45) can be written as

$$FkX = (u\frac{\partial k}{\partial x})_{i,j,k} = u_{i,j,k}^{n+1}(\frac{\partial k}{\partial x})_{i,j,k}^{n} \tag{4.47}$$

In the above expression, the derivative of k is computed as the n-th time level, which means that the explicit scheme is conducted. Regarding the discretization of the derivative of k, the form of $\partial u / \partial x$, that is, Eq. (4.20), is adopted. The other two components of the advection term are similarly treated.

The diffusion term in Eq. (4.45) is defined as

$$VISk = \left\{ \frac{\partial}{\partial x}(\frac{v_t}{\sigma_k} + v)\frac{\partial k}{\partial x} + \frac{\partial}{\partial y}(\frac{v_t}{\sigma_k} + v)\frac{\partial k}{\partial y} + \frac{\partial}{\partial z}(\frac{v_t}{\sigma_k} + v)\frac{\partial k}{\partial z} \right\}_{i,j,k}^{n} \tag{4.48}$$

The x-component of the diffusion term can be discretized with the central difference method, which is

$$\begin{aligned} \left\{ \frac{\partial}{\partial x}(\frac{v_t}{\sigma_k} + v)\frac{\partial k}{\partial x} \right\}_{i,j,k}^{n} &= \frac{(\frac{v_t}{\sigma_k} + v)_{i+\frac{1}{2},j,k}^{n}(\frac{\partial k}{\partial x})_{i+\frac{1}{2},j,k}^{n} - (\frac{v_t}{\sigma_k} + v)_{i-\frac{1}{2},j,k}^{n}(\frac{\partial k}{\partial x})_{i-\frac{1}{2},j,k}^{n}}{\Delta x_i} \\ &= \frac{1}{\Delta x_i}\left[(\frac{v_t}{\sigma_k} + v)_{i+\frac{1}{2},j,k}^{n} \frac{k_{i+1,j,k}^{n} - k_{i,j,k}^{n}}{\Delta x_{i+\frac{1}{2}}} - (\frac{v_t}{\sigma_k} + v)_{i-\frac{1}{2},j,k}^{n} \frac{k_{i,j,k}^{n} - k_{i-1,j}^{n}, k}{\Delta x_{i-\frac{1}{2}}} \right] \end{aligned} \tag{4.49}$$

Again, the other two components of the diffusion term can be obtained similarly.

In the production terms, the discretization of each component is, essentially, the discretization of the derivatives of velocities at the center or the sides of the computational cell. Therefore, the above schemes introduced in section (4.3.2) are used here for the corresponding terms.

4.5 Free surface evolution

Besides solving the fluid governing equations with finite difference method presented above, another challenging work in building up the numerical model is how to accurately

predict the evolution of water free surface. In this study, the Volume of Fluid (VOF) method (Gueyffier et al., 1999) is used to trace the free surface deformation. The concept of this method is to represent the free surface by the mixing cells which have averaged density of two kinds of fluids. By tracking and updating the averaged density in each cell, the free surface can be reconstructed.

Representing the water density, air density, and the averaged density in the mixing cell as ρ_w , ρ_a , and ρ , respectively, the advection equation of density for the mass conservation is given by,

$$\frac{\partial \rho}{\partial t} + u_i \frac{\partial \rho}{\partial x_i} = 0 . \tag{4.50}$$

A volume of fluid (VOF) function F is defined as:

$$F = \frac{\rho - \rho_a}{\rho_w - \rho_a}, \tag{4.51}$$

Substituting the definition, Eq. (4.51) and the mass conservation, Eq. (2.56) into Eq. (4.50) yields

$$\frac{\partial F}{\partial t} + \frac{\partial u_i F}{\partial x_i} = 0 , \tag{4.52}$$

where F represents the volumetric ratio between the water and air, which equals to 0 in air and 1 in water, and is between 0 and 1 for the interface. By tracking the VOF function in each computational grid, the reconstruction and motion of the interface can be obtained. Numerically, for a computational cell centered at (i, j, k), Eq. (4.52) can be rewritten in the following finite difference form,

$$F_{i,j,k}^{n} = F_{i,j,k}^{n-1} - \frac{\Delta t}{\Delta x_i}(u_{i+1/2,j,k}^{n} F_{i+1/2,j,k}^{n-1} - u_{i-1/2,j,k}^{n} F_{i-1/2,j,k}^{n-1})$$
$$- \frac{\Delta t}{\Delta y_j}(v_{i,j+1/2,k}^{n} F_{i,j+1/2,k}^{n-1} - v_{i,j-1/2,k}^{n} F_{i,j-1/2,k}^{n-1}) \quad (4.53)$$
$$- \frac{\Delta t}{\Delta z_k}(w_{i,j,k+1/2}^{n} F_{i,j,k+1/2}^{n-1} - w_{i,j,k-1/2}^{n} F_{i,j,k-1/2}^{n-1})$$

Eq. (4.53) suggests that the key issue to update the VOF function is to determine the net VOF fluxes in three directions for each computational cell. In the present model, a second-order piecewise linear interface calculation (PLIC) method is used to reconstruct the interface and to determine the VOF fluxes.

Given the VOF value of the concerned cell and that of all its neighboring cells, the normal vector is calculated using Youngs' (least squares) method (Rider and Kothe, 1998). Then the interface plane can be expressed as follows:

$$m_1 x + m_2 y + m_3 z = \alpha \quad (4.54)$$

where m_1, m_2, m_3 are the x-, y-, z-component of the unit normal vector **m**, respectively, α is the intercept which represents the smallest distance between the interface plane and the origin of the concerned cell.

After reconstructing the interface, the motion of the interface plane driven by the flow can be calculated by employing the Lagrangian-VOF interface tracking method. Describing the interface plane in a computational cell at time t^n by,

$$m_1 x^n + m_2 y^n + m_3 z^n = \alpha^n \quad (4.55)$$

Without losing generality, only the advection of the interface in *x*-direction is discussed here.

Denoting the velocity on west and east faces of the concerned cell by $u_{i\text{-}1/2}$ and $u_{i+1/2}$, and the length of the cell in *x*-direction by Δx. The velocity inside the cell can be calculated by a simple linear interpolation as follows,

$$u(x^n) = u_{i-1/2}(1-\frac{x^n}{\Delta x}) + u_{i+1/2}\frac{x^n}{\Delta x} \tag{4.56}$$

After the advection by the flow, the *x* coordinates of each point initially on the interface plane Eq. (4.55) change to be

$$x^* = x^n + u(x^n)\cdot\Delta t = \left[1+\left(\frac{u_{i+1/2}-u_{i-1/2}}{\Delta x}\right)\cdot\Delta t\right] + u_{i+1/2}\cdot\Delta t \tag{4.57}$$

Then x^n can be expressed in terms of x^* by:

$$x^n = \frac{x^* - u_{i-1/2}\cdot\Delta t}{1+\left(\frac{u_{i+1/2}-u_{i-1/2}}{\Delta x}\right)\cdot\Delta t} \tag{4.58}$$

Substituting Eq. (4.58) into Eq. (4.55), the equation of the interface plane yields,

$$m_1\left[\frac{x^* - u_{i-1/2}\cdot\Delta t}{1+\left(\frac{u_{i+1/2}-u_{i-1/2}}{\Delta x}\right)\cdot\Delta t}\right] + m_2 y^n + m_3 z^n = \alpha^n \tag{4.59}$$

Rewrite Eq. (4.59) in the standard form as Eq. (4.55):

$$m_1^* x^* + m_2 y^n + m_3 z^n = \alpha^* \tag{4.60}$$

where

$$m_1^* = \frac{m_1^n}{1+\left(\frac{u_{i+1/2}-u_{i-1/2}}{\Delta x}\right)\cdot\Delta t} \tag{4.61}$$

and

$$\alpha^{*} = \alpha^{n} + \frac{m_1^{n} \cdot u_{i-1/2} \cdot \Delta t}{1 + \left(\frac{u_{i+1/2} - u_{i-1/2}}{\Delta x} \right) \cdot \Delta t} \tag{4.62}$$

After obtaining the new normal vectors and intercepts, the volume flux, which is the "cut volume" in Figure 4.3, can be calculated using new normal vectors m_1^{*} and intercepts α^{*} at each grid as follows (Gueyffier et al., 1999),

$$V = \frac{1}{6 m_1 m_2 m_3} \left[\alpha^3 - \sum_{i=1}^{3} F_3 \left(\alpha - m_i \Delta x_i \right) + \sum_{i=1}^{3} F_3 \left(\alpha - \alpha_{\max} + m_i \Delta x_i \right) \right] \tag{4.63}$$

where,

$$\alpha_{\max} = \sum_{i=1}^{3} m_i \Delta x_i \tag{4.64}$$

and the function $F_n(y)$ defined as,

$$F_n \left(y \right) = \begin{cases} y^n, \text{ for } y > 0 \\ 0, \text{ for } y \le 0 \end{cases} \tag{4.65}$$

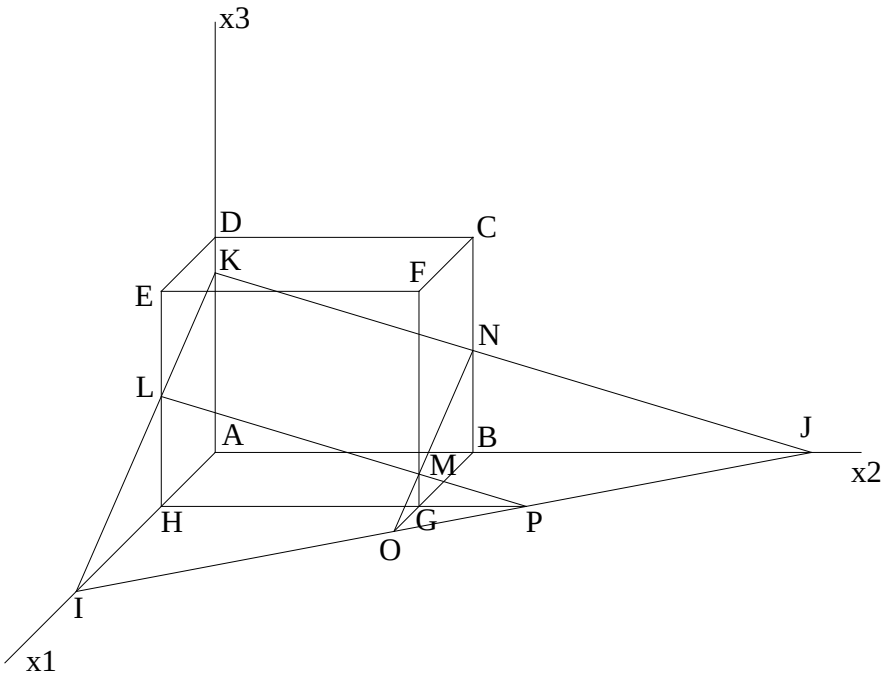

Figure 4. 3 Advection of the VOF flux in the computational cell. The “cut volume” refers to the region inside the rectangular parallelepiped *ABCDEFGH* of sides Δx_i (i = 1, 2, 3) and below the plane *IJK*, which has unit normal vector **m** = (m_1, m_2, m_3) and intercept α.

The procedures of advecting the interface planes in *y*- and *z*-direction are similar with that in *x*-direction. After calculating the volume flux in all three directions, the VOF function *F* can be updated to the next time step.

4.6 Initial and boundary conditions

In practical computations, the resolution near the physical boundaries is generally too coarse to resolve the boundary layers because of the limitation of grid size. Therefore, effective boundary conditions are necessary for the prediction of reasonable results near the boundaries. In this section, the implementation of the required initial conditions and boundary conditions will be discussed.

4.6.1 Initial conditions

The initial conditions for the flow can be based on the laboratory measurements or the analytical solutions. In most cases, the initial interface is specified as a still water with zero velocities. And hydrostatic pressure is used inside the domain.

4.6.2 Boundary conditions

Boundary conditions on impermeable solid boundary

Along a solid boundary Γ, the fluid velocity should be the same as that of the boundary itself, U_i, which is referred as no-slip boundary conditions:

$$u_i = U_i \tag{4.66}$$

However, in practical computation, the resolution of the boundary layer is only applicable when the grid is fine enough. Therefore, the free-slip boundary conditions is adopted when the fairly coarse grid is used, i.e.,

$$u_n = 0 \tag{4.67}$$

$$\frac{\partial u_t}{\partial n} = 0 \tag{4.68}$$

where u_n is the normal velocity and u_t is the tangential velocity applied on the solid boundary.

Inflow boundary conditions

At the inflow boundary, the velocity and interface displacement of the time histories should be specified based on the laboratory measurements, analytical solutions or the numerical output from other models. Special attention should be paid when the analytical solution of the linear wave is used to specify the inflow boundary condition, in which case the net mass transport in the same direction of wave propagation could result (Dean

& Dalrymple, 1991). For example, the averaged net mass flux of the linear wave during one period is to be (Dean & Dalrymple, 1991),

$$M = \frac{1}{8}\frac{\rho g H^2}{C_i} \tag{4.69}$$

where M is the averaged mass flux, H the wave height of the incident wave, and C_i the wave phase velocity at the inflow boundary.

Although the mass transport in (4.69) is of the second-order importance, it may be accumulated to a significant degree after a long time computation. To eliminate this effect, a compensation velocity is defined as:

$$u_c = \frac{M}{\rho d} \tag{4.70}$$

where d is the still water depth. By subtracting this value from the horizontal velocity of the analytical solution, the zero mass transport within one wave period is achieved and the program can run a long time given that there is no complication of the reflected waves.

Radiation boundary conditions

The radiation boundary condition is used to allow the wave going out of the computational domain without significant reflection. In this model, the radiation boundary on the east side of the computational domain is described by the following formula,

$$\frac{\partial \phi}{\partial t} + c_0 \frac{\partial \phi}{\partial x} = 0 \tag{4.71}$$

where c_0 is the phase celerity of the wave at the radiation boundary and φ denotes the wave property which could be the velocities and the interface displacement, etc..

4.7 Numerical stability

Most finite difference schemes are subject to numerical instability problem, which requires certain criteria to be satisfied. In this study, the so called von Neumann stability analysis (Jaluria and Torrance, 2003) is applied to analyze the stability conditions for the current scheme. Based the method, the following stability criteria is obtained:

$$\Delta t \le \min\left\{\frac{\alpha\Delta x}{U_{\max}}, \frac{\alpha\Delta y}{V_{\max}}, \frac{\alpha\Delta z}{W_{\max}}\right\} \tag{4.72}$$

$$\Delta t \le \min\left\{\frac{1}{2(\nu_t+\nu)}\left[\frac{1}{\frac{1}{\Delta x^2}+\frac{1}{\Delta y^2}+\frac{1}{\Delta z^2}}\right]\right\} \tag{4.73}$$

The condition (4.72) is set by the convection terms and (4.73) is by the diffusion terms. In the modeling, the time step is dynamically adjusted according to the above two conditions.

Chapter 5

Numerical Investigation of Vegetation Effect on Wave and Flow

In this chapter, the numerical model is first validated by several classical numerical examples whose results are compared with the analytical results or experimental data, or other published numerical results. After validation, the model is used to simulate the flow and wave problems with the presence of porous structures and vegetation. The results are compared with available experimental data. The full 3-D model is also used to examine the three dimensional features pertaining to tsunami waves passing through a vegetation region with a gap. Tsunami wave transformation, wave height variation within and behind vegetation region as well as the velocity field are analyzed in details to reveal the vegetation effects on the tsunami wave mitigation.

5.1 Solitary waves propagation on constant water depth

Solitary waves have been widely used in coastal engineering to simulate weakly non-linear and dispersive waves. It is usually used to represent the tsunami wave, and to study the damaging influence of the tsunami to the coasts. The solitary wave is a finite amplitude wave with the permanent shape. The nonlinearity and frequency dispersion are perfectly balanced during the wave propagation. The analytical solution for the wave profile, derived from the Boussinesq equation (Lee et al., 1982), is given by

$$\eta(x,t) = a\ \mathrm{sech}^2\left[\sqrt{\frac{3a}{4d^3}}(x-ct)\right] \tag{5.1}$$

where a is the wave amplitude and $c=\sqrt{gh(1+a/h)}$ is the wave celerity and d is still water depth.

The first numerical test is the simulation of a solitary wave propagating over constant depth. The purpose of this test is to demonstrate the robustness of VOF method on accurately tracking the free surface and to validate the inflow boundary condition for generating the incoming wave and the radiation boundary condition for absorbing the outgoing wave.

The computational domain with the length in x-direction of 100 m is discretized by a uniform 1000×1×120 (in terms of x, y and z) mesh system. The still water depth is set as h = 1.0 m. A solitary wave with the wave amplitude of 0.1 m is generated from the west inflow boundary by specifying the time history of interface displacement η and velocities u and w based on the Boussinesq analytical solution for a solitary wave (Lee et al., 1982). The time step Δt is automatically adjusted based on the maximum particle velocity in the whole domain during the computation to keep Cr = 0.3. This guarantees the practical stability as well as maintains the computational efficiency. The turbulence model is turned off and the molecular viscosity is set to zero in order to compare the numerical results to the analytical solutions derived from the potential flow, which is the assumption of solitary wave solutions.

Figure 5.1 shows the comparisons between the simulated wave profiles and the analytical solutions. It is observed that the numerical results agree with the analytical solution almost perfectly even after the propagation of about 100*h*. This test verifies the accuracy of the numerical model for tracking the free surface movement.

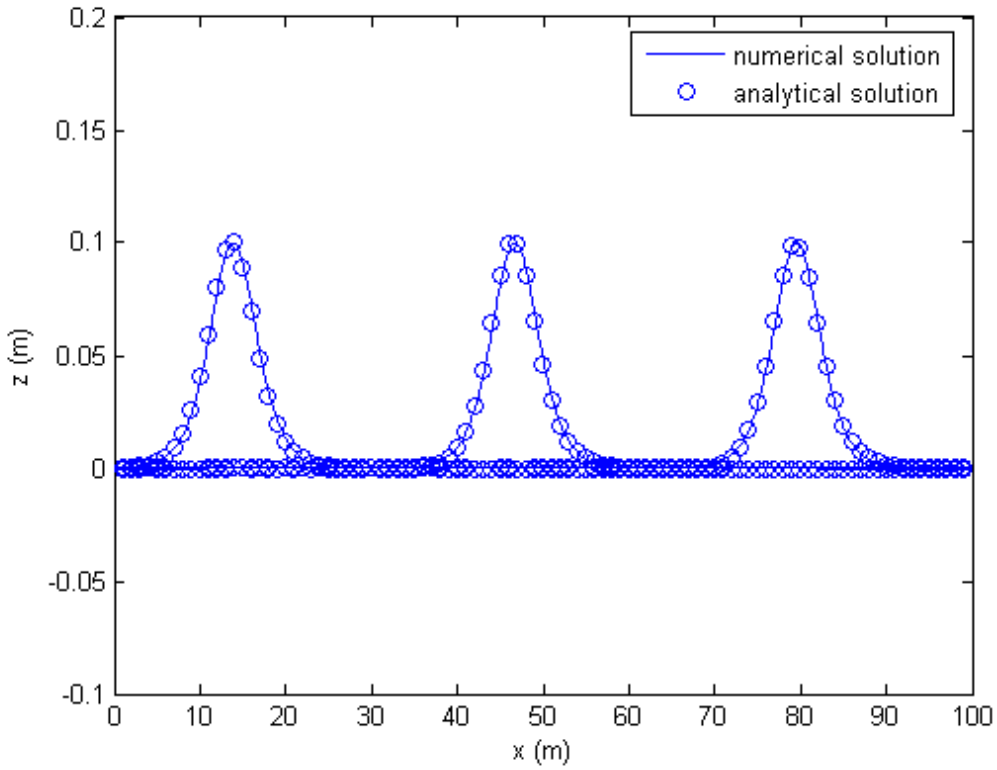

Figure 5. 1 Comparisons of interface displacement for a solitary wave propagation in a constant depth between numerical results (circles) and analytical solution (solid lines) at t = 10, 20, 30 s (from left to right).

5.2 Vortex structure behind a submerged body

Compared to free surface displacements, turbulent velocity fields are usually more challenging to model, especially when there is a strong vortex structure in the flow. From another point of view, this can be a good validation test for the applicability of turbulence model. For the problem of solitary wave propagating past a submerged bluff body, Lin(2006) presented his numerical result with σ-coordinate LES model and compared with the experimental measurements (Zhuang and Lee, 1996). This test is reconsidered to validate the current turbulence model. To simulate a rigid structure, many researchers have proposed different ways to include its effect on the flow field; for example, the curvilinear coordinate method (Lin, 2006), the immersed boundary method (Fadlum, et al., 2000), unstructured meshes (triangular or tetrahedral) (Wang and Wu, 2006) and Cartesian cut cell approaches (Qian, et al, 2003). In the current test, an elaborate way is adopted, which also provides a potential extension to the applicability of our model. Based on the definition of the porosity introduced in Chapter 2, when there is no fluid within the control volume, the porosity is zero. In this condition, the superficial average of a physical quantity is also zero. However, the whole governing equations in the superficial form still hold. Due to the disappearance of the integral discontinuities, the external forces, which arise from the pressure difference along the faces of discontinuities, will also turn to zero. Therefore, in our model, a rigid body could be simulated simply by setting zero porosity for the region covered by the structure. Meanwhile, as mentioned in the discussion of the second step of projection method in Chapter 4, the modified PPE is designed to work even under the condition of extreme porosity.

The problem setup is shown in Fig. 5.2. The parameters are summarized as follows: the still water depth is h = 0.228 m and wave height is H = 0.069 m. The rectangular obstacle has the height of h/2 = 0.114 m and length of L = 0.381 m. The time histories of horizontal and vertical velocities are measured at two points behind the obstacle, which are Point 1: 0.040 m above the bottom and 0.034 m downstream from the obstacle and Point 2: 0.017 m above Point 1. In the computation, the uniform mesh system is used with dx = 0.005 m for horizontal direction and dz = 0.002m for the vertical direction.

The comparisons between our numerical results and the experimental data obtained from Lin (2006) are made in Fig.5.3. It is found that the present numerical results compare well with the experimental data for both horizontal and vertical velocity at these two points. Compared with Lin's numerical results, generally they agree very well. Lin's results of vertical velocity at point 1 show a better agreement than the present model results. This may be because of the grid differences between the two models, where Lin used two times of horizontal grids than the present model.

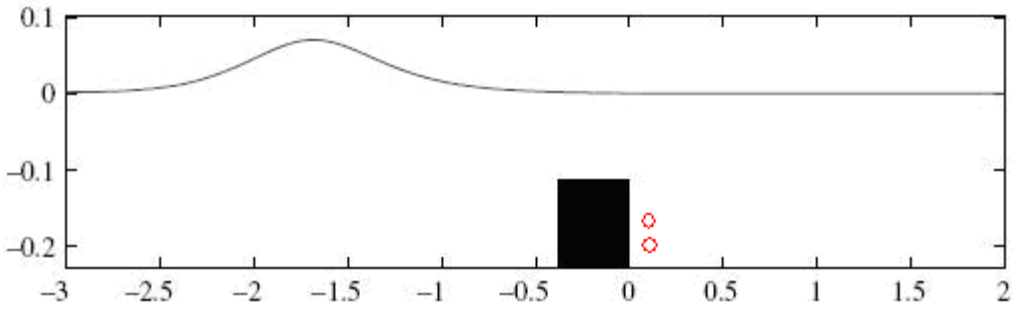

Figure 5. 2 The sketch of the model setup (in meters).

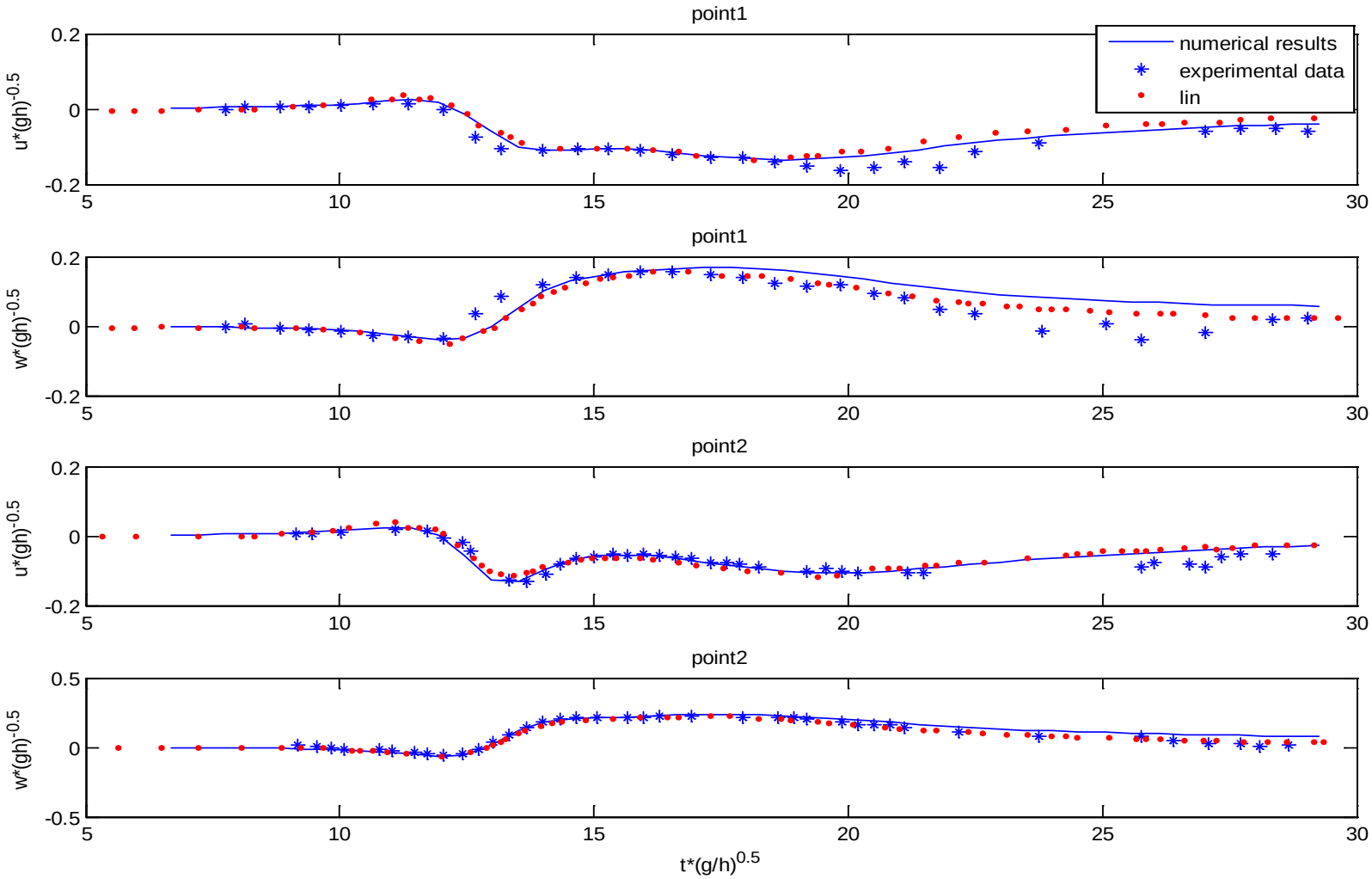

Figure 5. 3 Comparisons of the time histories of horizontal and vertical velocities at the two points behind the rectangular obstacle among the present model, Lin's model and the experience data.

5.3 Wave interaction with porous structures

In order to validate the model in simulating flows through porous medium, the experiments conducted by Liu, et al. (1999) are simulated.

The experiments by Liu et al. (1999) were conducted in a glass tank with length of 89cm, width of 44cm and height of 58cm. A porous block of 29x44x37 cm^3 was placed at the center of the tank. A gate was built 2cm away from the left edge of the porous block to hold the water in the left-side. Two porous materials were used in the experiments. One is the crushed rocks with an equivalent mean diameter of 1.59cm. The porosity of the rocks is 0.49. The other porous material is the uniform glass beads with a diameter of 0.3cm and a porosity of 0.39. The initial water depths are 23.85cm in the left-side reservoir and 2.4cm in the downstream for the case of crushed rocks, whereas they are 13.8cm and 2cm for the case of beads. The detailed setup specifications and processes of the experiments were recorded in Liu et al.(1999). In the numerical computations, a uniform grid system with dx=0.005m and dy=0.0025 is used. The initial conditions of the free surface profiles for the test are the same as the laboratory setting. As for the drag force coefficient, Karunarathna and Lin (2006) suggested a formula for the porous materials:

$$C_D = c_1 \frac{24.0}{\mathrm{Re}} + c_2 \left(\frac{3.0}{\sqrt{\mathrm{Re}}} + 0.34 \right) \left(1 + \frac{7.5}{\mathrm{KC}} \right) \tag{5.2}$$

where the values of $c_1 = 7.0$ and $c_2 = 4.0$ were recommended. By comparing Eq.(5.2) and Eq.(3.8), it can be seen that they have similar forms except for the term $24.0/\mathrm{Re}$ in Eq. (5.2), which is from the expression of drag force coefficient for a single sphere. As for the inertial force coefficient, both of the two models employ $C_M = 0.34$. Because the flow in the experiment is neither steady nor oscillatory, the KC number cannot be precisely defined. By analyzing the time history of water surface profile in the recorded images, the characteristic time scales (T, which is the time for water flowing through the porous dam) are estimated to be 1.0s and 3.0s, respectively, for the rocks and the beads.

Fig. 5.4 shows the time history of the free surface profiles of the flow past the porous block of crushed rocks within the tank. From the comparison between the numerical results and experimental data, excellent agreements are obtained, suggesting that the numerical model as well as the drag force coefficients could reproduce good results for this type of porous media. The numerical results from the current numerical model gives better results than the earlier Liu et al.'s porous flow model in the later stage of flow passage (e.g., t=1.6s, t=2.0s). Fig. 5.5 gives the comparisons for the case of beads. Again, two numerical results are close to each other and they provide reasonable comparisons to the measured data, although the comparisons are not as good as in the case of rocks. This example shows that it is possible to use the same set of empirical coefficients to simulate flows in different porous media, although further fine tuning of the model coefficients, especially the proper definition of KC for transient flows and the value of c_2, may still needed in the future based on larger amount of laboratory data. The influence of medium shape and packing pattern also needs to be further investigated.

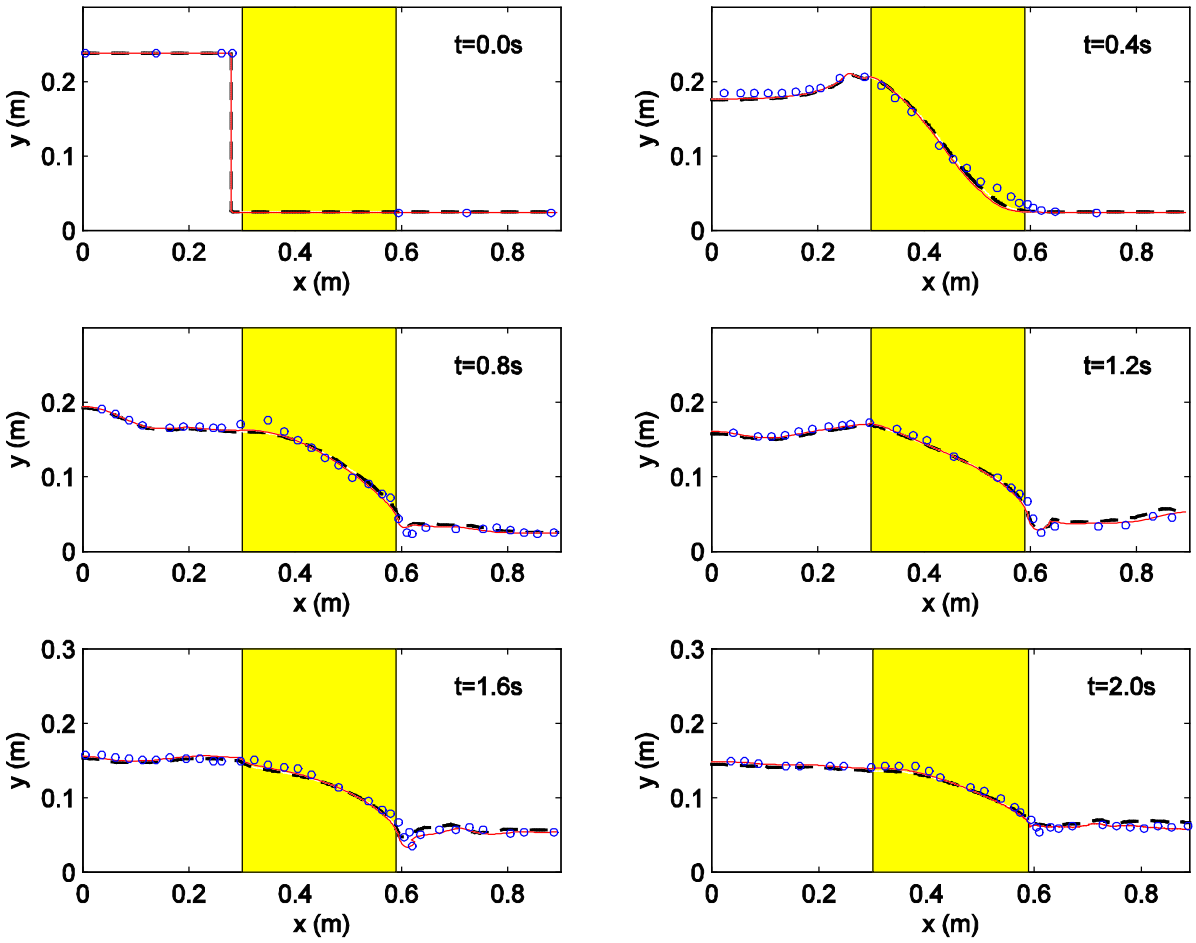

Figure 5. 4 Comparison of free surface displacement during flow passage through the porous block of crushed rocks between numerical results. (solid: current model; dashed: Liu et al., 1999a) and experimental data (circle).

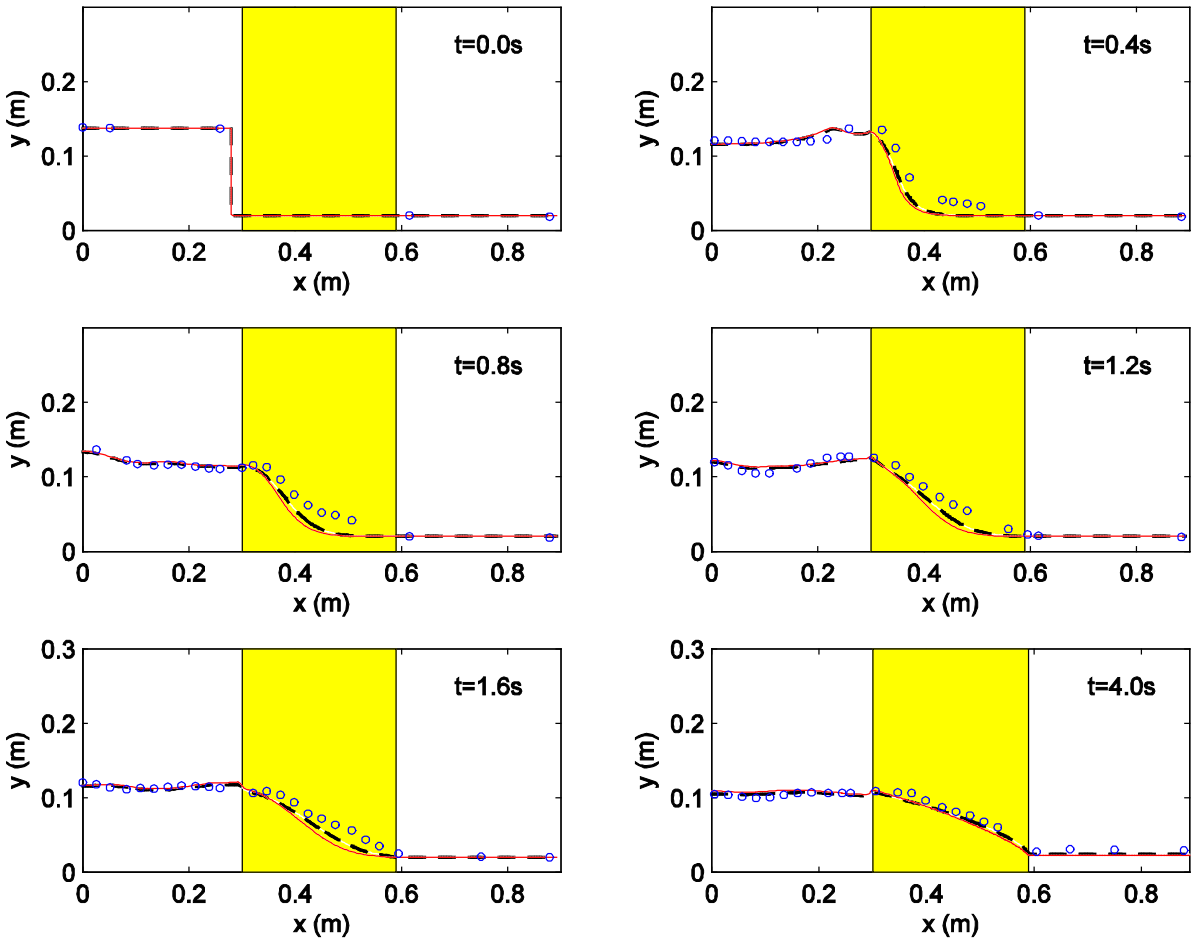

Figure 5. 5 Comparison of free surface displacement during flow passage through the porous block of beads between numerical results. (solid: current model; dashed: Liu et al., 1999a) and experimental data (circle).

5.4 Flow in straight open channel with vegetation

In order to validate the model for flow through vegetation, the experiments by Dunn et al. (1996) were used. Dunn et al. conducted several groups of channel flow experiments with vegetation in different combinations of flow conditions and distribution patterns of vegetation stems. The experiments were conducted in a laboratory flume 19.5m long, 0.91m wide and 0.61m deep under uniform flow condition. The vegetation was simulated by rigid wooden cylinders. These cylinders measured 6.4mm in diameter, and 12cm in height. The design of the experiment is shown in Fig 5.6. in this simulation, the eighth group was used. The corresponding experimental conditions were given as: flow depth=0.39m, bottom slope=0.0036, stem spacing d = 5.08cm, which is equivalent to vegetation density of 387.5 stems per m^2. The discharge is fixed at $0.18\, m^3/s$. The measurements were carried out in a circular region with diameter of 16cm centered on the centerline of the flume where the flow is fully developed and steady. In this circular region, two measurement points are placed randomly on two sides of the centerline.

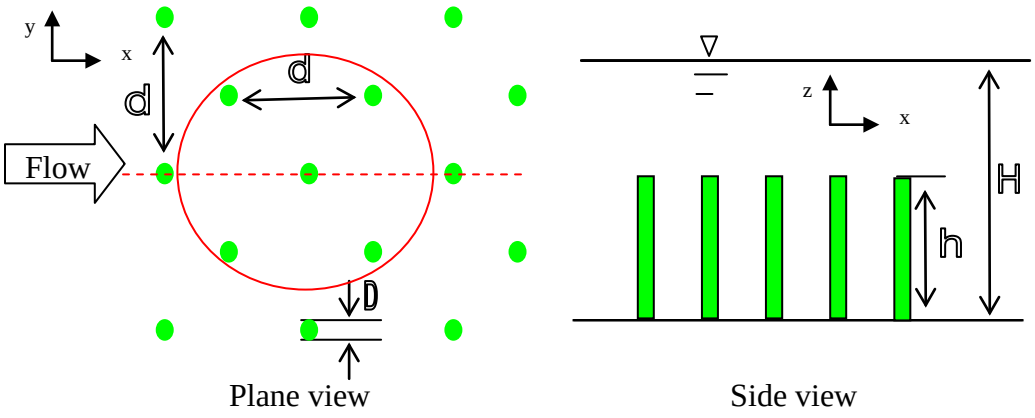

Figure 5. 6 The sketch of experimental layout. D represents the diameter of a stem of vegetation, and d is the spacing between the centers of two stems. The dashed red line is the centerline of the flume. The red circle is the measurement region in Dunn et al.'s experiments.

In the numerical test, the computational domain is 26m x 0.91m x 0.5m in x-y-z coordinate. Note that the vertical length of the computation domain is larger than water depth. The vegetation region covers the areas from 6m to 20m in streamwise direction, which is 6m away from the inlet to make the pure channel flow developed first before reaching the vegetation zone. In the modeling, the vegetation porosity is taken to be the same as the experiment, implying that the vegetation stems is in a regular pattern. The whole domain is discretized into uniform grids of 260x10x50 in x-y-z system. The cross-section for comparison is chosen at x=15m, where the flow within the vegetation is shown to be already fully developed by the comparison of numerical results with nearby cross-sections.

Before the vegetated case is modeled, the turbulent channel flow without vegetation is simulated first under the same numerical settings introduced above. Classically, the vertical distribution of streamwise velocities in the region out of the viscous sublayer of the turbulent open channel flow is broadly recognized by the "log-law" formula (Nezu, and Nakagawa, 1993), which can be expressed as:

$$u^+ = \frac{1}{\kappa}\ln(y^+) + A \tag{5.3}$$

where A is a constant of integration, $u^+ = u/u_*$ and $y^+ = yu_*/v$, in which u_* is the friction velocity. κ is the von Karman constant.

The computed vertical distribution of horizontal velocity is compared with the analytical formulae, Eq. (5.3). The comparison shown in Fig. 5.7 presents a good agreement between the numerical results and the analytical results. These reasonable numerical results provide a necessary base for the possible good prediction of vegetated flow.

Fig. 5.8 compares the computed horizontal velocity and turbulent kinetic energy at the vegetation region with the experimental data. On the whole, the agreement is good. In the two plots, the black dashed lines indicate the height of the vegetation. The velocity distribution shows that the velocity does not follow the log-law distribution. Around the top of vegetation, there is an inflection point where a strong shear layer is produced due to the drag discontinuities. The turbulent kinetic energy (TKE) reaches the maximum around the top of vegetation. From the top of the vegetation to the free surface and the

bottom, the TKE gradually decreases. The obvious strong shear layer indicates that intense turbulent mixing and transport of momentum occurs at the interface of the vegetation and the upper flow layers. Recently, Ghisalberti and Nepf (2006) argued that this shear flow with submerged vegetation renders Kelvin-Helmholtz instability through their experimental analysis.

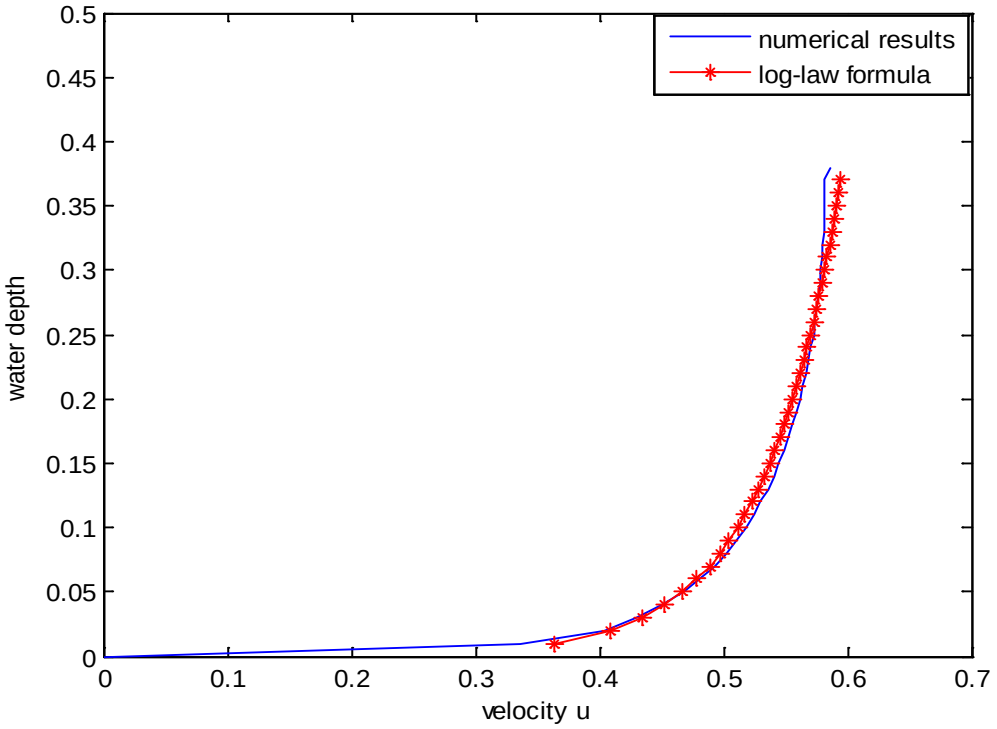

Figure 5. 7 Comparison of horizontal velocity between numerical results and analytical results for turbulent open channel flow.

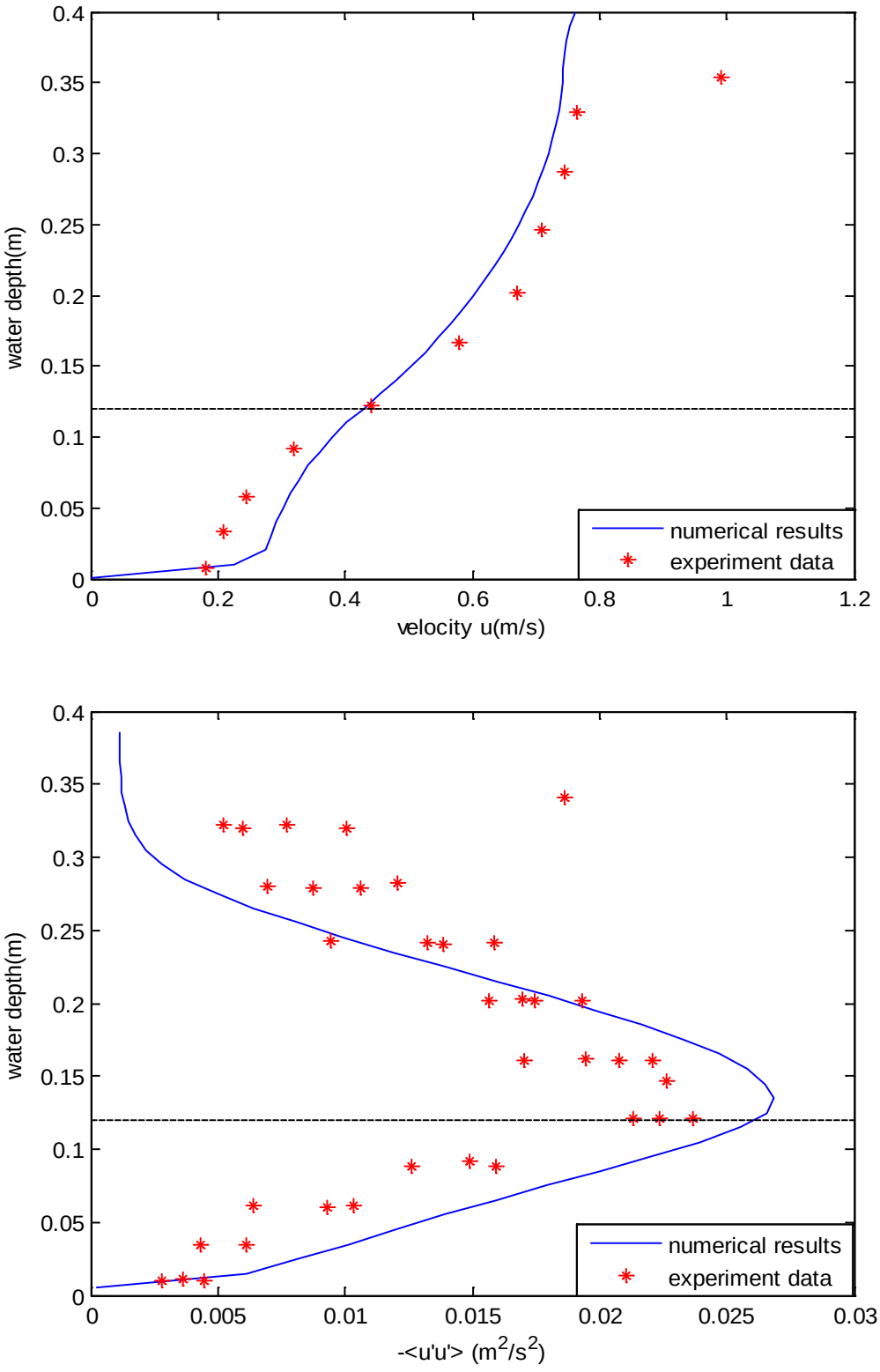

Figure 5. 8 Comparison of horizontal velocity and downstream component of TKE between numerical results and experimental data for vegetated open channel flow.

5.5 Regular periodic waves propagating past vegetation

A simulation of the wave experiments described in chapter 3 is also conducted. As indicated in Fig 3.5, 3 locations were chosen for monitoring within the vegetation region. The wave heights calculated from the recorded free surface elevation at these three locations are compared with numerical results. The numerical model covers a domain 8m in length and 0.45m in height, with a still water depth of 0.35m. Two wave frequencies, 1.2 Hz and 1.0 Hz, are simulated and compared with experiments. Based on the measurements of wave gauges in front of vegetation region, initial wave height was 1.46cm and 1.58cm respectively.

To generate linear sine wave, special attention should be paid when the analytical solution of the linear wave is used to specify the inflow boundary condition. The inflow boundary condition was prescribed using the method presented in section 4.6.2.

Fig. 5.9 shows a snapshot of the 1.2Hz sinusoidal wave train at the time t=10s from the starting time. It can be seen that the wave form and the total mass are conserved during the propagation. Once the vegetation region is incorporated in the domain (from 2.9m to 4.7m, corresponding to the experiments), the wave energy is dissipated with distance as anticipated. The wave height distributions along the vegetation region are plotted and compared with experimental points in Fig. 5.10. Reasonable agreements are observed, suggesting that the numerical model reproduce the wave dissipation process. The decrease in wave heights in both cases are over 10% of incident wave over a short distance of 1.8m, demonstrating the effectiveness of wave dissipation by the vegetation. In the Fig. 5.10, wave height dissipations in the vegetation of two other porosities (0.96 and 0.94) are also compared with the experimental condition. It can be seen that with the increase of the vegetation density (i.e. decrease of porosity), the dissipation is enhanced.

In Chapter 3, the empirical formula for Cd is proposed. However, due to the narrow range of wave periods and other wave characteristics in the experiments, the accuracy of the formula for other wave conditions has not been fully tested. To test the sensitivity of the variation of wave heights within vegetation region to the change of drag force coefficient, the drag coefficient is tuned by artificially increasing and decreasing α_2 of Eq. 3.10. All the other conditions are kept the same as in the above simulation. In this case, the three

values of α_2, 0.5, 7.5 and 75, correspond to the drag force coefficients of 1.2, 1.9 and 8.9 respectively.

Fig. 5.11 shows the dissipations of wave height within the vegetation region for a 1.2Hz wave. As expected, the wave height dissipation is enhanced with the increase of α_2 and hence the drag force coefficient. However, comparing with Fig. 5.10, it can be seen that the effect of drag force coefficient on the wave height dissipation is much smaller than the effect of porosity. With this comparison, it may be concluded that the porosity of vegetation, which is equivalent to the spacing of vegetation, plays a more significant role on the coastal wave dissipation. This also suggests that in the numerical simulation of wave height dissipation, the inaccuracy of drag force coefficient caused by using our formula may not change the conclusion on the wave dissipation in different vegetation conditions. Therefore, in the following simulation of large wave or nonlinear waves, the proposed formula, Eq. (3.10), will be employed. On the other hand, it should be noted that even though comparing with vegetation porosity, the drag force coefficient has smaller effect, it doesn't mean that the vegetation drag force coefficient has no effect. For the same porosity, a different drag force coefficient, corresponding to different vegetation distribution pattern or a different species of vegetation could still have various effects on the wave height dissipation. Furthermore, as stated in the chapter 2, the coefficients also have an impact on the energy budget equation. A different drag force coefficient corresponding to different skin conditions of vegetation stems may significantly influence the turbulent field.

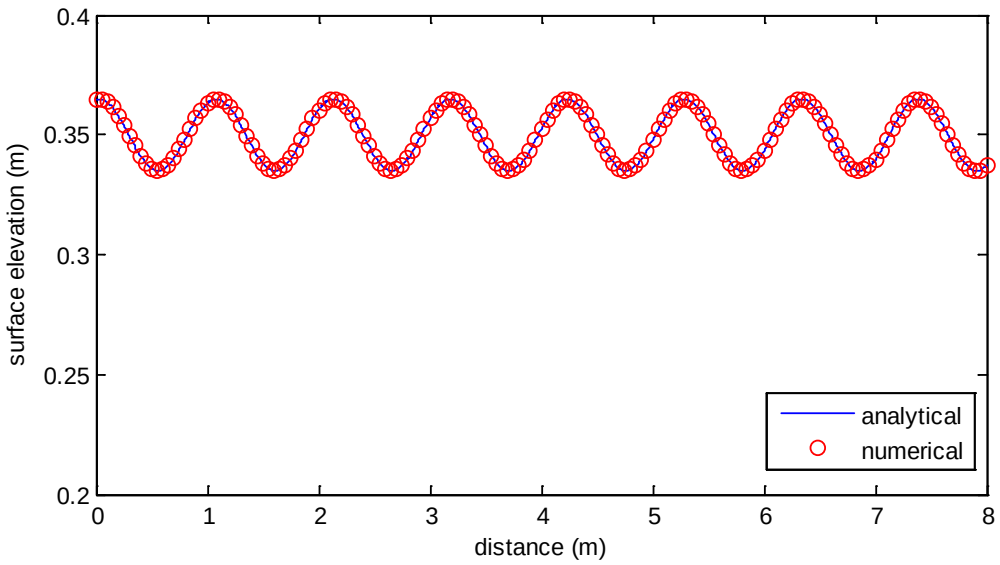

Figure 5. 9 Snapshot of pure sine wave train of 1.2Hz in the domain at the time t=10s from the starting time.

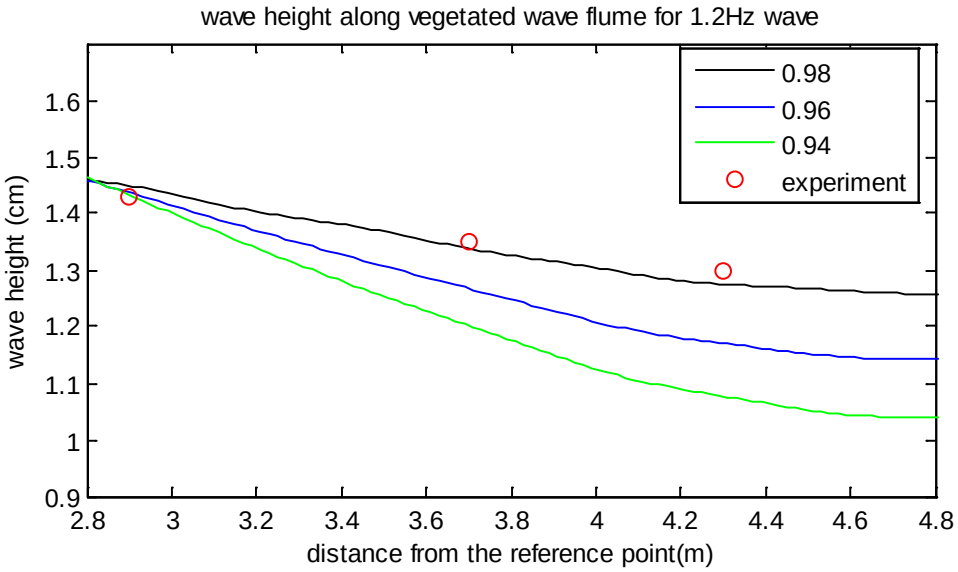

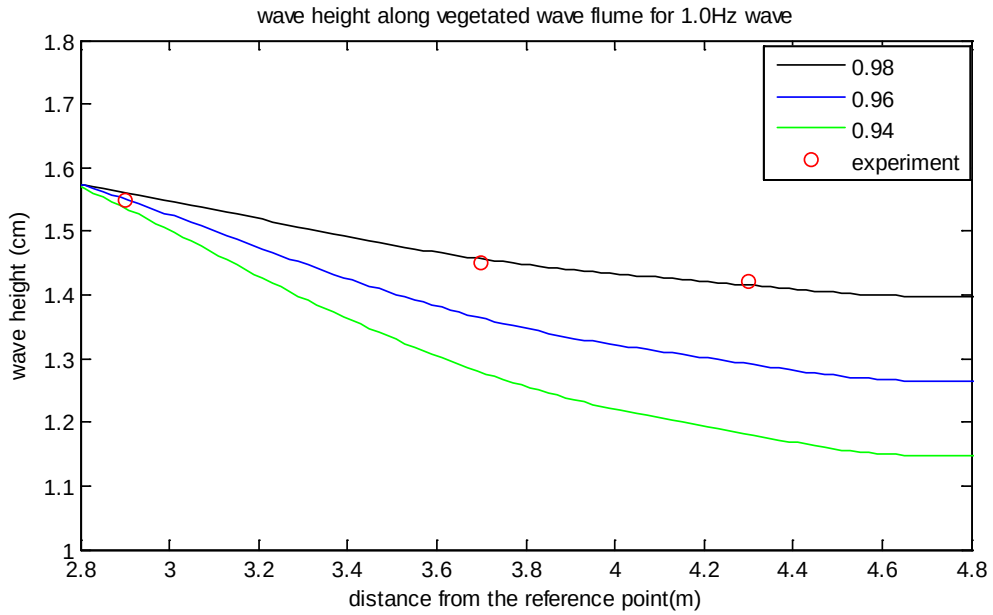

Figure 5. 10 Comparison of wave height along the flume between numerical results and experimental data for vegetated region.

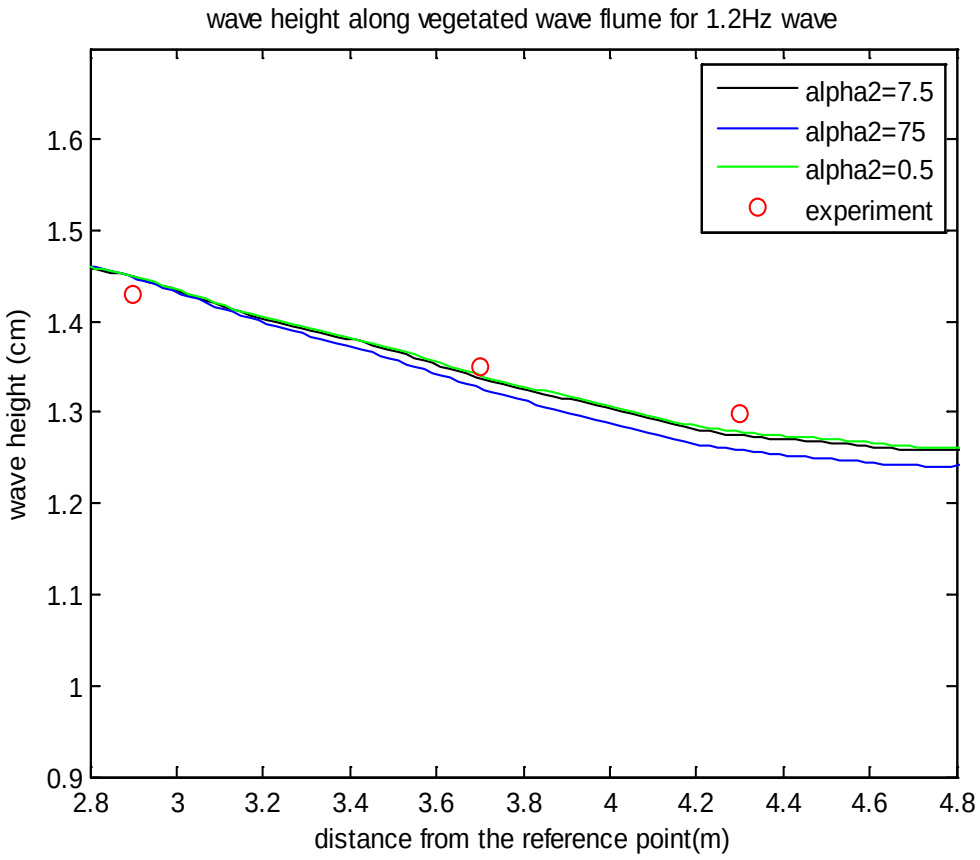

Figure 5. 11 Effect of α_2 on wave height dissipation along the vegetation region under the same porosity (0.98).

5.6 Non-breaking solitary wave runup and rundown on steep slope

To investigate the characteristics of the run-up of waves on the vegetated sloping beach, firstly, it's important to make sure that the numerical model can accurately predict the runup of the wave on the non-vegetated slope. Lin et al. (1999) presented a series of numerical simulations studying the wave runup and rundown on a sloping beach based on available experiments. The experiments are numerically repeated to validate the model performance on modeling the real scenario of solitary wave (tsunami) runup. In the experiments, the slope has an angle of 30^0 and s=tan(30^0)=0.577. The still water depth is h=0.16m and solitary wave has the wave height H=0.0027m. The particle image velocimetry (PIV) was used to determine the particle velocity and the free surface displacement. The numerical calculations are performed in a domain of $4.99m \le x \le 6.99m$ and $-0.16m \le z \le 0.11m$. This domain is discretized into a 125×45 uniform grid system. The time step is dynamically adjusted. The velocities u and w and free surface displacement η are specified at the left boundary. According to Lin et al. (1999), for nonbreaking waves, the energy dissipation due to viscous and turbulence effects is negligible. Therefore, in this case, the turbulence model is switched off and the molecular viscosity is set to be zero.

The runup and rundown processes of the nonbreaking solitary wave propagating on the sloping beach are shown in the Fig. 5.12-5.16. Fig. 5.12 shows the snapshot of the wave climbing up the slope (t=6.38). The fluid particles on the slope move in the direction parallel to the slope. At the runup tongue, the particles have the maximum velocity. The velocity becomes smaller away from the shoreline. The horizontal velocity component in constant water depth is nearly uniform throughout the depth (Fig. 5.12(b)). In general, the numerical predictions agree well with the experimental measurements. The difference between the experimental data and the numerical results are possibly from several reasons. One is because the used grid system is a little coarse under the consideration of efficiency. Another possible reason comes from the experimental inaccuracy, which was pointed by Lin.

Fig. 5.13-5.16 show the velocity distributions and the surface profiles when the wave almost reaches its highest run-up point and run down on the slope until it is approaching the lowest rundown point. Larger vertical variation in the horizontal velocity is observed in Fig. 5.15 and 5.16. The evolution of surface profiles and velocity fields indicates that the velocity near the surface during the run-down process is higher. This seems reasonable considering that the free surface moves faster than the bottom water which is retarded by the bottom friction. On the whole, the numerical results generally agree well with the experimental data. In this exercise, the slope is simulated by setting the porosity of the corresponding region to be 0. The snapshots have demonstrated that the treatment can model the impermeable structure well.

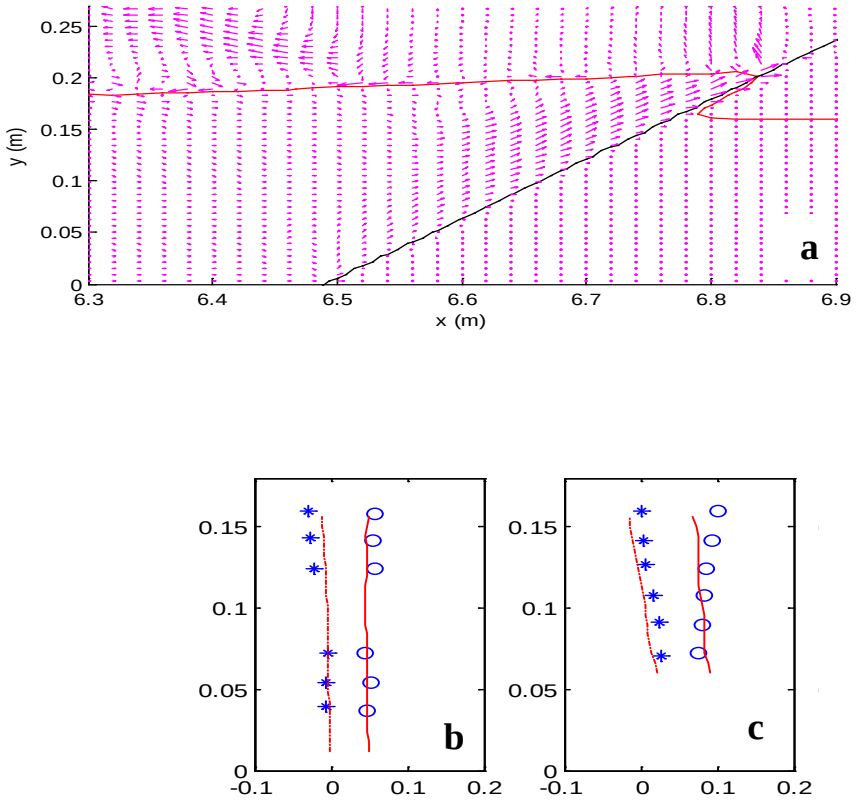

Figure 5. 12 Solitary Wave Runup at t=6.38s. (a) the surface profile and the velocity distribution for the numerical results . and the comparison of the vertical profile of velocities at (b) x=6.397m (c) x=6.556m (—and -- are u and v by numerical model, 。 and * are u and v by experiment)

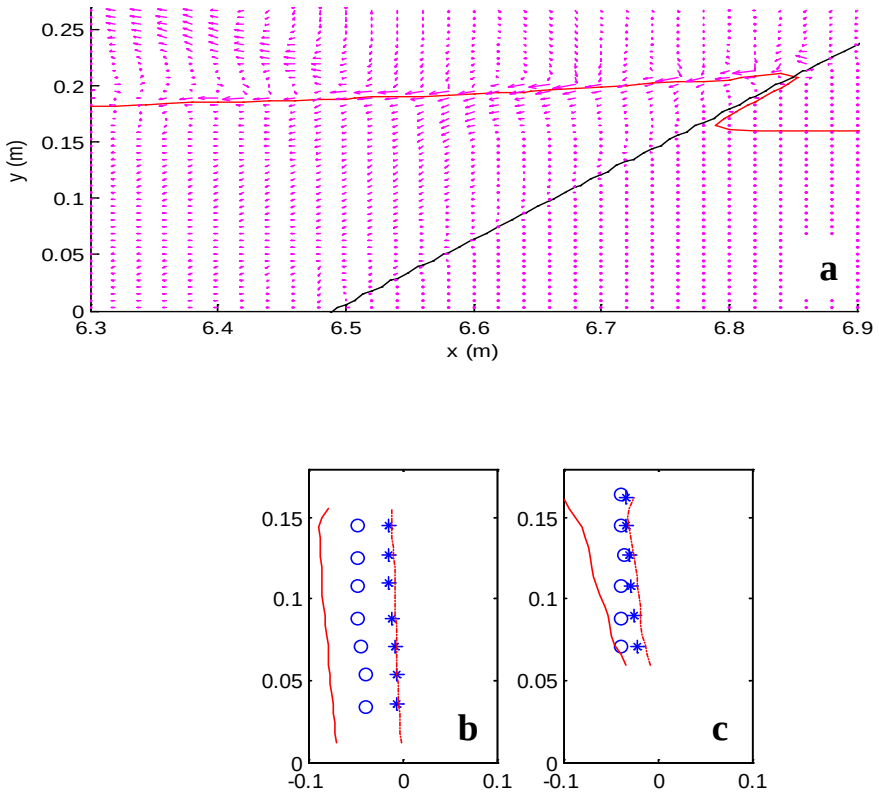

Figure 5. 13 Solitary Wave Runup at t=6.58s. (a) the surface profile and the velocity distribution for the numerical results . and the comparison of the vertical profile of velocities at (b) x=6.397m (c) x=6.556m (—and -- are u and v by numerical model, 。and * are u and v by experiment)

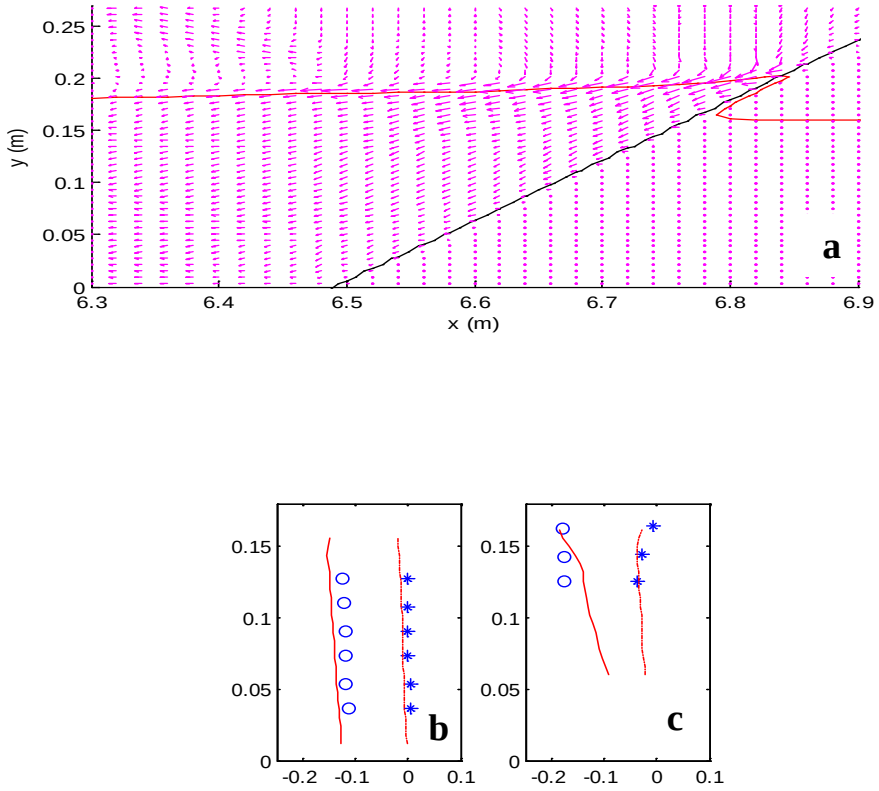

Figure 5. 14 Solitary Wave Runup at t=6.78s. (a) the surface profile and the velocity distribution for the numerical results . and the comparison of the vertical profile of velocities at (b) x=6.397m (c) x=6.556m (—and -- are u and v by numerical model, 。 and * are u and v by experiment)

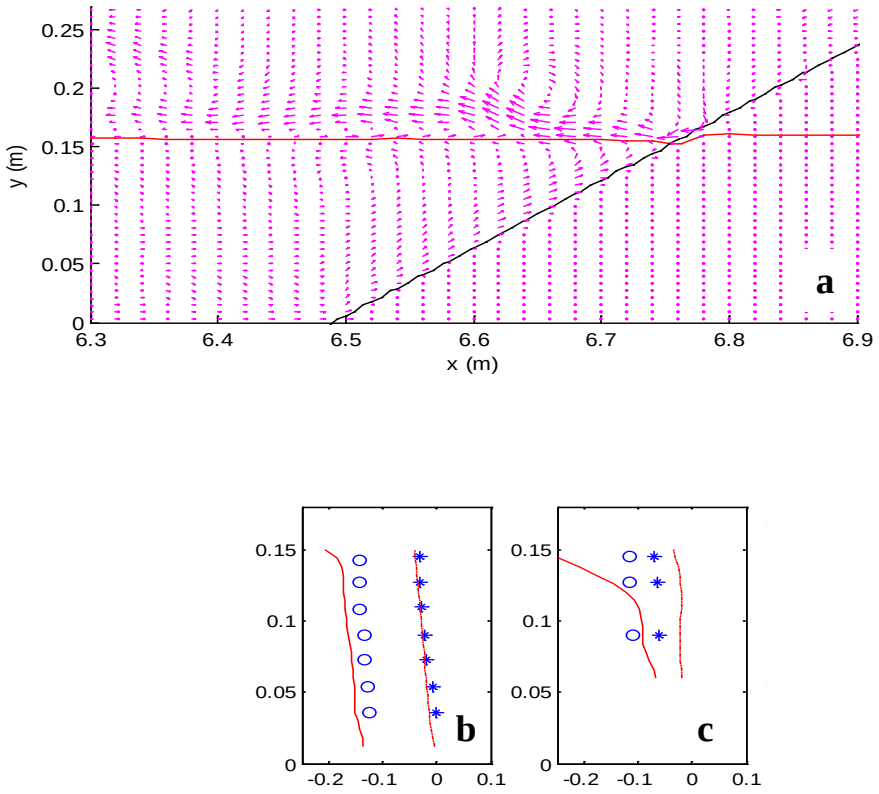

Figure 5. 15 Solitary Wave Runup at t=7.18s. (a) the surface profile and the velocity distribution for the numerical results . and the comparison of the vertical profile of velocities at (b) x=6.397m (c) x=6.556m (—and -- are u and v by numerical model, 。 and * are u and v by experiment)

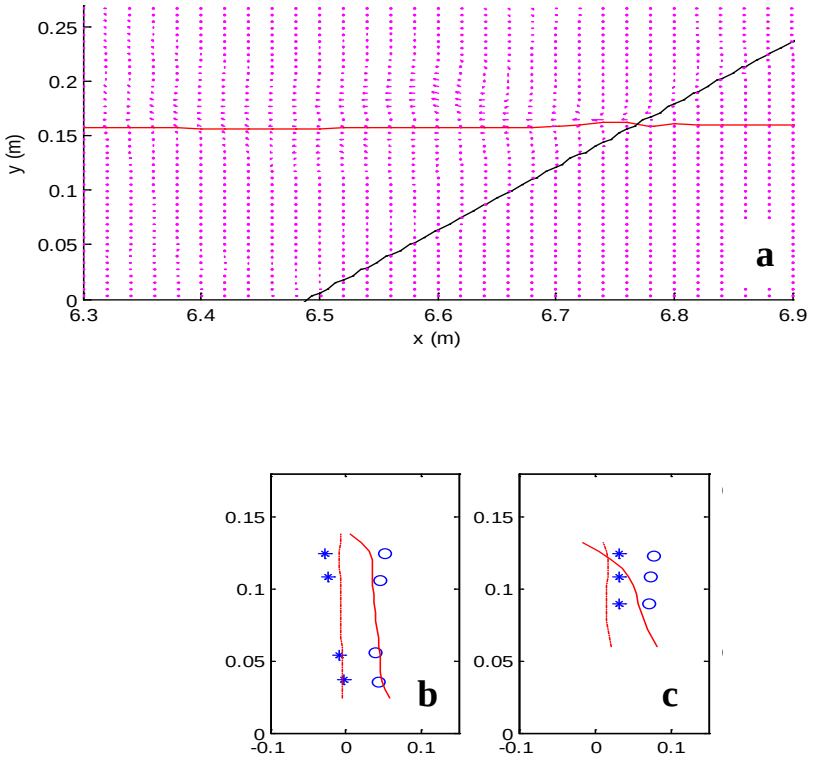

Figure 5. 16 Solitary Wave Runup at t=7.58s. (a) the surface profile and the velocity distribution for the numerical results . and the comparison of the vertical profile of velocities at (b) x=6.397m (c) x=6.556m (—and -- are u and v by numerical model, 。 and * are u and v by experiment)

5.7 Comparison of the wave runup on vegetated and non-vegetated slopes

For this simulation, the computational domain is shown in the top figure of Fig. 5.17. The domain covers 900m horizontally and 35m vertically. It is discretized by a uniform grid system with dx=5m and dz=0.5m after grid sensitivity test. The water depth is set at d=20m, while a solitary wave has a wave height of 6m, that is, H/d=0.3. Another difference with the previous nonbreaking solitary wave case is that the slope of the beach is s=1/20, which is commonly used in the numerical or experimental wave breaking studies. The vegetation is artificially planted on the slope from x=250m to x=500m with the canopy of them above the initial solitary wave crest.

In this study, the proposed drag force coefficient formula, Eq. (3.10) is used to calculate the external drag force. Even though the formula is proposed based on experiments with sinusoidal waves, the drag force coefficient is related with the characteristics of wave currents, such as Re, which is a common parameter for both sinusoidal and solitary waves. Hence, the formula is applicable in solitary wave conditions as well. For the inertial force coefficient, due to the lack of data or analytical formula, a constant value of 1.7 is adopted from Harada and Imamura (2005).

According to Lin et al. (1999), the wave would break during its run-up process on this mild slope with large wave steepness. In Fig 5.17, the red and black lines represent the free surface with and without vegetation effect respectively. In the second plot of Fig. 5.17, the solitary wave hasn’t propagated to the vegetation region, therefore the two solitary wave profiles coincide with each other. When the wave approaches the vegetation, the wave height becomes higher and steeper, while in the non-vegetated situation, the wave holds its profile to propagate. Subsequently, for the vegetated case, the wave height decreases and a large part of the wave is reflected seaward by the vegetation. On the other hand, without vegetation, the wave front gradually becomes steep and evolves to a roller until breaking. In the last plot, it can be seen that the tsunami wave generates a large run-up height and inundation region when there is no vegetation on the slope. On the contrary, the wave run-up is substantially reduced on the vegetated

slope. This comparison clearly demonstrates the effect of vegetation on reflecting and attenuating the wave energy and reducing the coastal inundation during the wave runup on the beach.

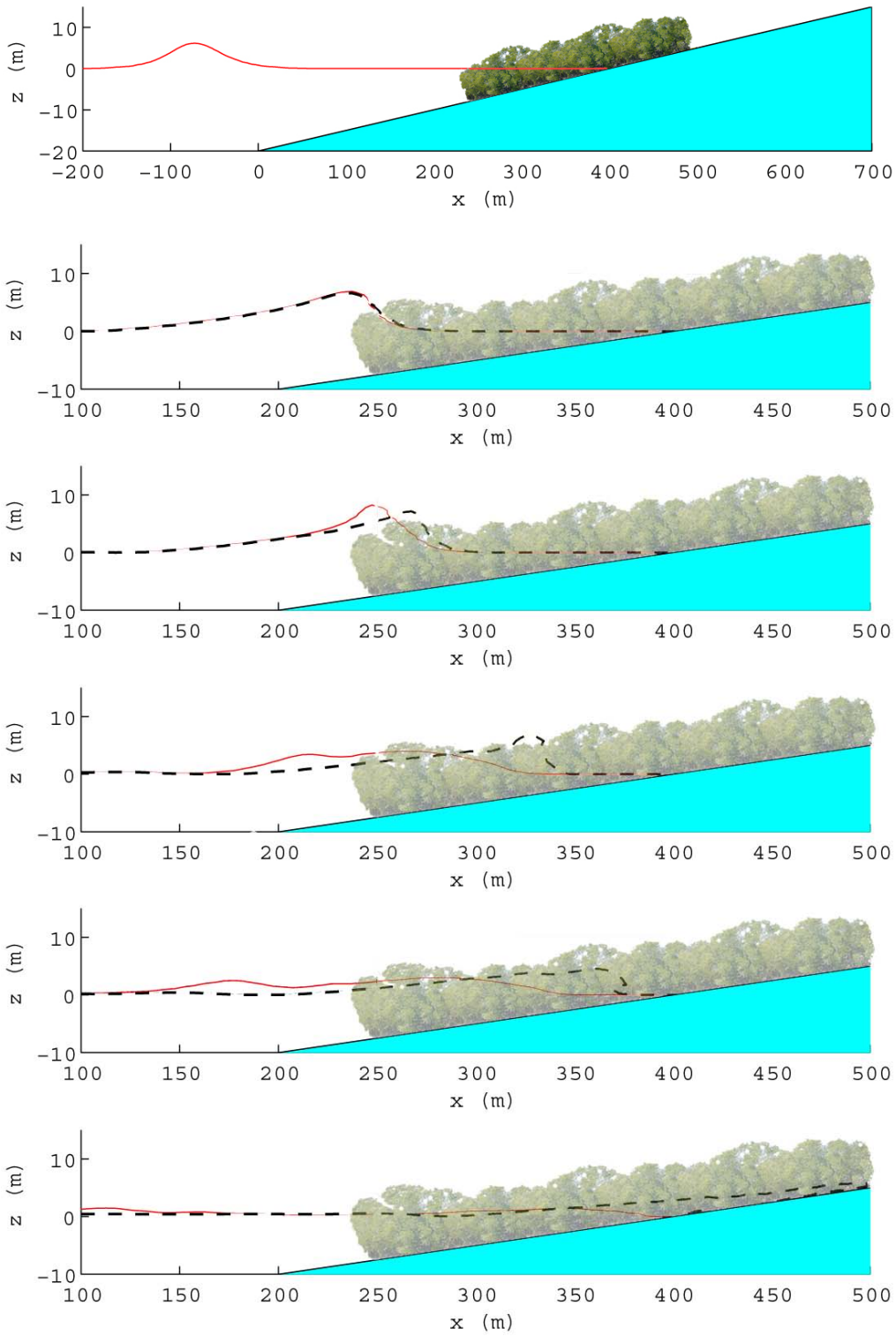

Figure 5. 17 Comparison of solitary wave run-up on a beach with (solid line) and without (dashed line) vegetation.top figure for problem setup of *H*=6m, *h*=20m, and *s*=1/20; the vegetation domain is from 250m to 500m and the vegetation has the mean stem diameter of 0.05m and the volume density of 1%.

To quantify the dissipation effect of vegetation on the solitary wave shown in Fig. 5.17, solitary waves propagating past a vegetated region are further simulated. In the simulation, in order to separate the vegetation effect from wave shoaling effect, a flat bottom is used in the simulation. The set-up of the problem is the same as the validation case in section 5.1, except that a region of non-submerged vegetation is incorporated into the model with various porosity and width, as shown in Fig. 5.18. The width of the vegetation region is given as 10m and 20m, while the porosity is set as 0.98 (the same as the experiment in chapter 3) and 0.96. At P1 and P2, upstream and downstream of the vegetation, the time histories of free surface elevations are recorded and analyzed.

Fig. 5.19 show that decrease of the porosity and increase of the width of the vegetation can both increase the dissipation of wave height. An interesting result is that doubling the density of the vegetation (equivalent to decrease the porosity from 0.98 to 0.96) has the same effect on reducing wave height as doubling the width of vegetation. In the current simulation, since the porosity is large, it could be assumed that each individual vegetation stem experiences the same wave force as the others and doesn't change with the spacing of vegetation stems. As a result, the doubling of the vegetation density and the doubling of vegetation width induce the same vegetation effect on wave height dissipation, provided that the bottom roughness and other energy dissipation factors are ignored. With the current set-up, the solitary wave height is reduced up to 50% after passing through 20m vegetated region with porosity of 0.96.

Fig. 5.20 shows the time histories of the free surface elevation at the reference point upstream of the vegetation. For different scenarios, the first leading waves coincided in the figure are the incident solitary wave before approaching the vegetation. After about 20s, the fluctuating free surfaces represent the reflected waves by the vegetation. It can be seen that in the reflected waves, the magnitude of the first peak mainly depends on the vegetation porosity. The lower the porosity is, the larger the initial reflection. However, after the initial reflection, the following reflections depend largely on the width of the vegetation. For 20m vegetation with porosity of 0.98, even thought the initial reflection is nearly half of the initial reflection of the vegetation with 0.96-porosity, the subsequent reflections are continuously larger than the 10m 0.96-prosity case. As a result, almost the

same energy is reflected, and the dissipated wave heights downstream of the vegetation are the same.

These results provide a general frame for the coastal forests planting. To make an expected effect, the vegetation spacing and width should be compromised considering the botanical characteristics of different species of vegetation.

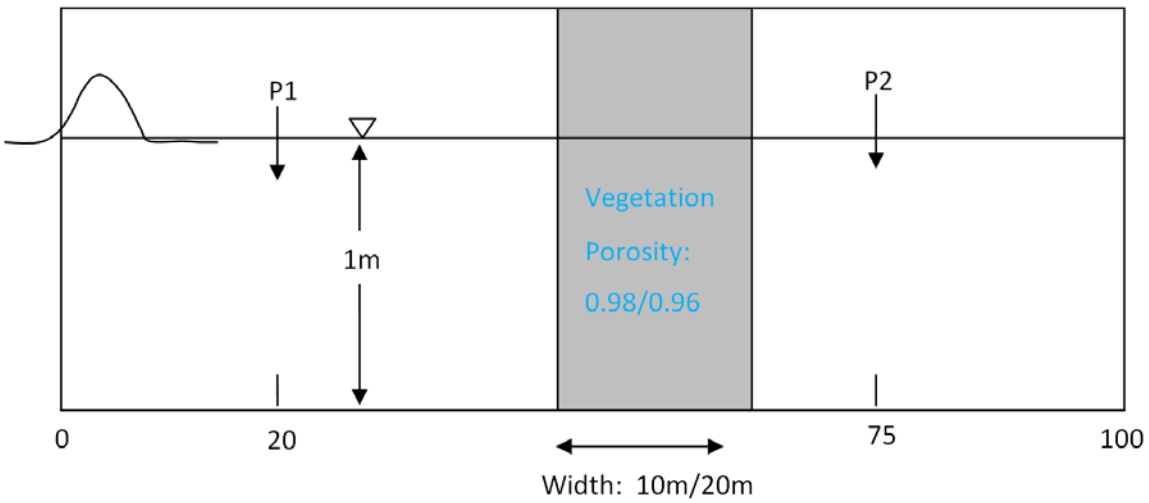

Figure 5. 18 Sketch of the numerical simulation set-up..

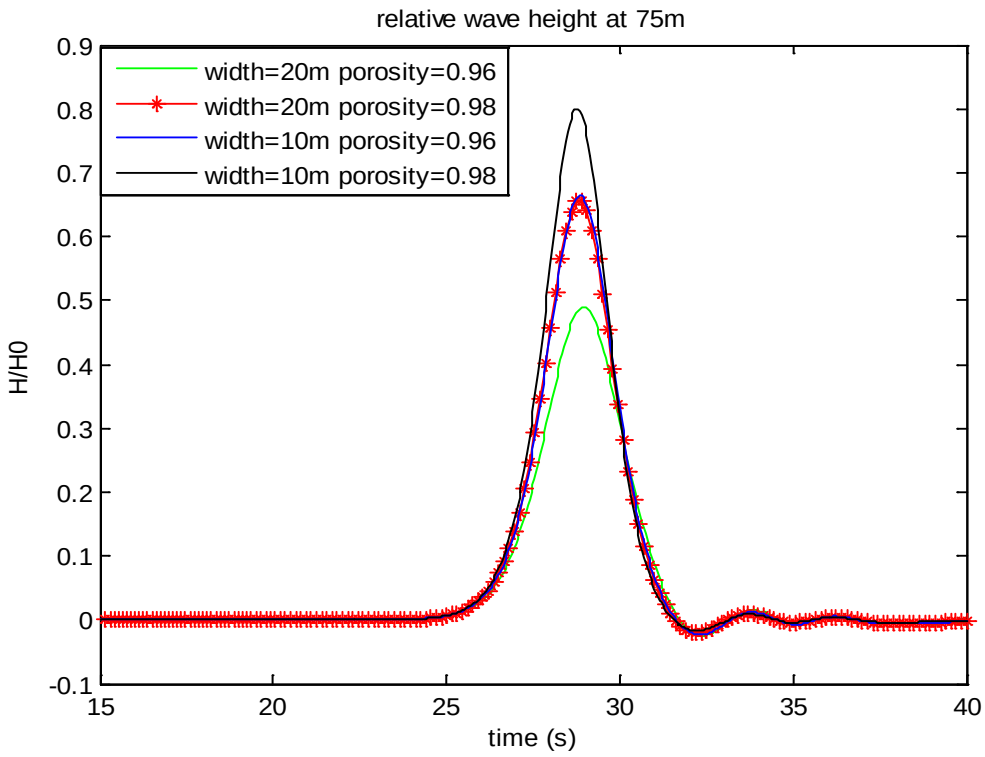

Figure 5. 19 Time series of the normalized wave height at 75m.

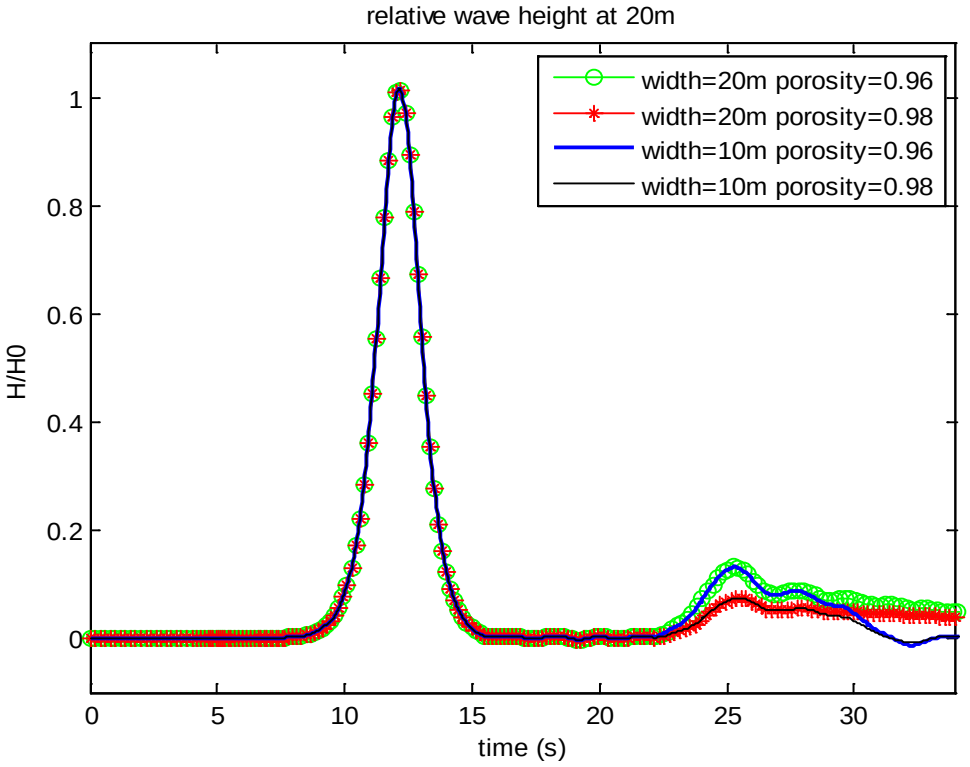

Figure 5. 20 Time series of the normalized wave height at 20m.

5.8 Solitary wave passing through the gap within vegetation on a slope

Corals and mangroves are generally believed to be effective in coastal protection against tsunami waves (Fernando et al., 2005). However, the results of the 2004 Sumatra Tsunami Survey in Sri Lanka suggests that the patchiness of the coral could lead to water jetting through the gaps and enhance the wave heights and water inundation (Liu et al., 2005). Motivated by such evidence, Fernando et al. (2008) experimentally investigated the transformation of a solitary wave in the presence of a porous barrier. In their experiments, the array of solid vertical rods was used to act as a submerged porous barrier. From another point of view, these cylinders can be viewed as submerged rigid vegetation on the sloped coastal region like the experiment conducted in this thesis.

Fernando et al.'s experiment was carried out in a 32 x 0.8 x 1.8 m long wave tank. The waves propagate first on a flat bottom of about 1m from the wave maker and then on a 1/24 uniform slope. Three different solitary wave heights were generated in the experiments, which corresponded to three wave maker stroke distances. Three sets of experiments were conducted for each wave paddle stroke, which were solitary wave run-up on the slope without vegetation, with the vegetation covering the entire width, and with the vegetation having a gap of width of 6.5cm in the middle. The last one mimicked the local removal of corals or vegetation. In the experiments, the rods were of diameter 1.25cm and height 20cm. Two packing densities of rods, 20% and 50%, were used, which are equivalent to the porosity of 80% and 50%. The velocities were measured at the selected locations in the lee of the barrier by ADV. The measurements were made at the same locations in the absence of porous structure, with the uniform barrier and with the barrier having a streamwise gap. Fig. 5.21 schematizes the layout of the experiment and the measurement locations. The details of the experimental set-up and procedure can be found in Fernando, et al. (2008).

In the current simulation, the initial wave height at the inflow boundary is tuned to obtain the wave height at the measurement point on the slope in the experiment. An initial solitary wave height of 5.6 cm yields good agreement. The case with a packing

density of 50% is modeled in current numerical study. The numerical domain covers 32m x 0.8m x 1.8m, the same as the dimensions of experimental wave tank. The horizontal and vertical resolutions of the grids are set as 0.1m and 0.01m respectively after grid sensitivity test. The vertical distributions of horizontal velocities are compared with the experimental measurements in Fig. 5.22. The numerical results agree well with the experimental data. The slight deviation may be attributed to the unreported bottom roughness and the inaccurate evaluation of drag force coefficient. Even though we have argued that the major factor of vegetation affecting the wave height dissipation is the porosity, the drag force coefficient and inertial force coefficient can influence the flow structure in a relatively small degree. Fig. 5.22 shows that the horizontal velocities after passing through the vegetation region are largely reduced comparing with the velocities on the slope without vegetation. However, the velocities in the gap clearly increase by about 10%, suggesting that a water jet is flushing out through the gap.

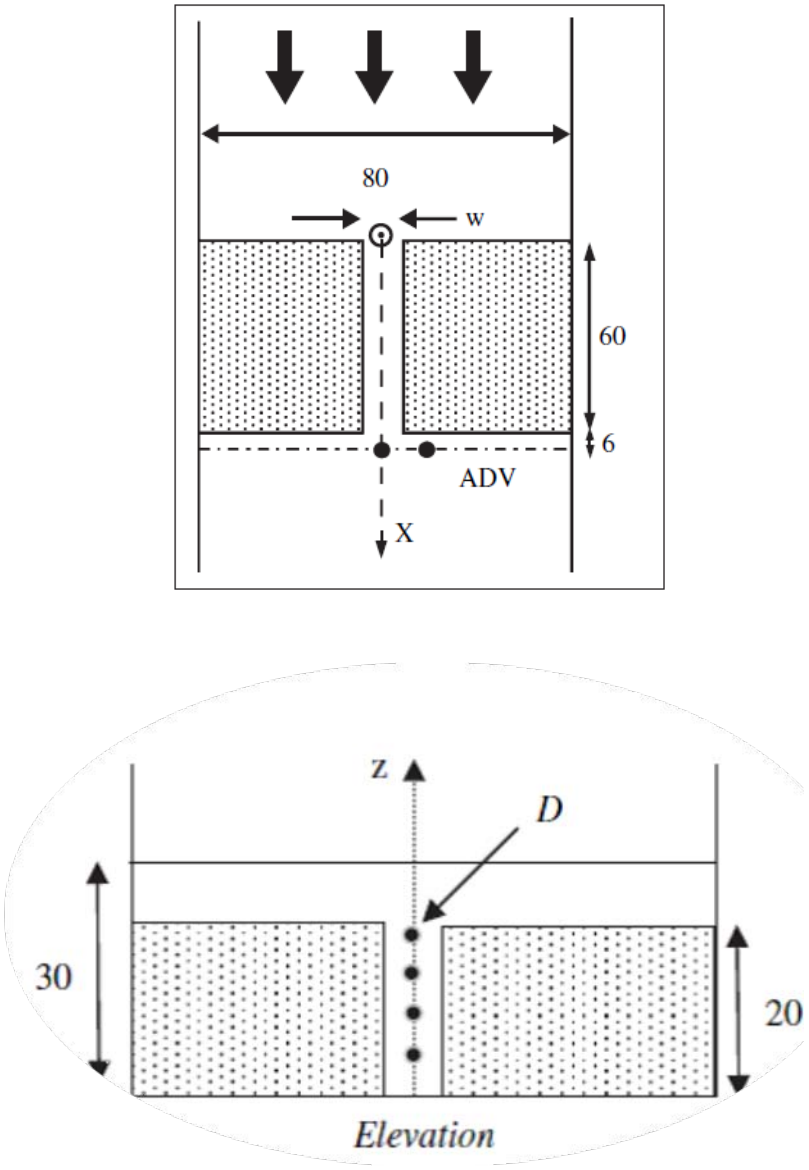

Figure 5. 21 Sketch of the experimental set-up (in cm). (a) top-view (b) side-view. The dots in (b) indicate the locations of the ADV measurement. (Fernando et al. 2008)

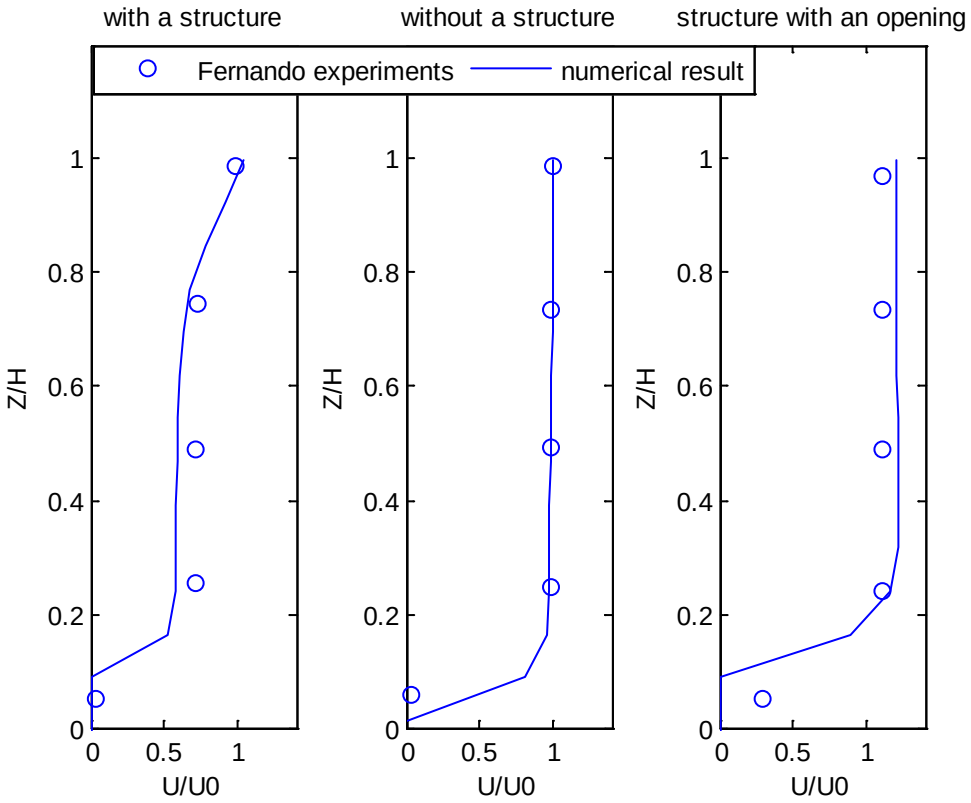

Figure 5. 22 The comparison of the horizontal velocities in the lee of the vegetation between the numerical results and experimental measurements. H is the height of the rods, and U0 is the measured maximum mean velocity at the ADV location without vegetation.

5.9 Three dimensional study of solitary wave passing two patchy vegetation regions on a flat bottom

In section 5.8, the tsunami wave propagation on a vegetated slope with or without a gap is simulated and compared with the experimental records. Both numerical and experimental results show that the vegetation on the slope can effectively reduce the wave velocity, and hence the potential run-up damage. They also show that the gap with the vegetation can amplify the local flow during the passage of a solitary wave, which leads to adverse impacts on coastal assets. However, practically, it is common to have some gaps disconnecting the coastal forests. To quantify the sensitivity of the amplification of the wave height and velocity to the size of the gap, a series of numerical tests are designed. The configuration of the simulated scenario is as shown in Fig. 5.23. The computational domain is 100m x 100m x 6m in the x-y-z coordinate, discretizing into 300 x 30 x 100 non-uniform grids with small grid size near the free surface and the gap region. The still water depth is 4.0m, with the designed incident solitary wave height set at 1.5m. This is to simulate the near-coast shallow water region where the slope is gentle and large areas of mangrove grow. To be within range of the mangrove environment, the porosity is set as 0.9 or 0.85, with stem diameter of 20cm. In the transverse direction, there is a gap without vegetation with spacing of 6m, 10m and 15m respectively. Six reference points are chosen to record the surface elevations on the middle line of the vegetation, and in the lee side of the vegetation as shown in Fig. 5.23.

Fig. 5.24 shows the time histories of wave height at six reference points for the case of porosity=0.9, width of vegetation in x direction = 10m, and spacing of gap=10m. Due to the symmetry of the reference points as shown in Fig. 5.23, wave heights at P1 and P3, P4 and P6 are coincides in Fig. 5.24. Fig. 5.24 also shows that the wave heights of solitary wave passing through the gap (P2, P5) are larger than the other position at the same stream-wise position. Within the vegetation, the arrival time of the wave peaks are delayed due to the velocity reduction by vegetation. In the lee side of the vegetation, the wave heights are largely reduced compared with the wave height within the gap.

Considering the symmetry of wave gauges, in the following discussion, only P1, P2, P4 and P5 will be analyzed.

Fig. 5.25-5.28 show the comparison of relative wave heights normalized by the incoming wave height H0 among different vegetation conditions for porosity of 0.90. At P1 (Fig. 5.25), the wave height within the 20m-wide vegetation region is reduced larger than within 10m-wide vegetation region. This is consistent with our expectation. Additionally, the spacing of the gap doesn't affect the wave height dissipation in the vegetation region because the reference point P1 is chosen far enough from the gap. Fig. 5.26 shows that, at P2 which is within the gap, the wave height is larger when the spacing of the gap is larger, suggesting that the larger the spacing of the gap is, the smaller the impact of the vegetation on the wave height at the center of the gap. However, due to the larger dissipation of wave height in the condition of wider vegetation, the wave heights in the gap of 20m-wide scenarios are systematically lower than the corresponding ones in 10m-wide scenarios. In 10m-wide scenarios, the wave height at P2 is slightly amplified when the spacing is 10m or 15m. This is because in 10m-wide scenarios, P2 is near to the leading edge of the vegetation region where the dissipation of vegetation is not large yet. Especially in larger spacing situation, wave height at P2 may not be affected by the vegetation, and hence may remain the incident wave height. On the other hand, due to the blockage of vegetation, some of the blocked water may converge into the gap, resulting in the amplified wave height at P2. Fig. 5.27 and 5.28 show the wave heights at P4 and P5 downstream of the vegetation. In general, at P4 and P5, the wave heights are further dissipated after propagating through the whole vegetation region. P4 and P5 present similar patterns with their upstream points P1 and P2. Since the width of vegetation in 20m-wide scenario is two times the 10m-wide scenario, the reduced wave height in the former scenario is about one half of the reduced wave height in the latter one. This is consistent with the results shown in section 5.7. At P5, the curves disperse largely, confirming the distribution of peak wave height for different scenarios discussed for P2. However, at P5, even for the least influenced scenario (width=10m, spacing=15m), the wave height is reduced by more than 15%. It is caused by the surrounding lower wave height (say, at P4). The higher wave at P5 has to spread water mass and energy to its neighbor waves, resulting in a gradually reduction of wave height in the center of the gap.

Furthermore, at P5, tailing waves are generated after the peak waves which may result in secondary impact in tsunami event. Fig. 5.29-5.32 show the similar results but for the porosity of 0.85. The figures show that the dissipation of wave energy increases with the increase of the vegetated zone. The size of gap has little effect on the transformation of the wave heights within the vegetation and in the lee side of it. However, the wave height variation along the gap shows that the smaller the spacing of the gap, the larger the wave height reduction. The reason may be that with the increase of the spacing of the gap, the effect of the side vegetation become small on the passing wave within the gap. The larger the spacing of the gap is, the smaller the wave height dissipation in the center of the gap.

Fig. 5.33-5.34 show the comparison of the relative wave height at different positions in the same run. They have similar pattern as Fig. 5.24. The interesting point is to examine relative magnitudes of the wave heights for P5 (black line) in each sub-plot of Fig. 5.33 and 5.34, which again shows the effect of the spacing of the gap on the wave heights in the downstream of the gap.

Fig. 5.35 shows the snapshots of the surface elevation in the computation domain for the case of vegetation covering from 50m to 70m and gap in y-direction ranging from 42.5m to 57.5m. Firstly, it can be seen that the wave propagates faster in the gap, which can also be seen in Fig. 5.33 and 5.34. The main reason for the decrease of the wave height in the gap may be due to the spreading of the water mass of the leading wave. A part of water blocked by the vegetation is reflected and propagates offshore. Fig. 5.36 and Fig. 5.37 show the horizontal velocity fields and magnitude contours at the height close to the still water depth. Since this is a typical shallow water problem, velocity profiles are typically uniform. The plots in Fig. 5.36 and Fig. 5.37 correspond to the snapshots of surface elevation in Fig. 5.35. Fig. 5.36 shows that when the tsunami wave approach vegetation, some water converge into the gap, which could amplify the wave height in the gap as discussed above. Fig. 5.37 indicates that when the wave enters the gap, a strong jet flushes out, and the front vegetation facing the incoming waves suffers relatively higher backward flow and the vegetation next to the gap experiences the largest shear force. These characteristics should be considered when designing a zone of coastal forests to protect the assets on the coasts. For example, the front vegetation facing the incident waves should be stiffer than the inner vegetation. Along the coast, the gap of vegetation

is usually connected with traffic roads. Additional coastal facilities (e.g. breakwaters) should be designed in front of the gap to protect the assets along the gap. However, the costs could be substantially reduced by only build breakwaters for the region having a vegetation gap.

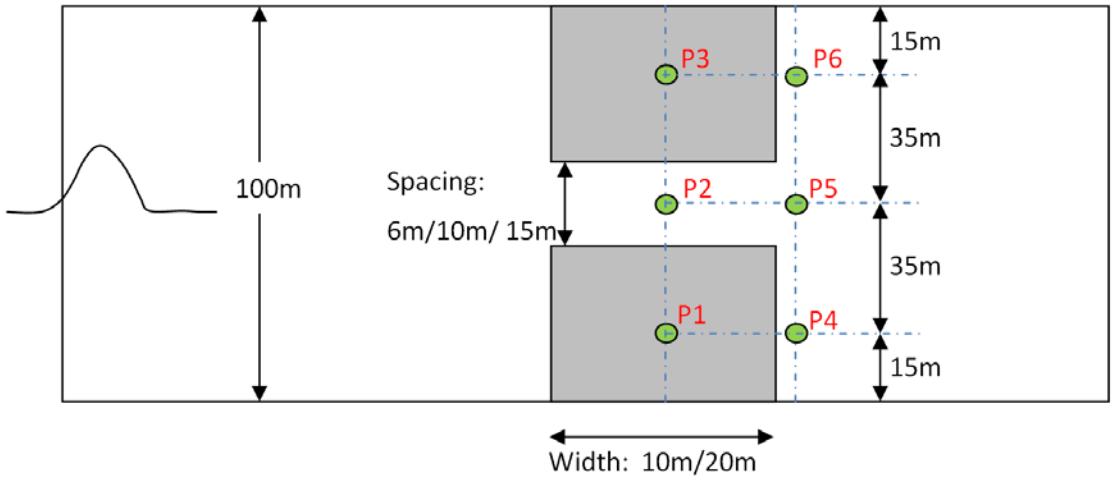

Figure 5. 23 The top-view of the layout of the numerical experiments.

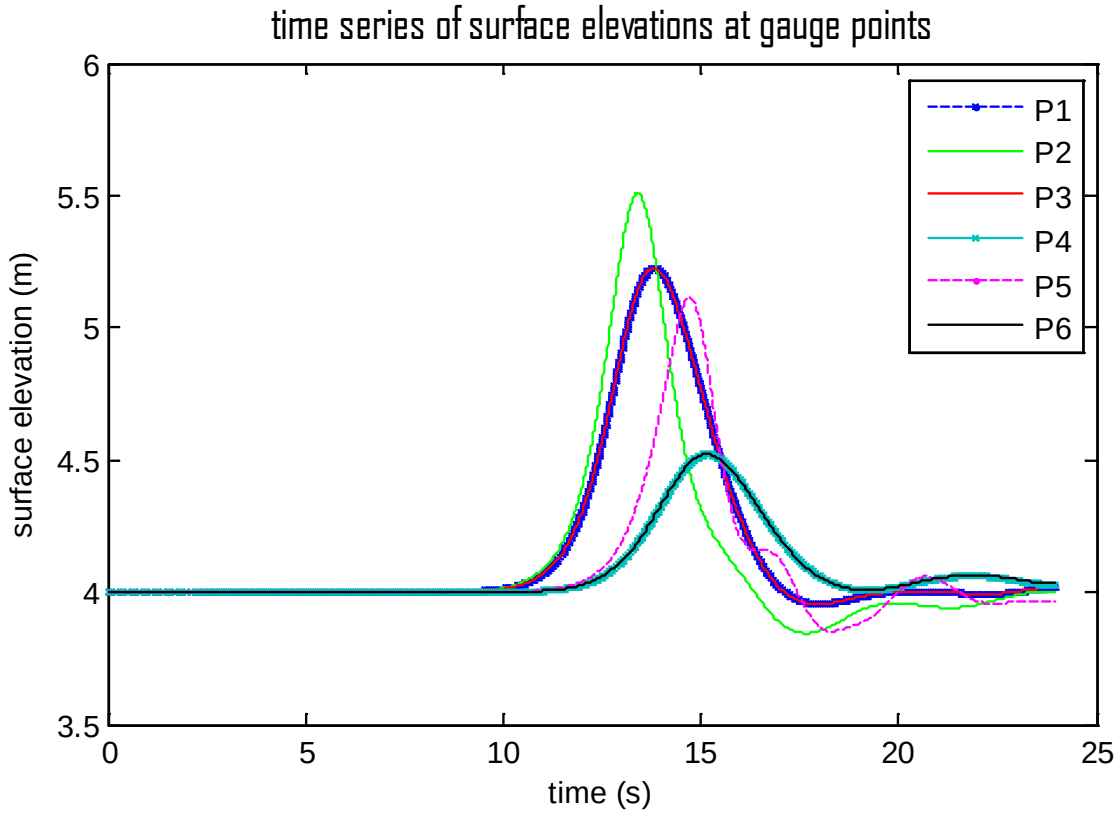

Figure 5. 24 the time histories of water level at the six gauge positions for the vegetation condition of porosity= 0.90, length=10m, gap spacing = 10m.

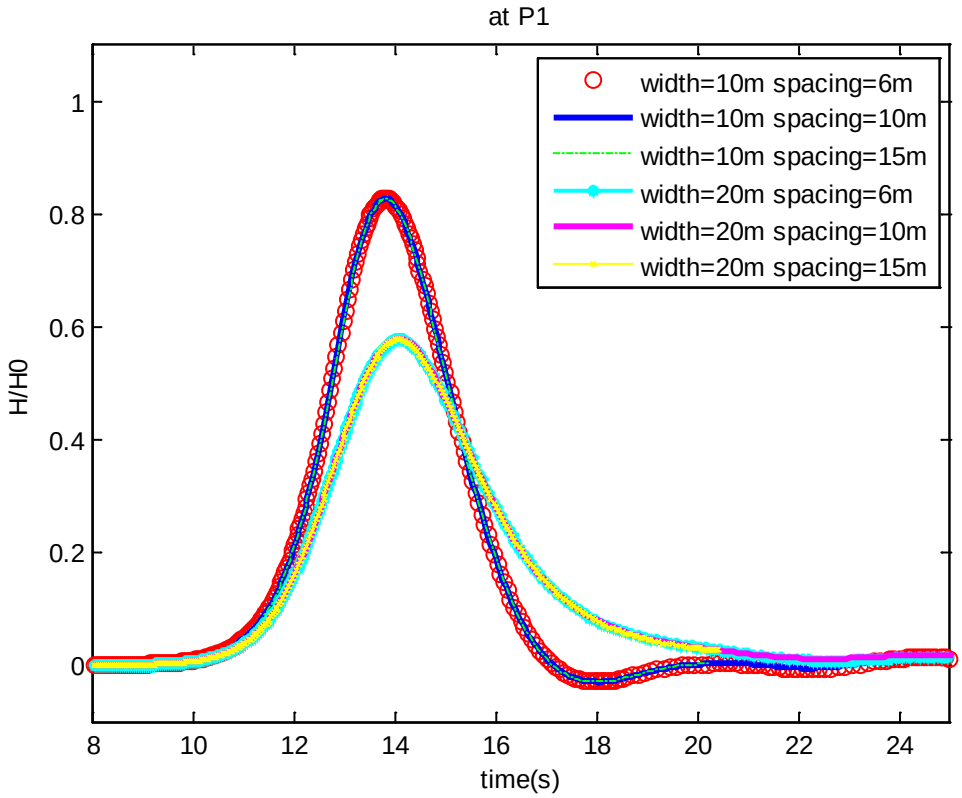

Figure 5. 25 the time histories of relative wave height at P1 for different vegetation conditions with porosity= 0.90.

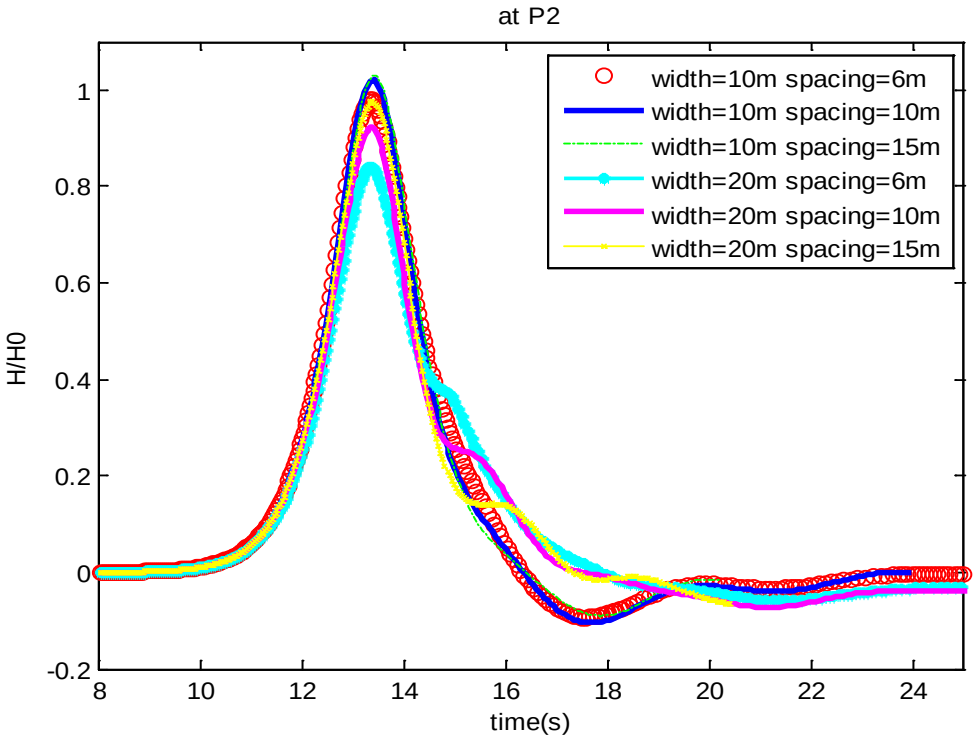

Figure 5. 26 the time histories of relative wave height at P2 for different vegetation conditions with porosity= 0.90.

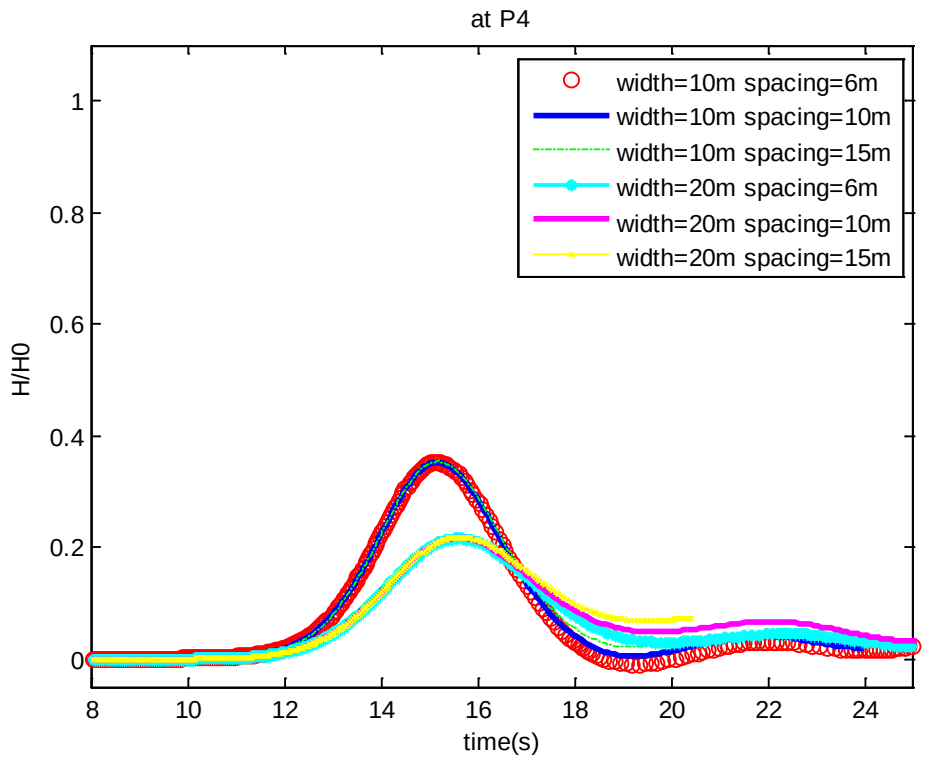

Figure 5. 27 the time histories of relative wave height at P4 for different vegetation conditions with porosity= 0.90.

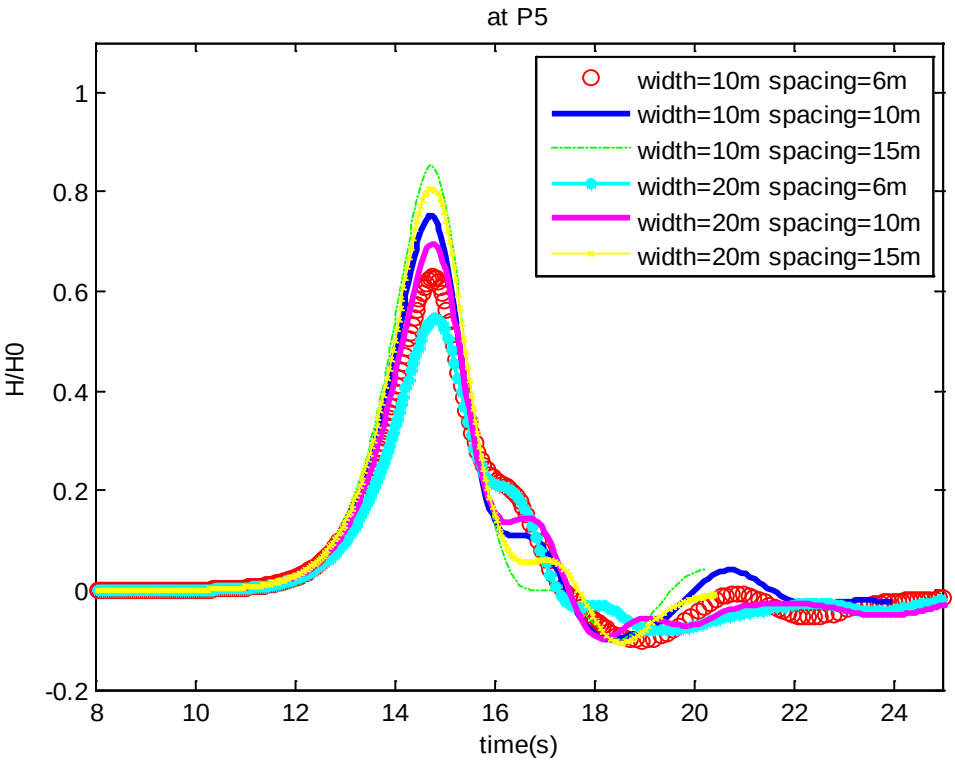

Figure 5. 28 the time histories of relative wave height at P5 for different vegetation conditions with porosity= 0.90.

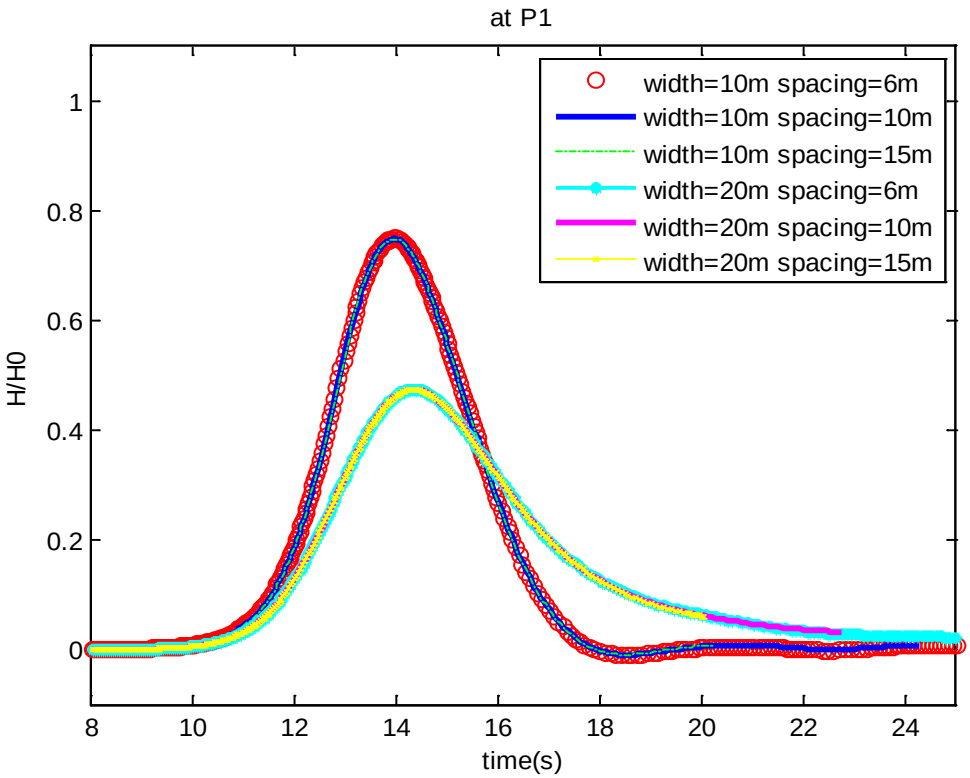

Figure 5. 29 the time histories of relative wave height at P1 for different vegetation conditions with porosity= 0.85.

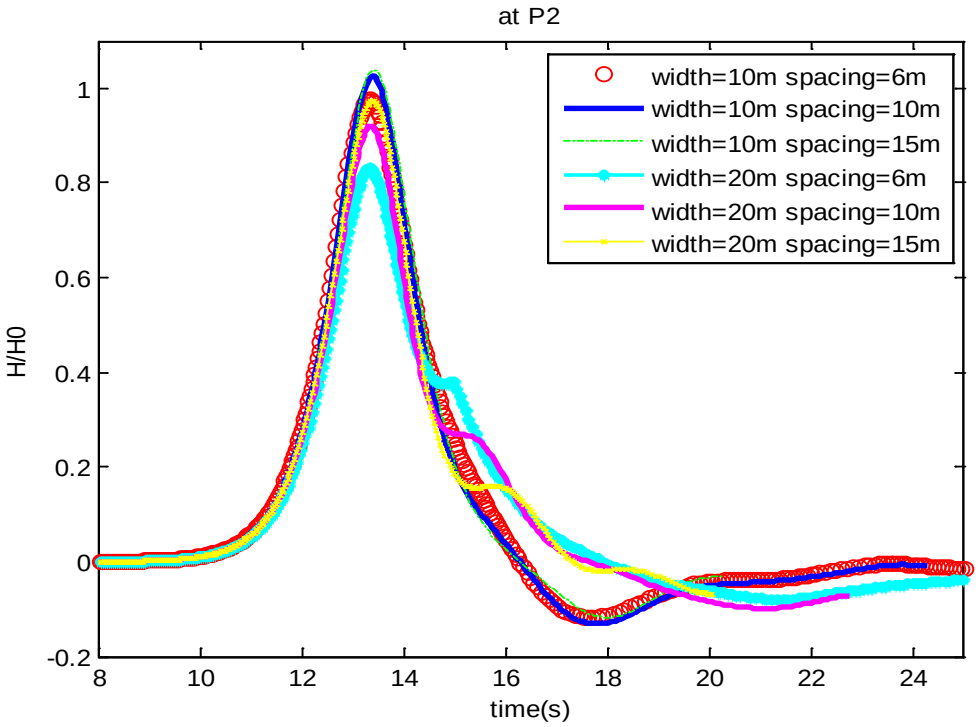

Figure 5. 30 the time histories of relative wave height at P2 for different vegetation conditions with porosity= 0.85.

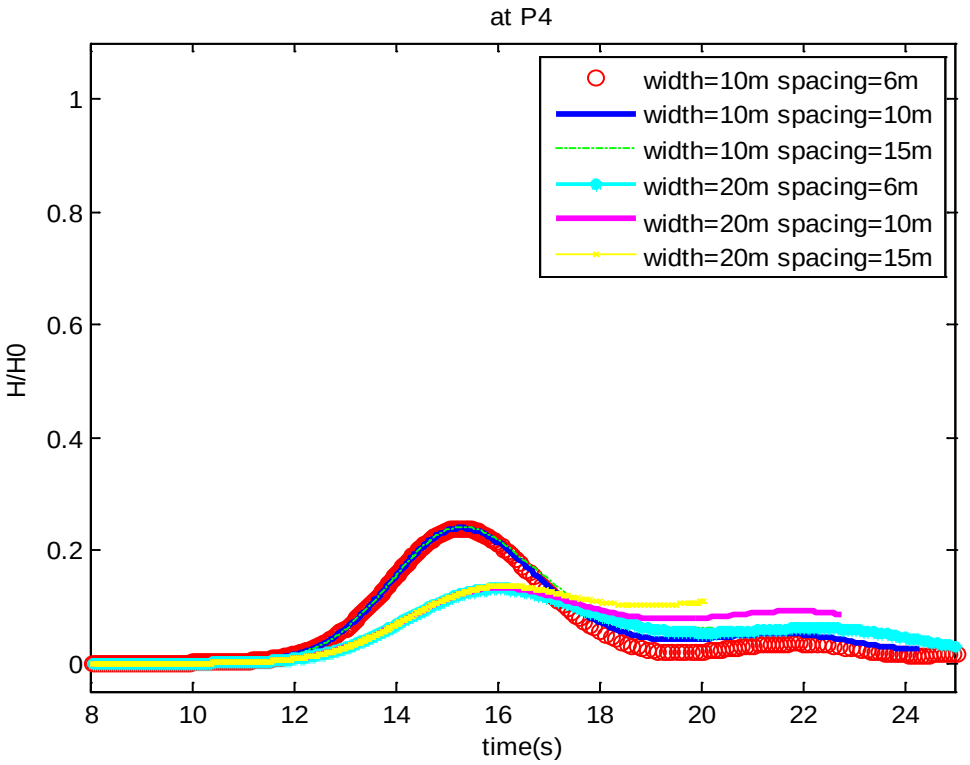

Figure 5. 31 the time histories of relative wave height at P4 for different vegetation conditions with porosity= 0.85.

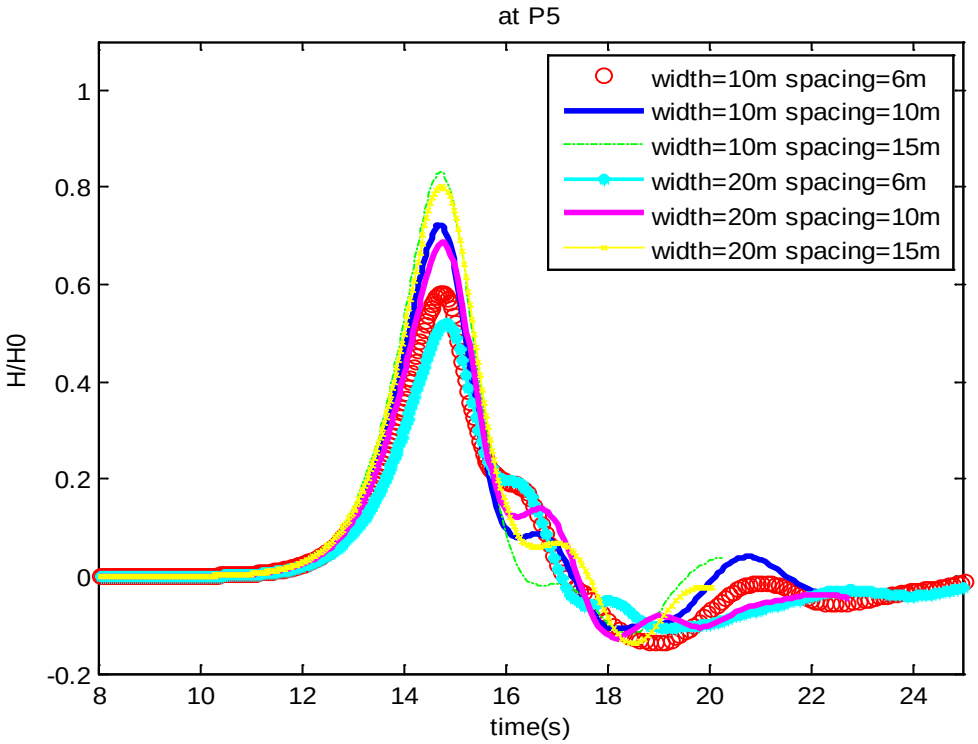

Figure 5. 32 the time histories of relative wave height at P5 for different vegetation conditions with porosity= 0.85.

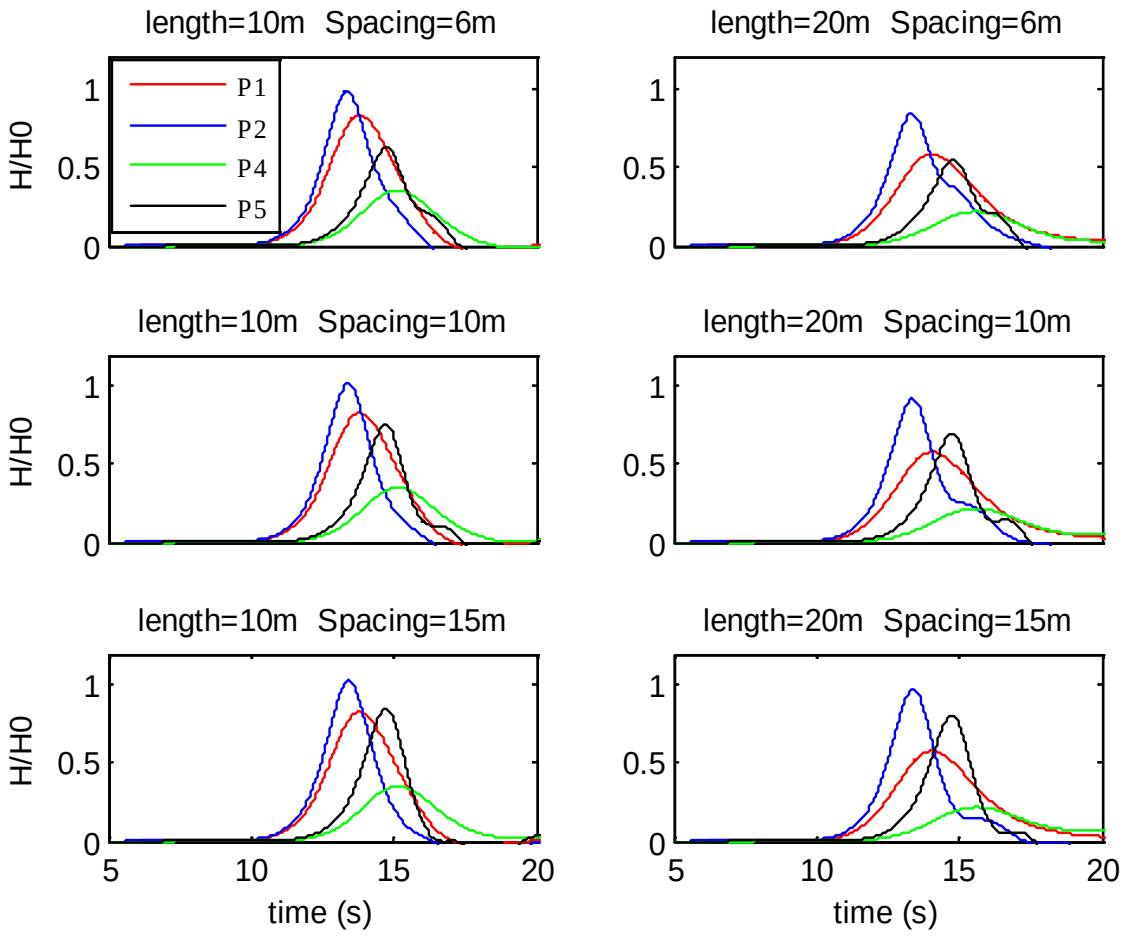

Figure 5. 33 the relative wave heights at four reference points for different test scenarios with porosity =0.90.

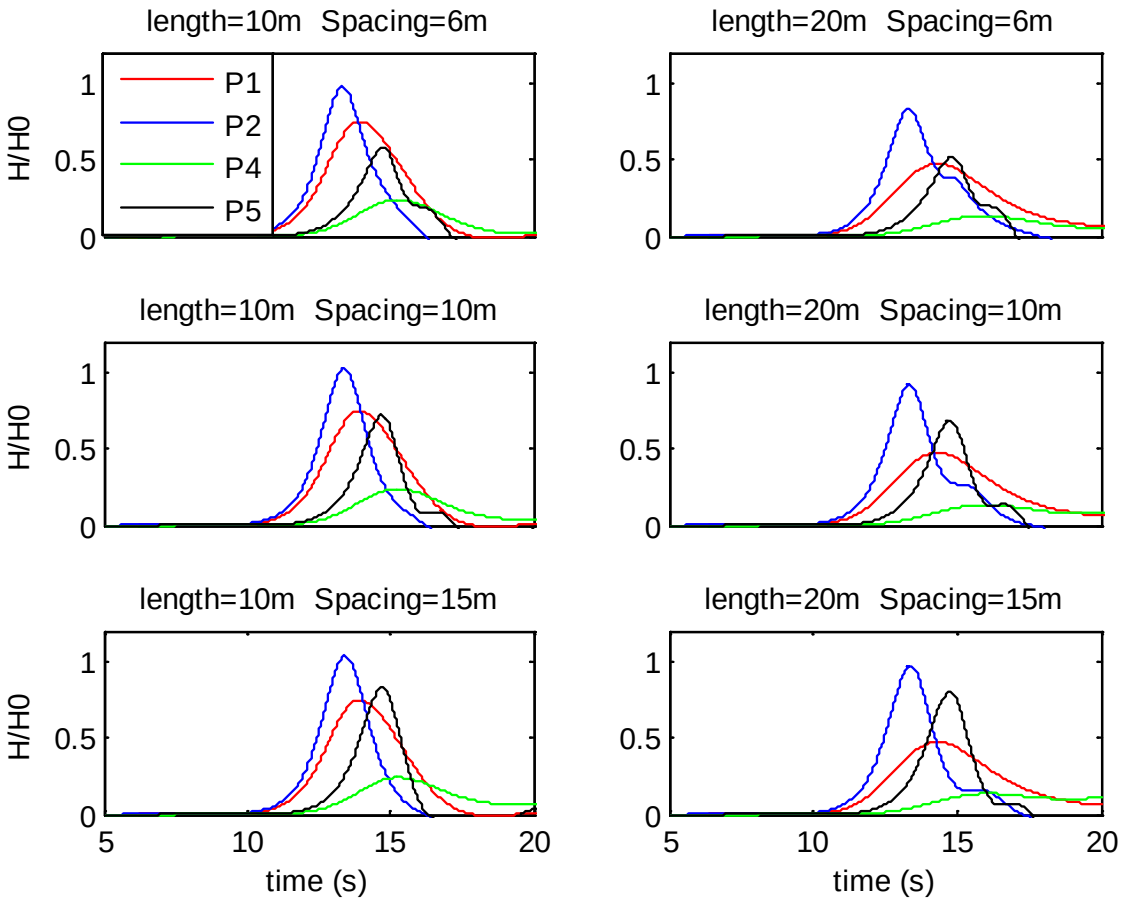

Figure 5. 34 the relative wave heights at four reference points for different test scenarios with porosity =0.85.

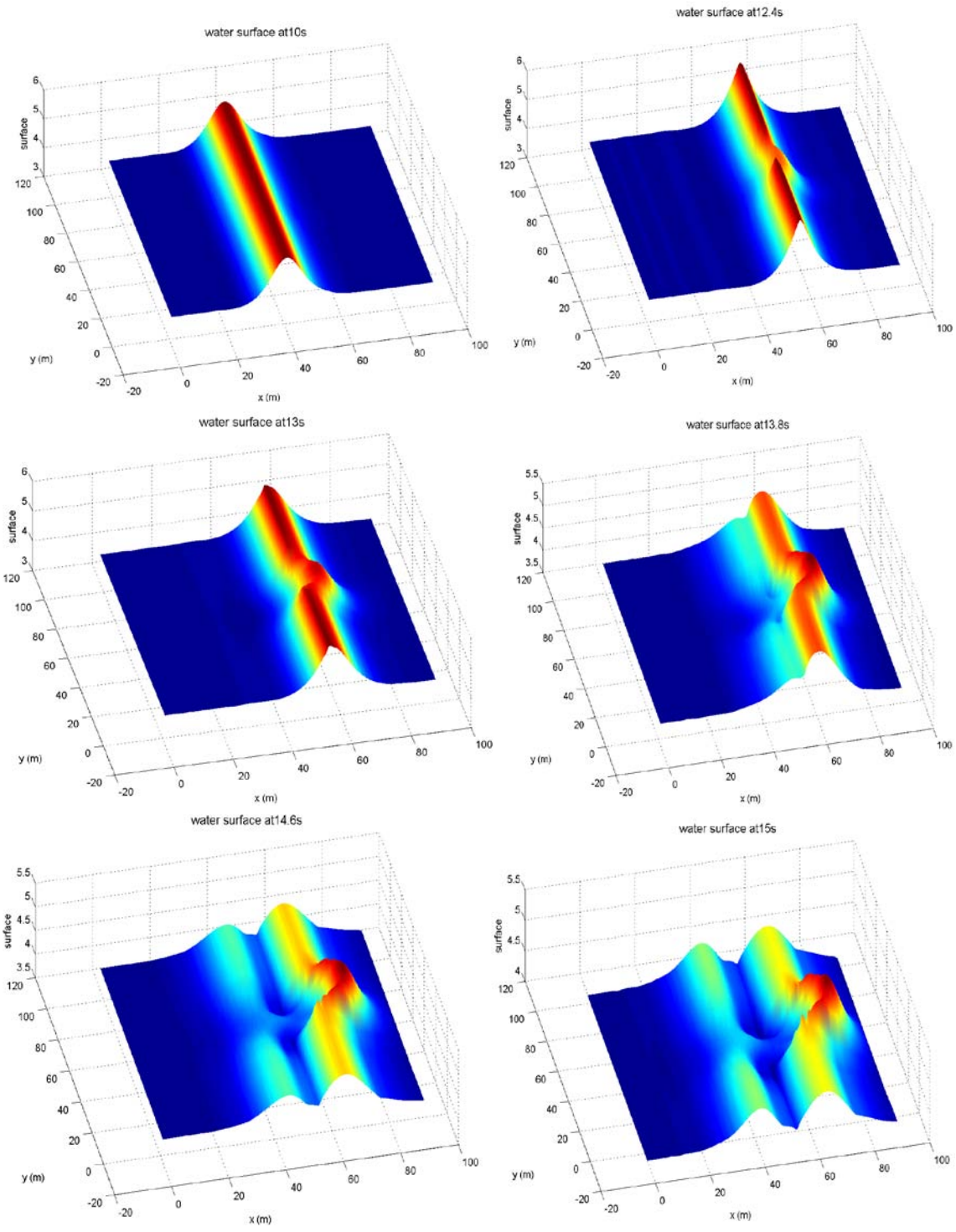

Figure 5. 35 Snapshots of surface elevation for the solitary wave passing through the 20m-vegetation region with a gap width of 15m at time 10s, 12.4s, 13s, 13.8s, 14.6s, and 15s respectively.

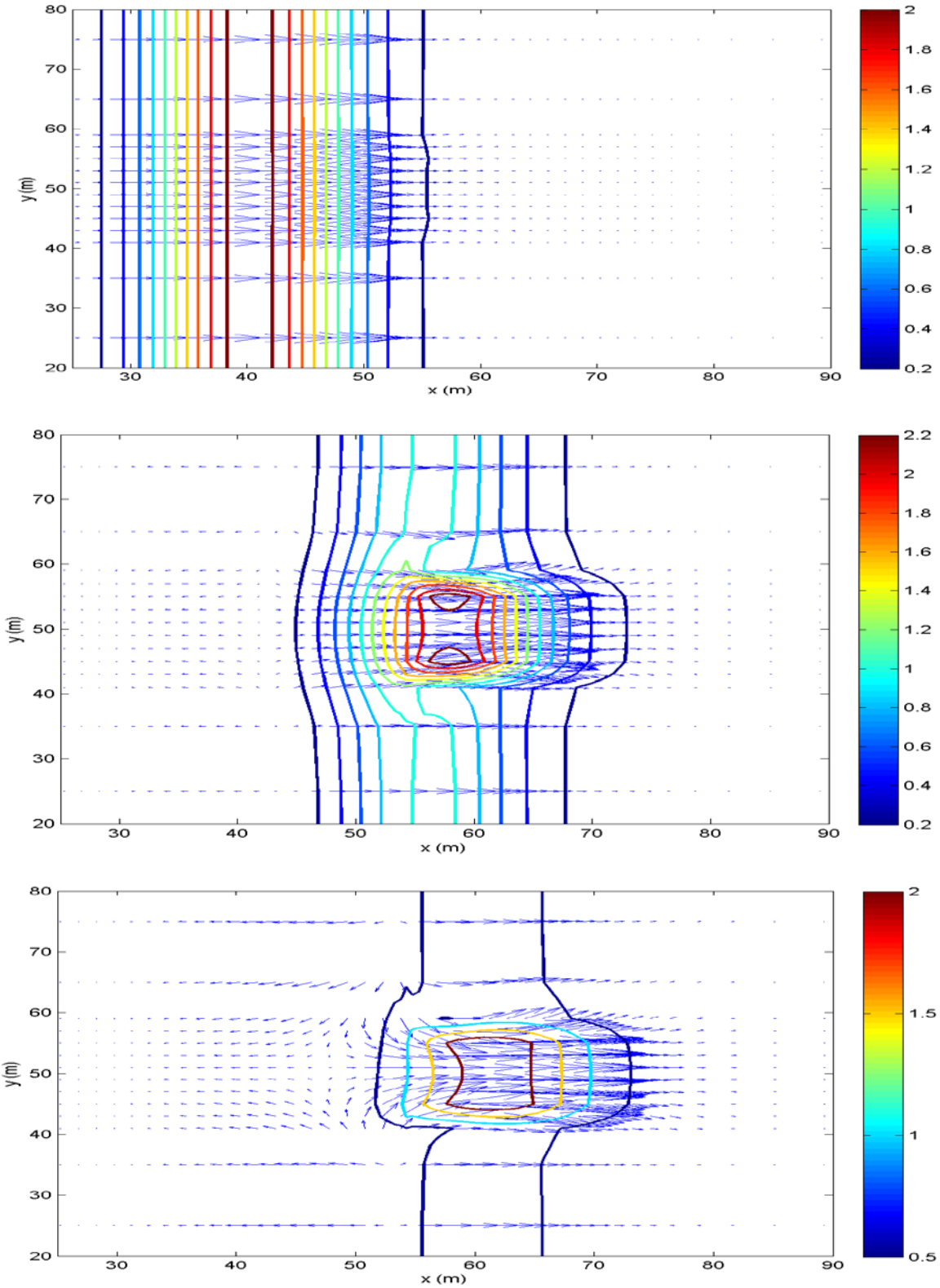

Figure 5. 36 Snapshots of velocity field and contour lines corresponding to the surface elevation at time 10s, 12.4s, 13s respectively. The color bars indicate the magnitude of velocities.

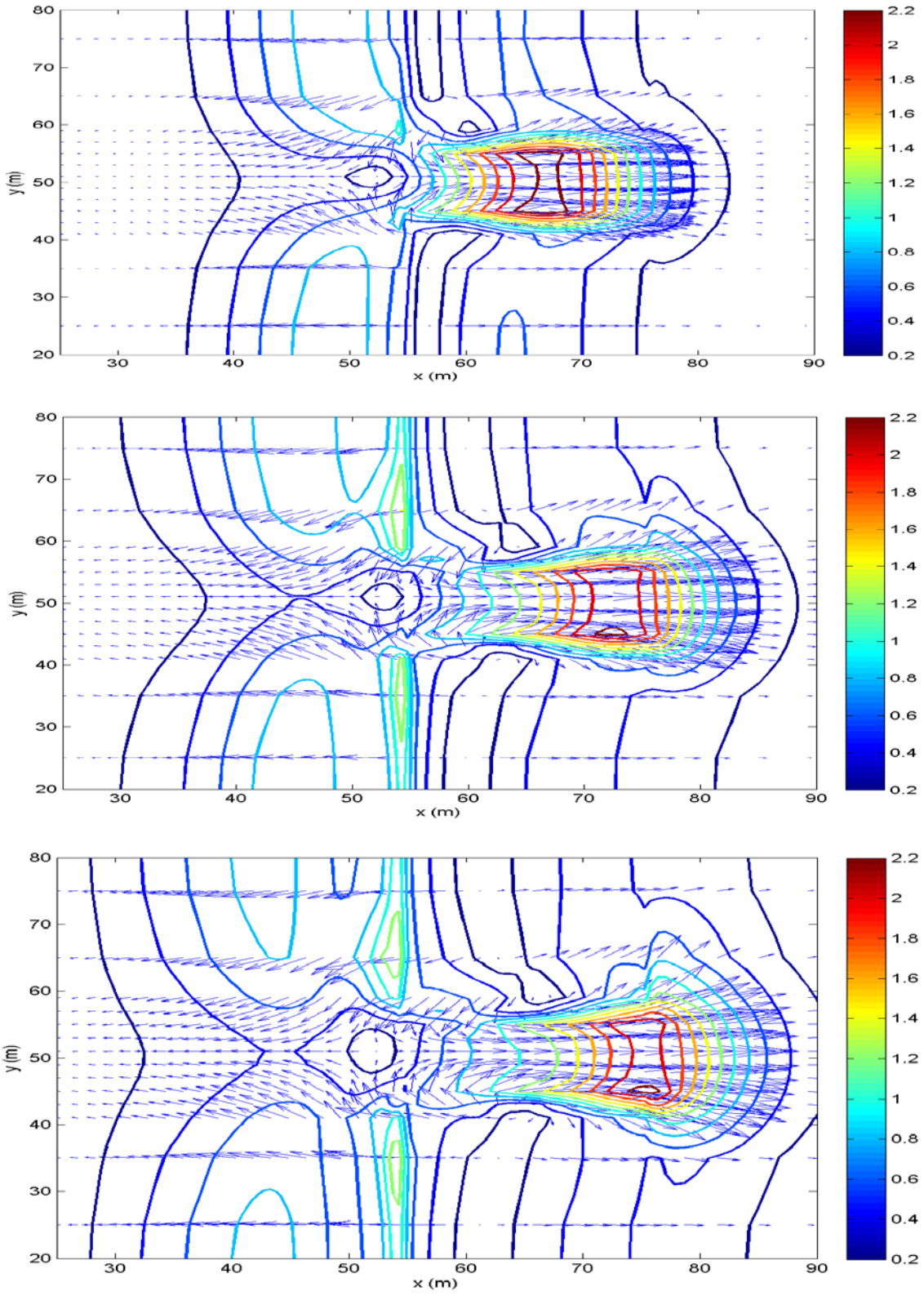

Figure 5. 37 Snapshots of velocity field and contour lines corresponding to the surface elevation at time 13.8s, 14.6s, and 15s respectively. The color bars indicate the magnitude of velocities.

Chapter 6

Conclusions and Future Work

6.1 Conclusions

In this thesis, a versatile 3-D numerical model for the study of wave-vegetation interaction has been developed and prescribed. The general three-dimensional governing equations of fluid motion in the vegetative region are rigorously derived. In particular, a temporal-volume double averaging method is employed to average the original three dimensional Navier-Stokes equations to introduce the vegetation effect into the fluid governing equations. This approach avoids the problem of a simple addition of the drag-related body force in the momentum equation which does not represent the energy budget correctly. After the double averaging, a system of modified momentum equations and energy budget equation is obtained by parameterizing the vegetation-related terms. The new system of equations has been successfully applied to the general three-dimensional fluid-vegetation problems, along with vegetation-related parameters that have been systematically derived, calibrated and validated.

In the above modified equations, drag force coefficient and inertial force coefficient are among the most significant parameters to be quantified. A series of experiments of wave propagating within the vegetation are conducted to investigate the variation of drag force coefficient and inertial force coefficient with wave conditions. Based on the experimental data, an empirical formula to calculate the vegetation drag force coefficient has been derived as a function of not only the Renolds number Re and porosity, which are largely

used in vegetation-open channel flow problem, but also KC number that can feature the wave characteristic. The formula can be used in the numerical modeling of vegetation effect on wave propagation.

Incorporating the above work, a new three-dimensional wave/flow model has been developed based on NEWTANK (Liu, D M, 2007) to study the fluid-vegetation interaction problem. The numerical model solves the newly derived system of equations for the two phase flow. The rigid vegetation is represented by the distribution of porosity which provides the convenient treatment of non-homogeneous distributed vegetation. A two-step projection method has been employed in the numerical solution, accompanied by a Bi-CGSTAB technique to solve the Pressure Poisson Equation (PPE) for the averaged pressure field. Volume-of-Fluid (VOF) method that is of second-order accuracy in interface reconstruction is used to track the free surface evolution. The drag and inertial force coefficients from current experiments are imbedded in the model.

The numerical model has been successfully validated against available analytical wave solutions and experiments without vegetation in terms of accuracies of free surface and velocity field. The model has also been used to study several cases of solitary wave propagating through vegetation. Even though the model is designed for variable porosity condition, the model was only run for cases with constant porosity at current stage. The results show that porosity and the coverage length of the vegetative region are two of the dominant factors on reducing wave height and current velocities. The effect of increasing the coverage length of vegetation can be equally achieved by reducing the porosity. In practice, an optimal arrangement of vegetation length and spacing should consider the vegetation characteristics. The force coefficients seem to be insignificant in the wave height dissipation at least in the condition of large porosity. The gap in vegetation region can amplify the current velocities and form a water jet which can cause more severe damages on the assets or human beings on its way. Therefore, for the general porosity of mangrove (85%-95%), the coverage length of 10-20m can reduce half of the incident wave height. However, special attention should be paid to the region having a vegetation gap. Coastal structures such as breakwaters are required to protect the assets along the gap. The spacing of the vegetation gap is suggested to be as small as possible with the fulfillment of usage. At last, the numerical model has been approved to be a robust model

for the study of wave-vegetation problem and can be used in the future coastal engineering studies. At last, the current numerical model mainly simulated the idealized vegetation conditions. In practice, the vegetation trunks may be broken up by large waves, which can in turn induce greater damages. Also, the debris in flow can affect the analysis and performance of numerical models. These effects are extremely difficult to be parameterized in the modeling, and therefore are not discussed in the current studies.

6.2 Recommendations for future extension

More studies of vegetation-wave interaction have been pursued in recent years due to its effectiveness in dissipating wave energy and in supporting the marine ecosystem. The studies presented in this thesis are attempts to better understand the physics of vegetation in mitigating tsunami waves. Although the first order physics have been addressed in the thesis, the following extensions may be worth pursuing.

1. To have a good representation of complex bathymetry or geometric features in practice, current treatment by setting the solid structures to be zero porosity requires extremely fine grids, which will be time-consuming or even unaffordable for a serial program. A natural extension to resolve this issue is parallelization of the model. At the same time, it will be more efficient to incorporate the terrain-following method into the model.
2. Even though the results show that the wave height dissipation is mainly affected by vegetation porosity and geometric configuration and not sensitive to the variation of force coefficients, the drag force and inertial force coefficients may still have significant impact on the turbulent energy budget and material diffusion among vegetation. More numerical and experimental studies are required to explore the effects of variable drag force and inertial force coefficients on the turbulent structures.
3. There have been studies revealing that vegetation has direct impact on coastal sediment transport. The mechanics of settling and re-suspension of sediments vary with the changing structures of the bottom shear layer and the turbulence

generated by the vegetation. The numerical program already has a preliminary sediment module. Coupling the sediment module with the well-calibrated vegetation module can advance the study of vegetation-affected sediment transport.

4. In this study, the vegetation is assumed to comprise of rigid cylinders. Field and laboratory experiments show that flexibility of vegetation in waves and currents may have a significant influence on the flow field and its turbulent structures. Further studies involving flexible vegetation would therefore be worthwhile. However, numerically simulating the motion of flexible vegetation and coupling the wave-vegetation interaction are major challenges and the use of bulk parameters backed by experimental studies may be necessary.

References

1. Andersen, B. G., Rutherfurd, I. D., and Western, A. W. 2006 An analysis of the influence of riparian vegetation on the propagation of flood waves. Environmental Modelling & Software, 21, 1290-1296.

2. Andersen, K.H., Mork, M., Nilsen, J.E.O., 1996. Measurement of the velocity profile in and above a forest of Laminaria hyperborean. SARSIA 81, 193–196.

3. Asano, T., Deguchi, H. and Kobayashi, N., 1993 Interaction between water waves and vegetation. *Proceedings of the 23rd coastal engineering conference,* pp2710-2723.

4. Baptist, M.J., Babovic, V., et al. 2007 On inducing equations for vegetation resistance. Journal of Hydraulic Res. 44(5), 435-450.

5. Barrett, R., Berry, M., et al, 2006 Templates for the Solution of Linear Systems: Building Blocks for Iterative Methods. Electronic version of the 2nd edition. SIAM.

6. Belcher, S. E., Jerram, N. and Hunt, J. C. R. 2003 Adjustment of a turbulent boundary layer to a canopy of roughness elements. J. Fluid Mech. 488, 369-398.

7. Breugem, W. P., Boersma, B. J., et al. 2005 The laminar boundary layer over a permeable wall. Transp. Porous Med., 59, 267-300.

8. Carrier, G.F. & Greenspan, H.P. 1958 Water waves of finite amplitude on a sloping beach. J. Fluid Mech. 4, 97-110.

9. Carrier, G.F., Wu, T.T. & Yeh, H. 2003 Tsunami run-up and draw-down on a plane beach. J. Fluid Mech. 475, 79-99

10. Chakrabarti, S.K., 1987 Hydrodynamics of offshore structures. WIT Press.

11. Chen, C-J, and Jaw, S-Y, 1998 Fundamentals of Turbulence Modeling. Taylor & Francis.

12. Chorin, A. J.. 1968 Numerical solution of the Navier-Stokes equations. Math. Comp., 22, pp. 745-762.

13. Chorin, A. J. 1969 On the convergence of discrete approximations of the Navier-Stokes equations. Math. Comp., 232, pp. 341-353.

14. Chow, V.T. 1954 Open Channel Hydraulics.

15. Christensen, E. D., 2006 Large eddy simulation of spilling and plunging breakers. Coastal Eng. Vol. 53, 463-485.

16. Chu, V. H., Wu, J. H. and K. E. 1991 Stability of transverse shear flows in shallow open channels. *J. Hydr. Engrg., ASCE,* Vol. 117, 10,pp1370-1381.

17. Cui, J. and Neary, V. S. 2002 Large eddy simulation (LES) of fully developed flow through vegetation. Proceedings of the Fifth International Conference on Hydroinformatics, UK, 39-44.

18. Dalrymple, R. A., Kirby, J. T., et al. 1984 Wave diffraction due to areas of energy dissipation. *Journal of Waterway, Port, Coastal and Ocean Engineering*, 110(1), 67-79.

19. Darby, S. E., and Thorne, C. R. 1996 Predicting Stage-discharge curves in channels with bank vegetation. *J. Hydr. Engrg*., 122(10), 583-586.

20. Darby, S. E. 1999 Effect of riparian vegetation on flow resistance and flood potential. *J. Hydr. Engrg*., 125(5), 443-454.

21. Dean, R. G. and R. A. Dalrymple. 1991 Water Wave Mechanics for Engineers and Scientists. Advanced Series on Ocean Engineering, edited by P. L.-F. Liu, 2. World Scientific.

22. Deardorff J. W. 1970 A numerical study of three-dimensional turbulent channel flow at large Reynolds numbers. J. Fluid Mech, 41: 453-480.

23. Defina, A., Bixio, A. C., 2005 Mean flow and turbulence in vegetated open channel flow. Water Resources Research 41:W07006. DOI 10.1029/2004WR003475.

24. Dubi, A.M., 1995. Damping of water waves by submerged vegetation: a case study on laminaria hyperborea. Ph.D. Thesis, University of Trondheim, Norway.

25. Dunn, C., López, F. and García, M. 1996 mean flow and turbulence in a laboratory channel with simulated vegetation. Civil Engineering Studies, Hydraulic Engineering Series No. 51. ISSN: 0442-1744.

26. Elwany, M. H. S., et al. 1995 Effects of southern California kelp beds on waves." *Journal of Waterway, Port, Coastal and Ocean Engineering*, 121(2), 143-150.

27. Elwany, M. H. S. and Flick, R. E. 1996 Relationship between kelp beds and beach width in Southern California. *Journal of Waterway, Port, Coastal and Ocean* Engineering, 122(1), 34-37.

28. Ergun, S. 1952. Fluid flow through packed columns. *Chem. Eng. Prog*., 48(2), 89-94.

29. Fadlum, E. A., Verzicco R, et al., 2000. Combined immersed-boundary finite-difference methods for three dimensional complex flow simulations. *J. Comput. Phys*., 161, 35-60.

30. Fathi-Maghadam, M. and Kouwen, N. 1997 Nonrigid, nonsubmerged, vegetative roughness on floodplains. J. Hydr. Eng., ASCE, 123(1), 51-57.

31. Fernando, H.J.S., McCulley, J.L., et al. 2005 Coral poaching worsens tsunami destruction. EOS 86(33).

32. Fernando, H.J.S., Samarawickrama, S.P., et al., 2008 Effects of porous barriers such as coral reefs on coastal wave propagation. Journal of Hydro-environment Research, 1, 187-194.

33. Finnigan, J. 2000 Turbulence in plant canopies. Annu. Rev. Fluid Mech. 32, 519-571.

34. Fischer-Antze,T., Stoesser, T., et al., 2001. 3D numerical modelling of open-channel flow with submerged vegetation J. Hydraulic Res., 39, 303-310.

35. Fitzmaurice, L., Shaw, R.H., Kyaw, T. P.U & Patton E.G. 2004 Three-dimensional scalar microfront systems in a large-eddy simulation of vegetation canopy flow. Boundary Layer Meteorol. 112:107-127

36. Ghisalberti, M. and H. Nepf. 2006. The structure of the shear layer over rigid and flexible canopies. *Environmental Fluid Mechanics* 6(3):277-301, DOI: 10.1007/s10652-006-0002-4.

37. Green, J. C. 2005 Modelling flow resistance in vegetated streams: review and development of new theory. Hydrol. Process. 19, 1245-1259(2005)

38. Grilli, S., & Svendsen, I. A. 1990 Computation of nonlinear wave kinematics during propagation and runup on a slope. Water wave kinematics, A. Torum and O. T. Gudmestad. Eds. NATO ASI Series E: Applied Sciences, 178, Kluwer Academic, Norwell , Mass

39. Grilli, S. T., M. A. Losada and F. Martin. 1994 Breaking Criterion and Characteristics for Solitary Wave Breaking Induced by Breakwaters. J. Waterw. Port C-ASCE, 120 (1), pp.74-92.

40. Grilli, S. T., I. A. Svendsen and R. Subramanya. 1997 Breaking Criterion and Characteristics for Solitary Wave Breaking on Slopes. J. Waterw. Port C-ASCE, 123 (3), pp.102-112.

41. Gu, Z., and Wang, H. 1991 Gravity waves over porous bottoms. Coastal Engineering, 15, 497-524.

42. Gueyffier, D., J. Li, A. Nadim, R. Scardovelli and S. Zaleski. 1999 Volume-of-fluid interface tracking with smoothed surface stress methods for three-dimensional flows. J. Comput. Phys., 152, 423-456.

43. Harada, K. and Imamura, F., 2005 Effects of coastal forest on tsunami hazard mitigation- a preliminary investigation. "*Tsunamis: Case Studies and Recent*

Developments", edited by K. Satake, 279-292.

44. Helmiö, T., 2002 Unsteady 1D flow model of compound channel with vegetated floodplains. Journal of Hydrology 269(2002) 89-99

45. Helmiö, T., 2005 Unsteady 1D flow model of a river with partly vegetated floodplains- application to the Rhine River. Environmental Modelling & Software 20(2005): 361-375

46. Henderson, F.M. 1966 Open Channel Flow, MacMillian, New York, pp552

47. Hendrickson, K. and D. K. P. Yue. 1997 Large-scale computations of free-surface turbulence. ONR Workshop on Free-surface and Wall-bounded Turbulence and Turbulence Flows, Pasadena, CA.

48. Howes, F. A. and Whitaker, S. 1985 The spatial averaging theorem revisited. Chemical Engineering Science, 40(8), 1387-1392.

49. Hsieh, P-C, Shiu, Y-S, 2006 Analytical solutions for water flow passing over a vegetal area. Advances in Water Resources, 29, 1257-1266.

50. Huthoff, F., Augustijn, D. C. and Hulscher, S.J.M.H., 2007 Analytical solution of the depth-averaged flow velocity in case of submerged rigid cylindrical vegetation. Water Resources Research, 43, W06413.

51. Ikeda, S., Ohta K. and Hasegawa H. 1994 Instability induced horizontal vortices in shallow open channel flows with an inflection point in skewed velocity profile. *J. Hydroscience and Hydr. Engrg. Tech.*, Japan Socity of Civil Engineers, Vol. 12 (2), pp69-84.

52. Ikeda, S., Yamada, T. and Toda Y. 2001 Numerical study on turbulent flow and honami in and above flexible plant canopy. *Int. J. Heat and Fluid Flow*. Vol. 22, pp252-258.

53. Imai K. and Matsutomi, H. (2005) "Fluid force on vegetation due to tsunami flow on a sand spit." "*Tsunamis: Case Studies and Recent Developments*", edited by K. Satake, pp293-304.

54. James, C. S., Birkhead, A. L., et al. 2004 Flow resistance of emergent vegetation. Journal of Hydraulic Research, 42(4), 390–398.

55. Järvelä, J. 2002 Flow resistance of flexible and stiff vegetation: a flume study with natural plants. Journal of Hydrology 269, 44-54

56. Järvelä, J. 2005 Effect of submerged flexible vegetation on flow structure and resistance. Journal of Hydrology 307, 233-241.

57. Jaluria, Y., Torrance, KE., 2003 Computational heat transfer. Taylor & Francis, New

York, USA.

58. Kanoglu, U. & Synolakis, C.E. 1998 Long wave runup on piecewise linear topographies. J Fluid Mech. 374, 1-28.

59. Karunarathna, S.A.S.A. and Lin, P.Z. 2006 Numerical simulation of wave damping over porous seabeds, *Coastal Eng. 5*3, 845-855.

60. Kim, J., P. Moin and R. Moser. 1987 Turbulence statistics in fully developed channel flow at low Reynolds number. J. Fluid Mech., 177, pp.133-166.

61. Kim, S.K., Liu, P.L.-F., and Liggett, J. A. 1983 Boundary integral equation solutions for solitary wave generation, propagation and runup Coast. Engrg. 7, 299-317

62. Kobayashi, N., Otta, A. and Roy, I. 1987 Wave reflection and runup on rough slopes. J. Wtrwy. Port, Coast. And Oc. Engrg., ASCE, 113(3), 282-298

63. Kobayashi, N., Raichle, A.W., Asano, T., 1993. Wave attenuation by vegetation. Journal of Waterway, Port,Coastal and Ocean Engineering, ASCE 119 (1), 30–48.

64. Kouwen, N., and Unny, T. E. 1973 Flexible roughness in open channels. J. Hydraul. Div., ASCE, 99(5), 713-828.

65. Kouwen, N., 1988 Field estimation of the biomechanical properties of grass. J. Hydr. Res. 26(5), 559-568.

66. Kouwen, N. 1992 Modern approach to design of grassed channels. J. Irrig. And Drainage Engrg. ASCE, 118(5), 713-728

67. Kouwen, N., Fathi-Moghadam, M., 2000 Friction factors for coniferous trees along rivers. Journal of Hydraulic Engineering, 126(10), 732-740

68. Lee, J.-J., J. E. Skjelbreia and F. Raichlen. 1982 Measurement of Velocities in Solitary Waves. ASCE J. of Waterway, Port, Coastal and Ocean Division, 108(WW2), pp. 200-218

69. Lemos, C. M. 1992 Wave Breaking. Springer.

70. Li, C. W. and Yan, K. 2007 Numerical Investigation of Wave–Current–Vegetation Interaction. Journal of Hydraulic Engineering 133(7) 794–803.

71. Li, R.-M, Shen, H.W. 1973 Effect of tall vegetations on flow and sediment. Journal of the Hydraulics Division, ASCE 99(5), 793-814

72. Lin, P., and P. L.-F. Liu. 1998a A numerical study of breaking waves in the surf zone. J. Fluid Mech., 359, pp. 239-264.

73. Lin, P., and P. L.-F. Liu. 1998b Turbulence transport, vorticity dynamics, and solute mixing under plunging breaking waves in surf zone. J. Geophys. Res., 103(C8), pp. 15,677-15,694.

74. Lin. P., Chang. K., P. L.-F. Liu, 1999 Runup and rundown of solitary waves on sloping beaches. J. Wtrwy. Port, Coast. And Oc. Engrg., Sep/Oct, 247-255

75. Lin, P., 2006 A multiple-layer σ-coordinate model for simulation of wave-structure interaction. Computers & Fluids, 35, 147-167.

76. Liu, D M, 2007 Numerical modeling of three-dimensional water waves and their interaction with structures. PhD thesis, NUS.

77. Liu, P. L.-F., and R.A. Dalrymple, 1984 The damping of gravity water waves due to percolation. Coastal Engineering, 8, 33-49.

78. Liu, P. L.-F., Yoon, S.B., Seo, S.N. and Cho, Y.-S. 1994 Numerical simulation of tsunami inundation at Hilo, Hawaii. Recent development in tsunami research. M.I. El-Sabh, ed. Kluwer Academic, Boston

79. Liu. P. L.-F., Cho, Y.-S., Briggs, M. J., Kanoglu, U., and Synolakis, C. 1995 Runup of solitary waves on a circular island. J. Fluid Mech. 302, 259-285

80. Liu, P. L.-F and P. Lin. 1997 A numerical model for breaking wave: the volume of fluid method. Research Rep. CACR-97-02. Center for Applied Coastal Research, Ocean Eng. Lab., Univ. of Delaware, Newark, Delaware 19716.

81. Liu, P. L.-F, Lin. P., et al. 1999. Numerical modeling of wave interaction with porous structures, Journal of Waterway, Port, Coastal, and Ocean Engineering, 125, 322-330.

82. Liu, P. L.-F, Lynett, P., et al. 2005, Observations by the International Tsunami survey team in Sri Lanka. Science 308 (10 June), 1595.

83. López, F. and García, M. 1997 Open-channel flow through simulated vegetation: turbulence modeling and sediment transport. Wetlands Research Program Rep. WRP-CP-10, U.S. Army Corps of Engineers, Washington, D. C.

84. López, F. and García, M. 1998 Open channel flow through simulated vegetation: suspended sediment transport modeling. Water resources research, Vol. 34(9), pp2341-2352.

85. López, F. and García, M. 2001 Mean flow and turbulence structure of open-channel flow through non-emergent vegetation. J. Hydraul. Eng. 127(5), 392-402.

86. Lovas, S.M., Torum, A., 2001. Effect of kelp Laminaria hyperborea upon sand dune erosion and water particle velocities. Coastal Engineering 44, 37–63.

87. Massel, S.R., Furukawa, K., Brinkman, R.M., 1999. Surface wave propagation in mangrove forests. Fluid Dynamic Research 24 (4), 219–249

88. Meijer, D., Van Velzen, E.H., 1999. Prototype-scale flume experiments on hydraulics roughness of submerged vegetation. Proceedings of 28th International Association for Hydraulic Research (IAHR) Conference. IAHR,Graz, Austria.

89. Mendez, F. J. and Losada, I. J. 2004 An empirical model to estimate the propagation of random breaking and nonbreaking waves over vegetation fields, *Coast. Eng*. 51, 103-118.

90. Moller, I., Spencer, T., et al. 1999 Wave transformation over salt marshes: a field and numerical modeling study from north Norfolk, England. *Estuarine, Coastal and Shelf Science*, 49(3), 411-426.

91. Moller, I. 2006. Quantifying saltmarsh vegetation and its effect on wave height dissipation: results from a UK east coast saltmarsh Estuarine. *Coastal and Shelf Science*, 69(3-4), 337-351.

92. Mork, M., 1996. The effect of kelp in wave damping. SARSIA 80, 323–327.

93. Murphy, E., M. Ghisalberti, and H. Nepf. 2007. Model and laboratory study of dispersion in flows with submerged vegetation. *Water Res. Res.* 43, W05438, doi:10.1029/2006WR005229.

94. Musleh, F. A., and Cruise, J. F., 2006 Functional relationships of resistance in wide flood plains with rigid unsubmerged vegetation. J. Hydrau. Eng., 132(2), 163-171.

95. Nadaoka, K. and Yagi, H. 1998 Shallow-water turbulence modeling and horizontal large-eddy computation of river flow. J. Hydr. Engrg., Vol. 124, pp493-500

96. Naot, D., Nezu, I. and Nakagawa, H. 1996 Hydrodynamic behavior of partly vegetated open channels. J. Hydr. Engrg., Vol. 122, No. 11, pp625-633.

97. Neary, V. S. 2003 Numerical solution of fully developed flow with vegetative resistance. Journal of Engineering Mechanics, 129(5), 558-563.

98. Nepf, H.M., 1999. Drag, turbulence and diffusion in flow through emergent vegetation. Water Resources Research 35, 479–489

99. Nepf, H.M., Vivoni, E.R., 2000. Flow structure in depth-limited, vegetated flow. Journal of Geophysical Research, 105 (C12), 28547–28557.

100. Nezu, I. and Nakagawa, H., 1993 Turbulence in Open-Channel Flows. A.A.Balkema, IAHR/AIRH Monograph.

101. Pasche, E., Rouvé, G. 1985 Overbank flow with vegetatively roughened flood plains. Journal of the Hydraulics Engineering, 111(9), 1262-1278

102. Patton, E.G., Shaw, R.H., Judd, M.J. and Raupach, M.R. 1998 Large Eddy Simulation of Windbreak Flow. Boundary Layer Meteorol. 87: 275-306.

103. Poggi, D., Porporato, A., Ridolfi, L., 2004 The effect of vegetation density on canopy sub-layer turbulence. Boundary layer Meteorology. 111: 565-587.

104. Qian, L., Causon, D. M., et al, 2003 Cartesian Cut Cell Two-Fluid Solver for Hydraulic Flow Problems. Journal of Hydraulic Engineering, 129 (9), 688-696.

105. Raupach, M. R. and Tom, A. S. 1981 Turbulence in and above plant canopies. *Annu. Rev. Fluid Mech.,* Vol. 13, 97-129.

106. Raupach, M.R. and Shaw, R.H. 1982 An averaging procedure for flow with vegetation canopies. Boundary Layer Meteorology 22,79-90.

107. Ree, W. O., and Palmer, V. J. 1949 Flow of water in channels protected by vegetative linings. Tech. Bull. No. 967, Soil Conservation Service, U.S. Department of Agriculture, Washington, D.C.

108. Rider, W. J. and Kothe, D. B. 1998 Reconstructing Volume Tracking. J. Comput. Phys., 141, 112-152.

109. Righetti, M. & Armanini, A. 2002 Flow resistence in open channel flows with sparsely distributed bushes. Journal of Hydrology 269: 55-64.

110. Rodi, W. 1984 Turbulence models and their application in hydraulics-a state of the art review. Second revised edition. IAHR.

111. Rogallo, R. S., 1981 Numerical Experiments in Homogeneous Turbulence. Technical Rep. TM81315, NASA.

112. Sand-Jensen K. 2003 Drag and reconfiguration of freshwater macrophytes. Freshwater Biology 48: 271-283.

113. Sawaragi, T. and Deguchi, I. 1992 Waves on permeable layers. Coastal engineering, 1531-1544.

114. Shaw, R.H. and Schumann, U. 1992 Large-Eddy Simulation of Turbulent Flow above and within a Forest. Boundary layer Meteorol. 61:47-64.

115. Schlichting, H. and Gersten, K., 2000 Boundary-Layer Theory. Springer; 8th edition.

116. Shimizu, Y., Tsujimoto, T., Nakagawa, H., 1992. Numerical study on turbulent flow over rigid vegetation-covered bed in open channels. J. Hydr., Coastal Environ. Eng. JSCE 447, 35-44 (in Japanese)

117. Shimizu, Y., and Tsujimoto, T. 1994 Numerical analysis of turbulent open-

channel flow over vegetation layer using a $k-\varepsilon$ turbulence model. *J. Hydrosci. Hydr. Eng*. 11(2), 57-67.

118. Skyner, D.. A 1996 Comparison of Numerical Predictions and Experimental Measurement of the Internal Kinematics of a Deep-water Plunging Wave. J. Fluid Mech., 315, pp. 51-64.

119. Stephan, U. & Gutknecht. D. 2002 Hydraulic resistance of submerged flexible vegetation. Journal of Hydrology 269(2002) 27-43

120. Su, X.H. & Li, C.W. 2002 Large eddy simulation of free surface turbulent flow in partly vegetated open channels. Int. J. Numer. Meth. Fluids. 39: 919-937

121. Synolakis, C.E. 1987 The run-up of solitary waves. J. Fluid Mech. 185, 523-545

122. Tamai, N., Asaeda, T. and Ikeda, H. 1986 Study on generation of periodical large surface eddies in a composite channel flow. *Water Resour. Res*., Vol. 27 (7), pp1129-1138.

123. Tanino, Y. and H. Nepf. 2008. Lateral dispersion in random cylinder arrays at high Reynods number, *J. of Fluid Mechanics*, 600: 339-371.

124. Teeter, A. M., et al. 2001 Hydrodynamic and sediment transport modeling with emphasis on shallow-water, vegetated areas (lakes, reservoirs, estuaries and lagoons). *Hydrobiologia*, 444: 1–23.

125. Tsujimoto, T. and Kitamura, T. 1992 Appearance of organized fluctuations in open channel flow with vegetated zone. *KHL- Commun.*, Kanazawa *Univ.*, No.3, pp37-45.

126. Türker, U., Yagci, O., and Kabdasli, M.S. 2006 Analysis of coastal damage of a beach profile under the protection of emergent vegetation. Ocean Engineering 33(2006) 810-828.

127. Wang, C. Z., Wu, G. X., 2006 An unstructured-mesh-based finite element simulation of wave interactions with non-wall-sided bodies. Journal of Fluids and Structures, 22, 441-461.

128. Watanabe, T. 2004 Large-eddy simulation of coherent turbulence structures associated with scalar ramps over plant canopies. Boundary Layer Meteorology. 112:307-341.

129. Wheeler, J. D. 1970 Method for calculating forces produced by irregular waves. *J. Petrol. Technol*. March, 119-137.

130. Whitaker, S. 1986 Flow in porous media I: a theoretical derivation of Darcy's Law. Transport in Porous Media 1, 3-25.

131. Whitaker, S. 1996 The Forchheimer equation: a theoretical development. Transport in Porous Media, 25, 27-61.

132. Wilson C.A.M.E., T. Stoesser, P.D. Bates, &A.B. Pinzen, 2003 Open channel flow through different forms of submerged flexible vegetation. Journal of Hydraulic Engineering. November 2003, 847-853

133. Wilson, N. R., and Shaw, R. H. 1977 A higher-order closure model for canopy flow. J. Appl. Meteorology, 16, 1198.

134. Wu. F.-C, Shen, H.W., Chou, Y-J., 1999 Variation of roughness coefficients for unsubmergedd and submerged vegetation. Journal of Hydraulic Engineering 125(9), 934-942

135. Yoshida, H. & Dittrich, A. 2002 1D unsteady-state flow simulation of a section of the upper Rhine. Journal of Hydrology 269: 79-88

136. Yasuda, T., H. Mutsuda, N. Mizutani. 1997 Kinematic of overturning solitary Waves and Their Relations to Breaker Types. Coastal Engng., 29, pp. 317-346.

137. Yen, B.C., 2002. Open channel flow resistance. Journal of Hydraulic Engineering 128, 20–39

138. Zhuang, F, and Lee J. J. 1996. A viscous rotational model for wave overtopping over marine structure. In Proc 25th Int. Conf. Coast Eng, ASCE, 2178–2191.

139. Zhang, J., Randall, R.E. and Spell, C. A. 1991. On wave kinematics approximate methods. In 23rd *Annual Offshore Technology Conference*, OTC 6522, 6-9 May, Houston, TX.

140. Zhao, Q., Tanimoto, K., 1998. Numerical simulation of breaking waves by large eddy simulation and VOF method. Proc. of the 26th Int. Conf. Coastal Eng., vol. 1. ASCE, pp. 892 – 905.